Study and modeling of the CO2 frosting on a gliding temperature evaporator

Joseph Toubassy

ParisTech
INSTITUT DES SCIENCES ET TECHNOLOGIES
PARIS INSTITUTE OF TECHNOLOGY

MINES ParisTech

École doctorale n° 432 : Sciences des Métiers de l'Ingénieur

Doctorat ParisTech

T H È S E

pour obtenir le grade de docteur délivré par

l'École nationale supérieure des mines de Paris

Spécialité " Energétique "

Présentée et soutenue publiquement par

Joseph TOUBASSY

Le 10 octobre 2012

ÉTUDE ET MODÉLISATION DU GIVRAGE DU CO_2 SUR UN ÉVAPORATEUR À GLISSEMENT DE TEMPÉRATURE

STUDY AND MODELING OF THE CO_2 FROSTING ON A GLIDING TEMPERATURE EVAPORATOR

CONFIDENTIELLE

Fin de confidentialité (10 octobre 2022)

Directeur de thèse : **Denis CLODIC**

Co-encadrement de la thèse : **Maroun NEMER**

Jury

M. Daniel FAVRAT, Professeur, EPFL STI IGM LENI	Rapporteur
M. Pierre NEVEU, Professeur des universités, PROMES CNRS	Rapporteur
M. Eckhard GROLL, Professeur, Purdue University	Rapporteur
M. Dominique MARCHIO, Professeur, MINES ParisTech	Examinateur
M. Denis CLODIC, Directeur de recherche émérite, MINES ParisTech	Directeur de thèse

MINES ParisTech
Centre Energétique et Procédés
5 Rue Léon Blum 91120 Palaiseau

T H È S E

"Excellence is never an accident.
It is always the result of high intention,
sincere effort, and intelligent execution;
it represents the wise choice of many
alternatives - choice, not chance,
determines your destiny."

Aristotle

Acknowledgments

I thank Denis CLODIC, who has directed and supported this work and I am sincerely thankful for his guidance, advice, encouragement and positive attitude throughout my Ph.D. studies.

It is a great honor for me that Mr. Daniel FAVRAT, Mr. Eckhard GROLL, and Mr. Pierre NEVEU accepted to evaluate this study. I also thank Mr. Dominique MARCHIO for accepting to be a member of the examination board.

I thank EReIE Company for supporting and funding this study.

I would like to thank Maroun NEMER, manager of the Centre for Energy and Processes – Paris Palaiseau (CEP), for providing me excellent working conditions and useful thoughts to complete the work, and for managing the thesis during the last two years.

I thank Youssef RIACHI for his great managing of the thesis during the first year. And thank you for supporting me throughout these three years. Your advices have helped me enormously in moving forward my thesis project.

I thank Anne-Marie BONNET for always being present when needed and helping me since my arrival in France. Thank you for your extended meticulous proofreading.

I would like to thank Dr. Khalil El KOURY, professor at the Faculty of Engineering of the Lebanese University. Thanks to him I had the opportunity to pursue my studies in France.

I also would like to thank all the administration staff of the CEP. I express my grateful thanks to Philomène ANGELOSANTO, Marie-Astrid KRAMES and Rocio VALDEZ.

I thank Elias BLOULAWZ and Mourad YOUNES for their scientific support.

I thank Philippe CALVET for his daily interventions on my computers.

I am very thankful to all my colleagues who helped me in the test bench realization: Baptiste DUJARDIN, Brett GUERARD, Erwan PRIMA, and Youssef LARABI. You have executed a great job! I also thank Franck FAYOLLE for ensuring the security during the test bench realization and for his important help for solving technical problems. And certainly I thank Gerard HELIE, your jokes made our days.

My sincere thanks for all my colleagues who shared with me the “Salle Soleil”, especially Ludovic De OLIVIERA and Olivier CALMELS. I thank also all the CEP working team, who created a suitable and encouraging working environment.

Thank you Cosette for your help. Without your encouragement I would have never finished this work.

Special thanks for all my friends who were sharing with me the same joys and suffering: Sorina, Grace, Haytham, Boutros, Samer, and Nada.

Finally I’m very thankful to my parents and my sisters who supported and encouraged me during my studies. Big thanks also to my uncles Elie, Mounir, and Marwan.

Contents

Nomenclature

Roman letter symbols

T: Temperature, K

p: Pressure, kPa

h: Specific enthalpy, kJ.kg^{-1}

a: The four vibrational contributions in the free energy, cal.mol^{-1} = 4.184 J.mol^{-1}

s: Specific entropy, kJ.kg^{-1}.K^{-1}

c_p: Heat capacity, kJ.kg^{-1}

ρ: Density, kg.m^{-3}

e: Saturation relative concentration, dimensionless

x: Mass concentration ratio, dimensionless

r: Specific gas constant, J.kg^{-1}.K^{-1}

R: Universal gas constant, J.mol^{-1}.K^{-1}

m: Mass, kg

M: Molar mass, kg.kmol^{-1}

V: Volume, m^3

v: Specific volume, m^3.kg^{-1}

Q: Cooling capacity, kW

ΔL: Heat of sublimation, kJ.kg^{-1}

$P_{elec.}$: Electrical power, kW

E_{fuel}: Used fuel heat capacity, kW

$\dot{N}$: Molar flow rate, mol.s^{-1}

δW_{min}: Minimum theoretical work of gas separation, J.mol^{-1}

t_{ind}: Induction period, s

t_r: Relaxation time, s

t_n: Time of formation, s

t_g: Time of nucleus growth, s

ΔT_{sup}: Supercooling driving potential, K

T_{sub}: Sublimation temperature, K

ΔG: Gibbs free energy change, J

ΔG_S: Surface free energy, J

ΔG_V: Volume free energy, J

r: Crystal radius, m

σ: Interfacial tension, N.m^{-1}

k_B: Boltzmann constant, J.K^{-1}

N_A: Avogadro number, mol^{-1}

S: Supersaturation ratio

v: Molecular weight, $kg.molecule^{-1}$

n_c: Nucleation coefficient $\#.m^{-3}.s^{-1}$

θ: Contact angle

r_c: Critical radius, m

I: Nucleation rate, $\#.\ m^{-3}.s^{-1}$

u: Velocity, $m.s^{-1}$

Y: Mass fraction

Greek letter symbols

η: Efficiency

Θ: Carnot factor

λ: Convective heat transfer coefficient, $W.m^{-2}.K^{-1}$

$\bar{\rho}$: Average density, $kg.m^{-3}$

δ: Frost thickness, m

φ: Porosity

α: Volume fraction

ϑ: Source term

$\bar{\bar{\tau}}_i$: Stress strain tensor

French Summary

Résumé

Introduction Générale

Le dioxyde de carbone est le principal gaz à effet de serre émis en 2004 au niveau mondial et il représente 76,7 % des émissions anthropiques. La production d'énergie constitue 78,8 % des émissions de CO_2 provenant des combustibles fossiles et des minéraux. Compte tenu de la quantité d'émissions de CO_2 dans le monde et ses impacts sur le climat, leur réduction est une nécessité urgente. La croissance rapide de la population et l'augmentation explosive de la demande d'énergie rend difficile la réduction de la consommation d'énergie. Le captage du dioxyde de carbone et son stockage appliqué à un grand nombre de sources fixes constitue une solution privilégiée pour réduire les émissions. Les procédés de captage du CO_2 sont regroupés en trois catégories principales : la postcombustion, l'oxy-combustion et la précombustion.

Une nouvelle méthode de captage de CO_2 en postcombustion, connue sous le nom "Anti-sublimation" est développée. Compte tenu du fait que la température de saturation du CO_2 est la plus élevée dans les fumées déshydratés, le CO_2 est le premier composant à se solidifier par refroidissement des fumées à des températures de l'ordre de -120 °C. A cet effet, un échangeur de chaleur de type tubes-ailettes est utilisé pour refroidir les fumées. Le CO_2 est séparé par anti-sublimation, passant directement de la phase vapeur à la phase solide en formant un dépôt sur les ailettes de l'échangeur. Comme le CO_2 est séparé par anti-sublimation sur des surfaces refroidies, sa concentration diminue tout au long de l'échangeur de chaleur (appelé CFX). Ainsi, des températures plus basses sont nécessaires pour assurer 90 % du captage du CO_2. Afin d'améliorer les performances du procédé, la consommation d'exergie de l'échangeur de chaleur doit être minimisée en réduisant la différence de températures entre les fluides frigorigènes et les fumées et en assurant un glissement de température (20 K) capable de former des dépôts homogènes de CO_2 solide.

Dans le Chapitre 1, l'analyse exergétique de l'échangeur de chaleur est présentée en montrant l'importance de l'optimisation de l'agencement de l'échangeur de chaleur et du glissement de la température du mélange de fluides frigorigènes. L'effet de l'optimisation exergétique du CFX sur l'ensemble du processus de captage est démontré. Le concept de travail théorique minimal de séparation des gaz est analysé pour calculer l'efficacité du procédé de captage du CO_2. Comme les propriétés physiques et thermodynamiques du CO_2 solide pour des températures inférieures au point triple ne sont pas définies, une étude bibliographique est réalisée pour assembler les mesures expérimentales disponibles. De nouvelles équations sont proposées pour calculer l'enthalpie du CO_2, son entropie et sa masse volumique pour des équilibres solide-vapeur. Pour représenter le procédé de captage du CO_2 par anti-sublimation, un graphique psychrométrique est développé en considérant un mélange binaire constitué d'azote et de dioxyde de carbone. Le diagramme psychrométrique est tracé, pour les fumées à pression atmosphérique, représentant le glissement de température nécessaire pour le captage du CO_2 dans le cas des fumées émises par des centrales électriques au charbon.

Afin d'optimiser l'échangeur de chaleur où s'effectue le givrage du CO_2, le phénomène d'anti-sublimation doit être compris. Dans le Chapitre 2, une étude bibliographique est réalisée afin d'identifier les paramètres qui affectent l'anti-sublimation du CO_2 sur les surfaces froides. En outre, la formation du dépôt de CO_2 solide sur les ailettes de l'échangeur de chaleur affecte le transfert de chaleur et de masse, et donc le procédé de séparation. Le contrôle des conditions de givrage est un élément clé pour assurer de meilleures performances exergétiques de l'échangeur en minimisant la différence de

températures entre les fluides frigorigènes et les fumées, et pour améliorer l'homogénéité du dépôt de CO_2 solide sur le côté externe de l'échangeur. Peu de données sont disponibles à propos du procédé de givrage du CO_2 et aucune corrélation n'a été déjà proposée pour prévoir le transfert de masse et de chaleur dans le cadre de ce procédé. La théorie classique de la nucléation est donc adoptée. Les théories de nucléation classiques cinétiques et thermodynamiques sont élaborées dans le but de comprendre le phénomène d'anti-sublimation, d'identifier les paramètres qui affectent le taux de nucléation et la morphologie du CO_2 solide en formation, et de modéliser mathématiquement l'anti-sublimation du CO_2. Une analyse de sensibilité est réalisée afin d'évaluer la variation du taux de nucléation et de la morphologie du givrage en fonction des conditions d'anti-sublimation.

Peu de recherches expérimentales ont été menées pour étudier le givrage du CO_2. Une étude expérimentale de l'anti-sublimation du CO_2 sur un échangeur de chaleur tubes-ailettes est d'un grand intérêt pour comprendre le phénomène de précipitation du CO_2 sur les ailettes en fonction du débit et d'autres paramètres de surface. Des études expérimentales qualitatives et quantitatives sont effectuées chapitre 3 afin d'étudier le dépôt de CO_2 solide. La morphologie du dépôt, sa formation et son accumulation sont étudiées par des observations visuelles et des mesures quantitatives. L'observation de la précipitation de CO_2 à fort grossissement (200x zoom optique) permet la compréhension de la théorie de la cristallisation étudiée au chapitre 2 et de vérifier l'effet de nombreux paramètres, tels que la concentration de CO_2 dans les fumées et le taux sursaturation. La visualisation de l'évolution de l'épaisseur de givre de CO_2 et de la vitesse de nucléation a permis le calcul de la masse volumique moyenne et de la porosité pour différentes concentrations de CO_2 et différentes températures de surface d'ailette. L'effet de la croissance du givre de CO_2 sur les performances du CFX, plus particulièrement sur le coefficient de transfert thermique global entre le mélange de fluides frigorigènes et les fumées, est étudié.

En plus des résultats expérimentaux, un modèle CFD multiphasique et transitoire pour un mélange de gaz, permet de prédire la formation du givre et sa croissance, ainsi que l'influence de la structure de l'échangeur de chaleur sur le phénomène de givrage. Ce modèle, pour la conception optimisée de l'échangeur de chaleur, est présenté dans le Chapitre 4. De même, les propriétés thermo-physiques du dépôt de CO_2 solide et la puissance frigorifique nécessaire à la séparation du CO_2 des fumées sont calculées. Les théories classiques de la nucléation sont utilisées pour calculer le transfert de masse entre les fumées et le dépôt solide. Ceci permet d'évaluer l'effet de plusieurs paramètres comme le profil de température sur les ailettes, le glissement de la température des fluides frigorigènes tout au long de l'échangeur en rapport avec le refroidissement des fumées, l'accumulation du givre de CO_2 et la variation du rendement exergétique de plusieurs architectures d'échangeurs. Les résultats de simulations sont validés par comparaison avec des résultats expérimentaux obtenus au Chapitre 3. Ce modèle de givrage de CO_2 peut être utilisé pour l'optimisation de l'échangeur de givrage du CO_2 (CFX) en se basant sur une configuration où le CO_2 contenu dans les fumées se givre en une couche solide homogène, et cela en réduisant la différence de températures entre les fumées et le mélange de fluides frigorigènes.

Chapter 1. Contexte et enjeux du captage de CO_2 par anti-sublimation

1.1 Introduction

Le Centre Energétique et Procédés (CEP) de l'école des MINES ParisTech a développé une méthode de captage de CO_2 par postcombustion connu sous le terme "Antisublimation" [CLO01]. Basé sur le fait que la température de saturation du CO_2 dans les fumées déshydratées est la plus élevée, le CO_2 est le premier composant qui se sépare des fumées lors du refroidissement des fumées. Dans le cas des centrales thermiques à charbon, le CO_2 s'anti-sublime sur des échangeurs tubes-ailettes (CFX) lors du refroidissement des fumées de -99 à -118 °C. On appelle anti-sublimation le passage direct de CO_2 de son état gazeux à l'état solide à des températures inférieures à la température de son point triple. En séparant le CO_2 tout au long de l'échangeur, sa concentration dans les fumées diminue, ce qui

explique la nécessité d'un glissement de température sur l'échangeur capable de suivre la variation de la température d'anti-sublimation du CO_2.

L'intégration du captage du CO_2 dans les centrales thermiques et les procédés industriels amène à la dégradation de leurs performances énergétiques globales. Par exemple, dans le cas de centrales électriques, l'efficacité globale de la production d'électricité après l'intégration du procédé de captage du CO_2 est calculée d'après l'équation (1.1) :

$$\eta = \frac{P_{elec.} - W_{capture}}{E_{fuel}} \tag{1.1}$$

$P_{elec.}$ est la puissance électrique produite par la centrale sans l'intégration du procédé de captage de CO_2, $W_{capture}$ est la puissance électrique consommée par le procédé de captage du CO_2 et E_{fuel} est le pouvoir calorifique du combustible consommé par la centrale. Ainsi, pour maintenir la même puissance électrique produite par une centrale électrique avec des émissions réduites de CO_2, il est essentiel d'augmenter la production de l'usine. Pour ces raisons, il est toujours nécessaire de définir la quantité de CO_2 évitée et non pas la quantité de CO_2 captée pour expliciter l'efficacité d'un procédé de captage du CO_2. La Figure 1.2 explique le concept de CO_2 capté et de CO_2 évité.

Afin d'améliorer les performances énergétiques du procédé de captage du CO_2, il est nécessaire d'améliorer l'efficacité les échangeurs utilisés. Pour ce faire, il faut diminuer les pertes exergétiques générées par le givrage du CO_2 sur les échangeurs, et réduire la différence de températures entre le mélange de fluides frigorigènes et les fumées. L'efficacité du procédé de captage de CO_2 est calculée en comparant la puissance totale consommée par le procédé par rapport à la puissance théorique minimale consommée en séparant une certaine quantité de CO_2 à partir d'un mélange de flux gazeux. La puissance théorique minimale consommée est développée pour le cas d'une séparation parfaite et d'une séparation imparfaite.

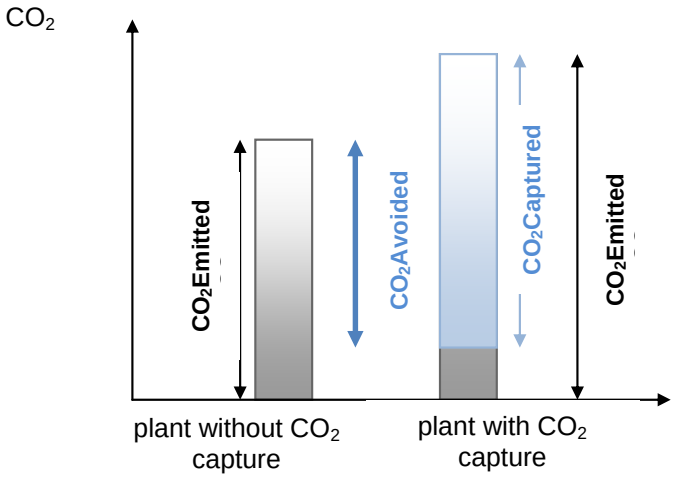

Figure 1.1 : Concept du CO_2 capté et du CO_2 évité

Afin d'étudier le procédé de captage de CO_2 par anti-sublimation, l'équilibre de phase solide-vapeur du CO_2 est déterminé à des températures inférieures à la température du point triple à partir des mesures des propriétés du CO_2 trouvées dans la littérature. Pour représenter le captage du CO_2 par le procédé d'anti-sublimation, un diagramme psychrométrique a été développé. Les propriétés du mélange de gaz constituant les fumées peuvent être calculées à partir de ce diagramme.

1.2 Le procédé de captage du CO_2 par antisublimation

Le procédé de captage du CO_2 par antisublimation est un procédé postcombustion. Le captage du CO_2 en postcombustion consiste à séparer le CO_2 des fumées produites par les centrales thermiques et les procédés industriels (Figure 1.2).

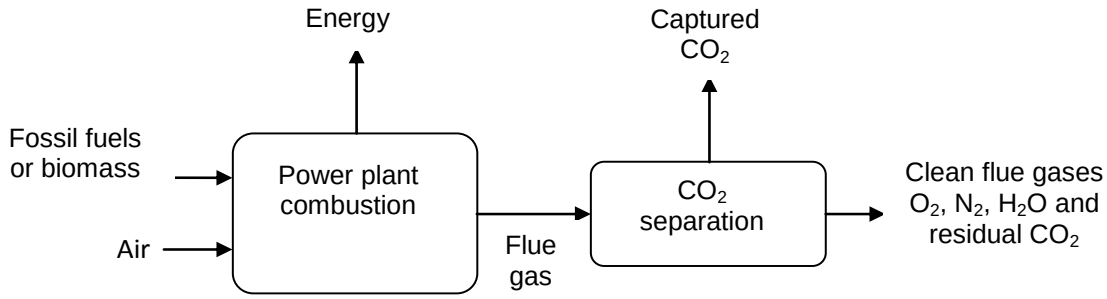

Figure 1.2 : Captage du CO_2 par postcombustion

La pénalisation énergétique des technologies de captage du CO_2 dépend de la concentration du CO_2 dans les fumées. Selon le Groupe d'experts Intergouvernemental sur l'Evolution du Climat (GIEC), la plupart des sources d'émissions ont une concentration en CO_2 inférieure à 15 % vol. et moins de 2 % de ces sources ont une concentration de CO_2 supérieure à 95 % vol. Dans le cas d'une centrale thermique au charbon, cette concentration ne dépasse pas 14 % vol. Pour ces fumées, le captage du CO_2 par antisublimation à la pression atmosphérique se produit à -100 °C (fumées déshydratées). Le changement de phase constitue une méthode de séparation du CO_2 des autres composants des fumées. Le Tableau 1.1 montre la composition des fumées à l'entrée de l'unité de captage du CO_2. Le CO_2 est le seul composant à changer de phase lors du refroidissement des fumées. Plus de 90 % de ce CO_2 est capté sur l'écart de températures entre -99 °C et -118 °C. Le lavage initial des fumées associé à un pré-refroidissement jusqu'à -95 °C permet d'obtenir du CO_2 à une haute pureté, ce qui le rend exploitable.

Tableau 1.1 : Composition des fumées d'une centrale thermique au charbon, avant et après captage de 90 % du CO_2

	Entrée de l'unité de captage du CO_2			*Sortie de l'unité de captage du CO_2*		
	% masse	*Pression (kPa)*	*Température de saturation*	*% masse*	*Pression (kPa)*	*Température de saturation*
CO_2	*22,06 %*	*15,608*	*-99 °C*	*2,75%*	*1,812*	*-118 °C*
Azote	*72,99 %*	*81,132*	*-198 °C*	*91,06%*	*94,190*	*-196 °C*
Oxygène	*3,72 %*	*3,620*	*-206 °C*	*4,64%*	*4,202*	*-202 °C*
Argon	*1,24 %*	*0,965*	*-212 °C*	*1,54%*	*1,121*	*-212 °C*

Dans l'unité d'antisublimation, le CO_2 se dépose sous forme solide sur des échangeurs de chaleur tubes-ailettes (figure 1.3) et le sépare ainsi des fumées. La puissance frigorifique disponible à la fois dans les fumées qui sortent à -120 °C et dans le CO_2 givré est récupérée pour accroître l'efficacité énergétique du procédé d'anti-sublimation. Après avoir été capté, le CO_2 est sublimé, puis passe en phase liquide lorsque le couple pression température du point triple est atteint (figure 1.4).

Ce processus de captage nécessite deux ou plusieurs échangeurs de givrage et de dégivrage fonctionnant en alternance. Pendant que l'une des unités est refroidie à -120 °C et fonctionne comme une unité de captage, l'autre unité fonction en dégivrage de CO_2. Le déclenchement du cycle de dégivrage est effectué lorsque le dépôt de CO_2 solide sur les ailettes augmente par trop les pertes de pression sur les fumées circulantes.

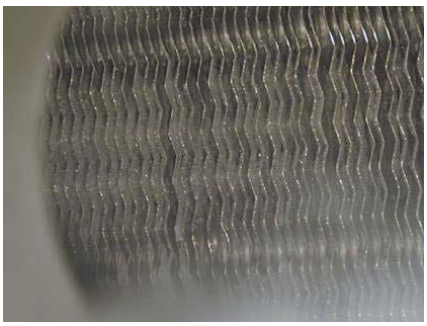

Figure 1.3 : CO_2 givré sur les ailettes de l'échangeur

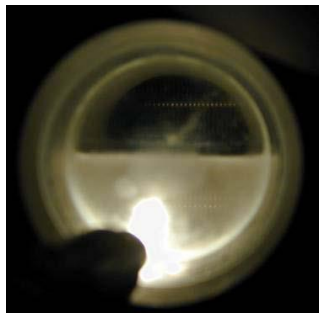

Figure 1.4 : CO_2 liquide après son dégivrage et sa récupération

Les fumées rejetées par les centrales thermiques à charbon présentent une pression partielle de CO_2 de l'ordre de 15,6 kPa. Cette pression partielle définit la température d'antisublimation pour laquelle le CO_2 atteint les conditions de saturation vapeur-solide et commence à se givrer sur les ailettes de l'échangeur de chaleur. La figure 1.5 montre la variation de la pression partielle du CO_2 tout au long des CFX en fonction de la température des fumées en supposant que le CO_2 passe à l'état solide une fois sa température d'antisublimation atteinte. Lorsque les fumées atteignent la température de -118 °C, la pression partielle du CO_2 est de 1,8 kPa assurant ainsi le captage de 90 % du CO_2. Comme la concentration de CO_2 dans les fumées n'est pas constante, un profil de température doit être imposé par les CFX afin d'assurer un dépôt de CO_2 solide homogène et minimiser les surfaces d'échange.

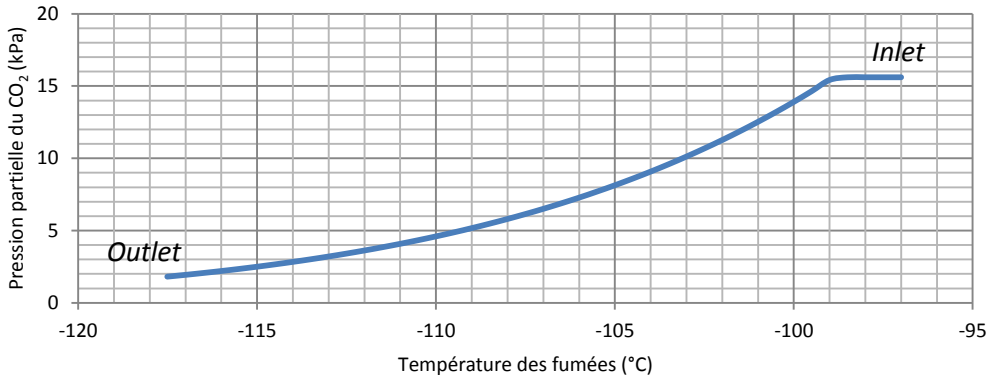

Figure 1.5 : CO_2 partial pressure variation as a function of flue-gas temperature

La figure 1.6 montre la configuration des échangeurs tubes-ailettes utilisés pour le captage de CO_2. L'évaporation d'un mélange de fluides frigorigènes dans les tubes de l'échangeur permet le refroidissement des fumées et le givrage du CO_2 sur les surfaces froides des ailettes. L'enjeu de cette étude est de minimiser l'écart de températures entre le fluide frigorigène et les fumées pour améliorer les performances énergétiques du procédé et maîtriser le profil de la température d'évaporation tout au long de l'échangeur.

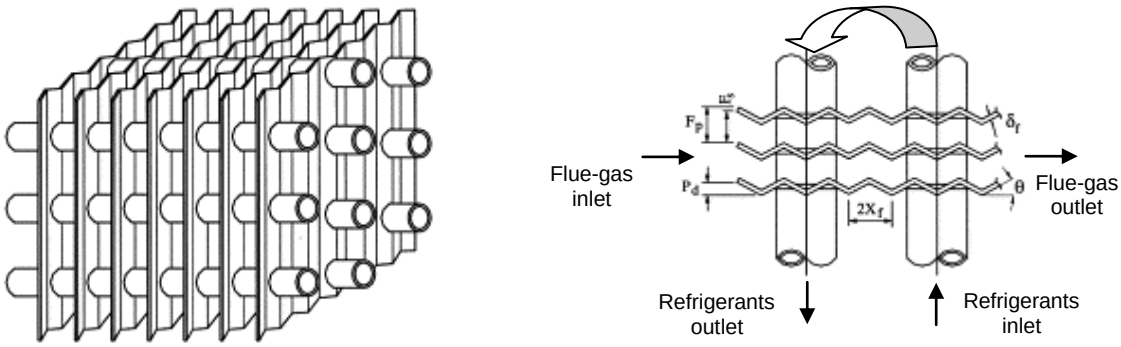

Figure 1.6 : Echangeurs tubes-ailettes de givrage de CO_2

1.2.1 Calcul de la courbe de glissement de température des fumées

Dans cette section, la puissance frigorifique nécessaire pour le givrage du CO_2 des fumées émises par une chaudière à charbon est calculée afin de déterminer la courbe de glissement de température dans les CFX. Les fumées sont supposées être à pression constante égale à la pression atmosphérique. Les pertes de pression tout au long de l'échangeur ne sont pas prises en considération. Les CFX sont divisés en éléments par pas de température constante.

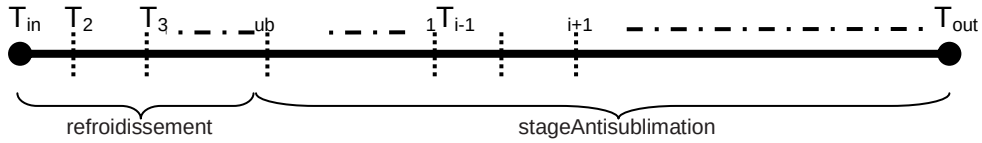

Figure 1.7: L'évolution de la température des fumes dans les CFX: $(T_i - T_{i-1} = -0.1\ K)$.

Les fumées sont supposées se comporter comme un gaz parfait en contact avec le dépôt de CO_2 solide sur les ailettes. Les hypothèses suivantes sont faites [SON03] :

1. *La phase solide ne contient pas de gaz dissous ;*
2. *La phase gazeuse peut être traitée comme un mélange de gaz parfaits ;*
3. *Lorsque les fumées et le dépôt de CO_2 solide sont à une pression et une température données, l'équilibre entre le CO_2 solide et sa vapeur n'est pas influencé par la présence d'autres composants dans les fumées. Cela signifie que lorsque l'équilibre thermodynamique est atteint, la pression partielle de la vapeur est égale à la pression de saturation correspondante à la température de mélange ;*
4. *Aucune perte de pression ne se produit dans les fumées.*

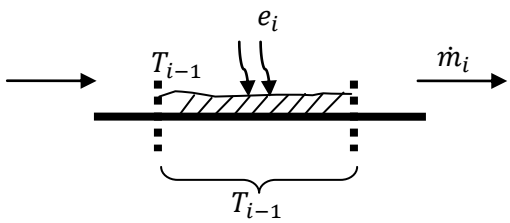

Figure 1.8 : Représentation de l'élément e_i de pas de température constante

La puissance frigorifique nécessaire pour refroidir les fumées dans chaque élément est calculée par l'équation (1.2) pour un CO_2 surchauffé et par l'équation (1.3) pour l'antisublimation de CO_2 à la températureT_{i-1}.

$$Q_{c,i} = [\dot{m}_i(h_i - h_{i-1})]_{N_2} + [\dot{m}_i(h_i - h_{i-1})]_{O_2} + [\dot{m}_i(h_i - h_{i-1})]_{Ar} + [\dot{m}_i(h_i - h_{i-1})]_{CO_2} \quad (1.2)$$

$$Q_{c,i} = [\dot{m}_i(h_i - h_{i-1})]_{N_2} + [\dot{m}_i(h_i - h_{i-1})]_{O_2} + [\dot{m}_i(h_i - h_{i-1})]_{Ar} + \left[\dot{m}_i\left(h_{g,i} - h_{g,i-1}\right)\right]_{CO_2} + \left[(\dot{m}_{i-1} - \dot{m}_i)\left(h_{s,i-1} - h_{g,i-1}\right)\right]_{CO_2} \quad (1.3)$$

Les puissances frigorifiques latente et sensible nécessaires au refroidissement des fumées et au givrage du CO_2 sont représentées figure 1.9.

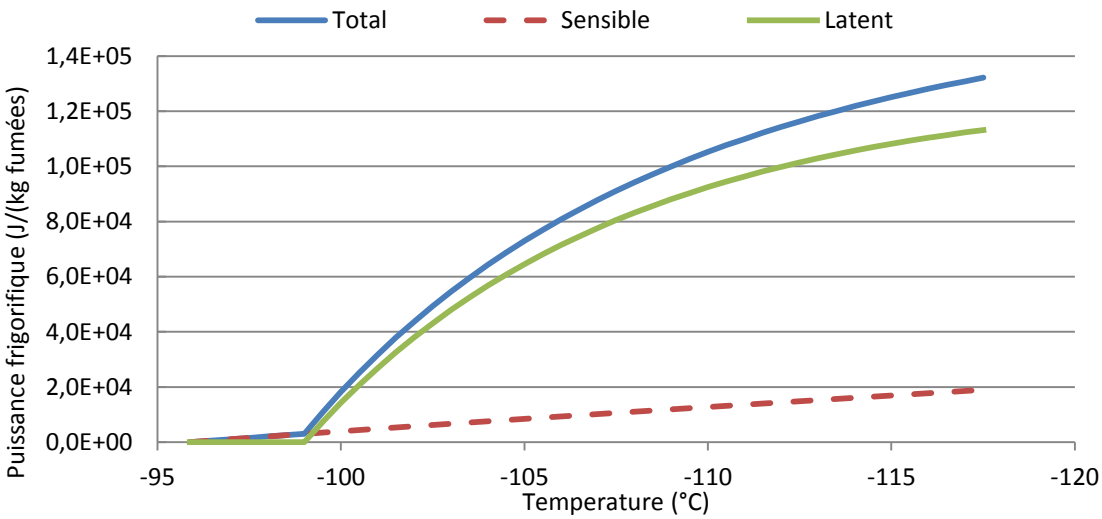

Figure 1.9 : Variation des capacités frigorifiques latente, sensible et totale dans les CFX

La figure 1.10 représente la variation de la masse de CO_2 givrée sur les échangeurs pour des variations de température de 0,5 K. Comme la concentration du CO_2 diminue tout au long de l'échangeur, la précipitation du CO_2 diminue, ce qui explique l'allure de la puissance frigorifique associée à la chaleur latente d'antisublimation présentée figure 1.9.

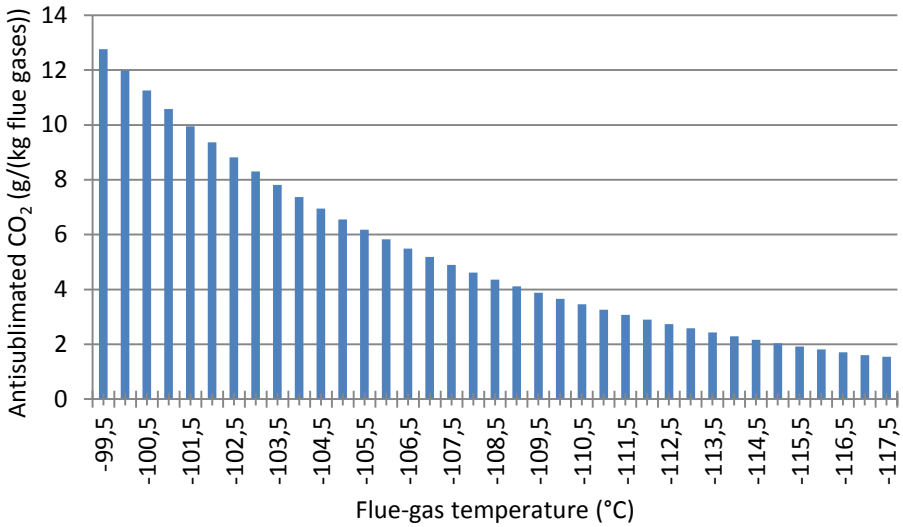

Figure 1.10 : CO_2 antisublimé pour chaque 0,5 K de diminution de la température des fumées

1.3 Travail minimal de séparation d'un mélange gazeux binaire

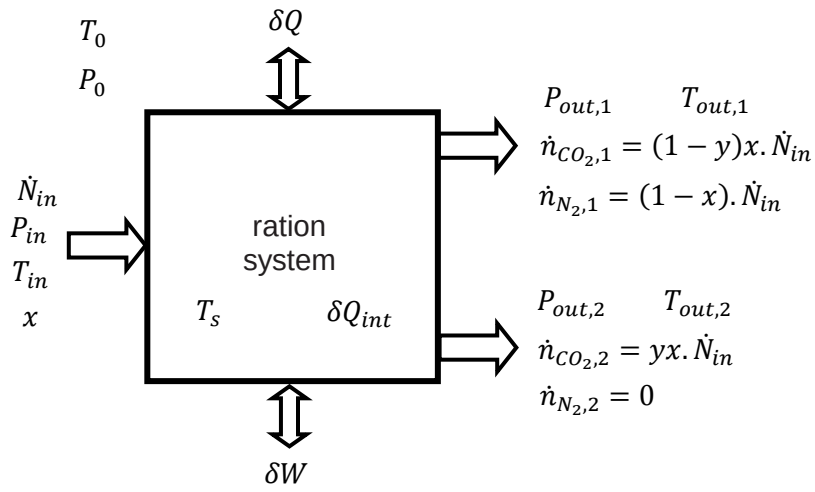

Figure 1.11 : Système continu et stationnaire de séparation d'un mélange de gaz binaire

L'efficacité énergétique d'un procédé de captage de CO_2 est calculée en comparant la puissance énergétique totale consommée et la puissance théorique minimale de séparation d'une certaine quantité de CO_2 du reste des gaz constituants les fumées. Dans cette section, le travail théorique minimal nécessaire pour la séparation d'une mole de CO_2 est calculé.

La Figure 1.11 représente un système stationnaire ouvert de séparation du CO_2 d'un mélange N_2 – CO_2. x est la concentration molaire du CO_2 à l'entrée du système. y est le taux de séparation de CO_2 à la sortie du système. Pour une séparation appelée parfaite, la concentration molaire de l'azote dans le CO_2 séparé est nulle. δQ et δW sont respectivement la chaleur et le travail mécanique échangés avec le système. Les irréversibilités internes du système génèrent une quantité de chaleur exprimé par δQ_{int}. En appliquant les bilans de masse, d'énergie, d'entropie et d'exergie pour le système, les équations suivantes sont déduites :

$$\dot{\mathrm{N}}_{\mathrm{in}} = \dot{\mathrm{N}}_{\mathrm{out},1} + \dot{\mathrm{N}}_{\mathrm{out},2} \tag{1.4}$$

$$\mathrm{x}.\dot{\mathrm{N}}_{\mathrm{in}} = \mathrm{yx}.\dot{\mathrm{N}}_{\mathrm{in}} + (1-\mathrm{y})\mathrm{x}.\dot{\mathrm{N}}_{\mathrm{in}} \tag{1.5}$$

$$\sum_{in} \dot{n}_i h_i - \sum_{out} \dot{n}_i h_i + \delta Q + \delta W = 0 \tag{1.6}$$

$$\sum_{in} \dot{n}_i s_i - \sum_{out} \dot{n}_i s_i + \frac{\delta Q}{T_s} + \frac{\delta Q_{int}}{T_s} = 0 \tag{1.7}$$

$$\sum_{in} \dot{n}_i ex_i - \sum_{out} \dot{n}_i ex_i + \delta Q\left(1 - \frac{T_0}{T_s}\right) - T_0 \frac{\delta Q_{int}}{T_s} + \delta W = 0 \tag{1.8}$$

$$ex_i = h_i - T_0 s_i \tag{1.9}$$

En supposant que la séparation du CO_2 est un phénomène réversible isotherme, qui se déroule à la même température que celle du gaz à l'entrée du système, égale à la température ambiante, les équations (1.10) et (1.11) sont déduites.

$$\delta W_{min} = -\delta Q \tag{1.10}$$

$$\frac{\delta Q}{T_0} = \sum_{out} \dot{n}_i s_i - \sum_{in} \dot{n}_i s_i \tag{1.11}$$

Pour un mélange de gaz se comportant comme un gaz parfait, le travail minimal de séparation du gaz est calculé par l'équation (1.12). Pour le cas de séparation parfaite du CO_2 d'un mélange binaire, le travail minimal est calculé par l'équation (1.13).

$$\delta W_{min} = -\bar{R}T_0\left(\sum_{in}\dot{n}_i \ln\frac{P_i}{P_0} - \sum_{out}\dot{n}_i \ln\frac{P_i}{P_0}\right) \quad (1.12)$$

$$\delta W_{min} = -\dot{N}_{in}\bar{R}T_0[xy\ln x - x(1-y)\ln(1-y) + (1-xy)\ln(1-xy)] \quad (1.13)$$

Le travail minimal de la séparation parfaite de CO_2 est représenté figure 1.12 en fonction de la concentration du CO_2 dans le mélange initial et pour différents taux de séparation.

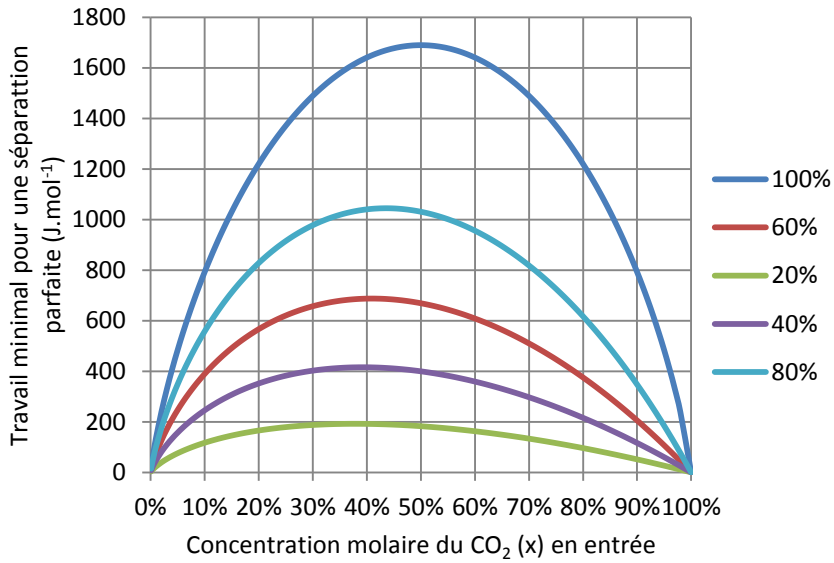

Figure 1.12 : Travail minimal de séparation du CO_2 en fonction de sa concentration initiale dans le mélange

Amelkin et al. [AME03] ont défini la séparation imparfaite d'un mélange dans le cas où les deux composants du mélange se retrouvent dans les deux écoulements à la sortie du système. En considérant un cas de séparation imparfaite où x est la concentration du CO_2 à l'entrée du système et z_1 et $z_2$les concentrations de CO_2 aux deux sorties, le travail minimal de séparation est calculé par l'équation (1.14).

$$\begin{aligned}\delta W_{min,imp.} = -\dot{N}_{in}\bar{R}T_0\Big\{&x\ln x \\ &+ (1-x)\ln(1-x) - \frac{x-z_2}{z_1-z_2}[z_1\ln z_1 + (1-z_1)\ln(1-z_z)] \\ &- \frac{z_1-x}{z_1-z_2}[z_2\ln z_2 + (1-z_2)\ln(1-z_2)]\Big\}\end{aligned} \quad (1.14)$$

L'efficacité globale d'un procédé de captage de CO_2 est donc calculée par l'équation (1.15):

$$\eta_{process} = \frac{\delta W_{min}\left(W.mol^{-1}_{sep.CO_2}\right)}{\delta W_{process}\left(W.mol^{-1}_{sep.CO_2}\right)} \quad (1.15)$$

1.4 Les propriétés thermodynamiques du CO_2 solide à basse température et le diagramme psychrométrique CO_2 - N_2

Afin d'étudier le captage du CO_2 en postcombustion par le processus d'antisublimation, l'équilibre solide-vapeur doit être connu pour toutes les concentrations de CO_2 dans l'azote, qui est le principal composant des fumées. Dans cette étude, les propriétés du CO_2 sont déterminées pour des températures inférieures au point triple. A ces températures, le CO_2 se retrouve en équilibre de phase vapeur-solide. La pression de sublimation, l'enthalpie vapeur et solide, l'entropie vapeur et solide et la masse volumique vapeur et solide sont calculées permettant de tracer un nouveau diagramme T-s de CO_2 allant jusqu'à 140 K.

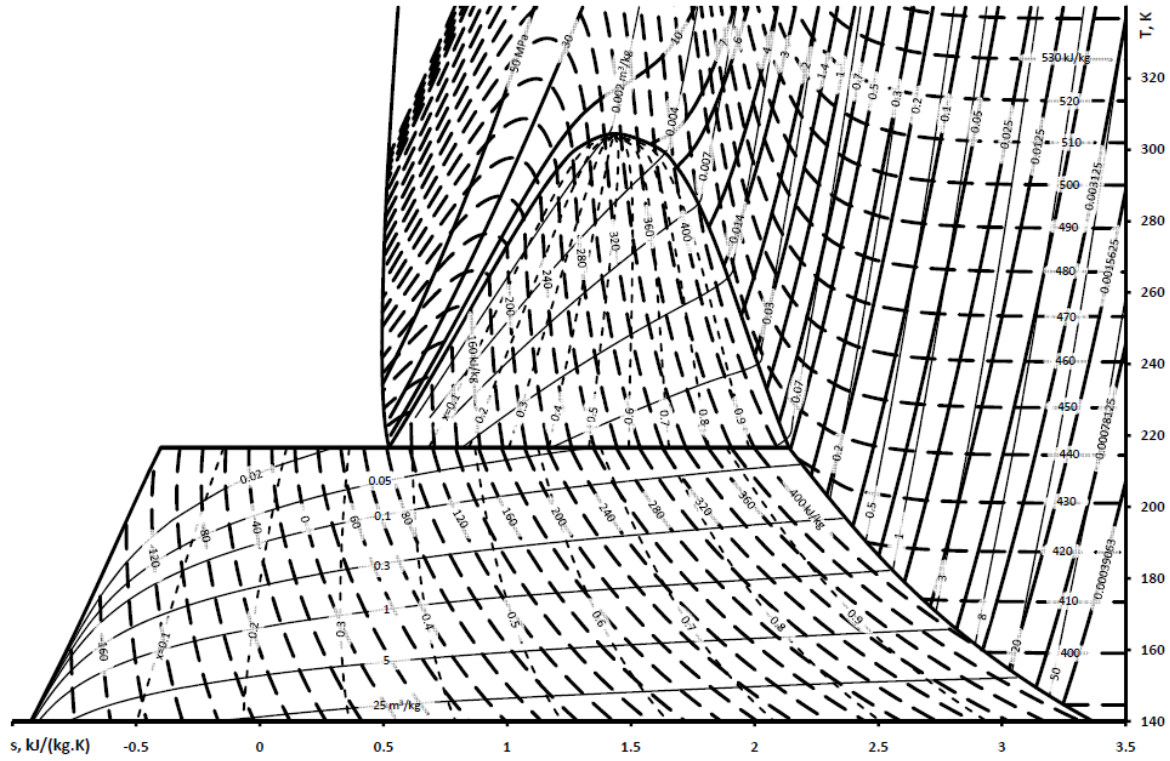

Figure 1.13 : Diagramme T-s du dioxyde de carbone

Pour représenter plus aisément le captage du CO_2 par le processus d'antisublimation, un diagramme psychrométrique a été développé. En plus du dioxyde de carbone et de l'azote, les fumées contiennent de l'oxygène, de l'argon et d'autres gaz à l'entrée de l'unité de captage du CO_2. Le diagramme psychrométrique est tracé pour un mélange gazeux binaire composé uniquement d'azote et de dioxyde de carbone, afin de simplifier les calculs. Cette approximation conduit à une erreur inférieure à 1 % dans le calcul de l'enthalpie, de l'entropie, de la masse volumique et de la pression partielle du CO_2 dans le mélange. Les méthodes de calcul des courbes isochores, isenthalpes et isentropes sont exposées. Le diagramme psychrométrique est tracé pour des fumées à pression atmosphérique (101,325 kPa), ce qui est le cas de la majorité des sources d'émission de CO_2.

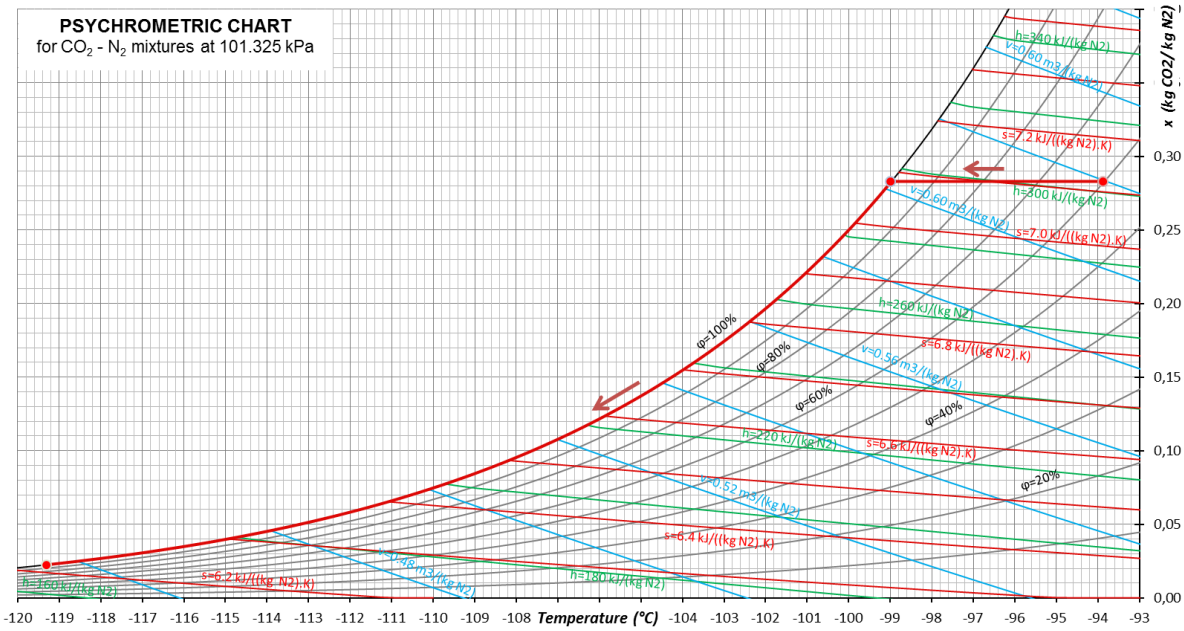

Figure 1.14 : Représentation du procédé de captage du CO_2 par antisublimation sur le diagramme psychrométrique CO_2 - N_2 pour des fumées émises par une chaudière à charbon.

1.5 Conclusions

Dans ce chapitre, l'enjeu des émissions de CO_2 provenant de la production d'énergie et des procédés industriels est présenté. Le dioxyde de carbone est le principal gaz à effet de serre émis dans le monde et représente 76,7 % des émissions anthropiques de gaz à effet de serre en 2004 [IPCC05].

Le procédé de captage du CO_2 par antisublimation, développé par le Centre Energétique et Procédés (CEP) de MINES ParisTech a été présenté. Afin d'améliorer les performances du procédé, l'optimisation des échangeurs de chaleur est une nécessité. Pour calculer l'efficacité totale de procédé de captage du CO_2, le travail théorique minimal consommé par la séparation d'une quantité de CO_2 à partir d'un mélange de gaz est calculé.

Les propriétés thermodynamiques du CO_2 pour des températures inférieures au point triple sont calculées. Ces propriétés sont représentées sur un nouveau diagramme T-s tracé jusqu'à 140 K. De même, le diagramme psychrométrique du mélange CO_2-N_2 est développé pour calculer les propriétés des fumées lors de la séparation du CO_2 par antisublimation.

Chapter 2. Théorie de l'antisublimation

2.1 Introduction

Dans ce chapitre, le processus d'antisublimation est modélisé. La revue de la littérature, telle qu'effectuée, montre que les recherches menées sur le givrage du CO_2 sont peu nombreuses et peu de données sont disponibles. Une analogie avec le phénomène d'antisublimation de la vapeur d'eau, soit son givrage à une température inférieure au point triple, peut aider à comprendre l'antisublimation de CO_2. L'objectif est d'identifier les paramètres qui peuvent affecter l'antisublimation du CO_2 sur les échangeurs tubes-ailettes. Il faut bien noter que seules les études qui prennent en considération le givrage de la vapeur d'eau à des températures inférieures au point triple de l'eau sont considérées.

Les termes antisublimation, désublimation et précipitation sont utilisés pour décrire les mêmes phénomènes. C'est la solidification directe d'un composé à partir de sa phase gazeuse. Dans le cas du captage du CO_2 par antisublimation, les fumées sont considérées comme **la solution** où le CO_2 est **le soluté** dissout dans le solvant. **Le solvant** est un mélange de gaz (de l'azote, de l'oxygène et de l'argon) qui ne précipitent pas sur la même plage de température de saturation que celle du soluté. D'après la littérature, la condensation et l'antisublimation de la vapeur d'eau sont simulées en utilisant la théorie classique de la nucléation (CNT) afin de définir la vitesse de la formation du givre d'eau sur les évaporateurs. L'antisublimation du CO_2 implique une formation de nucléides, puis un réseau de CO_2 solide se forme lors de la croissance de ces nucléides. Dans cette étude, la CNT est adoptée puisque les études menées sur le givrage de la vapeur d'eau ont montré une bonne adéquation entre des résultats de simulations et des résultats expérimentaux.

2.2 La nucléation

La nucléation est la formation d'une nouvelle phase à partir de la phase d'origine appelée phase mère. Le soluté change d'état en formant une nouvelle phase dispersée dans le mélange. Selon Mullin, la nucléation est divisée en deux phases : la nucléation primaire et la nucléation secondaire. La nucléation primaire se déroule en absence de cristaux de soluté déjà formés dans le mélange. La nucléation primaire est constituée de deux types : la nucléation homogène et la nucléation hétérogène. La nucléation homogène se produit lorsque les nucléides se forment dans la solution de gaz sans aucun contact avec la surface de refroidissement ou d'autres particules étrangères telles que les impuretés. La nucléation hétérogène a lieu lorsque les cristaux se forment sur un substrat qui peut être une particule étrangère ou une surface solide comme la surface froide d'un échangeur de givrage de CO_2. Les nucléations hétérogènes et homogènes sont représentées figure 2.1 montrant l'angle de contact entre le nucléide de givre et le substrat. Pour un angle de contact de 180°, la nucléation est considérée comme étant homogène.

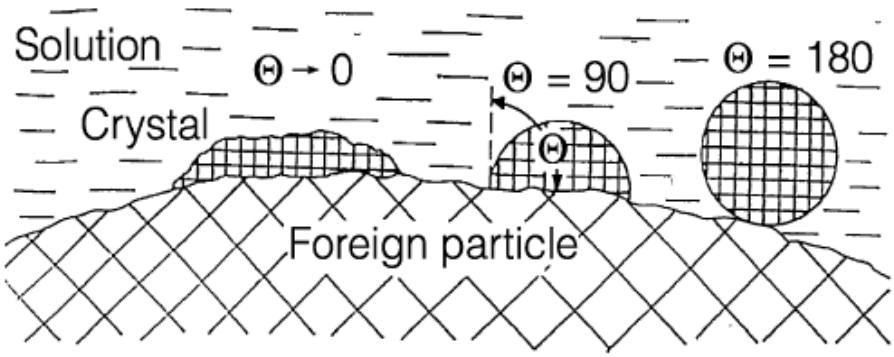

Figure 2.1 : Nucléations homogènes et hétérogènes, Mersmann et al. [MERS02]

La nucléation secondaire se produit lorsque les cristaux de soluté sont déjà présents dans la solution.

Plusieurs types de nucléation secondaire sont cités dans la littérature. Selon Gyulai [MUL01], la nucléation secondaire est induite par le mouvement de la solution pouvant arracher une partie de la surface du cristal pour former des nouveaux nucléides. La nucléation secondaire peut également se produire par la nucléation de contact où les collisions nucléide-nucléide induisent la formation d'un nouveau cristal stable. La figure 2.2 résume les différentes catégories et types de nucléation tels que décrit dans la littérature.

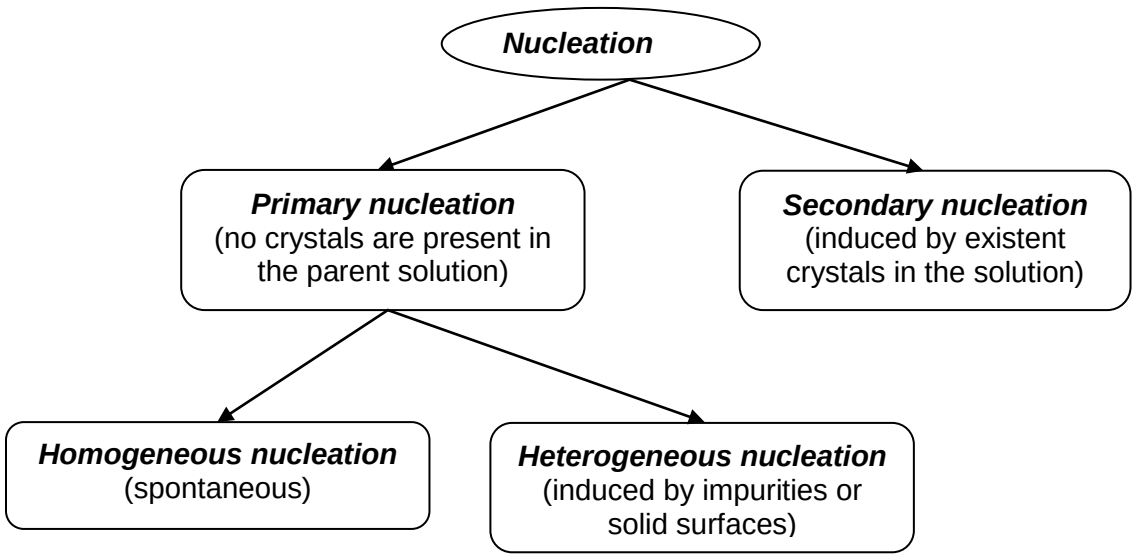

Figure 2.2 : Les différentes catégories de la nucléation

2.2.1 La sursaturation

Selon l'étude bibliographique, un soluté se cristallise quand il est présent dans la solution à des conditions de sursaturation. Dans le cas du givrage du CO_2, sa sursaturation est assurée par le sous-refroidissement des fumées. Le sous-refroidissement est la différence entre la température de saturation du soluté dans le mélange et la température du mélange. La sursaturation est exprimée par la différence entre la concentration du CO_2 dans le mélange de fumées et sa concentration de saturation. Elle peut être exprimée en tant que taux de sursaturation ou sursaturation relative :

$$\Delta x = x - x_{sub} \tag{2.1}$$

$$S = \frac{x}{x_{sub}} = \frac{P}{P_{sub}} \tag{2.2}$$

$$S_{\%} = \frac{P - P_{sub}}{P_{sub}} = \frac{\Delta x}{x_{sub}} \tag{2.3}$$

$$\Delta T_{sup} = T - T_{sub} \tag{2.4}$$

Le taux de sursaturation est un paramètre clé à prendre en considération pour la modélisation du givrage. En supposant que la nucléation se produise lorsque le soluté est saturé dans le mélange, pour une température définie de gel à la surface, le taux de transfert de masse de l'air humide au dépôt de givre **est surestimé de 20 % par rapport aux résultats expérimentaux** [NA03A]. Dans la figure 2.3, le procédé de sous-refroidissement des fumées pour le captage de CO_2 par antisublimation est représenté en prenant en considération le taux de sursaturation. Une zone métastable existe entre la ligne de

saturation et la ligne de nucléation. Une nucléation qui se déroule dans cette zone est réversible.

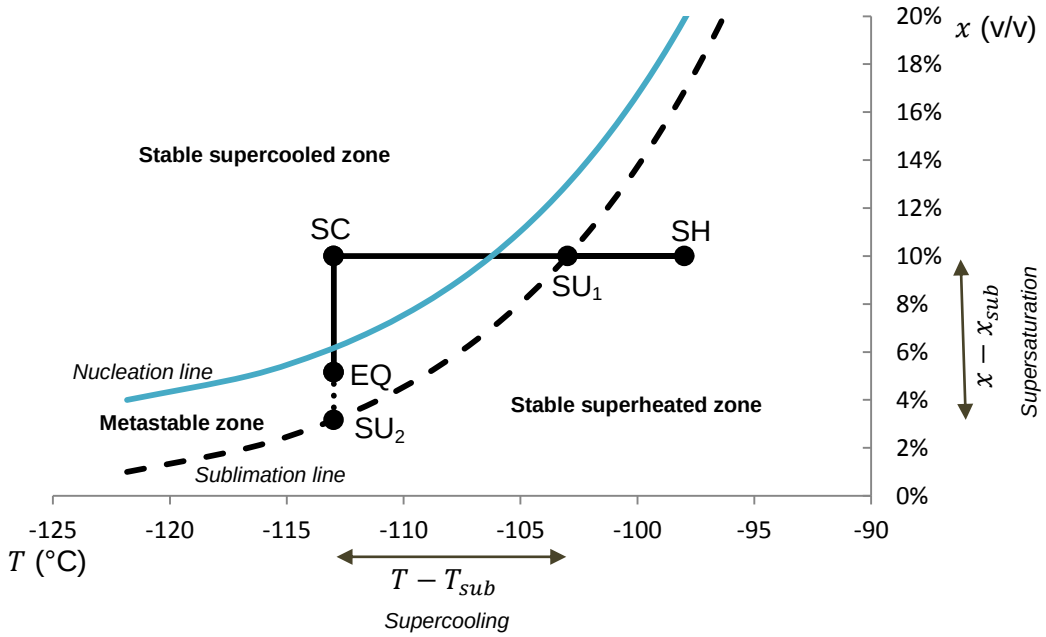

Figure 2.3 : Représentation de la sursaturation du CO_2

2.2.2 La nucléation homogène

2.2.2.1 Aspects thermodynamiques

La théorie classique de la nucléation est basée sur les études de Gibbs sur la condensation de la vapeur d'eau. Cette théorie est appliquée à tous les phénomènes de cristallisation. À température et pression constantes, l'énergie de Gibbs, nommée aussi l'énergie libre, nécessaire pour former un embryon est exprimée par l'équation (2.5) :

$$\Delta G = \Delta G_S + \Delta G_V \tag{2.5}$$

L'énergie libre totale transférée entre la nouvelle phase solide et son soluté est la somme de l'énergie libre surfacique ΔG_S (positive) et l'énergie libre volumique ΔG_V (négative pour un soluté sursaturé). Pour un nucléide sphérique, l'excès de l'énergie libre est exprimé par l'équation (2.6) :

$$\Delta G = 4\pi r^2 \sigma + \frac{4}{3}\pi r^3 \Delta G_v \tag{2.6}$$

Où r est le rayon du nucléide (m), σ est la tension surfacique entre le nucléide et la solution ($N.m^{-1}$) et ΔG_v est la variation de l'énergie libre par unité de volume ($J.m^{-3}$).

$$\Delta G_v = -\frac{k_B T \ln S}{v} \tag{2.7}$$

$k_B = R/N_A = 1.3805 \,.\, 10^{-23}$ $J.K^{-1}$, Constante de Boltzmann

S est le taux de sursaturation, T est la température (K) et v est la volume moléculaire (m^3). Les variations de ΔG_S, de ΔG_V et l'énergie libre totale sont représentées en fonction du rayon du nucléide figure 2.4.

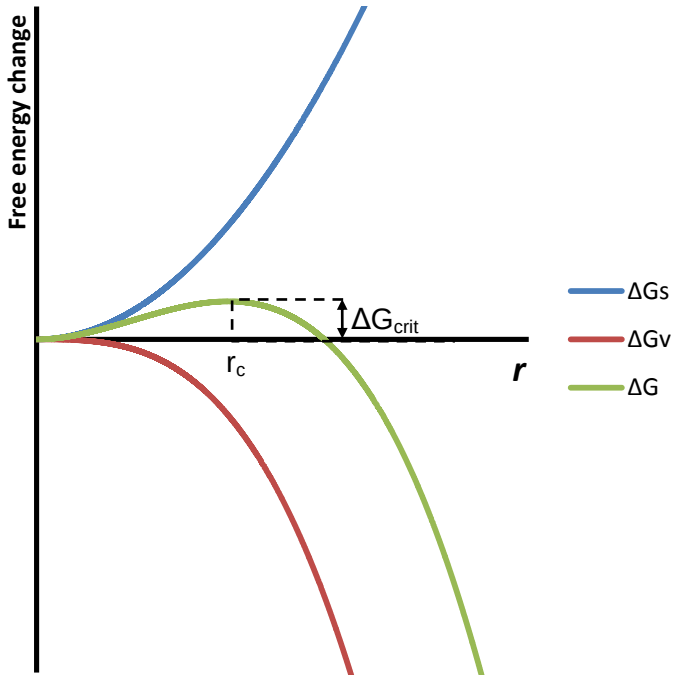

Figure 2.4 : Variation de l'énergie libre en fonction du rayon du nucléide

En effet, lors du changement de phase à partir de la phase vapeur à la phase solide, la création d'un cristal signifie un gain en énergie de surface du cristal et une perte d'énergie volumétrique, à la suite de la diminution de la température du nucléide. Selon la variation d'énergie libre de Gibbs, un nouveau nucléide de taille inférieure au rayon critique se ré-évapore alors qu'un autre plus grand que le rayon critique forme un nucléide stable. La figure 2.5 résume cette théorie.

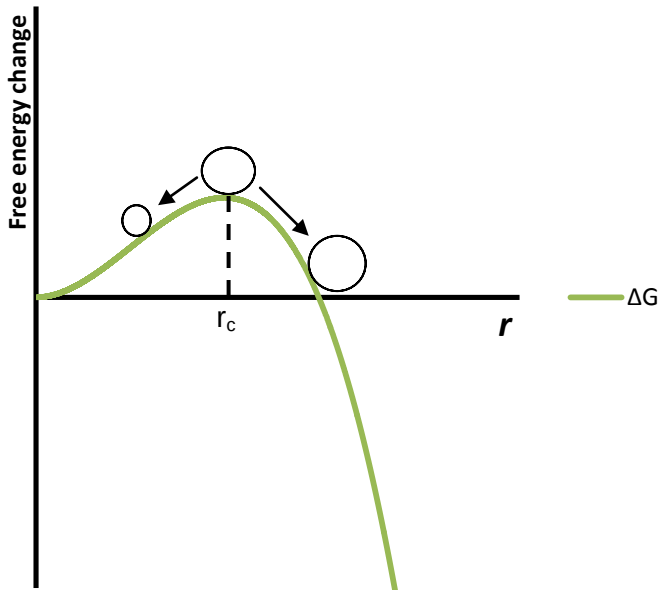

Figure 2.5 : Variation du rayon des nucléides en fonction de la variation l'énergie libre totale [SCH05]

Le rayon critique est calculé ainsi que la variation de l'énergie libre critique nécessaire pour la formation d'un nucléide stable.

$$r_c = \frac{-2\sigma}{\Delta G_v} \tag{2.8}$$

$$\Delta G_{crit} = \frac{4}{3}\pi\sigma r_c^2$$

En utilisant la relation de Gibbs-Thomson, la sursaturation est exprimée en fonction de la tension surfacique, de la température, du volume moléculaire et du rayon des nucléides :

$$\ln S = \frac{2\sigma v}{k_B T r} \tag{2.9}$$

$$-\Delta G_v = \frac{2\sigma}{r_c} = \frac{k_B T \ln S}{v} \tag{2.10}$$

D'où :

$$r_c = \frac{2\sigma v}{k_B T \ln S}$$
$$\Delta G_{crit} = \frac{16\pi\sigma^3 v^2}{3(k_B T \ln S)^2} \tag{2.11}$$

Ces équations montrent que pour une pression et une température constantes, le rayon critique et la variation de l'énergie libre critique diminuent en augmentant la sursaturation de la solution. Il est évident que pour des rapports de sursaturation plus élevés, l'énergie libre critique nécessaire pour la formation d'un nucléide diminue améliorant la nucléation spontanée ou homogène.

L'effet de la température sur la nucléation est représenté figure 2.6. Plus la température du mélange de gaz est faible, plus le rayon critique d'un cristal et l'énergie libre nécessaire pour le former sont faibles.

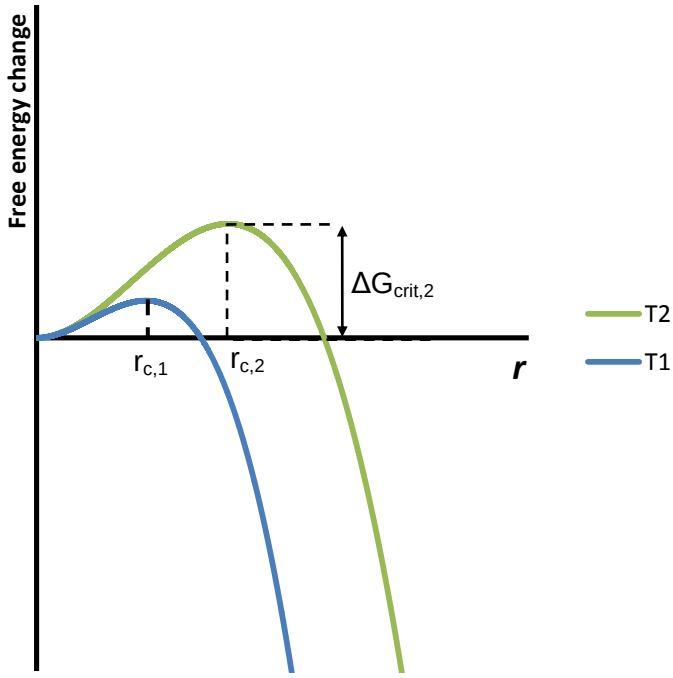

Figure 2.6 : Variation de l'énergie libre en fonction du rayon de nucléation pour deux températures différentes $T_1 < T_2$

2.2.2.2 Aspects cinétiques

Pour calculer le transfert de masse de soluté à partir de la phase-mère vers la nouvelle phase, la vitesse de nucléation I doit être définie. C'est le nombre de nucléides formés par

unité de volume pendant une unité de temps. Selon la théorie classique de la nucléation, le taux de nucléation est défini en utilisant l'équation d'Arrhenius :

$$I = n_c \exp\left[-\frac{\Delta G_{crit}}{k_B T}\right] \tag{2.12}$$

Où n_c est le coefficient de nucléation maximal (# de nucléides.m^{-3}.s^{-1}). Le taux de nucléation est donc exprimé par l'équation (2.13). Le taux de nucléation dépend principalement de la sursaturation et de la température.

$$I = n_c \exp\left[-\frac{16\pi\sigma^3 v^2}{3{k_B}^3 T^3 (\ln S)^2}\right] \tag{2.13}$$

2.2.3 La nucléation hétérogène

On appelle nucléation hétérogène la formation de nucléides sur des surfaces solides. Dans le cas des échangeurs de givrage de CO_2, les surfaces froides des ailettes forment le substrat sur lequel la cristallisation hétérogène du CO_2 a lieu.

2.2.3.1 Aspects thermodynamiques

La nucléation hétérogène est représentée figure 2.7. Deux cas sont représentés pour différentes affinités entre le nucléide et la surface solide. La nouvelle phase de cristaux solides est référencée par l'indice s, la phase vapeur est référencée par l'indice v et la plaque solide par l'indice p.

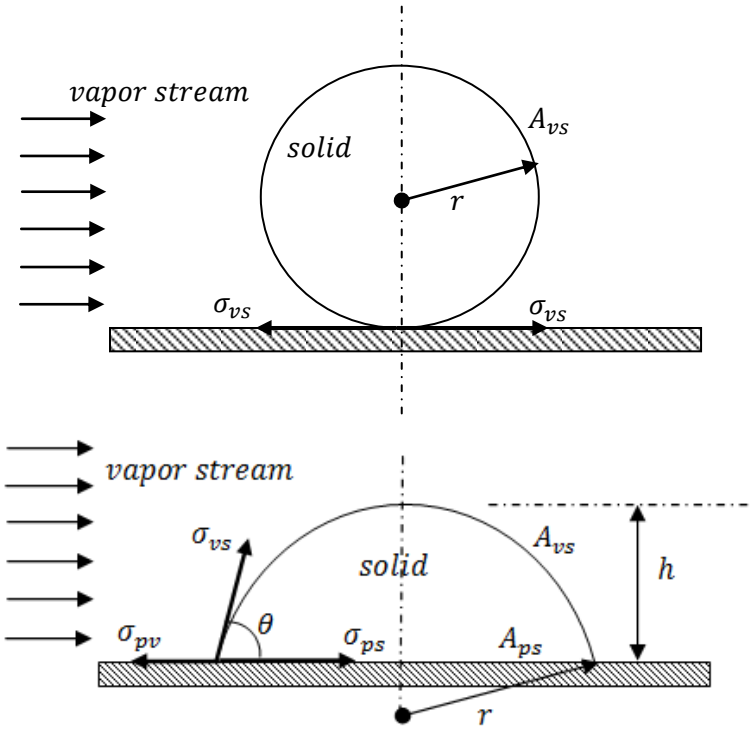

Figure 2.7 : Modèle de Fletcher de la nucléation hétérogène
a) $\theta = 180°$; *b)* $0 < \theta < 180°$

L'équation de Young permet d'exprimer les tensions surfaciques en fonction de l'angle de contact θ.

$$\sigma_{pv} = \sigma_{ps} + \sigma_{vs} \cos\theta \tag{2.14}$$

Pour la nucléation hétérogène, la variation de l'énergie libre de Gibbs nécessaire pour la formation d'un nucléide est exprimée par l'équation (2.15).

$$\Delta G = V_{embryo}\Delta G_v + A_{vs}\sigma_{vs} + A_{ps}(\sigma_{ps} - \sigma_{pv}) \quad (2.15)$$

Comme pour le cas de la nucléation hétérogène, le rayon critique et la variation de l'énergie libre nécessaire pour la formation d'un nouveau nucléide sur la surface froide sont exprimés par les équations (2.16) et (2.17) :

$$r_c = -\frac{2\sigma_{vs}}{\Delta G_v} \quad (2.16)$$

$$\Delta G'_{\text{crit}} = \frac{16\pi}{3}\frac{\sigma_{vs}^3}{{\Delta G_v}^2}\frac{(2+\cos\theta)(1-\cos\theta)^2}{4} \quad (2.17)$$

Pour comparer la nucléation homogène à la nucléation hétérogène, la variation du rapport de l'énergie libre critique est représentée figure 2.7 en fonction de l'angle de contact entre la phase solide du soluté en train de se former et la surface de la plaque froide. Ce rapport varie entre 0 et 1 pour une variation de l'angle de contact entre 0 et 180°.

$$\frac{\Delta G'_{\text{crit}}}{\Delta G_{crit}} = \varphi(\theta) = \frac{(2+\cos\theta)(1-\cos\theta)^2}{4} \quad (2.18)$$

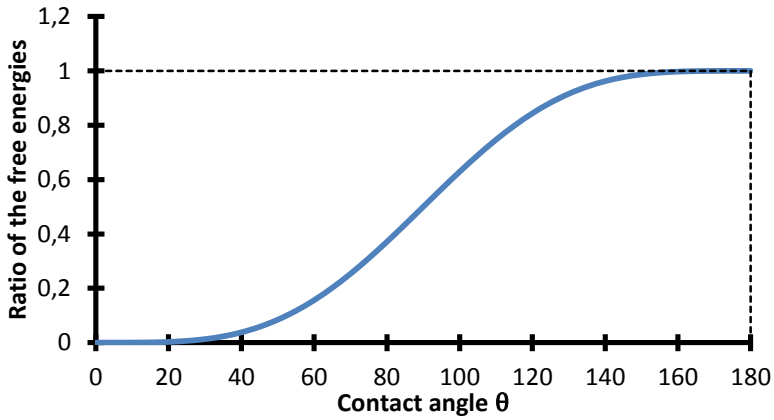

Figure 2.7 : Variation du rapport des énergies libres critiques en fonction de l'angle de contact

Dans le cas de la cristallisation du CO_2 par refroidissement des fumées, la surface des échangeurs, constituée par les surfaces des ailettes et des tubes, doit être choisie afin d'améliorer la nucléation hétérogène au début du cycle de givrage. Selon la CNT, une bonne affinité entre le CO_2 solide et la surface des ailettes peut réduire le taux de sursaturation nécessaire pour lancer le phénomène de nucléation.

2.2.3.2 Aspects cinétiques

Comme pour la nucléation homogène, le taux de nucléation est exprimé pour la nucléation hétérogène sous forme de l'équation d'Arrhenius.

$$I = n_c \exp\left[-\frac{\Delta G'_{\text{crit}}}{k_B T}\right] = n_c \exp\left[-\frac{\varphi(\theta)\,\Delta G_{crit}}{k_B T}\right] \quad (2.19)$$

On peut constater que ce taux est considérablement affecté par l'affinité entre les cristaux et la surface du substrat.

2.3 Analyse de sensibilité de la théorie de nucléation

Dans cette étude, une analyse de sensibilité a été effectuée afin d'évaluer l'effet de la variation de la concentration du CO_2 et de la température sur les conditions de givrage du CO_2. Il est important de vérifier l'effet de la variation des paramètres de nucléation, à travers l'échangeur de chaleur sur les conditions de givrage, ainsi que l'homogénéité du dépôt solide.

2.3.1 Analyse de sensibilité à la variation de la concentration de CO_2 dans les fumées

En considérant une température de nucléation et une tension surfacique constantes, le taux de nucléation est seulement affecté par la variation de la concentration du CO_2. La sensibilité est calculée par la méthode de la différence unilatérale [OST05]. Le cas considéré est pour une température de -100 °C. α_c est la variation de la concentration molaire du CO_2.

$$\frac{I(c_{CO_2}+\alpha_c)-I(c_{CO_2})}{I(c_{CO_2})}=\exp\left\{-\frac{B}{\left[\ln\left(\frac{c_{CO_2}+\alpha_c}{c_{CO_2,sat}}\right)\right]^2}+\frac{B}{(\ln S)^2}\right\}-1 \tag{2.20}$$

La variation relative du taux de nucléation en fonction de la variation de la concentration de CO_2 est représentée figure 2.9 pour différents taux de sursaturation.

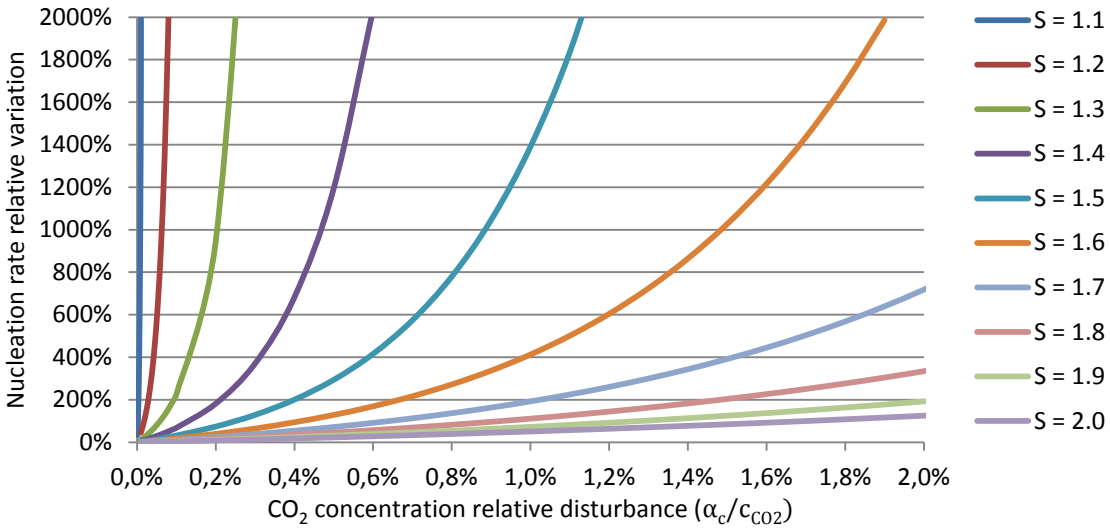

Figure 2.9 : Variation relative du taux de nucléation
en fonction de la variation de la concentration de CO_2, T = -100 °C.

La figure 2.9 montre une forte variation du taux de nucléation en raison de la perturbation de la concentration de CO_2. À titre d'exemple, pour un taux de sursaturation de 1,3 une augmentation de 0,06 % de la concentration de CO_2 apporte une augmentation relative du taux de nucléation de presque 100 %.

Comme pour le taux de nucléation, la variation relative du rayon critique est exprimée dans l'équation (2.21) et représentée figure 2.10 pour différents taux de sursaturation compris entre 1,1 et 2,0.

$$\frac{\left|r_c(c_{CO_2}+\alpha_c)-r_c(c_{CO_2})\right|}{r_c(c_{CO_2})}=\left|\frac{\ln S}{\ln\left(S+\frac{\alpha_c}{c_{CO_2,sat}}\right)}-1\right| \tag{2.21}$$

Il est important de noter que, selon l'équation (2.11), le rayon critique du cristal diminue lorsque la concentration du CO_2 augmente. Ainsi, la valeur absolue de la variation du rayon critique des cristaux de CO_2 solide est tracée en fonction de la variation de la concentration de CO_2.

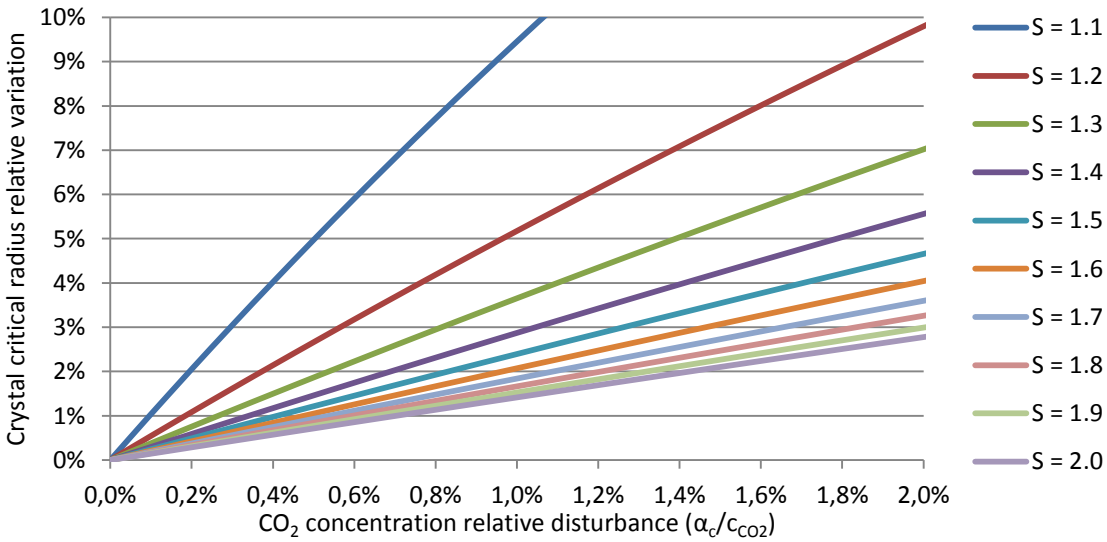

Figure 2.10 : Variation relative du rayon critique de nucléation en fonction de la variation de la concentration de CO_2, T = -100 °C

Cette analyse de la sensibilité du phénomène de nucléation en fonction de la concentration en CO_2 dans les fumées indique que le transfert de masse à partir de la phase vapeur à la phase solide est largement dépendant de la sursaturation. Le transfert de masse peut être multipliée par un facteur de 20 et plus lorsque cette concentration varie de seulement 0,01 % à faibles taux de sursaturation. La morphologie du dépôt de CO_2 solide provenant de la cristallisation homogène n'est pas largement affectée par les variations de concentration de CO_2 puisque le rayon critique de nucléation ne varie pas significativement avec ces perturbations.

2.3.2 Analyse de sensibilité à la variation de la température des fumées

Comme la nucléation homogène dépend principalement de la température du mélange gazeux, une étude de sensibilité est réalisée en considérant une variation α_T de la température du mélange gazeux.

$$\frac{I(T-\alpha_T)-I(T)}{I(T)} = \exp\left\{-\frac{B'}{(T-\alpha_T)^3.\left[\ln\left(\frac{c_{CO_2}}{c'_{CO_2,sat}}\right)\right]^2}+\frac{B'}{T^3.(\ln S)^2}\right\}-1 \qquad (2.22)$$

Où:

$$B' = \frac{16\pi\gamma^3}{3\mathrm{K}_B^3} \qquad (2.23)$$

$c'_{CO_2,sat}$ est la concentration molaire de saturation de CO_2 calculée pour une température de $T-\alpha_T$. La tension surfacique est supposée rester constante pour ces petites variations de température.

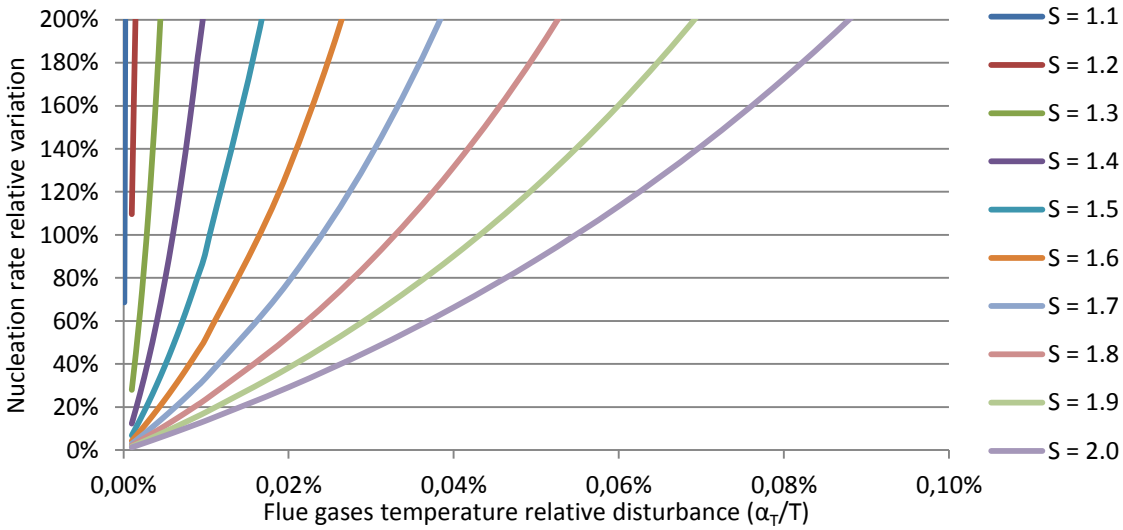

Figure 2.11 : Variation relative du taux de nucléation
en fonction de la variation de la température des fumées, T = -100° C

La Figure 2.11 montre que le taux de nucléation varie considérablement lors de la diminution de la température des fumées. Le taux de nucléation est plus sensible à la variation de la température du mélange gazeux qu'à la variation de la concentration du soluté.

La variation du rayon critique de cristallisation est aussi étudiée en fonction de la variation de la température.

$$\frac{|r_c(T-\alpha_T)-r_c(T)|}{r_c(T)} = \left| \frac{T\,.\ln S}{(T-\alpha_T).\ln\left(\frac{c_{CO_2}}{c'_{CO_2,sat}}\right)} - 1 \right| \qquad (2.24)$$

La variation du rayon critique produite par une diminution de la température est représentée figure 2.12. Le rayon critique est considérablement affecté par la variation de la température par rapport à la variation de la concentration de CO_2.

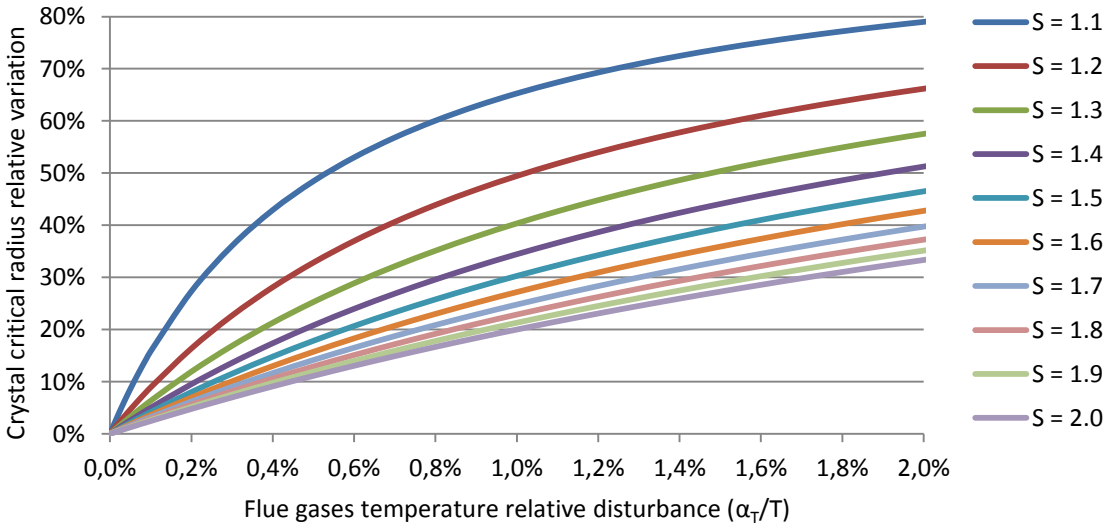

Figure 2.12 : Variation relative du rayon critique
en fonction de la variation de la température des fumées, T = -100 °C

2.4 Conclusions

Dans ce chapitre, le transfert de masse d'une phase mère à une nouvelle phase est étudié. La théorie classique de la nucléation est utilisée en expliquant les différents types de

nucléation : nucléation homogène et hétérogène, primaire et secondaire. Les théories de la nucléation homogène et hétérogène sont exposées, calculant la vitesse de nucléation, le rayon critique des nouveaux nucléides formés et le taux de transfert de masse entre les deux phases. La variation d'énergie libre critique capable d'initier la nucléation est également calculée. Pour une nucléation hétérogène primaire, l'effet de l'angle de contact entre le soluté cristallisé et la surface refroidie est déterminé. Dans le cas de la nucléation hétérogène, un degré de sursaturation plus faible est capable d'initier la nucléation par rapport au cas homogène. L'équation de la vitesse de réaction d'Arrhénius est utilisée afin de calculer la vitesse de nucléation pour les deux cas.

Une analyse de sensibilité est réalisée afin d'évaluer l'effet de la variation de la concentration de CO_2 et de la température des fumées sur les conditions de givrage du CO_2. Les sensibilités de la vitesse de nucléation homogène et du rayon critique sont calculées afin d'évaluer l'effet de la concentration et des perturbations de la température sur le taux de transfert de masse et de la morphologie du dépôt solide. L'analyse de sensibilité a montré une grande variation du taux de nucléation et du rayon critique en raison de la perturbation de la concentration de CO_2. Par conséquence, la sursaturation est un paramètre clé qui doit être contrôlé afin de contrôler le transfert de masse de la phase vapeur à la nouvelle phase solide. Les effets d'autres paramètres comme la vitesse des fumées, la diffusion moléculaire, la porosité du dépôt de givre, la masse volumique et la conductivité thermique ont été exposés et discutés.

Chapter 3. Etude expérimentale de l'antisublimation du CO_2 sur un échangeur tubes-ailettes

3.1 Introduction

Une étude expérimentale de l'antisublimation du CO_2 sur un échangeur tubes-ailettes est d'un grand intérêt pour comprendre le phénomène de précipitation du CO_2 sur les ailettes des échangeurs de chaleur en fonction des propriétés de l'écoulement des fumées et des surfaces froides de l'échangeur. En fait, le captage du CO_2 par antisublimation sur des sources industrielles concentrées doit prendre en compte des concentrations molaires de CO_2 comprises entre 4 % et 29 %. De plus, au cours de la décarbonation des fumées, la concentration en CO_2 diminue tout au long des CFX, d'où la nécessité de l'étude de l'effet de la concentration en CO_2 sur la morphologie et les propriétés du givrage.

Une nouvelle configuration des échangeurs tubes-ailettes doit être conçue en prenant en compte la variation dynamique du coefficient de transfert de chaleur externe qui affecte considérablement le transfert du CO_2 de la phase vapeur à la phase solide. En effet, la formation du dépôt de CO_2 solide sur l'échangeur a une incidence sur la température de surface, la vitesse des fumées et la variation du transfert de chaleur et de masse sur le côté externe de l'échangeur de chaleur.

Peu de recherches expérimentales ont été menées pour étudier le givrage du CO_2 sur des échangeurs de chaleur tubes-ailettes ou sur des plaques planes. Shchelkunov [SHC85] a effectué une étude expérimentale pour mesurer l'évolution dans le temps des caractéristiques thermo-physiques du givrage de CO_2 à partir d'un mélange N_2-CO_2 sur une plaque cryogénique. Les résultats de cette étude ne sont pas exploitables dans le cadre de notre étude parce que les plages de température et de sursaturation étudiées sont différentes des conditions de givrage souhaitées. De même, les résultats de l'étude expérimentale de T. Cook et G. Davey [COO76] dans le cadre d'optimisation des pompes à vide cryogéniques ne peuvent pas être utilisés car les pressions partielles de CO_2 et la température de mélange des gaz sont très faibles par rapport à l'application de givrage du CO_2 des fumées.

Plusieurs études ont été menées afin de mesurer et de visualiser la formation de givre d'eau et son développement sur des plaques planes, des surfaces cylindriques et des échangeurs de chaleur tubes-ailettes [VER02], [ALJ08], [LEE01], [SHIN03], [LIU06] [DENG03], [ARG01], [MAO92] et [FAH96]. Ces études sont considérées dans ce chapitre afin de prendre en compte les techniques expérimentales utilisées pour mesurer les propriétés du givrage telles que la masse volumique et la conductivité thermique.

Une analyse qualitative et quantitative doit être effectuée afin d'étudier le dépôt de CO_2 solide. La morphologie du dépôt, sa formation, son accumulation et son homogénéité sur la totalité de la surface du CFX et pour différentes conditions de givrage doivent être étudiées par observation visuelle. Une observation, à fort grossissement, de la précipitation de CO_2 permet la compréhension de la théorie de la cristallisation étudiée au chapitre 2 et la vérification de l'effet de nombreux paramètres tels que la concentration en CO_2, le taux de sursaturation, la température de la surface solide, la rugosité de la surface solide et la vitesse des fumées. La forme et la taille des cristaux de CO_2 peuvent également être observées en utilisant un grossissement optique de 200x. Les caractéristiques du givre formé sur la surface des CFX sont calculées par les mesures quantitatives. Le suivi de l'évolution temporelle de l'épaisseur de givre de CO_2 et de la vitesse de nucléation permet le calcul de la masse volumique moyenne et de la porosité du givre. En outre, l'évolution de la concentration en CO_2, de la température des fumées et la température du fluide frigorigène est suivie tout au long des CFX. Les effets de la croissance du givre de CO_2 sur les performances des CFX, plus particulièrement sur le coefficient de transfert thermique global entre le mélange de fluides frigorigènes et les fumées, sont étudiés.

3.2 Description du banc d'essais

Deux sous-systèmes principaux constituent le banc d'essais : la cascade intégrée et le circuit des fumées équivalentes. Le mélange de gaz équivalent aux fumées est un mélange à composition contrôlée de N_2 / O_2 et de CO_2. La cascade intégrée est une machine frigorifique utilisée pour produire 4,4 kW de puissance frigorifique à des températures allant jusqu'à -130 °C.

Le banc d'essais couple la cascade intégrée au circuit fermé des fumées équivalentes dans le but de tester les conditions d'exploitation réalistes du processus de captage du CO_2 par antisublimation. Les deux évaporateurs de la cascade intégrée sont installés dans la boucle de fumées équivalentes et fonctionnent alternativement en mode givrage, dégivrage et conditionnement en température. Un système d'injection de CO_2 contrôle la concentration en CO_2 à l'entrée des CFX. Une résistance électrique contrôle la température des fumées équivalentes après qu'elles soient ré-enrichies en CO_2.

3.2.1 L'échangeur tubes-ailettes de givrage et de dégivrage de CO_2

Un échangeur de chaleur tubes-ailettes est utilisé comme un évaporateur à basse température (CFX) de la cascade intégrée. L'évaporation du mélange de fluides frigorigènes dans les tubes refroidit les fumées équivalentes. Lorsque la température de ces fumées devient inférieure à la température d'antisublimation du CO_2, en fonction de sa pression partielle, le CO_2 givre et précipite sur les ailettes de l'évaporateur. Les CFX sont conçus pour assurer une puissance de refroidissement de 4,3 kW à des températures comprises entre -120 °C et -100 °C. Ces échangeurs de chaleur ne sont pas optimisés de manière à assurer un glissement de température optimal mais plutôt pour visualiser la nucléation du CO_2 et mesurer son taux de nucléation pour différentes concentrations. Afin de mesurer le taux de nucléation du CO_2 à travers les échangeurs de chaleur, la composition des fumées est mesurée en aval et en amont des échangeurs de chaleur et également sur quatre emplacements à l'intérieur de l'échangeur de chaleur. La température des fumées et du mélange de fluides frigorigènes est également mesurée afin d'analyser les pincements de température entre les fumées et le mélange de fluides. De plus, le débit massique des fumées équivalentes est mesuré pour calculer le bilan massique à l'entrée et à la sortie de l'évaporateur et donc calculer la quantité de CO_2 déposée sur l'échangeur.

Figure 3.1 : Echangeur tubes-ailettes de givrage de CO_2 (CFX)

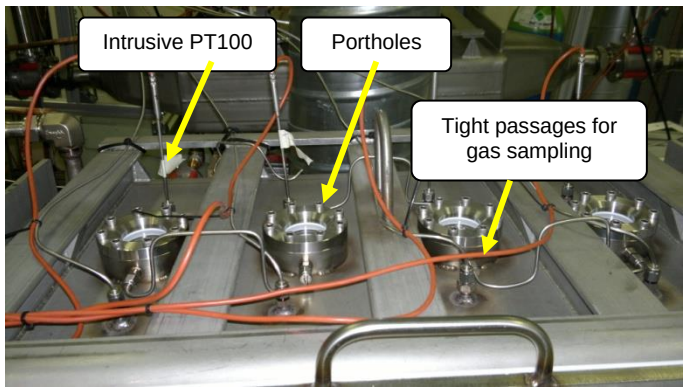

Figure 3.2 : Mesure de la température des fumées et son échantillonnage à travers l'enceinte

Le microscope numérique VHX-1000 est utilisé pour visualiser l'antisublimation dynamique du CO_2 sur les ailettes de l'échangeur de chaleur. L'objectif VH-Z20R est utilisé permettant un grossissement optique entre 20x et 200x. Un faible grossissement (30x) est utilisé pour visualiser l'évolution de la couche de CO_2 solide sur les ailettes et le grossissement élevé (100x) permet de suivre la formation et le développement de cristaux de CO_2. La taille des cristaux de CO_2 et du dépôt solide est mesurée par le traitement d'images par le logiciel VHX-1000.

Figure 3.3 : Moteur pas à pas, caméra et objectif

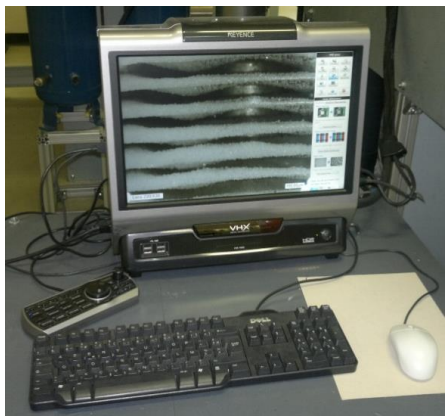

Figure 3.4 : Ordinateur de traitement et de contrôle d'image, VHX-1000

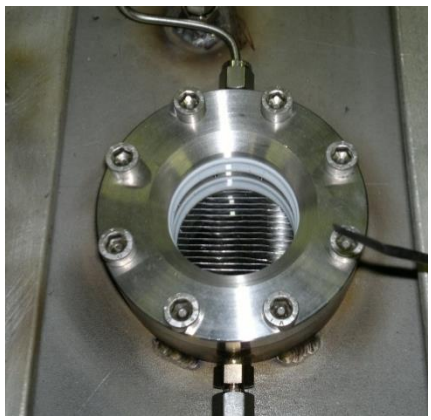

Figure 3.5 : Hublot de visualisation des CFX

3.3 Procédure expérimentale

Dans cette étude, seule l'antisublimation du CO_2 sur l'évaporateur est étudiée. La morphologie du givre de CO_2, le taux de nucléation et la variation de la masse volumique sont aussi étudiés. A cet effet, seule une partie de l'échangeur de chaleur est étudiée où la température des fumées équivalentes et leur composition sont contrôlées. La zone testée de l'échangeur de chaleur est limitée à trois rangs à la sortie de l'échangeur où les fumées équivalentes sont déjà refroidies.

Après la déshumidification et le refroidissement de la boucle des fumées équivalentes, le CO_2 est injecté et sa concentration est contrôlée à l'entrée de l'échangeur testé. La visualisation en temps réel des ailettes de l'évaporateur au niveau des rangs testés permet l'analyse de l'évolution de la couche de givre.

3.3.1 Contrôle de la composition des fumées équivalentes

Les fumées sont simulées en mélangeant du CO_2 avec un mélange de N_2 et d'O_2. Ce mélange permet de simuler les fumées émises par les centrales thermiques à charbon à une concentration de 15 % v/v de CO_2 et pour une autre au gaz naturel, soit une concentration de CO_2 de 3 % v/v. A cet effet, un régulateur de débit est utilisé pour injecter du CO_2 gaz à la sortie échangeur de chaleur avant de le faire re-circuler en contrôlant sa température. Le contrôle analogique du débit de CO_2 injecté assure une variation de la concentration en CO_2 inférieure à 1 % par rapport à la valeur de consigne à l'entrée de l'échangeur de chaleur à tester. Cette variation de concentration est représentée figure 3.6 pour trois essais réalisés à 3, 8 et 15 % v/v de CO_2.

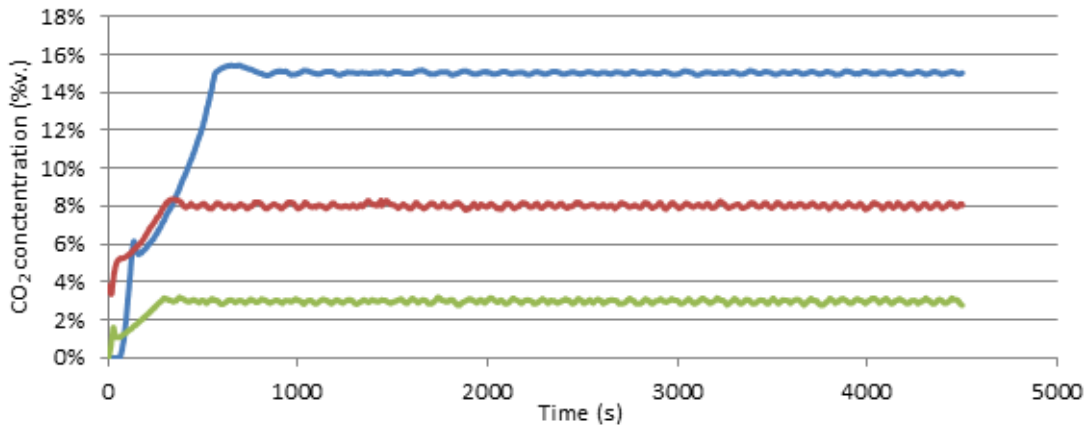

Figure 3.6 : Régulation de la concentration en CO_2 à l'entrée de l'échangeur testé

3.3.2 *Contrôle de la température des fumées équivalentes et du mélange de fluides frigorigènes*

La température des fumées à l'entrée des rangs testés de l'échangeur est contrôlée par la puissance fournie par le réchauffeur de gaz. La régulation assure une variation de température inférieure à 1 % par rapport à la température consigne. En outre, la température du mélange de fluides frigorigènes est contrôlée en contrôlant la basse pression de la cascade intégrée avec une précision de 1 % (figure 3.7).

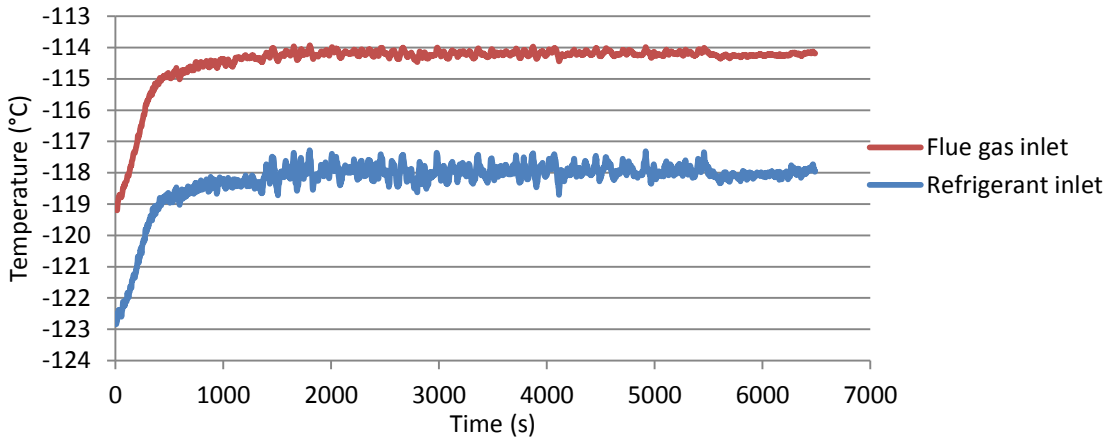

Figure 3.7 : Contrôle de la température des fumées équivalentes et des fluides frigorigènes

3.3.3 *Contrôle du débit des fumées équivalentes*

Le débit massique des fumées équivalentes est également contrôlé à l'entrée de l'échangeur de chaleur testé. La figure 3.8 représente le débit massique des fumées équivalentes mises en circulation par un ventilateur à vitesse variable.

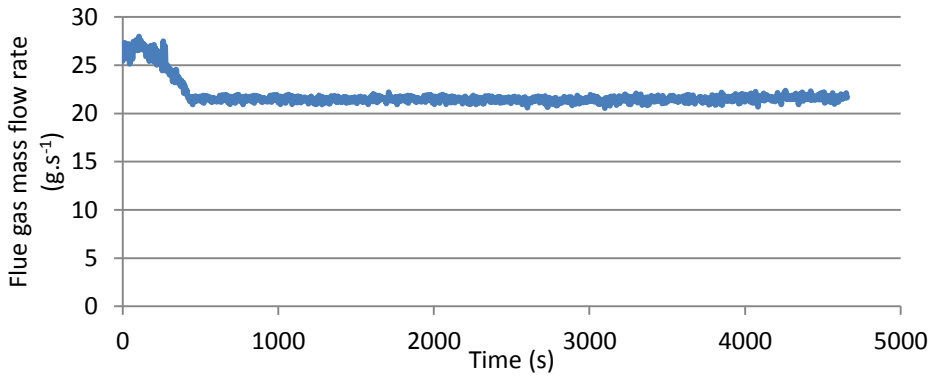

Figure 3.8 : Régulation du débit massique des fumées reconstituées

3.4 Résultats des essais

3.4.1 *Mesure de la sursaturation*

La pression partielle du CO_2 à l'entrée et à la sortie de l'échangeur de chaleur testé est calculée en mesurant la pression totale des fumées équivalentes et la concentration molaire du CO_2. La pression d'équilibre solide-vapeur du CO_2, ou la pression d'antisublimation, est calculée à l'aide de Refprop V9.0 en fonction de la température des fumées.

$$S_{CO_2}(t) = \frac{P_{CO_2}}{P_{sub,CO_2}(T_{fg})} = \frac{P_{fg} \,.\, v_{CO_2}}{P_{sub,CO_2}(T_{fg})} \tag{3.1}$$

Les taux de sursaturation mesurés à l'entrée d'échangeur de chaleur testé et à sa sortie sont tracés sur les figures 3.9 et 3.10.

Dans le premier cas, les fumées ont un faible taux de sursaturation compris entre 1,1 et 1,15 à la sortie de l'échangeur de chaleur. A la fin du cycle de givrage les fumées équivalentes sont saturées à la sortie de l'échangeur de chaleur. Pour le second cas de concentration de CO2 de 15% v/v, les fumées sont plus sursaturées ayant un taux de sursaturation de 1,2 à la sortie. A l'entrée, la sursaturation augmente et atteint 1,2 à la fin du cycle de givrage.

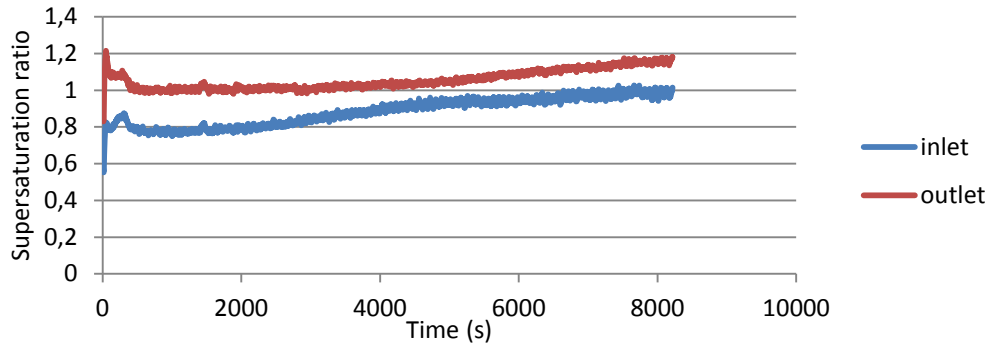

Figure 3.9 : Taux de sursaturation à l'entrée et à la sortie de l'échangeur de chaleur testé (8 % v/v).

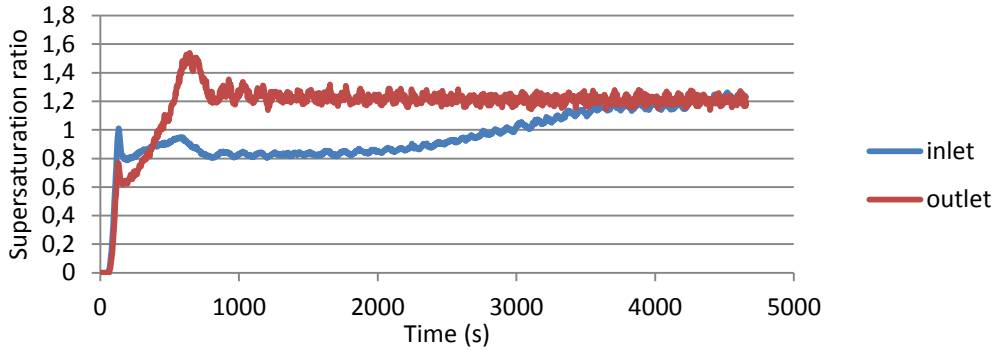

Figure 3.10 : Taux de sursaturation à l'entrée et à la sortie de l'échangeur de chaleur testé (15 % v/v).

La sursaturation est mesurée avec une incertitude type composée égale à ± 2.75E^{-02}. L'effet de cette différence de taux de sursaturation sur la formation de givre est analysé dans les sections suivantes. Une grande différence de taux de nucléation est mesurée entre ces deux conditions de sursaturation.

3.4.2 La morphologie des cristaux et du dépôt de givre de CO_2

3.4.2.1 La morphologie des cristaux

Selon l'étude bibliographique effectuée au chapitre 2, l'antisublimation de CO_2 se déroule selon la théorie de nucléation. Selon cette théorie, au début du cycle de givrage, la nucléation primaire hétérogène doit avoir lieu aboutissant à la forme de nucléides de CO_2 solide sur les ailettes de l'échangeur de chaleur. Afin de vérifier cette théorie, les ailettes de l'échangeur de chaleur sont visualisées sous de faibles (X30) et hauts (X200) grossissements. Indépendamment de la concentration en soluté, la nucléation hétérogène primaire se produit dans le procédé d'antisublimation de CO_2. Des nucléides sphériques se forment sur les ailettes montrant une bonne affinité entre les le CO_2 solide et l'alliage d'aluminium constituant les ailettes. La figure 3.11 montre la formation de cristaux de CO_2 solide sur les ailettes en aluminium. La formation de ces nucléides au début du cycle de givrage est essentielle pour la formation du dépôt solide et sa croissance. Après le premier dépôt de ces embryons, le transfert de masse est induit par la croissance des embryons et par la nucléation secondaire, où de nouveaux embryons se forment sur les anciens.

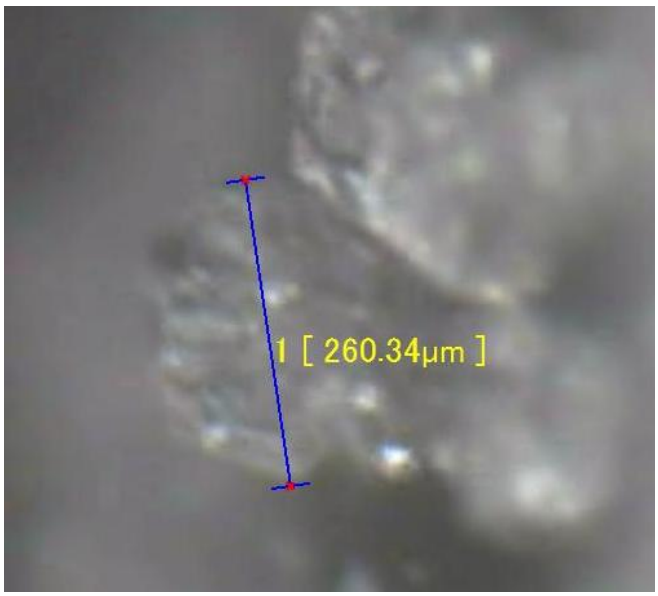

Figure 3.11 : Cristal sphérique de CO_2 solide (200x de grossissement)

3.4.2.2 La morphologie du dépôt solide

Contrairement à la morphologie des cristaux solides, la morphologie de dépôt dépend de la concentration en CO_2 dans les fumées. A des concentrations élevées de CO_2 (8 %, 15 % et 18 % v/v) le dépôt solide a un aspect granulaire. Par contre à de faibles concentrations (3 % v/v) des réseaux cristallins peuvent être identifiés. La figure 3.12 représente les deux couches solides obtenues à 15 % (a) et à 3 % v/v (b).

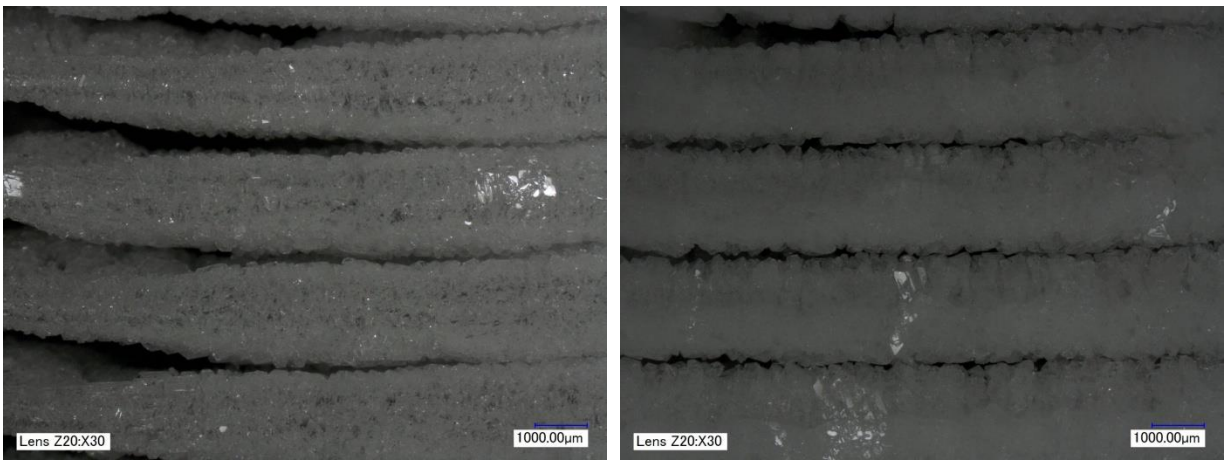

a) 15% v/v *b) 3% v/v*

Figure 3.12 : La morphologie du dépôt de CO_2 solide en fonction de sa concentration dans les fumées

3.4.3 La mesure de l'épaisseur du dépôt de CO_2 solide

La visualisation du dépôt de givre permet de suivre l'évolution en temps réel de son épaisseur. Dans cette étude, le dépôt de CO_2 solide est suivi à l'aide d'un microscope numérique et des photos de la couche de givre sont prises toutes les 15 s. Un grossissement de 30x permet aussi d'étudier la morphologie du dépôt. L'épaisseur de la couche de givre est mesurée en utilisant le logiciel VHX-1000 pour le traitement de l'image. L'utilisation de ce logiciel permet d'effectuer les mesures avec une précision de ± 0,01 µm. La plus grande incertitude de mesure est due à des erreurs de lecture de l'opérateur et elle est estimée être de l'ordre de 5 µm.

La figure 3.13 représente l'évolution de l'épaisseur du dépôt solide de CO_2 pendant le cycle de givrage. Pour les trois tests effectués à différentes concentrations de CO_2, l'évolution de l'épaisseur a un aspect similaire et elle est divisée en 3 périodes. Au cours de la première

période, un premier dépôt a lieu. Des embryons séparés se forment et se développent sur les ailettes. A la fin de la première période, la température de surface du cristal augmente en limitant la formation du dépôt et sa croissance dans le sens perpendiculaire à la surface de l'ailette. Durant la seconde période, le transfert de masse s'effectue à l'intérieur de la couche solide en formant de nouveaux nucléides sur les ailettes et par la croissance latérale des nucléides déjà existants. Après la phase de densification du givre, la conductivité thermique de la couche solide augmente, diminuant la température de surface du givre et permettant le début de la troisième période de givrage. Pendant cette période, l'épaisseur de la couche augmente linéairement avec une masse volumique moyenne constante. Les trois périodes de givrage décrites sont représentés figure 3.13.

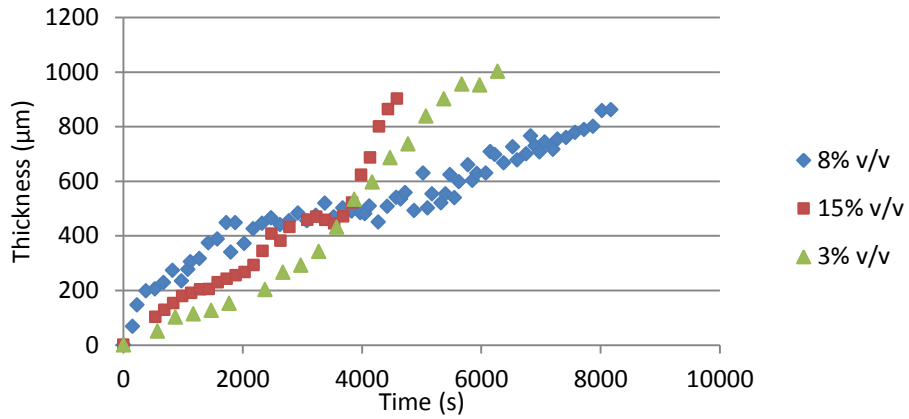

Figure 3.13 : Evolution de l'épaisseur du dépôt de CO_2 solide

Une différence de l'évolution de l'épaisseur du givre est observable entre le cas des fumées à 8 % de concentration de CO_2 et les deux autres cas, pour lesquels l'épaisseur croît plus rapidement. De ce fait, l'évolution de l'épaisseur du givre est indépendante de la concentration de CO_2 mais dépend plutôt du taux de sursaturation. L'essai avec 8 % de CO_2 est effectué avec le taux de sursaturation le plus faible.

3.4.4 Mesure du transfert de masse

La mesure continue de la composition des fumées équivalentes à l'entrée et à la sortie de l'échangeur testé, ainsi que la mesure du débit massique des fumées à l'entrée de l'échangeur permettent la mesure du transfert de masse de CO_2 entre les fumées et la surface givrée. Le taux de nucléation par unité de surface est calculé en divisant le transfert de masse de CO_2 par la surface de l'échangeur testé, soit 2,14 m^2. La masse totale du dépôt de CO_2 solide est aussi mesurée.

3.4.4.1 Le taux de nucléation

La figure 3.14 présente les taux de nucléation mesurés pour deux concentrations différentes de CO_2. Cette différence de taux de nucléation n'est pas induite par la différence de concentration mais plutôt par la différence du taux de sursaturation. Pour les deux cas, un taux de nucléation élevé est mesuré au début du cycle de givrage et il diminue au cours de la formation de la couche solide. Cette diminution du taux de nucléation est due à la diminution du coefficient de transfert thermique global entre les fumées et le fluide frigorigène.

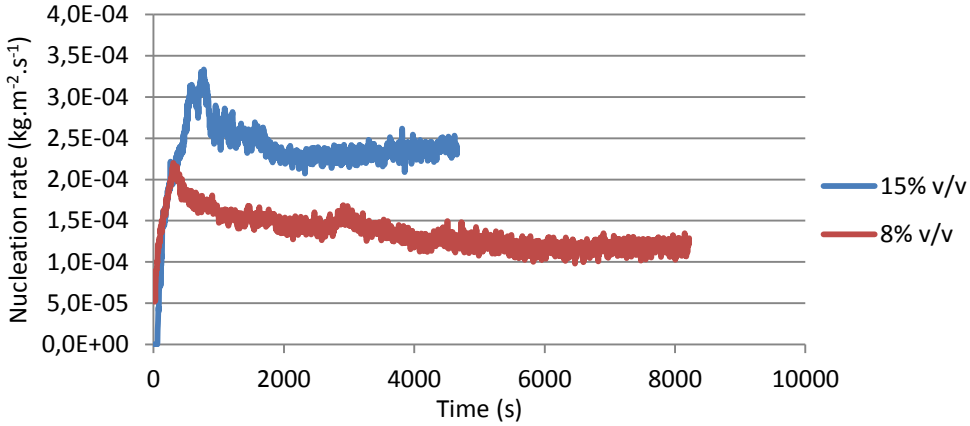

Figure 3.14 : Variation du taux de nucléation pour les essais à 15 % et 8 % v/v de CO_2

3.4.4.2 Evolution de la masse totale du dépôt de CO_2 solide

La figure 3.53 présente l'évolution de la masse totale du givre de CO_2. Trois cas sont représentés pour différentes concentrations de CO_2 et à différents taux de sursaturation. Comme indiqué dans le paragraphe précédent, l'accumulation de CO_2 solide ne dépend pas de la concentration. Ce fait est observable figure 3.15. Le taux d'accumulation diminue à la fin du cycle de givrage dû à la vitesse de nucléation décroissante.

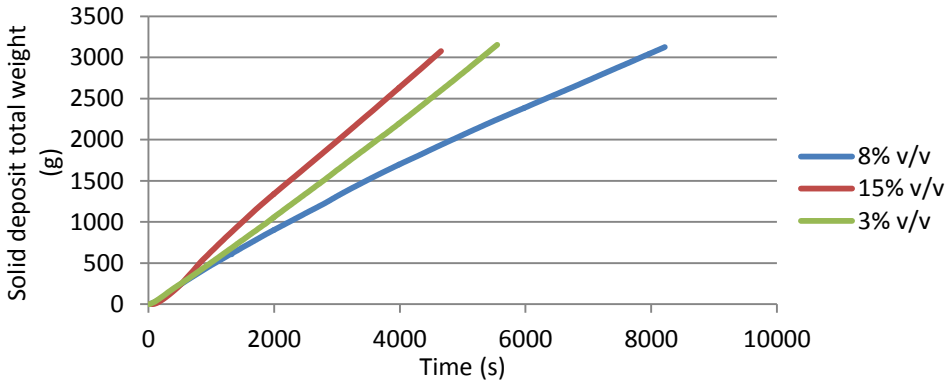

Figure 3.14 : Evolution de la masse totale du dépôt de CO_2 solide

3.4.5 La masse volumique moyenne et la porosité du givre de CO_2

La masse volumique moyenne de dépôt du CO_2 solide est calculée connaissant la masse totale de CO_2 givré et l'épaisseur du dépôt. La masse totale du dépôt de givre n'inclut pas la masse négligeable du gaz qui remplit les pores du givre.

$$\bar{\rho}_{dep,CO_2}(t) = \frac{m_{s,CO_2}(t)}{\delta(t)\,.\,A_{HX}} \tag{3.2}$$

La porosité de la couche de givre est le rapport entre le volume du gaz piégé dans le givre et le volume total du dépôt. Cette porosité est calculée par l'équation (3.3) en supposant que la température du givre est égale à la température moyenne entre l'entrée et la sortie de l'échangeur testé.

$$\varphi_{dep,CO_2}(t) = \frac{V_v}{V_{deposit}} = \frac{\bar{\rho}_{dep,CO_2}(t) - \rho_{s,CO_2}(T)}{\rho_{fg}(T) - \rho_{s,CO_2}(T)} \tag{3.3}$$

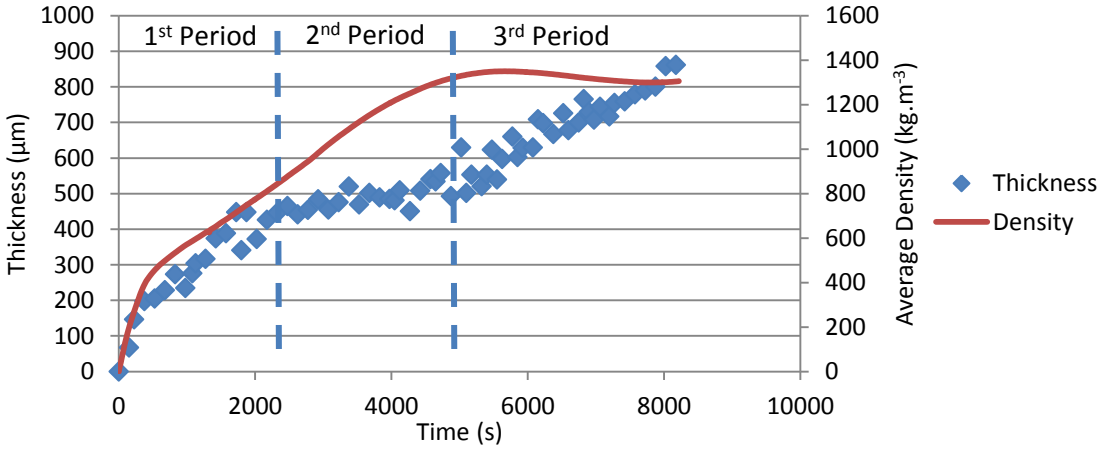

Figure 3.15 : Evolution de la masse volumique du CO_2 solide et de son épaisseur (8 % v/v)

La figure 3.15 présente les évolutions de la masse volumique moyenne du dépôt solide et de son épaisseur. Les trois phases de la croissance du dépôt de givre sont observables. Après la première formation de givre à une faible masse volumique (de 0 à 2 000 s), une période de densification se déroule au cours de laquelle le transfert de masse se produit à épaisseur constante. Au cours de cette densification, la conductivité thermique du dépôt solide augmente permettant la diminution de la température de la surface de dépôt. Le calcul de la conductivité thermique du dépôt n'est pas possible car la température de la surface de dépôt n'est pas mesurable pour cette configuration d'échangeur de chaleur. La dernière phase de la croissance du dépôt a lieu à masse volumique moyenne constante.

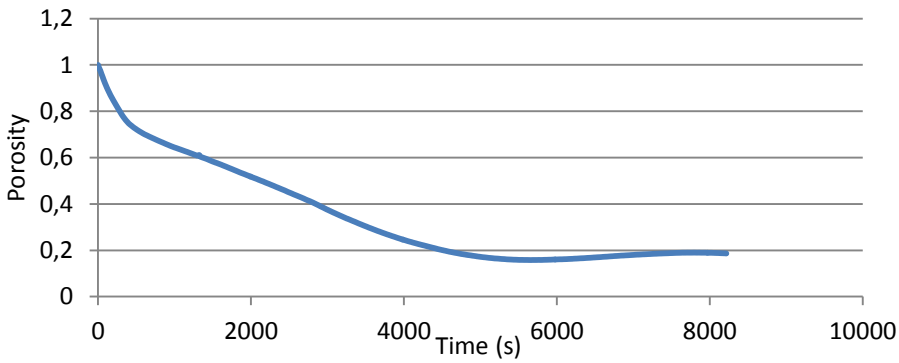

Figure 3.16 : Evolution de la porosité du dépôt de CO_2 solide (8 % v/v)

3.5 Conclusions

L'étude expérimentale de l'antisublimation de CO_2 sur un échangeur de chaleur tubes-ailettes montre que l'antisublimation se déroule selon la théorie classique de la nucléation. La visualisation de la formation des cristaux de CO_2 solide montre une bonne affinité entre le CO_2 solide et les ailettes en alliage d'aluminium de l'échangeur de chaleur. Cette bonne affinité, telle que décrite dans la théorie de la nucléation hétérogène, favorise la formation de nucléides de CO_2 sur la surface des ailettes. La formation des nucléides sphériques est indépendante de la concentration en CO_2 des fumées. La même morphologie cristalline est observée pour des concentrations de CO_2 faibles et élevées. Une différence de morphologie de la couche de givre est remarquée pour différentes concentrations de CO_2. À des concentrations élevées, 8 %, 15 % et 18 % v/v, la couche solide présente une morphologie granulaire avec une masse volumique relativement élevée. A des concentrations plus faibles, de 3 % v/v, le dépôt solide a une morphologie de réseau de cristaux où les arêtes des plans de cristaux sont visibles. Le dépôt formé à faible concentration en soluté est relativement poreux par rapport au dépôt formé à des concentrations élevées.

Par la visualisation de la croissance du dépôt de CO_2 solide, trois périodes de givrage sont identifiées. Le premier dépôt a lieu sous la forme de nucléation hétérogène primaire et est directement affecté par le taux de sursaturation. La deuxième période de givrage se produit

à une épaisseur constante de givre pour laquelle le transfert de masse procède par diffusion du CO_2 dans le dépôt poreux. Au cours de cette période, la masse volumique moyenne du dépôt augmente, ce qui accroît à son tour la conductivité thermique. Cette densification conduit à la diminution de la température de surface du givre permettant le début de la troisième période de givrage.

Les résultats expérimentaux sont utilisés au chapitre 4 afin de valider le modèle CFD dynamique simulant le givrage de CO_2 sur un échangeur de chaleur tubes-ailettes.

Chapter 4. Modèle CFD pour la prévision du givrage de CO_2 sur un échangeur de chaleur tubes-ailettes

4.1 Introduction

Dans ce chapitre, un modèle CFD 3D est réalisé, basé sur le modèle proposé par J. Cui et al. [CUI11A], pour simuler la formation transitoire de givre de CO_2 et sa croissance sur un échangeur de chaleur tubes-ailettes. Ce modèle permet d'étudier l'influence des propriétés géométriques de l'échangeur, comme le pas d'ailettes et le facteur de forme, sur le givrage de CO_2. Ce modèle identifie également l'effet de la température du fluide frigorigène sur le comportement du givre CO_2. La température du fluide frigorigène est considérée comme une condition aux limites pour le modèle. Ce modèle est basé sur la théorie de la nucléation étudiée au chapitre 2 afin de quantifier le transfert de masse entre la phase gaz et la phase solide, et également pour prédire la structure du givre qui dépend de la distribution de la température sur l'ailette et de la température des fumées. En outre, l'épaisseur moyenne du dépôt, la masse volumique moyenne et la puissance frigorifique sont calculées par le modèle. Les résultats des simulations sont validés par comparaison avec les résultats expérimentaux obtenus au chapitre 3.

4.2 Modèle CFD dynamique de l'antisublimation de CO_2 sur un échangeur tubes-ailettes

Dans cette section est présenté le modèle CFD réalisé pour simuler la formation de givre de CO_2 et sa croissance sur un échangeur de chaleur. Le modèle physique représentant l'échangeur de chaleur est décrit et ensuite les équations du modèle diphasique eulérien sont introduites. Le transfert de masse et les termes sources sont calculés pour chaque phase en utilisant la théorie classique de la nucléation. L'effet de la formation du givre est intégré dans les équations de conservation en ajoutant des termes sources aux équations de conservation de la masse, de la quantité de mouvement et de l'énergie.

4.2.1 Description du modèle physique

Dans la Figure 4.1 est représenté le modèle physique pris en compte pour simuler la formation de givre sur un échangeur de chaleur tubes-ailettes. Les deux plans verticaux latéraux sont considérés comme des surfaces de symétrie. La surface horizontale supérieure est également considérée comme un plan de symétrie divisant le volume compris entre deux ailettes consécutives. La surface horizontale inférieure est considérée comme l'ailette plane de l'échangeur de chaleur. Contrairement à l'échangeur à ailettes ondulées, testé dans l'étude expérimentale, des ailettes planes sont prises en compte dans ce modèle afin de simplifier le système.

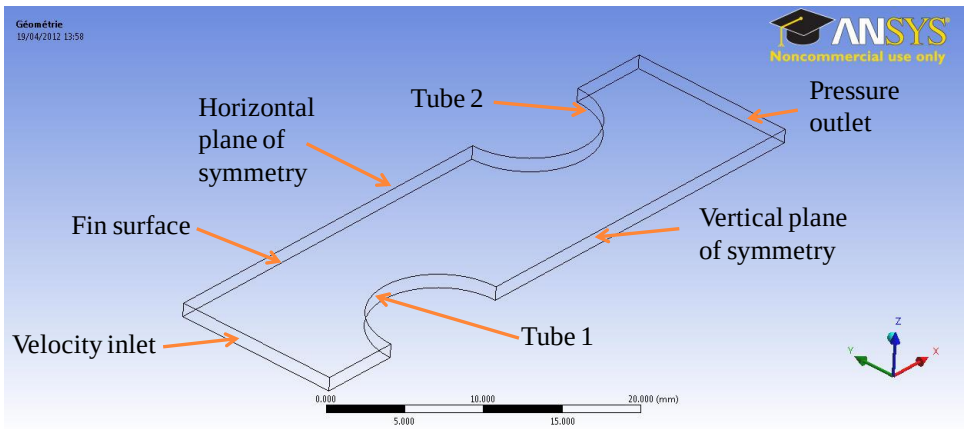

Figure 4.1 : Domaine de calcul 3D de l'échangeur de chaleur

4.2.2 Modèle mathématique

Pour simuler un écoulement diphasique, la mécanique des fluides numérique fournit actuellement deux approches : l'approche Euler-Lagrange et l'approche Euler-Euler. L'approche Euler-Euler traite les différentes phases en diffusion continue et en utilisant le concept de la fraction volumique de phase pour identifier la présence des différentes phases dans des volumes finis du modèle étudié. Fluent propose trois différents modèles multiphasiques selon l'approche Euler-Euler : le modèle de volume de fluide (VOF), le modèle de mélange et le modèle eulérien. Le modèle eulérien résout un ensemble d'équations de continuité pour chaque phase séparément des autres phases. Ce modèle est utilisé lorsque les phases dispersées sont concentrées dans certaines régions du domaine. Cette modélisation de l'antisublimation du CO_2 considère la phase solide comme une phase secondaire dans le domaine qui se forme à proximité des surfaces des ailettes et des tubes. La phase primaire est la phase continue des fumées.

Les équations du modèle diphasique à multi-composants sont résumées dans cette section. Compte tenu du modèle diphasique, la notion de fraction volumique est utilisée. La fraction volumique α_q de la phase q est le volume occupé par la phase q dans un volume défini, soit :

$$V_q = \int_V \alpha_q \, dV \tag{4.1}$$

$$\sum_{q=1}^{n} \alpha_q = \alpha_s + \alpha_{fg} = 1 \tag{4.2}$$

L'indice s est utilisé pour indiquer la phase de CO_2 solide et l'indice fg est utilisé pour se référer à la phase gaz des fumées.

Les équations de conservation de la masse pour les deux phases étudiées sont :

$$\frac{\partial \alpha_s \rho_s}{\partial t} + \nabla \cdot (\alpha_s \rho_s \overrightarrow{u_s}) = \vartheta_{m_s} \tag{4.3}$$

$$\frac{\partial \alpha_{fg} \rho_{fg}}{\partial t} + \nabla \cdot \left(\alpha_{fg} \rho_{fg} \overrightarrow{u_{fg}}\right) = \vartheta_{m_{fg}} \tag{4.4}$$

ϑ_{m_s} et $\vartheta_{m_{fg}}$ sont les termes sources de masse pour chaque phase et ils sont reliés par l'équation (4.5).

$$\vartheta_{m_s} = \left|\vartheta_{m_{fg}}\right| \tag{4.5}$$

Outre les équations de conservation de masse, des équations de conservation des composants sont nécessaires. Au cours de givrage, le transfert de masse de CO_2 se produit entre le CO_2 gaz présent dans les fumées et le CO_2 solide. L'équation de la conservation des composants de la phase primaire est donnée dans l'équation (4.6).

$$\frac{\partial \left(\alpha_{fg} \rho_{fg} Y_{fg}^i\right)}{\partial t} + \nabla \cdot \left(\alpha_{fg} \, \rho_{fg} \overrightarrow{u_{fg}} \, Y_{fg}^i\right) = -\nabla \cdot \alpha_{fg} \, \vec{J}_{fg}^{\,i} + \vartheta_{Y_{fg}^i} \tag{4.6}$$

$\vartheta_{Y_{fg}^i}$ représente les termes sources des composants induits par le transfert de masse entre les fumées et la phase solide secondaire. Pour la phase primaire, la somme des concentrations volumiques des composants est égale à un.

$$\sum_{i=1}^{3} Y_{fg}^i = 1 \tag{4.7}$$

L'équation de conservation de la quantité de mouvement de la phase i est représentée par l'équation (4.8). Les indices i et j représentent les différentes phases simulées. ϑ_{ui} est le terme source de quantité de mouvement suite au transfert de masse.

$$\frac{\partial(\alpha_i \rho_i \overrightarrow{u_i})}{\partial t} + \nabla \cdot (\alpha_i \, \rho_i \overrightarrow{u_i} \, \overrightarrow{u_i}) = -\alpha_i \, \nabla \mathrm{p} + \nabla \cdot \overline{\overline{\tau_i}} \cdot + K_{ji}\left(\overrightarrow{u_j} - \overrightarrow{u_i}\right) + \vartheta_{ui} \tag{4.8}$$

L'équation de conservation de l'énergie est écrite en prenant en considération la variation de l'enthalpie spécifique de chaque phase. ϑ_{hi} est le terme source de l'énergie transférée entre les phases associées au transfert de masse.

$$\frac{\partial(\alpha_i \rho_i h_i)}{\partial t} + \nabla \cdot (\alpha_i \, \rho_i \overrightarrow{u_i} \, h_i) = \nabla \cdot (k_i \nabla T_i) + \vartheta_{hi} \tag{4.12}$$

Afin de simuler le comportement de l'écoulement pendant le cycle de givrage, le modèle de turbulence $k - \varepsilon$ standard est utilisé. Un ensemble d'équations de transport est utilisé pour chaque phase en prenant en considération l'interaction entre les deux phases.

4.2.2.1 Les termes sources

Afin de quantifier le transfert de masse entre les fumées et le givre de CO_2, la théorie classique de la nucléation développée au chapitre 2 est utilisée. La prédiction du transfert de masse définit les termes sources des équations de conservation pour les phases primaire et secondaire du modèle. Afin de simplifier le modèle, le processus de nucléation est supposé se produire par nucléation homogène sphérique négligeant l'effet de la surface des ailettes et la présence d'impuretés durant le processus de nucléation.

Pour chaque itération, le transfert de masse est calculé en fonction des propriétés du CO_2 solide et de la concentration de CO_2 dans les fumées pour chaque volume fini. Le taux de transfert de masse $\dot{m}_{CO_2 \to s}$ $(kg.m^{-3}.s^{-1})$ est ainsi représenté par l'équation (4.15) :

$$\dot{m}_{CO_2 \to s} = \frac{4}{3}\pi \rho_s I r_c^3 + 4\pi \rho_s \eta \bar{r}^2 \frac{\partial \bar{r}}{\partial t} \tag{4.15}$$

Par conséquent, les termes sources de masse des équations de continuité sont donnés dans l'équation (4.17). Dans chaque volume fini, la masse de CO_2 perdu par les fumées est additionnée à la masse de la phase solide.

$$\vartheta_{ms} = -\vartheta_{m\,fg} = \dot{m}_{CO_2 \to s} \tag{4.17}$$

En outre, le terme source de l'équation de conservation des composants pour le CO_2 de la phase primaire est calculé par l'équation (4.18).

$$\vartheta_{Y_{fg}^{CO_2}} = -\dot{m}_{CO_2 \to s} \tag{4.18}$$

Les termes sources des équations de conservation de la quantité de mouvement sont calculés par les équations (4.19) et (4.20).

$$\vartheta_{u\,fg} = -\dot{m}_{CO_2 \to s} \, \vec{u}_{fg} \tag{4.19}$$

$$\vartheta_{u\,s} = \dot{m}_{CO_2 \to s} \, \vec{u}_s \tag{4.20}$$

Les termes sources des équations de conservation de l'énergie sont calculés par les équations (4.21) et (4.22).

$$\vartheta_{h\,fg} = -\dot{m}_{CO_2 \to s} \, h_{CO_2} \tag{4.21}$$

$$\vartheta_{h\,s} = \dot{m}_{CO_2 \to s} \left(h_{CO_2} + \Delta H_{sub}\right) \tag{4.22}$$

4.2.3 Conditions aux limites

La modélisation de givrage de CO_2 est effectuée pour les conditions d'essai en prenant en compte des fumées à 15 % v/v en CO_2 à l'entrée du domaine. La température des fumées à

l'entrée du domaine, ainsi que la température des tubes sont prises identiques à celles des mesures expérimentales afin de comparer la simulation aux résultats expérimentaux.

$$\bar{Y}_{in,fg}^{CO2} = 15\%\ v/v$$

$$Y_{in,fg}^{N_2} + Y_{in,fg}^{CO_2} = 1$$

$$\bar{u}_{fg,in} = 0.27\ m.s^{-1}$$

$$T_{fg,in} = -98.8°C$$

$$\alpha_s = 0$$

Afin de tenir compte de l'aspect périodique de l'échangeur de chaleur tubes-ailettes, des profils de vitesse et de composition des fumées sont affectés à l'entrée du domaine.

L'ailette est considérée comme une paroi d'aluminium d'une épaisseur fixe de 0,1 mm en prenant en compte leur conduction thermique et leur géométrie. De ce fait, un profil de température est calculé sur la surface de l'ailette, prenant en considération l'effet du débit et de la température des fumées, ce qui aboutit à simuler la formation du front de givre dans des conditions les plus réalistes possible. Les deux tubes sont considérés comme des surfaces à température constante, égale à la température du fluide frigorigène circulant à l'intérieur de ces tubes.

4.3 Résultats des simulations et comparaison avec les résultats expérimentaux

La simulation est effectuée avec un pas de temps de 0,1 s pour un cycle de givrage de 100 s. Cette simulation est réalisée uniquement pour prédire la formation de givre pendant la première période de givrage en vue de prédire l'homogénéité de la couche de givre tout au long de l'ailette. Le comportement du dépôt de givre, son épaisseur, le taux de transfert de masse, la masse volumique locale moyenne sont calculés.

4.3.1 Le comportement du dépôt de CO_2 solide

La présence de la phase solide dans une maille du domaine est quantifiée à l'aide de la fraction volumique de la phase secondaire. Par conséquent, le processus de givrage est suivi par l'évolution de la fraction volumique de CO_2 solide dans le domaine. La figure 4.7 présente l'évolution de la couche de givre sur l'échangeur de chaleur tubes-ailettes à deux rangs.

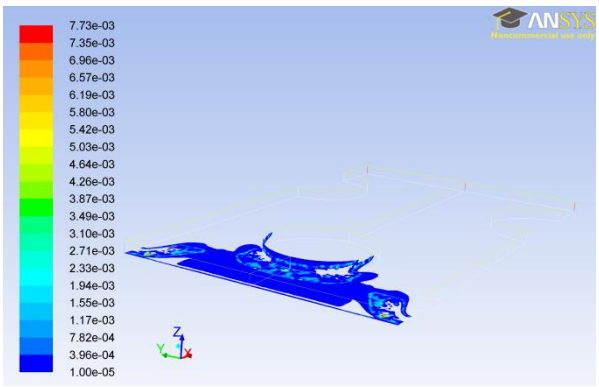

a) t = 1 s

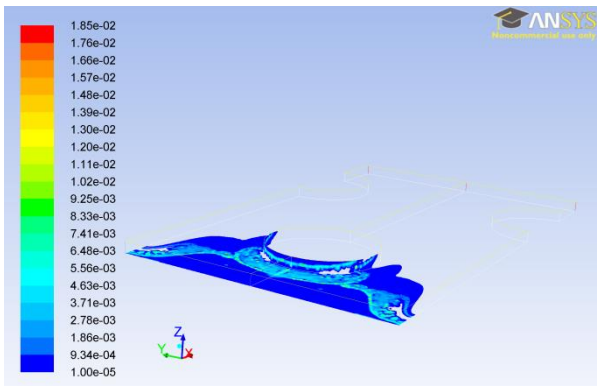

b) t = 10 s

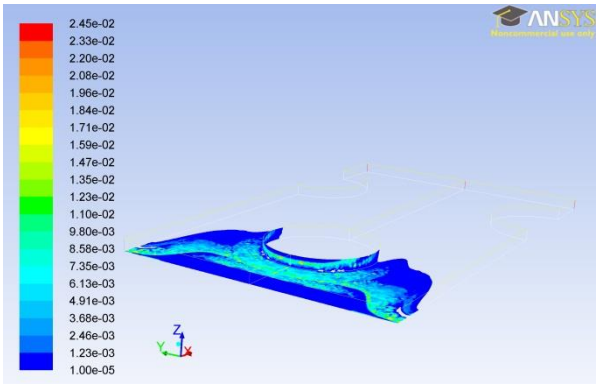

c) t = 20 s

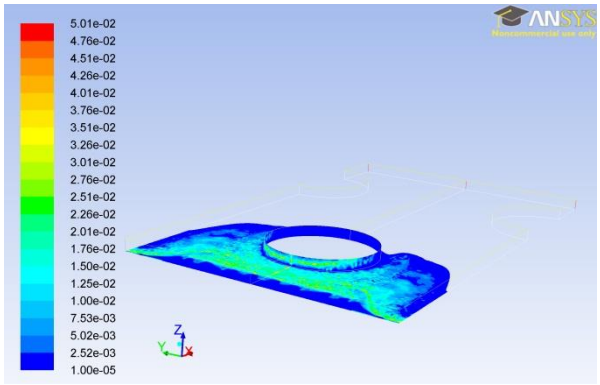

d) t = 40 s

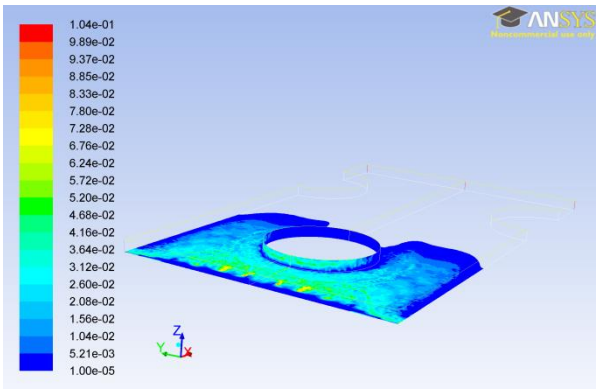

e) t = 80 s

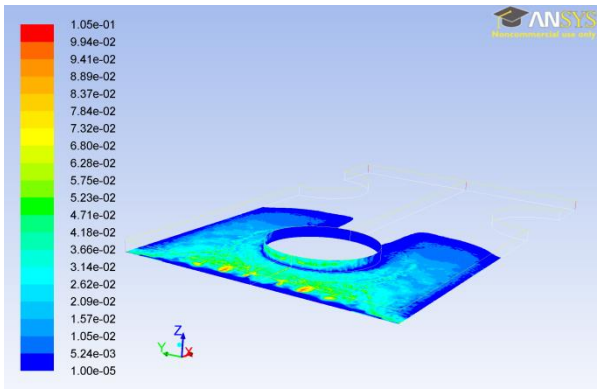

f) t = 100 s

Figure 4.7 : Evolution de la couche de givre sur la surface de l'échangeur de chaleur tubes-ailettes à deux rangs

L'évolution de la formation du givre est observable. Le givre commence à se former à l'entrée du domaine, puis il s'étend dans le sens de l'écoulement. Etant donné que le CO_2 est givré à partir de l'entrée de l'échangeur de chaleur, sa concentration dans les fumées diminue, ce qui retarde la formation du givre à la partie aval de l'ailette pour ces conditions de simulation.

En augmentant la vitesse des fumées, $\bar{u}_{fg,in} = 0.41\ m.s^{-1}$, le front du givre sera mieux réparti sur la totalité de l'ailette comme représenté figure 4.8.

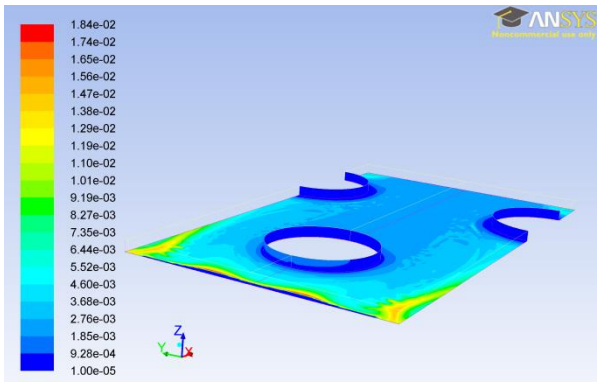

Figure 4.8 : Profil du dépôt de givre pour $\bar{u}_{fg,in} = 0.41\ m.s^{-1}$, t = 10 s

4.3.2 Evolution de l'épaisseur moyenne du dépôt de givre

La méthode de calcul de l'épaisseur locale du givre de CO_2 est illustrée figure 4.9. L'épaisseur moyenne $\bar{\delta}_{fr}$ du givre sur toute la surface de l'ailette simulée est calculée par l'équation (4.23) :

$$\bar{\delta}_{fr} = \frac{\sum \delta_{fr} \,.\, A_i}{\sum A_i} \tag{4.23}$$

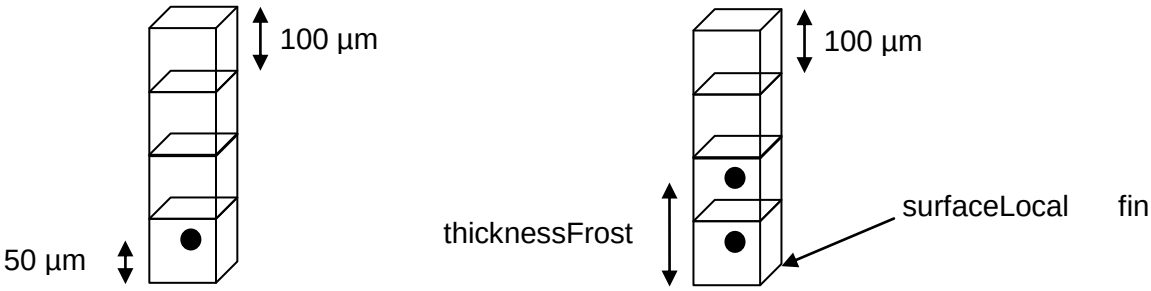

a) Premier dépôt de givre de CO_2 b) Croissance du givre de CO_2

Figure 4.9 : Méthode de calcul de l'épaisseur locale du givre

Dans la Figure 4.10 sont tracées les variations de l'épaisseur moyenne du givre, obtenues par l'étude expérimentale et par le modèle de prédiction de givrage de CO_2 montrant un bon accord entre les deux résultats. La différence d'épaisseur observable au début du cycle de givrage est due à la méthode utilisée pour calculer l'épaisseur du givre qui débute à 50 µm lors du traitement des résultats de la simulation.

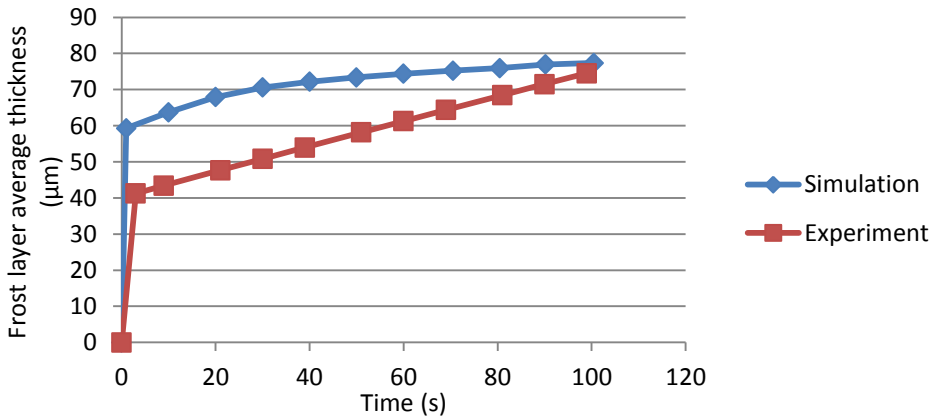

Figure 4.10 : Evolution de l'épaisseur moyenne du givre obtenue par modélisation et par expérimentation

4.3.3 L'évolution du transfert de masse

Le taux de nucléation de CO_2 dans l'ensemble du domaine de calcul est calculé à chaque pas de temps en additionnant les termes sources de masse de toutes les mailles (équation 4.17).

Les variations du taux de nucléation de CO_2 prédites par le modèle CFD et mesurées lors de l'essai sont présentées figure 4.11. Ces résultats montrent un bon accord entre le taux de nucléation prévu et mesuré. Comme la nucléation est supposée être homogène, le modèle CFD sous-estime légèrement le transfert de masse par rapport aux résultats obtenus par l'étude expérimentale.

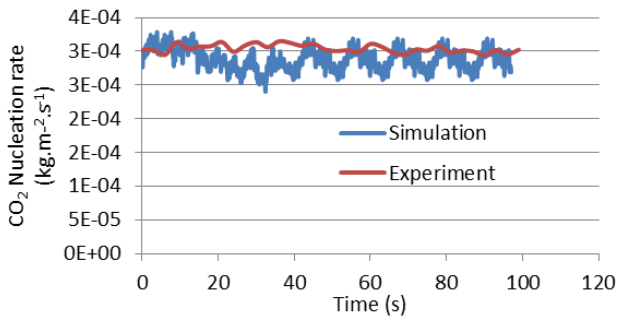

Figure 4.11 : Evolution du taux de nucléation de CO_2 prédit par le modèle CFD comparé aux résultats expérimentaux

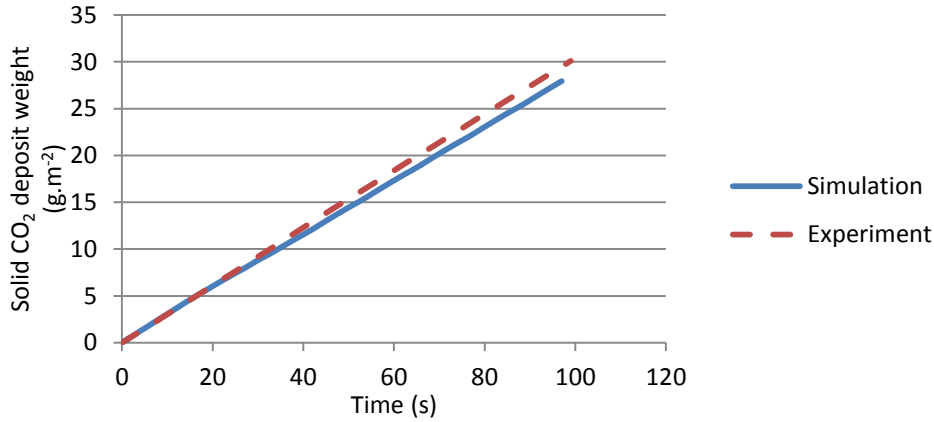

Figure 4.12 : Evolution de la masse totale de CO_2 givré

4.3.4 Evolution de la masse volumique moyenne du dépôt de givre

La masse volumique moyenne du givre est calculée dans le domaine de simulation en fonction des fractions volumiques des phases primaire et secondaire et de leurs masses volumiques. Après le premier dépôt de givre, la masse volumique de la couche de givre augmente et atteint 300 $kg.m^{-3}$ à l'entrée du domaine.

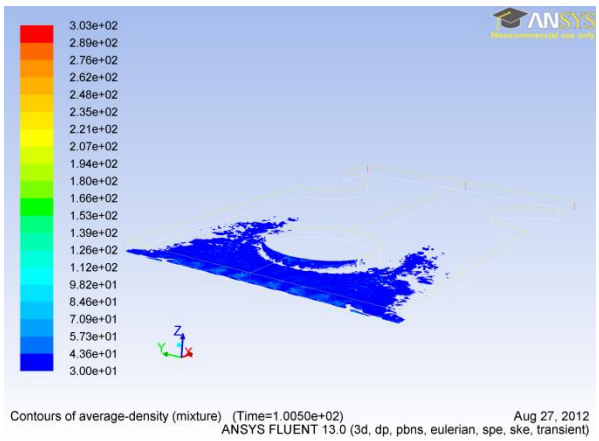

Figure 4.13 : Masse volumique locale moyenne, t = 100 s

La figure 4.14 présente l'évolution de la masse volumique moyenne du dépôt global. Le processus de densification de la couche de givre est observable montrant la formation de givre par la diffusion volumique de CO_2 dans la couche de givre.

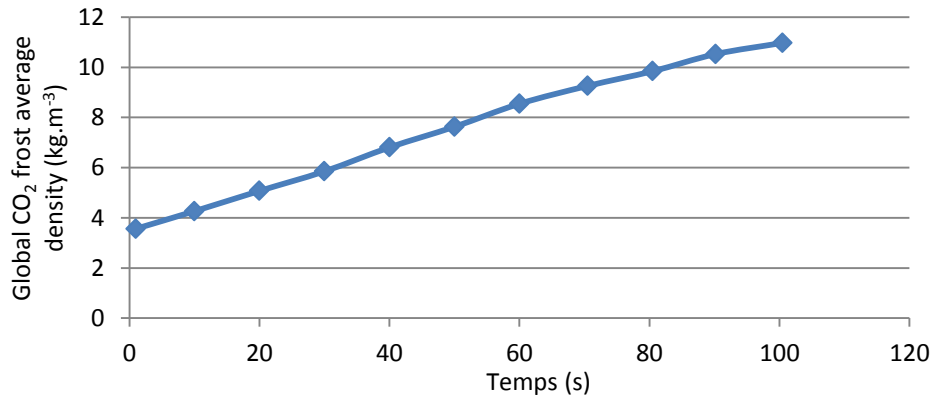

Figure 4.14 : Evolution de la masse volumique moyenne de la globalité du dépôt de givre

4.4 Conclusions

Dans ce chapitre, un modèle CFD diphasique est développé afin de prédire la formation de givre de CO_2 et sa croissance sur un échangeur de chaleur tubes-ailettes. En considérant les fumées comme la phase primaire et le dépôt de CO_2 solide formé comme la phase secondaire, les transferts de masse, de quantité de mouvement et d'énergie entre ces phases sont calculés en ajoutant des termes sources à l'ensemble des équations de conservation. Le transfert de masse est calculé en se basant sur la théorie classique de la nucléation. Le modèle est validé par comparaison de l'épaisseur moyenne du givre et de sa masse avec les valeurs expérimentales mesurées pour les mêmes conditions de givrage.

L'influence de la vitesse des fumées sur le comportement de la couche de givre de CO_2 est identifiée. Pour une vitesse plus élevée, le dépôt solide se forme plus rapidement sur toute la surface de l'ailette. L'influence de la température du tube, de la température d'entrée des fumées et de la concentration à l'entrée de CO_2 peut être analysée à l'aide de ce modèle. En outre, l'effet de la structure de l'échangeur de chaleur sur la formation de givre peut être identifié.

Par conséquent, ce modèle peut être utilisé pour la conception et l'optimisation de l'échangeur de chaleur de givrage de CO_2. De nombreuses configurations d'échangeurs de chaleur tubes-ailettes peuvent être comparées par une analyse d'efficacité thermique sous certaines conditions de givrage. De plus, l'effet de la température du fluide frigorigène peut être analysé dans le but d'optimiser le glissement de température entre le mélange de fluides frigorigènes et les fumées.

Conclusions et Perspectives

Dans cette étude le procédé de captage de CO_2 en post-combustion par antisublimation est présenté. L'analyse exergétique des échangeurs de chaleur lors du givrage et du dégivrage du CO_2 permet d'améliorer les performances énergétiques globales du procédé. Cette analyse exergétique de l'échangeur de chaleur montre l'importance de l'optimisation de l'architecture de l'échangeur de chaleur et du glissement de la température du mélange des fluides frigorigènes. En outre, l'effet de l'optimisation exergétique des CFX sur l'ensemble du procédé de captage de CO_2 est démontré en étudiant l'effet de la diminution de la température d'évaporation des fluides frigorigènes dans les CFX sur les performances énergétiques de la cascade intégrée. L'optimisation de l'architecture de l'échangeur de chaleur et du mélange de fluides frigorigènes vise à maintenir un glissement de température approprié pour obtenir un dépôt homogène de CO_2 sur la surface des ailettes de l'échangeur. Le travail théorique minimum requis pour la séparation du CO_2 des fumées est élaboré pour sa séparation parfaite et imparfaite. Ce travail minimum est utilisé pour calculer l'efficacité globale du procédé de captage de CO_2. Les manques de données existantes dans la littérature concernant les propriétés thermo-physiques du CO_2 solide au-dessous du point triple sont comblés par une synthèse et une mise en forme de la littérature scientifique spécialisée. L'enthalpie, l'entropie, la masse volumique et la conductivité thermique du CO_2 solide sont exprimées par des équations empiriques développées à l'aide de plusieurs données recueillies dans la littérature. Le diagramme T-s du CO_2 est tracé jusqu'à une température de 140 K inférieure à la température du point triple. Le procédé de captage du CO_2 par antisublimation est représenté à l'aide du diagramme psychrométrique du mélange CO_2 - N_2. L'évolution des propriétés thermodynamiques des fumées à travers le processus de séparation est tracée sur ce diagramme.

Le phénomène d'anti-sublimation se produit selon les lois de la nucléation. La théorie classique de la nucléation est utilisée afin de quantifier le taux de transfert de masse entre les fumées et le dépôt de CO_2 solide. Les théories des nucléations homogène et hétérogène, primaire et secondaire, sont exposées selon deux approches thermodynamique et cinétique. Ces théories permettent de calculer la vitesse de nucléation, le rayon critique des nucléides formés et le taux de transfert de masse entre les deux phases. L'effet de l'affinité entre les cristaux de CO_2 et la surface solide est étudié. Dans le cas de la nucléation hétérogène, une bonne affinité entre le CO_2 solide et les surfaces froides de l'échangeur conduit à améliorer le procédé de nucléation, en augmentant le taux de nucléation, et en diminuant la variation de l'énergie libre nécessaire pour former de nouveaux embryons. De plus, dans le cas de la nucléation hétérogène, l'affinité entre les cristaux de CO_2 et la surface froide permet de réduire le taux de sursaturation capable de givrer le CO_2. Les principaux paramètres qui influent sur le processus de nucléation sont identifiés. Une analyse de sensibilité est réalisée afin d'évaluer l'effet de la concentration de CO_2 et la variation de la température des fumées sur les conditions de givrage de CO_2. La variation de la vitesse de nucléation et du rayon critique des cristaux en fonction de la concentration de CO_2 et de la variation de température sont analysés. Une grande variation du coefficient de transfert de masse et de la morphologie des dépôts est induite soit par une perturbation du taux de sursaturation, soit de la température des fumées. Le taux de sursaturation est un paramètre clé qui doit être contrôlé afin de contrôler le transfert de masse à partir de la phase vapeur vers la nouvelle phase solide. L'effet d'autres paramètres comme la vitesse du gaz, la diffusion moléculaire, la porosité du dépôt de givre, sa masse volumique et sa conductivité thermique sont exposés et discutés.

En se basant sur l'étude expérimentale, la visualisation de CO_2 à grand grossissement prouve que l'anti-sublimation se déroule selon la théorie classique de la nucléation. Une bonne affinité est constatée entre les cristaux de CO_2 solide et les ailettes en aluminium de l'échangeur de chaleur. Cette affinité, conséquence du faible angle de contact entre les deux solides, prouve que les ailettes en aluminium sont appropriées pour le procédé de captage

de CO_2 en améliorant le phénomène de nucléation. Pour des concentrations de CO_2 élevées (15 % v/v) et faibles (3 % v/v), les embryons sphériques hétérogènes sont formés montrant l'indépendance du phénomène de nucléation de la concentration du soluté, le CO_2, dans les fumées. Au contraire, la visualisation du dépôt de givre à de faibles taux de grossissement montre une différence d'aspect entre les couches solides formées à de hautes et de basses concentrations de CO_2. À des concentrations élevées, le dépôt présente un aspect granuleux alors qu'on observe une morphologie d'un réseau de cristaux multidirectionnel à de faibles concentrations. Par conséquent, le dépôt formé à faibles concentrations en soluté est relativement poreux par rapport au dépôt formé à des concentrations plus élevées.

Trois périodes de la formation du givre et de sa croissance sont identifiées. Le premier dépôt s'effectue via une nucléation hétérogène primaire et est directement affectée par le taux de sursaturation. Pour un taux de sursaturation plus élevé, un plus grand nombre d'embryons solides se forme améliorant le transfert de masse au cours de la deuxième période de givrage. La deuxième période de formation de givre se produit à une épaisseur du dépôt constante durant laquelle le transfert de masse se déroule par diffusion du CO_2 dans la couche solide poreuse. Au cours de cette période, la masse volumique moyenne du dépôt augmente, augmentant ainsi sa conductivité thermique. Cette densification conduit à la diminution de la température de surface du givre permettant le début de la troisième période de formation de givre qui se déroule à masse volumique constante. Des mesures quantitatives montrent que le taux de nucléation dépend principalement du taux de sursaturation. Pour de faibles taux de sursaturation, la masse volumique moyenne du givre qui se dépose sur les ailettes de l'échangeur est élevée. Au début du cycle de givrage, le sous-refroidissement des surfaces des ailettes conduit à améliorer la nucléation hétérogène, donc la formation d'un dépôt plus homogène et plus dense.

Afin de prédire la formation du givre de CO_2 et sa croissance sur les ailettes d'un échangeur de chaleur tubes-ailettes à deux rangs, un modèle CFD multiphasique est développé. Ce modèle est validé en comparant l'épaisseur moyenne prédite du dépôt de CO_2 ainsi que sa masse avec les résultats expérimentaux. En considérant les fumées comme une phase primaire et les cristaux de CO_2 solides comme une phase de précipitation secondaire, l'interaction entre elles est simulée par l'ajout au modèle CFD des termes sources de transfert de masse, de quantité de mouvement et d'énergie. Le coefficient de transfert de masse est calculé en utilisant la théorie classique de la nucléation. L'originalité de ce modèle réside dans sa capacité à prédire la formation de la couche de givre de CO_2 en fonction de la structure des surfaces de l'échangeur tubes-ailettes. L'influence de la vitesse des fumées sur le comportement de la couche de givre de CO_2 à l'entrée de l'échangeur est qualitativement identifiée. Pour obtenir une vitesse plus élevée, le dépôt solide se forme plus rapidement tout au long de la surface d'ailette. Les effets de la température du fluide frigorigène, de la température à l'entrée des fumées et de la concentration de CO_2 peuvent être analysés à l'aide de ce modèle.

Ce modèle peut être utilisé pour la conception et l'optimisation des échangeurs de givrage de CO_2 du procédé de captage de CO_2 par antisublimation. De nombreuses configurations d'échangeurs de chaleur tubes-ailettes peuvent être comparées en utilisant ce modèle, en analysant l'efficacité thermique des ailettes dans des conditions de givrage. De nombreuses configurations d'échangeurs de chaleur peuvent être comparées afin d'identifier l'effet de l'architecture de l'échangeur et du pas d'ailettes sur l'efficacité du transfert de masse et sur l'homogénéité du dépôt solide. La configuration optimale de l'échangeur de chaleur dépend de la vitesse des fumées, de leur température et de la concentration en CO_2 à l'entrée des CFX. En outre, l'effet de la température du fluide frigorigène doit être analysé par la simulation du givrage de CO_2 pour des conditions de fumées définies. Le glissement de température optimal des mélanges de fluides frigorigènes est optimisé pour givrer le CO_2 sur la base d'une analyse exergo-énergétique.

Une étude expérimentale couplant l'évaporation d'un mélange de fluides frigorigènes à l'intérieur des tubes de l'échangeur de chaleur et le refroidissement des fumées avec précipitation du CO_2 sur la surface des ailettes est nécessaire pour comprendre les conditions réelles de fonctionnement des CFX. Après le calcul du glissement de température

fatal sur les fumées, défini par les compostions entrée / sortie en CO_2 des fumées, des mélanges de fluides frigorigènes sont étudiés afin d'assurer une efficacité optimale des échangeurs et améliorer les performances énergétiques du procédé. Les pertes de pression subies par les mélanges de fluides frigorigènes sont importantes à étudier vu qu'elles affectent directement la température d'évaporation. Il est important de noter que la différence de températures entre l'entrée et la sortie de l'échangeur de chaleur peut atteindre 20 K, d'où l'importance de l'optimisation du glissement de température du côté du mélange de fluides frigorigènes. L'effet de la formation du givre de CO_2 sur le transfert de chaleur global entre les fumées et le fluide frigorigène doit être identifié. La variation de la puissance frigorifique au cours d'un cycle de givrage de CO_2 affecte les conditions de fonctionnement de la cascade intégrée affectant en retour le rendement global du procédé. En outre, afin d'améliorer l'efficacité énergétique du procédé, le cycle de givrage de CO_2 doit être contrôlé en déterminant la durée optimale du cycle de givrage, en prenant en compte la dégradation du taux de séparation de CO_2 lors de l'épaississement de la couche de givre, le transfert de chaleur total à travers l'échangeur de chaleur, et l'augmentation des pertes de pression sur les fumées provoquées par la croissance du givre.

Enfin l'aspect économique doit être pris en compte lors de la conception de l'échangeur de chaleur de givrage de CO_2. A cet effet, une étude exergo-économique doit être effectuée. L'utilisation de l'optimisation exergétique n'est pas suffisante. En fait, l'augmentation de la température moyenne d'évaporation du mélange de fluides frigorigènes assurant un fonctionnement à faible taux de sursaturation conduit à diminuer le taux de nucléation de CO_2 ($kg.m^{-2}.s^{-1}$) sur la surface de l'échangeur. D'où la nécessité d'augmenter les surfaces de givrage pour assurer la séparation du CO_2 à un débit de fumées constant. Un taux de nucléation optimal doit être défini en tenant compte de la performance exergétique du procédé et aussi de sa compétitivité économique avec d'autres procédés de captage de CO_2.

General Introduction

Carbon dioxide is the main greenhouse gas globally emitted and it accounted for 76.7% of anthropogenic greenhouse-gas emissions in 2004. Power generation constitutes 78.8% of CO_2 emissions from fossil fuels and minerals. Considering the amount of CO_2 emissions in the world and its climate impacts, their reduction is an urgent necessity. The rapid growth of population and the explosive increase in energy demand makes it difficult to reduce energy consumption. The carbon dioxide capture and storage, intended for use on large amount of CO_2 stationary sources, is the solution to reduce emissions. CO_2 capture processes are regrouped in three main categories: post-combustion, oxycombustion, and pre-combustion processes.

A new method of post-combustion CO_2 capture known as "Antisublimation" is developed. Based on the fact that the saturation temperature, in dehydrated flue gases, is the highest for CO_2, is the first component to solidify by cooling flue gases down to -120°C. For this purpose, a fin-and-tube heat exchanger is used to cool down flue gases and the CO_2 is separated by antisublimation, passing directly from vapor to solid phase forming a deposit on the heat-exchanger fins. The CO_2 concentration decreases through the heat exchanger (named CFX) since it antisublimates on the chilled surfaces and so, progressively, lower temperatures are required to ensure 90% of CO_2 capture. In order to improve the process performance, the heat-exchanger efficiency has to be optimized so as to reduce the temperature difference between the refrigerants and the flue gases and to ensure a gliding temperature (20 K) able to form homogeneous CO_2 deposit.

In Chapter 1, the optimization importance of the heat-exchanger arrangement and of the refrigerant blend gliding temperature is represented. The effect of the CFX gliding temperature optimization on the whole capture process is demonstrated. The concept of minimum theoretical work of gas separating is analyzed to calculate the CO_2 capture-process efficiency. Since the CO_2 properties under the triple point are not defined, a literature study is performed to collect the available measured properties. New equations are proposed to calculate CO_2 enthalpy, entropy, and density for solid-vapor equilibrium. To represent the CO_2 capture by antisublimation process, a psychrometric chart is developed considering a binary gas mixture composed of nitrogen and carbon dioxide. The psychrometric chart is plotted for flue gases at atmospheric pressure representing the flue-gas gliding temperature for coal-fired power plants.

In order to optimize the frosting heat exchanger, the CO_2 antisublimation phenomenon has to be understood. In Chapter 2, a literature survey is conducted to identify the parameters that affect CO_2 anti-sublimation on the chilled surfaces. In addition, the CO_2 frost formation on the fin-and-tube heat-exchanger external side affects the heat and mass transfer, then the separation process. The control of the frosting conditions is a key to ensure better heat-exchanger performances minimizing the temperature difference between refrigerants and flue gases and to improve the homogeneity of the solid deposit. Few data are available on the CO_2 frosting process and no correlations, predicting mass transfer and thermo-physical properties, have been already proposed. Hence, the classical nucleation theory is adopted. The kinetic and thermodynamic classical nucleation theories are elaborated in order to understand the antisublimation phenomena, to identify parameters that affect the nucleation rate and frost morphology, and to mathematically model the CO_2 antisublimation in the context of our study. A nucleation sensitivity analysis is performed to evaluate the nucleation rate and morphology variation as a function of anti-sublimation conditions.

Few experimental investigations have been conducted to study the CO_2 frosting and they are performed under different thermal and flow conditions. An experimental study of the CO_2 antisublimation on a fin-and-tube heat exchanger is of high interest to understand the precipitation phenomenon on the heat-exchanger fins as a function of the flow and the surface parameters. Qualitative and quantitative experimental investigations are performed

in Chapter 3 in order to study the solid CO_2 deposition. The deposit morphology, its formation, and its accumulation are studied by visual observations and quantitative measurements. A high magnification (200x optical zoom) observation of the CO_2 precipitation allows the understanding of the crystallization theory studied in Chapter 2 and to verify the effect of many parameters, like CO_2 concentration and super-saturation ratio. The time evolution monitoring of the CO_2 frost thickness and of the nucleation rate allowed the calculation of the average density and porosity for different CO_2 concentrations and fin-surface temperatures. The effect of CO_2 frost growth on the performance of the CFX, more especially on the overall heat-transfer coefficient between the refrigerant blend and flue gases, are studied.

In addition to the experimental results, a CFD multiphase and multi-component transient model able to predict the frost formation and growth, showing the influence of the heat-exchanger structure on the frosting process, and allowing the prediction of the optimal heat-exchanger configuration is proposed in Chapter 4. In addition to the frost formation and growth predicting, the thermo-physical properties of the solid layer and the cooling capacity required for CO_2 separation are calculated. The classical nucleation theory is used to calculate the mass transfer between the flue-gas and the solid phase, and also to predict the frost structure that depends on the fin and flue-gas temperature distribution. This model identifies also the effect of the refrigerant temperature on the CO_2 frost behavior and on the efficiency of the studied heat-exchanger configuration. The simulation results are validated by comparison with the experimental results obtained in Chapter 3. This frosting model is able to be used for CO_2 frosting heat-exchanger (CFX) optimization based on the design of a configuration able to frost the flue-gas CO_2 in a homogeneous solid layer and to minimize the temperature difference between the gas flow and the refrigerant blend.

Chapter 1. Background and issues for antisublimation CO_2 capture

1.1 Introduction

Carbon dioxide is the main greenhouse gas globally emitted and it accounted for 76.7% of anthropogenic greenhouse-gas emissions in 2004 [IPCC05]. Energy production constitutes 78.8% of CO_2 emissions from fossil fuels and minerals. Coal-fired power plants constitute 56.7% of these emissions. Plants using natural gas are in the second place as a source of CO_2 with a percentage of 5.7% of total emissions.

Considering the amount of CO_2 emissions in the world and its climate impacts, their reduction is an urgent necessity. The rapid growth of population and the explosive increase in energy consumption makes it difficult to reduce energy consumption. Then the carbon dioxide capture and storage (CCS) is the solution that can reduce CO_2 emissions immediately. Several methods of CO_2 capture are being developed. All these methods are intended for use on large amount of CO_2 stationary sources. Power plants using fossil fuels, refineries, and other industrial fields such as natural gas sweetening, steel industry, cement production, and petrochemical industry are the main domains for the implementation of CO_2 capture. CO_2 capture processes are regrouped in three main categories: post-combustion, oxycombustion and pre-combustion.

The Center for Energy and Processes (CEP) of MINES ParisTech has developed a method of post-combustion CO_2 capture known as "Antisublimation" [CLO01]. Based on the fact that the saturation temperature, in dehydrated flue gases, is the highest for CO_2 that is approximately -99°C for coal-fired-boiler flue gases, CO_2 will be the first component to solidify by cooling down flue gases. For this purpose, a fin-and-tube heat exchanger is used. CO_2 passes directly from vapor to solid phase forming a solid deposit on the heat-exchanger (CFX) fins by cooling down flue gases from -99 to -118°C.

In order to improve the process performance, heat exchanger efficiency optimization will be used. The effect of the CFX optimization on the whole capture process is demonstrated. Theoretical energy consumption of the CO_2 frosting for coal-fired-boiler flue gases is calculated showing the flue-gas temperature gliding curve during antisublimation CO_2 capture.

Total CO_2 capture-process efficiency is calculated by comparing the total work consumed by the process to the minimum theoretical work consumed by separating an amount of CO_2 from the gas stream mixture. The minimum work consumed per unit mole of separated CO_2 will be calculated in order to calculate the total efficiency of a CO_2 capture process.

In order to study the antisublimation CO_2 process, the solid-gas equilibrium has to be known for all CO_2 concentrations in nitrogen, which are the main component in flue gases. CO_2 properties are determined for conditions above the triple point. Few studies have been carried out to determine the CO_2 properties in its solid-vapor equilibrium state. An experimental study to measure CO_2 properties at low temperatures is a complex task. CO_2, unlike most fluids, presents high vapor pressure in its solid state. To represent the CO_2 capture by antisublimation process, a psychrometric chart has been developed. In addition to carbon dioxide and nitrogen, flue gases contain oxygen, argon and other gases at the inlet of the capture unit. The psychrometric chart is plotted for a binary gas mixture composed of only nitrogen and carbon dioxide in order to simplify the calculations. This approximation leads to an error lower than 1% in calculating enthalpy, entropy, density, and partial pressure of the mixture. Methods for calculating isenthalpic and constant specific volume curves are exposed. The NIST reference fluid thermodynamic and transport properties database, Refprop V9.0, is used. The psychrometric chart is plotted for flue gases at atmospheric pressure (101.325 kPa), which is the case of the majority of CO_2 emission sources.

1.2 CO_2 emissions

The Kyoto Protocol has set the six main greenhouse gases (GHGs) contributing to global warming. The six gases or family of gases of concern are: carbon dioxide (CO_2), methane (CH_4), nitrous oxide (N_2O), hydrofluorocarbons (HFCs), perfluorocarbons (PFCs), and sulfur hexafluoride (SF_6). CO_2 is the main greenhouse gas emitted in the world. In 2004, it accounted for 76.7% of the greenhouse gases emitted by human activities (Figure 1.1).

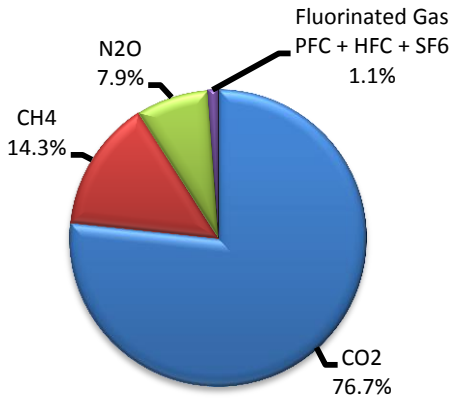

Figure 1.1: Global emissions of the six principal greenhouse gases in 2004 [IPCC05].

Table 1.1 summarizes CO_2 emissions in the world coming from sources that emit more than 0.1 Mt per year. These emissions are divided according to their sources into two main categories, which themselves are divided into sub-categories. The first category is based on emissions from the consumption of fossil fuels and minerals, and the second on emissions from biomass. The first main category includes: power generation, gas purification, cement production, refineries, steel industry, petrochemical industry, and other sources. The second category is divided into two sub-categories: bioenergy and fermentation.

Energy production constitutes 78.8% of CO_2 emissions from fossil fuels and minerals in the world. Coal-fired power plants constitute 56.7% of these emissions. Plants using natural gas are in the second place as a source of CO_2 with a percentage of 5.7% of total emissions.

In 1992, the United Nations Framework Convention on Climate Change (UNFCCC) was adopted in Rio de Janeiro by 154 states plus the European Community. The main objective of this convention is to stabilize concentrations of greenhouse gases in the atmosphere at a level that would prevent interference with the climate system.

Signed on 11 of December in 1997, the Kyoto Protocol is intended to implement the UNFCCC. The objective of this Protocol is to reduce, by at least 5% over the period 2008 to 2012, emissions from 39 countries in Annex B compared with 1990. This target is shared between the countries in Annex B according to their economic situations and their potential for development called "burden sharing". Other protocols and national conferences were held to reduce emissions of CO_2 and other GHGs and to fulfill their commitments by the Kyoto Protocol.

Table 1.1: Profile of worldwide large CO_2 stationary sources emitting more than 0.1 $MtCO_2$ per year [IPCC05].

Process	**CO_2 concentration in flue gases % by vol.**	**Number of sources**	**Emissions ($MtCO_2$)**	**% of total CO_2 emissions**	**Cumulative total CO_2 emissions (%)**	**Average emissions/source ($MtCO_2$ per source)**
CO_2 from fossil fuels or minerals						
Power						
Coal	12 to 15	2,025	7,984	59.69	59.69	3.94
Natural gas	3	985	759	5.68	65.37	0.77
Natural gas	7 to 10	743	752	5.62	70.99	1.01
Fuel oil	8	515	654	4.89	75.88	1.27
Fuel oil	3	593	326	2.43	78.31	0.55
Other fuels[a]	NA	79	61	0.45	78.77	0.77
Hydrogen	NA	2	3	0.02	78.79	1.27
Natural-gas sweetening						
	NA[b]	NA	50[e]	0.37	79.16	
Cement production						
Combined	20	1175	932	6.97	86.13	0.79
Refineries						
	3 to 13	638	798	5.97	92.09	1.25
Iron and steel industry						
Integrated steel mills	15	180	630[d]	4.71	96.81	3.50
Other processes[d]	NA	89	16	0.12	96.92	0.17
Petrochemical industry						
Ethylene	12	240	258	1.93	98.85	1.08
Ammonia: process	100	194	113	0.84	99.70	0.58
Ammonia: fuel combustion	8	19	5	0.04	99.73	0.26
Ethylene oxide	100	17	3	0.02	99.75	0.15
Other sources						
Non-specified	NA	90	33	0.25	100.00	0.37
		7,584	**13,375**	**100**		**1.76**
CO_2 from biomass[e]						
Bioenergy	3 to 8	213	73			0.34
Fermentation	100	90	17.6			0.2

[a] Other gas, other oil, digester gas, landfill gas.

[b] A relatively small fraction of these sources has high concentration of CO_2. In Canada, only two plants out of a total of 24 have high CO_2 concentrations.

[c] Based on an estimate that about half of the annual worldwide natural-gas production contains CO_2 at concentrations of about 4% mol and that this CO_2 content is normally reduced from 4% to 2% mol.

[d] This amount corresponds to the emissions of those sources that have been individually identified in the reference database. The worldwide CO_2 emissions, estimated by a top-down approach, are larger than this amount and exceed 1 Gt (Gielen and Moriguchi, 2003).

[e] For North America and Brazil only. All numbers are for 2003, except for power generation from biomass and waste in North America, which is for 2000.

1.3 CO_2 capture processes

Considering the amount of CO_2 emissions in the world and its climate impacts, their reduction is an urgent necessity. To reduce these emissions several strategies exist. The reduction of energy consumption can reduce anthropogenic emissions. The rapid growth of population during the 20th century and the explosive increase in energy consumption make it difficult to reduce energy consumption. The International Energy Agency (IEA) provides a 57% increase in energy consumption between 2004 and 2030. Renewable energies play an important role in reducing CO_2 emissions by limiting the consumption of fossil fuels. Another way to reduce emissions and the CO_2 concentration in the atmosphere is to enhance natural sinks of CO_2 such as reforestation that will reduce emissions of 3.7 Gt CO_2 by 2050 [IFP10]. All previous strategies do not constitute rapid solutions and cannot be effective because of the world population growth, the increase in energy consumption, and the large demands in fossil fuels. The last strategy involves capturing CO_2 from its emission sources. The carbon dioxide capture and storage (CCS) is a solution that can reduce emissions immediately. The purpose of CO_2 capture is to produce concentrated amounts of CO_2 that can be transported and stored.

Several methods of CO_2 capture are being developed. All these methods are intended for use on large amount of CO_2 stationary sources. Power plants using fossil fuels, refineries, and other industrial fields such as natural gas sweetening, steel industry, cement production, and petrochemical industry are main domains for the implementation of CO_2 capture. For power plants, CO_2 capture methods can reduce current CO_2 emissions by 80 to 90% per kWh [IPCC05].

CO_2 capture systems reduce the efficiency of power plants and other industrial processes. These systems use part of the energy produced by power plants, and consequently cause the increase in the quantities of fuels used in the process. Then power plants including the CO_2 capture systems have lower efficiency than power plants without CO_2 capture. The new power plant efficiency is calculated by the Equation (1.1):

$$\eta = \frac{P_{elec.} - W_{capture}}{E_{fuel}} \tag{1.1}$$

Where $P_{elec.}$ is the electrical power produced by the power plant without CO_2 capture, $W_{capture}$ is the electrical power consumed by the capture process, and E_{fuel} is the heating value of the fuel used. So, to keep the same electrical power produced by a CO_2-reduced-emission power plant, it is essential to increase the plant productivity. For these reasons, it is always necessary to define the amount of CO_2 avoided and not the amount of CO_2 captured to show the effectiveness of a CO_2 capture process. Figure 1.2 explains the concept of CO_2 captured and CO_2 avoided.

This concept shows the need to increase the efficiency of power plants in addition to reduce energy consumption of CO_2 capture systems. These priority objectives will be to reduce the negative environmental impacts and costs of the production of clean electricity.

CO_2 capture processes are organized in three main categories:

- Post-combustion CO_2 capture,
- Oxycombustion CO_2 capture,
- Pre-combustion CO_2 capture.

CO_2 capture by post-combustion consists in separating CO_2 from flue gases resulting from combustion of fossil fuels. The oxycombustion process separates oxygen from air, then to use it as an oxidizing gas for fossil fuels instead of air. So flue gases contain mainly CO_2 and water vapor and are more easily separated. The pre-combustion is the conversion of fossil fuel into CO_2 and H_2. Then H_2 is burned in power plants and flue gases contain only water vapor. Industrial processes for CO_2 capture use one or more of the above methods.

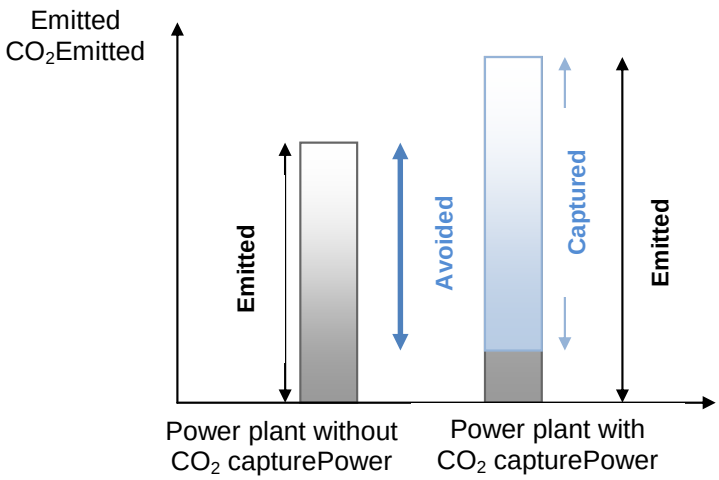

Figure 1.2: CO_2 captured and CO_2 avoided.

1.3.1 Post-combustion CO_2 capture

The post-combustion CO_2 capture consists in separating CO_2 from flue gases produced from burning fossil fuels or biomass with air (Figure 1.3). Before being released to the atmosphere, flue gases enter the separation process that separates most of the CO_2 from other gases. Captured CO_2 is then stored.

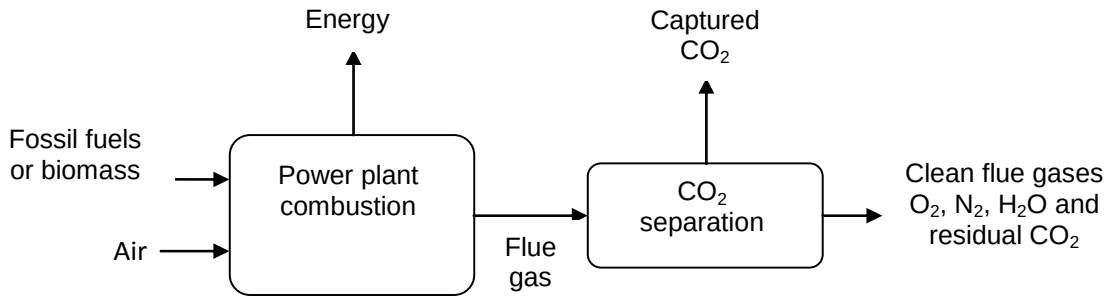

Figure 1.3: Post-combustion CO_2 capture.

The advantage of such processes is the possibility of installing them on existing plants. Available space nearby conventional power plants can be an issue; the CO_2 capture plant needs a surface area as large as the power plant itself. Post-combustion CO_2 capture processes have to integrate flue gas cleaning before capture.

The CO_2 concentration in flue gases is the second constraint. Table 1.2 shows that in coal power plants this concentration does not exceed 14% vol. and for other industrial sources it is limited to 33% vol. Obviously, the higher the CO_2 concentration in flue gases, the easier its separation from other gases, which penalizes severely the post-combustion CO_2 capture processes.

Table 1.2: Properties of candidate flue gases that can be inputted to a capture process [IPCC05].

Source	**CO_2 concentration % vol (dry)**	**Pressure of flue gases MPa[a]**	**CO_2 partial pressure MPa**
CO_2 from fuel combustion			
• Power station flue gas: Natural gas fired boilers	7-10	0.1	0.007-0.010
Gas turbines	3-4	0.1	0.003-0.004
Oil fired boilers	11-13	0.1	0.011-0.013
Coal fired boilers	12-14	0.1	0.012-0.014
IGCC[b]: after combustion	12-14	0.1	0.012-0.014
• Oil refinery and petrochemical plant fired heaters	8	0.1	0.008
CO_2 from chemical transformations + fuel combustion			
• Blast furnace gas: Before combustion	20		
After combustion	27	0.1	0.027
• Cement Kiln off-gas	14 - 33	0.1	0.014 - 0.033
CO_2 from chemical transformations before combustion			
• IGCC: synthesis gas after gasification	18 - 20	2 - 7	0.16 - 1.4

[a] 0.1 MPa = 1 bar.

[b] IGCC: Integrated gasification combined cycle.

[c] Blast furnace gas also contains significant amounts of carbon monoxide that could be converted to CO_2 using the so-called shift reaction.

According to the Intergovernmental Panel on Climate Change (IPCC), most of emission sources have a CO_2 concentration below 15% vol. and less than 2% of sources have a CO_2 concentration above 95% vol. Other constraints on the post-combustion capture processes arise as the flue-gas temperature is often high, the large volume of flue gases to be treated, and oxides of sulfur and nitrogen produced by combustion causing disruption of capture installations (installation corrosion and chemical degradation of solvents).

Several post-combustion CO_2 capture technologies are being developed. Four main categories regroup these technologies: CO_2 absorption in solvents, CO_2 adsorption on solids, CO_2 membrane separation, and CO_2 antisublimation.

1.4 Antisublimation CO_2 capture process (AnSU)

Antisublimation (direct phase change from the gas to the solid phase) of CO_2 at atmospheric pressure and for a concentration of 14% on dry flue gases occurs at -100°C. This phase change is a separation method of CO_2 from the other flue-gas components. Table 1.3 shows coal-fired-boiler flue-gas composition after dehydration and the saturation temperature of every component before and after 90% CO_2 separation.

Table 1.3: Coal-fired-boiler flue-gas composition before and after 90% CO_2 capture.

	CO_2 Capture unit inlet			CO_2 Capture unit outlet		
	% mass	Pressure (kPa)	Saturation temperature	% mass	Pressure (kPa)	Saturation temperature
CO_2	22.06%	15.608	-99°C	2.75%	1.812	-118°C
Nitrogen	72.99%	81.132	-198°C	91.06%	94.190	-196°C
Oxygen	3.72%	3.620	-206°C	4.64%	4.202	-202°C
Argon	1.24%	0.965	-212°C	1.54%	1.121	-212°C

The antisublimation CO_2 capture principle is to cool down flue gases until frosting CO_2 at temperature between -99°C and -118°C. Before reaching the stage of CO_2 separation from flue gases, they must undergo several processes to achieve high-purity captured CO_2 at the end of the process. The first step is to cool down and clean flue gases. These flue gases outgoing at 120°C pass through a water vapor condensing unit and they are cooled to 15 to 20°C. The condensing unit is a gas-liquid direct-contact heat exchanger where the cooling water is sprayed on flue gases. The cooling water collects water vapor, dust, and SO_2 from flue gases. Then the cooling water is cleaned and SO_2 is removed by a chemical process. In the second stage, flue gases will be cooled to 3°C. They are cooled by cold and decarbonized flue gases. Then the flue gases are cooled to -40°C by a brine of $CaCl_2$ and water. This cooling is necessary to reduce flue-gas water concentration to avoid ice formation in the process. Then the water vapor mass concentration is less than 0.1 g/kg of dry flue gases.

Before entering the CO_2 capture unit, flue gases are cooled to -100°C in a flue gases/ decarbonized flue gases heat exchanger recovering the cooling capacity contained in decarbonized flue gases exiting the separation unit at -120°C. Flue gases enter the antisublimation unit where they are cooled down to -120°C by an integrated cascade refrigerating system that is the main driver of the process.

In the antisublimation unit, the CO_2 will be deposited in solid form on a fin-and-tube heat exchanger (Figure 1.4). In this way, it will be separated from flue gases exiting the unit with low CO_2 concentration. The cooling capacity contained in flue gases that come out at -120°C and in the solid CO_2 is recovered to increase the process efficiency. After being captured the CO_2 is liquefied (Figure 1.5) and compressed to 10 MPa to be transported and sequestered in natural reservoirs.

This capture process requires two or more frosting/defrosting heat exchangers (CFXs) that operate alternately. As one of the units is cooled to -120°C and operates as a CO_2 capture unit, the other is operating in CO_2 recovery. The switch from one CFX to the other takes place when the solid CO_2 deposit increases significantly flue-gas pressure losses and reduces the heat and mass transfer between flue gases and the refrigerant. The swap point will be optimized in order to increase the process efficiency.

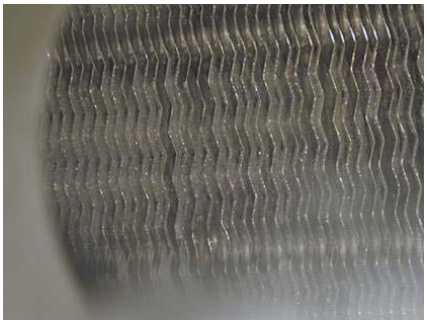

Figure 1.4: Frosted CO_2 on the heat exchanger.

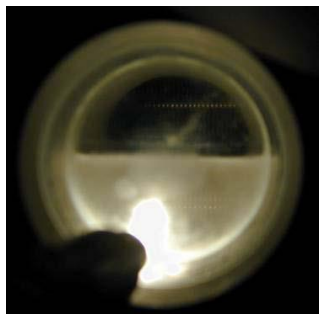

Figure 1.5: Liquid CO_2 recovered after defrosting.

1.4.1 CO_2 antisublimation heat exchanger (CFX)

The CO_2 Hex (CFXs) consists of a fin-and-tube heat exchanger. The refrigerant is a mixture of hydrocarbons and flue gases pass through the fins where the CO_2 is separated by antisublimation. The CO_2 pass directly from vapor to solid phase forming a solid deposit on the heat-exchanger fins.

At the entrance of the CFX, flue gases have been necessarily dehydrated. They are at atmospheric pressure and at temperature close to the CO_2 sublimation temperature. Table 1.3 summarizes the dehydrated flue-gas composition at the inlet and the outlet of the capture unit. The case studied is a coal-fired-boiler flue gases.

In this case, the CO_2 partial pressure in the flue-gas flow is 15.6 kPa. This partial pressure defines the sublimation temperature at which the CO_2 begins to frost on the heat exchanger fins. According to the sublimation line of CO_2 defined in REFPROP V9.0, the CO_2 sublimation temperature at this partial pressure is -99°C. Two steps occur in the CFX: step 1 is to cool flue gases down to the sublimation temperature without the CO_2 mass transfer and, step 2, when the fin temperature is lower than the CO_2 sublimation temperature then it starts to drop.

Limiting CO_2 capture to 90% of its mass flow rate in flue gases, the final flue-gas compositions at the CFX outlet are presented in Table 1.3. Hence the CO_2 partial pressure is fixed to 1.8 kPa at the CFX outlet, the outlet flue-gas temperature is -118°C. It is the sublimation temperature of the CO_2 at this partial pressure. Decarbonized flue gases contain only N_2, O_2, Ar, and residual CO_2. Their cooling capacity is recovered before their release to the atmosphere in order to increase the process efficiency.

Figure 1.6 shows the CO_2 partial pressure variation throughout the CFX. It is plotted as a function of the flue-gas temperature assuming that flue gases are saturated during antisublimation. The CO_2 concentration is constant at the CFX inlet because the CO_2 sublimation temperature is not reached. As soon as the flue-gas temperature reaches -99°C, the CO_2 partial pressure begins to decrease from 15.6 down to 1.8 kPa at the exit ensuring 90% of solid CO_2 separation from the gas stream.

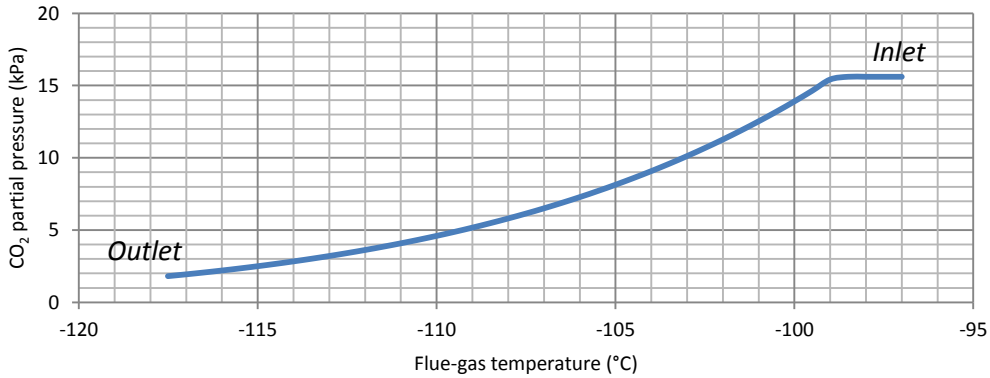

Figure 1.6: CO_2 partial pressure variation as a function of flue-gas temperature.

Because the flue-gas CO_2 concentration at the CFX is not constant, a temperature profile has to be imposed ensuring a homogeneous solid CO_2 deposit throughout the CFX. Otherwise, a non-compatible temperature profile leads to form a thicker solid CO_2 layer in the regions where the CO_2 vapor concentration is high. This problem could take place at the CFX inlet and lead to plug it. As well, the optimization of the temperature profile and of the temperature difference between flue gases and the refrigerant blend in the CFX leads to make the capture process more efficient.

1.4.2 CFX optimization necessity

As seen in the previous paragraph, the CO_2 antisublimation CFX is a fin-and-tube heat exchanger used in a cross-counter flow configuration (Figure 1.7). Flue gases are cooled by heat transfer with the refrigerant mixture that evaporates in the tubes. In order to increase the efficiency of the CFX, the temperature difference between the flue gases and the refrigerant mixture has to be minimized.

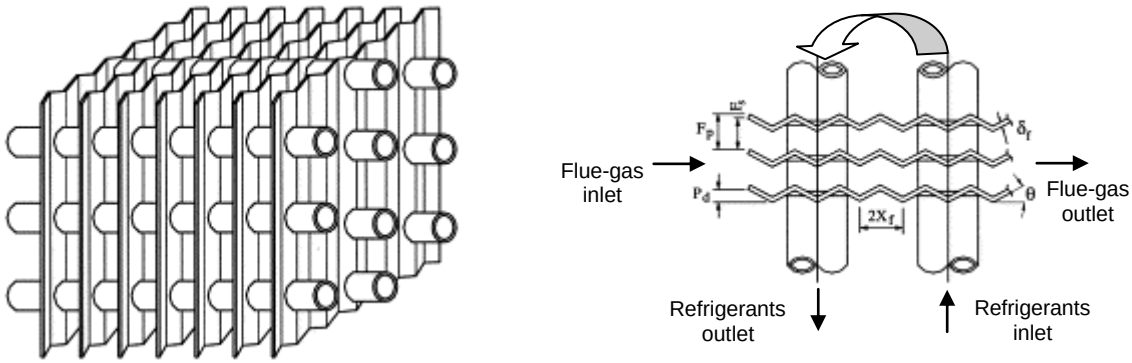

Figure 1.7: Fin-and-tube CFX used in a cross-counter flow configuration.

1.4.2.1 Flue-gas temperature gliding curve calculation

In this section, the energy consumption of the CO_2 frosting for coal-fired-boiler flue gases is calculated in order to calculate the temperature gliding curve. At the inlet of the low-temperature heat exchanger, CFX, flues gases are water free. After dehydration at -40°C and a pre-cooling to a temperature lower than -90°C, the water vapor partial pressure is lower than 9.4 10^{-06} kPa thus its volumetric concentration is less than 9.3 10^{-08} %v. As well, flue gases do not contain impurities like oxides of nitrogen (NO_x) and oxides of sulfur (SO_x). Flue gases are at a pressure close to the atmospheric one equal to 101.325 kPa. Flue-gas compositions at the CFX inlet and outlet are summarized in Table 1.4. At the outlet, flues gases are decarbonized by 90% of the inlet CO_2 concentration.

The pressure loss across the CFX is not taken into account in this calculation, thus the total pressure all over the CFX is assumed to be 101.325 kPa.

Table 1.4: Coal-fired-boiler flue gases composition at the inlet and the outlet of the CFX after 90% CO_2 capture.

	CFX inlet			CFX outlet		
	% vol.	% mass.	Partial pressure (kPa)	% vol.	% mass.	Partial pressure (kPa)
Water	0.00%	0.00%	0	0.00%	0.00%	0
CO_2	15.40%	22.06%	15.608	1.79%	2.75%	1.812
Nitrogen	80.07%	72.99%	81.132	92.96%	91.06%	94.190
Oxygen	3.57%	3.72%	3.620	4.15%	4.64%	4.202
Argon	0.95%	1.24%	0.965	1.11%	1.54%	1.121

To calculate the CO_2 capture energy consumption, the CFX is divided into elements. Every element represents a temperature gradient of -0.1 K. Therefore these elements do not have any significant geometrical meaning on the heat exchanger.

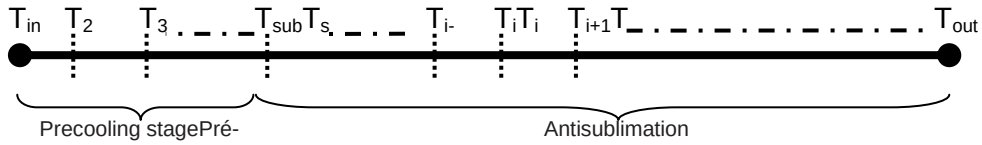

Figure 1.8: Flue-gas temperature evolution: $(T_i - T_{i-1} = -0.1\ K)$.

Flue gases are assumed to behave as an ideal gas that is in contact with the frosted CO_2 on the CFX fins. The following assumptions are considered [SON03]:

5. *The solid phase contains no dissolved gases;*
6. *The gas phase can be treated as a mixture of ideal gases;*
7. *When the gas mixture and the* CO_2 solid *phase are at a given pressure and temperature, the equilibrium between the solid CO_2 phase and its vapor is not influenced by the presence of other components. This means that when equilibrium is achieved, the vapor partial pressure will be equal to the saturation pressure corresponding to the mixture temperature;*
8. *No pressure losses occur to the gas stream.*

The inlet flue-gas temperature is assumed to be higher, by 3 K, than the sublimation temperature for which the CO_2 capture begins. For total gas-stream pressure of 101.325 kPa where the CO_2 partial pressure is 15.608 kPa, the inlet temperature is -95.9°C. The outlet temperature is equal to the CO_2 sublimation temperature for which the capture of 90% of the CO_2 is achieved. It is equal to -117.5°C in this case.

Assuming that CO_2 antisublimates at the inlet temperature of an element e_i, so the layer of the solid CO_2 formed in Element e_i is at T_{i-1}. For each temperature T_i, the volumetric and the mass concentrations, the partial pressure, the enthalpy, and the entropy of vapor components are calculated using Refprop V9.0. Thermodynamic properties of solid carbon dioxide are calculated using equations of Paragraph 1.6.

For temperatures where CO_2 antisublimation occurs, the CO_2 entropy and enthalpy are calculated for the sublimation line. The mass of frosted CO_2 in an element e_i is calculated assuming that the CO_2 partial pressure at the outlet is equal to the sublimation pressure corresponding to the mixture temperature. Vapor CO_2 is in equilibrium with its solid phase. Calculations are made for 1 kg/s flue-gas mass flow rate at the inlet.

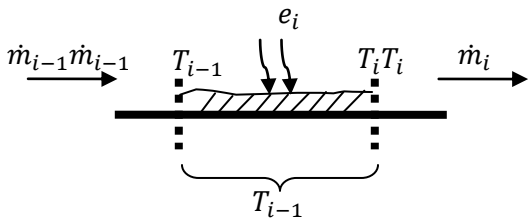

Figure 1.9: Element e_i representation.

The cooling capacity needed to cool down flue gases in every element from T_{i-1} to T_i and to anti-sublimate part of the CO_2 is calculated. Equation (1.2) is used to calculate the cooling capacity $Q_{c,i}$ in an element e_i where all flue-gas components are superheated.

$$Q_{c,i} = [\dot{m}_i(h_i - h_{i-1})]_{N_2} + [\dot{m}_i(h_i - h_{i-1})]_{O_2} + [\dot{m}_i(h_i - h_{i-1})]_{Ar} + [\dot{m}_i(h_i - h_{i-1})]_{CO_2} \quad (1.2):$$

For temperatures where the CO_2 is anti-sublimated $Q_{c,i}$ is calculated using Equation (1.3):

$$Q_{c,i} = [\dot{m}_i(h_i - h_{i-1})]_{N_2} + [\dot{m}_i(h_i - h_{i-1})]_{O_2} + [\dot{m}_i(h_i - h_{i-1})]_{Ar} + \left[\dot{m}_i\left(h_{g,i} - h_{g,i-1}\right)\right]_{CO_2} + \left[(\dot{m}_{i-1} - \dot{m}_i)\left(h_{s,i-1} - h_{g,i-1}\right)\right]_{CO_2} \quad (1.3)$$

The last term in the second member of Equation (1.3) is the latent heat $Q_{L,i}$ able to antisublimate part of the CO_2 and the other terms are the sensible heat able to cool down flue gases from T_{i-1} to T_i.

Figure 1.10 represents the CO_2 partial pressure variation along the CFX. This pressure is constant at the inlet where the flue-gas temperature is higher than the CO_2 sublimation temperature.

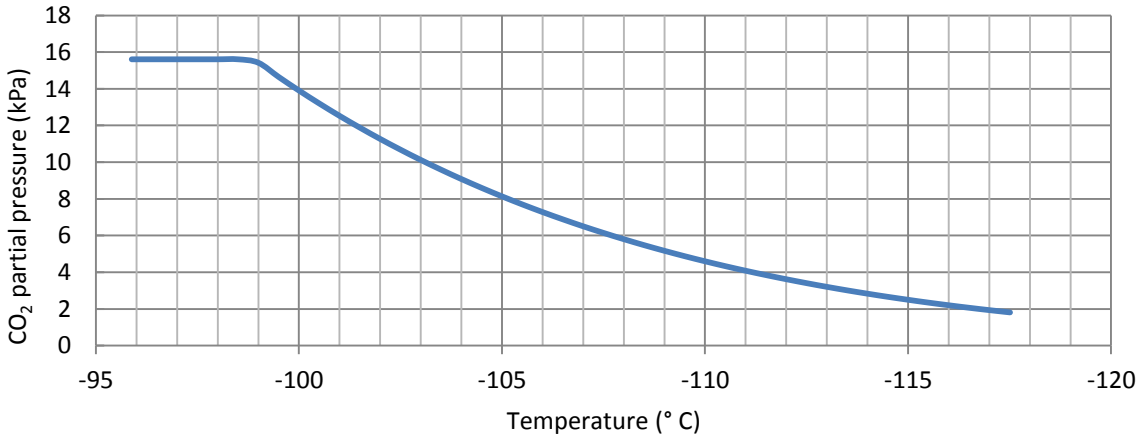

Figure 1.10: CO_2 partial pressure variation

Sensible, latent, and total cooling capacity, calculated as a function of the temperature, are plotted in Figure 1.11. The plotted cooling capacity is the capacity consumed by the flue-gas streams that are cooled down from their inlet temperature to the temperature T_i. At the CFX inlet, where the CO_2 is superheated, the latent cooling capacity is nil. Sensible heat is consumed to cool down flue gases until they reach the CO_2 sublimation temperature.

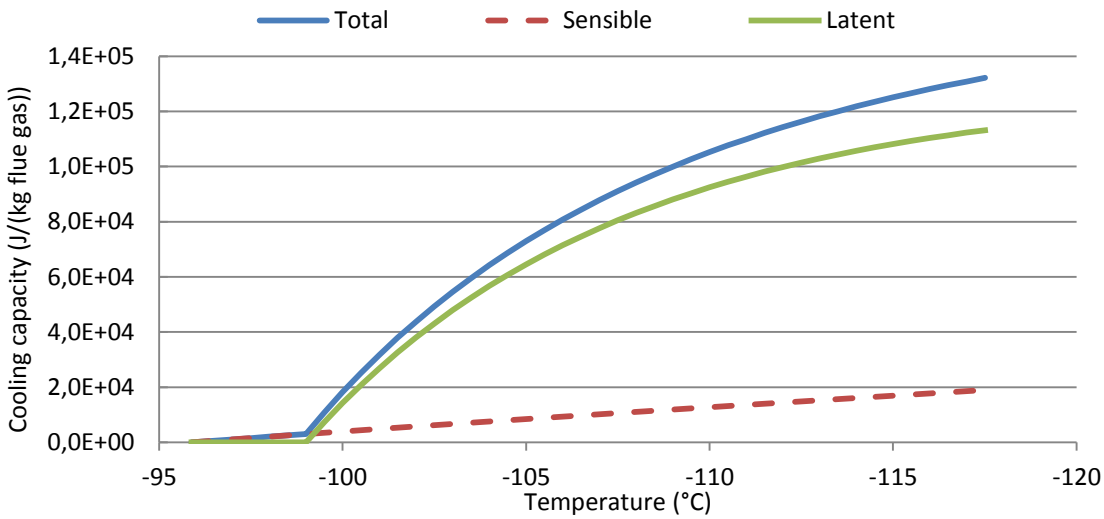

Figure 1.11: Sensible, latent and total cooling capacity variation.

The sensible cooling capacity increases linearly with the decreasing temperature while the latent cooling capacity increases rapidly when the CO_2 antisublimation starts and then it increases slowly. This tendency of slow increase in the latent cooling capacity needed throughout the CFX as the temperature decreases is caused by the decreasing antisublimating CO_2 mass all over the cooling process. Figure 1.12 shows the tendency of the CO_2 antisublimated weight throughout the heat exchanger. At the inlet 2.09 g CO_2/kg flue gases are captured for every 0.5 K cooling. This value diminishes to 0.35 g CO_2/kg flue gases at the CFX outlet. This decrease is due to the CO_2 partial pressure decrease all over the cooling process.

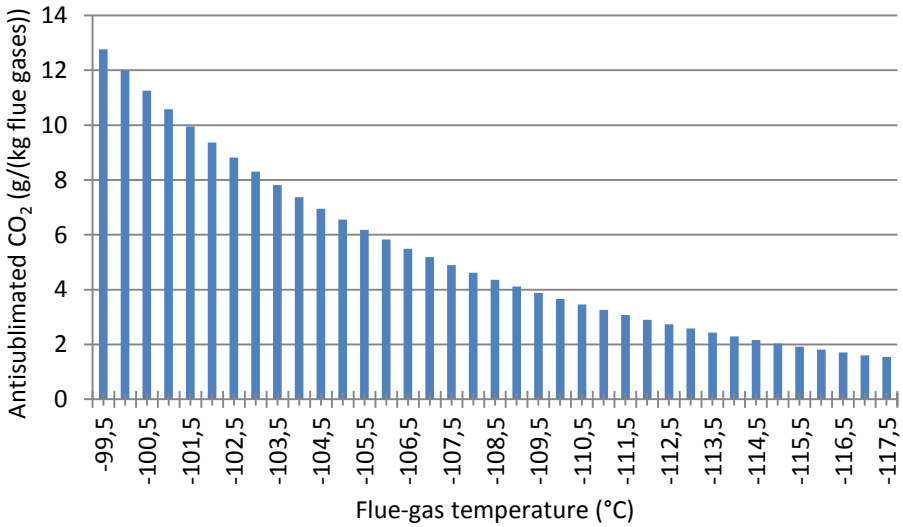

Figure 1.12: Antisublimated CO_2 for every 0.5 K of flue gases temperature decreasing.

For coal-fired-boiler flue gases and for 90% CO_2 capture the theoretical cooling capacity needed is 132 kJ/(kg flue gases) by cooling them down of about 22 K.

In Figure 1.13 is plotted the Carnot factor variation as a function of the cooling capacity transferred from the flue-gas stream to the refrigerant blend. The reference temperature is assumed to be equal to the ambient temperature $T_a = 15°C$. In this case the warm and cold fluids are at temperatures lower than the ambient temperature, and then Carnot factors are negative.

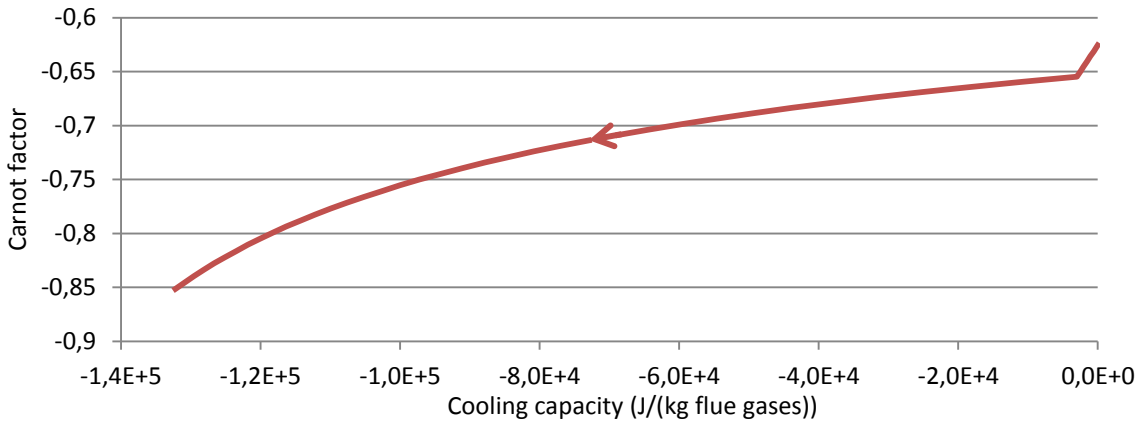

Figure 1.13: Coal-fired-boiler flue-gas temperature gliding curve for 90% CO_2 antisublimation.

The optimization of the CO_2 antisublimation heat exchanger consists in minimizing the temperature difference between the flue gases and the refrigerant for a required cooling capacity. For this purpose, a new fin-and-tube heat exchanger configuration has to be designed using a new hydrocarbon blend. This design has to take into account the dynamic variation of the exterior heat transfer conditions. In fact, the solid CO_2 deposit formation on the heat exchanger is the reason of the surface temperature, the flue-gas velocity, and the heat and the mass transfer variation on the exterior side of the heat exchanger. These temporal variations during the CO_2 antisublimation cycle have to be taken into account for the heat-exchanger optimization.

1.4.2.2 Integrated cascade efficiency variation as a function of the minimum cooling temperature

The refrigerant blend temperature optimization has an important effect on the efficiency improvement of the CO_2 frosting CFX. In addition, the mean evaporating temperature of the refrigerant has a major effect on the refrigerating system that is the main driver of the CO_2 capture process. An integrated cascade is used to produce the required cooling capacity at these low temperatures. The refrigerant used is a blend of hydrocarbons that evaporates at these temperatures.

This integrated cascade operates between the mean evaporating temperature and the ambient temperature. In order to show the effects of the mean evaporating temperature on the refrigerating system efficiency, the coefficient of performance of Carnot cycle, COP_{Carnot}, is represented as a function of the temperature. The ambient temperature is assumed to be 15°C.

$$\mathrm{COP_{Carnot}} = \frac{\overline{\mathrm{T}}_{\mathrm{evap}}}{\mathrm{T_a} - \overline{\mathrm{T}}_{\mathrm{evap}}} \quad , \qquad \mathrm{T_a} = 15\ °\mathrm{C} \tag{1.4}$$

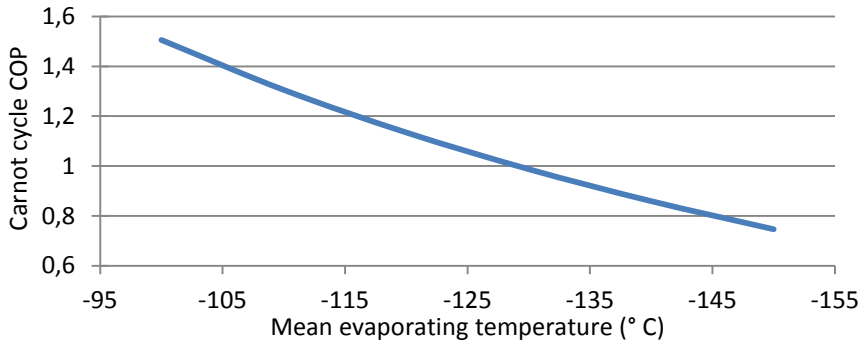

Figure 1.14: Carnot cycle COP evolution as a function of the mean evaporating temperature.

As represented in Figure 1.14, the efficiency of a refrigerating cycle decreases with the mean evaporating temperature decrease. So the optimization of the CO_2 frosting heat exchanger allows increasing the mean evaporating temperature and consequently the total efficiency of the CO_2 capture process.

1.5 Minimum work consumption for binary mixture gas separation

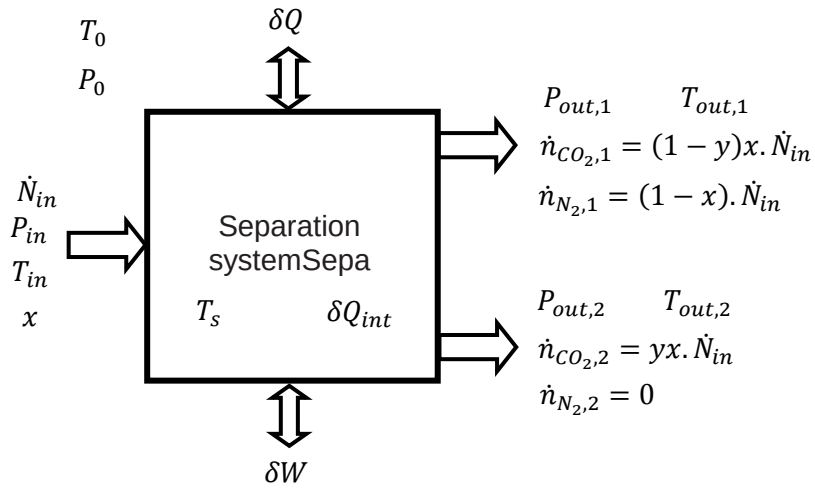

Figure 1.15: Continuous steady-state gas separation system.

The CO_2 capture-process efficiency is calculated by comparing the total work consumed by the process to the minimum theoretical work consumed by separating an amount of CO_2 from the whole gas stream mixture. In this section the minimum work consumed per unit mole of separated CO_2 is calculated in order to calculate the total efficiency of a CO_2 capture process.

Consider a continuous steady state gas separation system represented in Figure 1.15 [SEA05] with one inlet (the mixture) and two outlets (the decarbonized mixture and the pure liquid CO_2). At the inlet, a $\dot{N}_{in}$ molar flow rate of N_2 – CO_2 gas mixture enters the system at pressure and temperature P_{in} and T_{in}. x is the CO_2 molar concentration at the system inlet. The separation system allows a pure CO_2 separation, named also perfect separation [AME03], with a rate of separation y. $\dot{n}_{CO_2} = yx$. $\dot{N}_{in}$ is the pure CO_2 molar flow rate at Outlet 2 of the system. Nitrogen and residual carbon dioxide exit the system through Outlet 1 at the pressure $P_{out,1}$ and the temperature $T_{out,1}$. δQ and δW are respectively the heat and the mechanical powers transferred from the ambient to the system. The internal irreversibilities of the system generate a heating capacity δQ_{int}. By applying the mass, energy, entropy and exergy balances to the system, following equations are deduced.

Mole flow rate and CO_2 balance:

$$\dot{\mathrm{N}}_{\mathrm{in}} = \dot{\mathrm{N}}_{\mathrm{out,1}} + \dot{\mathrm{N}}_{\mathrm{out,2}} \tag{1.5}$$

$$\mathrm{x}.\dot{\mathrm{N}}_{\mathrm{in}} = \mathrm{yx}.\dot{\mathrm{N}}_{\mathrm{in}} + (1-\mathrm{y})\mathrm{x}.\dot{\mathrm{N}}_{\mathrm{in}} \tag{1.6}$$

Energy balance:

$$\sum_{in} \dot{n}_i h_i - \sum_{out} \dot{n}_i h_i + \delta Q + \delta W = 0 \tag{1.7}$$

Where h_i and $\dot{n}_i$ are the molar total enthalpy and the mole flow rates of all components entering and exiting the system.

Entropy balance:

$$\sum_{in} \dot{n}_i s_i - \sum_{out} \dot{n}_i s_i + \frac{\delta Q}{T_s} + \frac{\delta Q_{int}}{T_s} = 0 \tag{1.8}$$

Exergy balance:

$$\sum_{in} \dot{n}_i ex_i - \sum_{out} \dot{n}_i ex_i + \delta Q \left(1 - \frac{T_0}{T_s}\right) - T_0 \frac{\delta Q_{int}}{T_s} + \delta W = 0 \tag{1.9}$$

ex_i is the molar exergy of all components entering and exiting the system.

$$ex_i = h_i - T_0 s_i \tag{1.10}$$

The minimum theoretical work of separation of pure CO_2 from the gas mixture is obtained using a reversible isothermal system at ambient temperature and pressure. Molar flows at the inlet and the outlet of the system are also at ambient temperature and pressure. In this case, Equations (1.7) and (1.8) are written as follows:

$$\delta W_{min} = -\delta Q \tag{1.11}$$

$$\frac{\delta Q}{T_0} = \sum_{out} \dot{n}_i s_i - \sum_{in} \dot{n}_i s_i \tag{1.12}$$

Assuming that the gas mixtures at the inlet and the outlet of the system behave as an ideal gas, the entropy of a component is calculated using Equation (1.13):

$$s_i = c_p \ln \frac{T_i}{T_0} - \bar{R} \ln \frac{P_i}{P_0} \tag{1.13}$$

Then

$$\delta W_{min} = -\bar{R}T_0\left(\sum_{in}\dot{n}_i \ln\frac{P_i}{P_0} - \sum_{out}\dot{n}_i \ln\frac{P_i}{P_0}\right) \quad (1.14)$$

$\bar{R} = 8.314\, J.mol^{-1}.K^{-1}$ is the ideal gas constant and P_i is the partial pressure of component i. For CO_2 separation from the binary gas mixture with a rate of separation y, the minimal work of separation is:

$$\delta W_{min} = -\dot{N}_{in}\bar{R}T_0[xy\ln x - x(1-y)\ln(1-y) + (1-xy)\ln(1-xy)] \quad (1.15)$$

The minimum work of perfect CO_2 separation per unit mole flow rate of system inlet, δw_{min}, is represented in Figure 1.16 as a function of the inlet CO_2 molar concentration x.

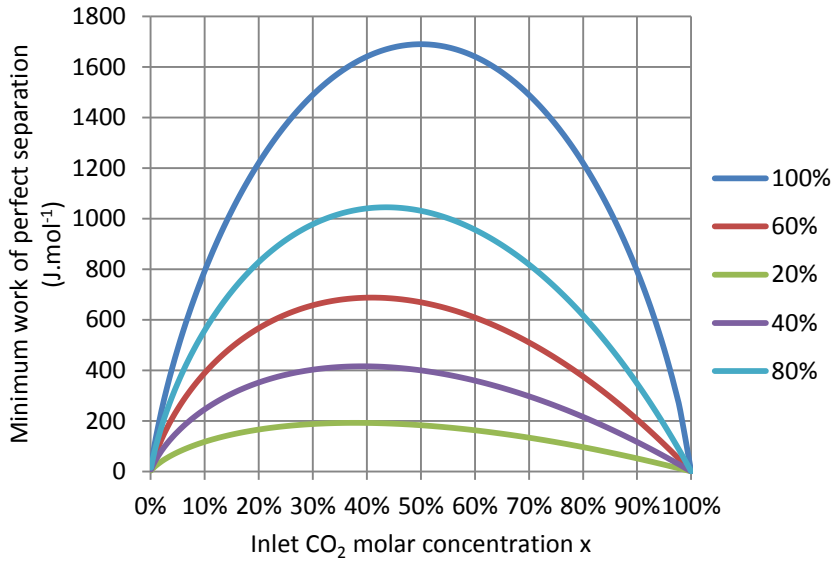

Figure 1.16: Minimum work of perfect separation per unit mole flow rate of system inlet.

The minimum work of perfect separation per unit of separated CO_2 mole flow rate is plotted in Figure 1.17 as a function of the separated CO_2 mole flow rate.

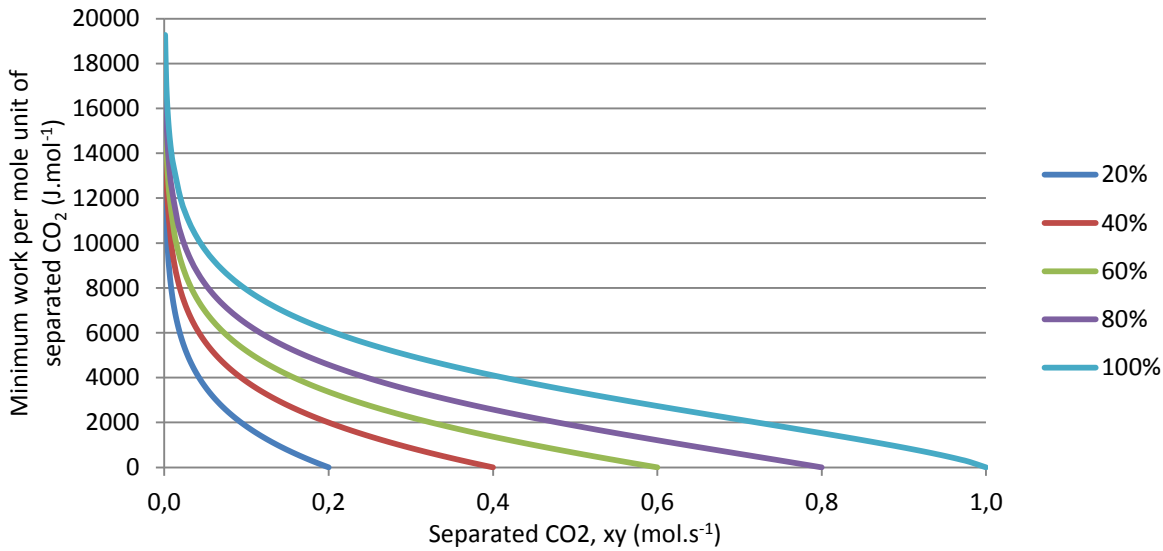

Figure 1.17: Minimum work of perfect separation per unit of separated CO_2.

Figures 1.16 and 1.17 show that for a constant initial CO_2 concentration, the higher the separation rate, the higher the minimum work of perfect separation.

Amelkin et al. [AME03] defined the imperfect separation of a binary gas mixture as a separation where the two components are present in both products at the separation system outlet. For a separation system where x, z_1 and z_2 are respectively the CO_2 concentration at the inlet and the concentrations at the two outlets, the minimum work of imperfect separation is calculated by applying mole, energy, and entropy balances to the system:

$$\delta W_{min,imp.} = -\dot{N}_{in}\bar{R}T_0\left\{x\ln x + (1-x)\ln(1-x) - \frac{x-z_2}{z_1-z_2}[z_1\ln z_1 + (1-z_1)\ln(1-z_z)] - \frac{z_1-x}{z_1-z_2}[z_2\ln z_2 + (1-z_2)\ln(1-z_2)]\right\} \quad (1.16)$$

The CO_2 capture process efficiency is calculated using Equation (1.17) by dividing the minimum work by the real work consumed by the separation process [BOL06]. In order to use this efficiency as a comparison criterion between different CO_2 capture processes, the minimum work calculated and the work consumed per unit mole of separated CO_2 are used.

$$\eta_{process} = \frac{\delta W_{min}\left(W.mol^{-1}_{sep.CO_2}\right)}{\delta W_{process}\left(W.mol^{-1}_{sep.CO_2}\right)} \quad (1.17)$$

1.6 Solid CO_2 low-temperature thermodynamic properties and CO_2 – N_2 psychrometric chart

This section is written in the form of a scientific paper, which is presented to be published in the “International Journal of Greenhouse Gas Control”.

In order to study the CO_2 post-combustion capture by antisublimation process, the solid gas equilibrium has to be known for all CO_2 concentrations in nitrogen, which is the main component in flue gases. CO_2 properties are determined for conditions above the triple point. Few studies have been carried out to determine the CO_2 properties in its solid-vapor equilibrium state. An experimental study to measure CO_2 properties at low temperatures is a complex task. CO_2, unlike most fluids, has a high vapor pressure in its solid state. To represent the CO_2 capture by antisublimation process, a psychrometric chart was developed. In addition to carbon dioxide and nitrogen, flue gases contain oxygen, argon, and other gases at the inlet of the capture unit. The psychrometric chart is plotted for a binary gas mixture composed of only nitrogen and carbon dioxide in order to simplify calculations. This approximation leads to an error lower than 1% in calculating enthalpy, entropy, density, and partial pressure of the mixture. Methods for calculating isenthalpic and constant specific volume curves are exposed. The NIST reference fluid thermodynamic and transport properties database, Refprop V9.0, is used. The psychrometric chart is plotted for flue gases at atmospheric pressure (101.325 kPa), which is the case of the majority of CO_2 emission sources.

Solid CO_2 low temperature thermodynamic properties and CO_2 - N_2 psychrometric chart

Joseph TOUBASSY[a], Youssef RIACHI[a], Denis CLODIC[a]

[a] MINES ParisTech, CEP- Centre énergétique et procédés, 60 Bd St Michel 75272 Paris Cedex 06, France

Abstract

In order to study the CO2 post-combustion capture by antisublimation process, the solid-gas equilibrium has to be known for all CO_2 concentrations of CO_2-Nitrogen mixtures, which are the main flue-gas components. CO_2 thermodynamic properties are determined for conditions lower than the triple point. Few studies have been carried out to determine CO_2 properties in solid-vapor equilibrium state. An experimental study to measure CO_2 properties at low temperatures is a complex task. CO_2, unlike most fluids, presents a high vapor pressure in solid state. To represent the CO_2 capture by antisublimation process, a psychrometric chart was developed. In addition to carbon dioxide and nitrogen, flue gases contain oxygen, argon, and other gases at the inlet of the capture unit. The psychrometric chart is plotted for a binary gas mixture composed only of nitrogen and carbon dioxide in order to simplify calculations. This approximation leads to an error lower than 1% in calculating enthalpy, entropy, density, and partial pressure of the mixture. Methods for calculating isenthalpic and constant specific volume curves are presented. The NIST reference fluid thermodynamic and transport properties database, Refprop V9.0, is used. The new CO_2 –N_2 psychrometric chart is plotted at atmospheric pressure (101.325 kPa).

Keywords: CO_2 capture, Antisublimation, Post-combustion, solid carbon dioxide, thermodynamic properties, psychrometric chart, low temperature.

Nomenclature:

T: Temperature, K

p: Pressure, kPa

h: Enthalpy, kJ.kg^{-1}

a: The four vibrational contributions in the free energy, cal.mol^{-1} = 4.184 J.mol^{-1}

s: Entropy, kJ.kg^{-1}.K^{-1}

c_p: Heat capacity, kJ.kg^{-1}

ρ: Density, kg.m^{-3}

e: Saturation relative concentration, dimensionless

x: Mass concentration ratio, dimensionless

r: Specific gas constant, J.kg^{-1}.K^{-1}

R: Universal gas constant, J.mol^{-1}.K^{-1}

m: Mass, kg

M: Molar mass, kg.kmol^{-1}

V: Volume, m^3

v: Specific volume, m^3.kg^{-1}

Q: Cooling capacity, kW

ΔL: Heat of sublimation, kJ.kg^{-1}

Subscripts:

s: Solid phase

g: Vapor phase

m: Mixture

1. Introduction

We call antisublimation the direct transformation from the gas phase to the solid phase. Modeling the antisublimation CO_2 process or frosting process requires knowing the CO_2 thermodynamic properties for temperatures ranging from 217 K to 140 K (Clodic et al., 2005). Kayukawa and Fujii (2010) evaluated the thermodynamic CO_2 properties by conducting a statistical investigation for a large set of CO_2 thermodynamic properties. All their references are for temperatures above the CO_2 triple point. In this study, additional references for the calculation of solid CO_2 properties are investigated in order to determine equations that provide precisely CO_2 thermodynamic properties.

Reynolds (1979) plotted the carbon dioxide (T, s) diagram for temperatures between 180 and 400 K. He gives empirical shapes for P-v-T, c_v^0, saturation pressure, and saturated liquid density equations. The stated properties do not include equations of state for CO_2 in solid state.

Azreg-Aïnou (2005) presents an empirical method for CO_2 vapor pressure determination for temperatures ranging between 154 and 196 K. An equation of state of solid CO_2 is also developed for temperatures between 12.5 and 189.8 K. Computational algebra schemes are used to extrapolate and find equations based on solid CO_2 data available in the literature. A comparison between developed equations, literature equations, and experimental data shows a good agreement between them. In addition, Azreg-Aïnou (2005) demonstrates that the CO_2 vapor behaves as an ideal gas for temperatures below 150 K.

Mass and Barnes (1926) described experiments and measurements used to determine the latent heat of fusion, the latent heat of sublimation, and the heat capacities of the solid and liquid phases of carbon dioxide for temperatures ranging from 89 to 273 K. They used an adiabatic calorimeter to measure the CO_2 latent heats of sublimation and fusion. They found also an empirical equation calculating the solid CO_2 heat capacity as a function of the temperature. In addition, measurements of the solid CO_2 density as a function of the temperature are carried out.

In this paper calculations and empirical equations for low-temperature carbon dioxide properties found in the literature are presented. Calculations of CO_2 sublimation pressure, solid and vapor enthalpy, solid and vapor entropy, solid heat capacity, and latent heat of sublimation are described. A CO_2 - N_2 psychrometric chart is developed to represent the CO_2 antisublimation process showing temperature and CO_2 concentration variations. This psychrometric chart allows the calculation of temperature variation and cooling capacity for different flue-gas CO_2 concentrations.

2. CO_2 Low temperature thermodynamic properties

2.1 CO2 sublimation pressure

The CO_2 sublimation pressure is calculated by different empirical equations that will be presented and compared. The first method used to calculate the CO_2 sublimation pressure as a function of the temperature is the Antoine's equation for temperatures ranging from 154.3 to 195.9 K (Azreg-Aïnou, 2005).

$$p_A = 100 \times \exp\{\bar{A}_1 - [\bar{B}_1/(T + C_1)]\} \quad (154.3 \leq T \leq 195.9\ K) \tag{1}$$

Where p_A is the pressure calculated in kPa, $\bar{A}_1 = A_1 \ln 10$, and $\bar{B}_1 = B_1 \ln 10$. The constants $A_1 = 6.81228$, $B_1 = 1301.679$, and $C_1 = -3.494$ have been evaluated by the National Institute of Standards and Technology (NIST).

Giauque and Egan (1937) use an empirical equation to calculate the sublimation pressure as a function of temperature. Their equation is valid for temperatures between 154 and 196 K.

$$p_{G\&E}(kPa) = 101.325/760 \times 10 \exp[(a_1/T) + b_1 + c_1 T + d_1 T^2] \quad (154 \leq T \leq 196\ K) \tag{2}$$

Where $a_1 = -1354.210 \times \ln 10$, $b_1 = 8.69903 \times \ln 10$, $c_1 = 0.001588 \times \ln 10$, and $d_1 = -4.5107 \times 10^{-6} \times \ln 10$.

Azreg-Aïnou (2005) calculated the CO_2 sublimation pressure for temperatures under triple point. This pressure is given by Equation (3):

$$p_M = CT^{5/2} Z_r Z_v \exp\{[\Delta h_s - T s_s - \varepsilon_0 - B(T)p]/RT\} \tag{3}$$

Where $B(T)$ is assumed to follow Berthelot's equation:

$$B(T)p = R l_1 [1 - (l_2/T^2)]p \tag{4}$$

$$l_1 = 9 \times 304.1/(128 \times 72.8 \times 101.325\ )\ (K.kPa^{-1})$$

$$l_2 = 6 \times 304.1^2\ (K^2) \qquad C = 7.575455 \times 10^5$$

$$Z_r = [T + \theta_r/3].(2\theta_r)^{-1} \qquad Z_v = {Z_{v1}}^2 \times Z_{v2} \times Z_{v3}$$

$$Z_{vi} = [1 - \exp(-\theta_{vi}/T)]^{-1}$$

$$\theta_{v1} = 0.561\ K \qquad \theta_{v2} = 1890\ K$$

$$\theta_{v3} = 3360\ K \qquad \theta_r = 0.561\ K$$

$$\varepsilon_0 = 6273.4\ cal.mol^{-1} \qquad R = 1.98724\ cal.K^{-1}.mol^{-1}$$

Δh_s is the heat of sublimation and s_s is the solid CO_2 entropy. ε_0 is the heat of sublimation at 0 K, wich is the binding energy of the solid particles. By linearization of Equation (3) the pressure could be calculated:

$$p_M(kPa) = \frac{101.325/760 \times p_{ideal}}{\{1 + l_1[1 - (l_2/T^2)]p_{ideal}/T\}} \quad (T \geq 5) \tag{5}$$

$$p_{ideal}(kPa) = CT^{5/2} Z_r Z_v \exp\{[\Delta h_s - T s_s - \varepsilon_0]/RT\}\, 10^{-3} \tag{6}$$

p_{ideal} is the pressure of the ideal gas. Azreg-Aïnou (2005) claims that CO_2 vapor behaves as an ideal gas for temperatures below 155 K.

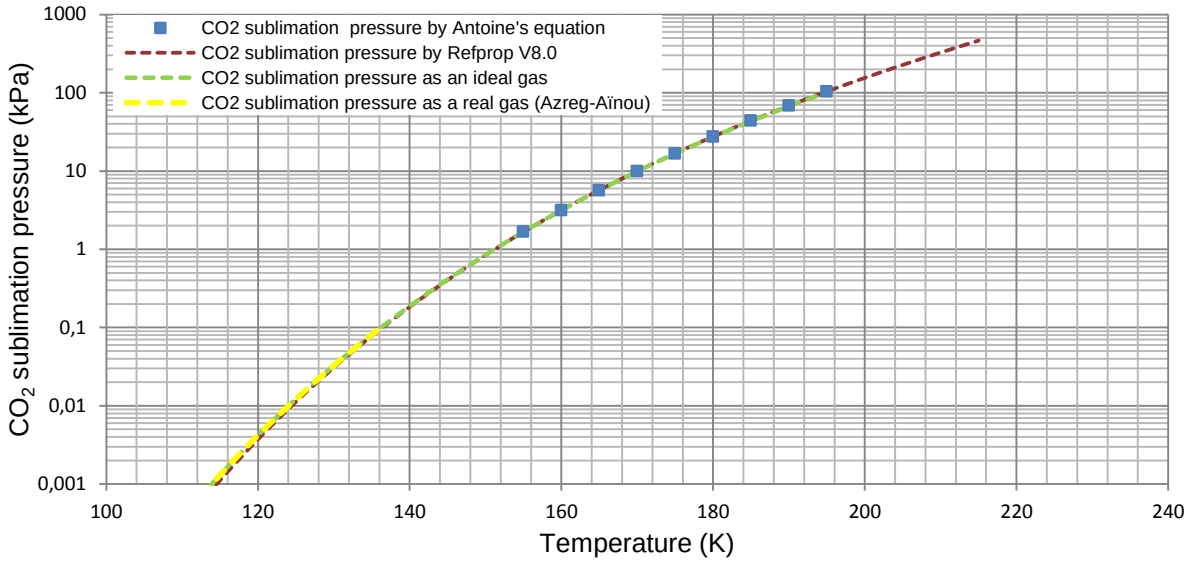

Figure 1: CO_2 Sublimation pressure calculated using different equations.

Figure 1 shows good agreement between CO_2 sublimation pressures calculated by the four aforementioned methods.

2.2 Low temperature CO_2 enthalpy

2.2.1 Solid state

Calculation of the solid CO_2 enthalpy as a function of the temperature requires the knowledge of the solid CO_2 heat capacity. Azreg-Aïnou (2005) uses experimental results collected by Giauque and Egan (1937) for temperatures ranging from 15.5 to 189.8 K and the Debye heat capacity for temperatures below 15 K to find the solid CO_2 heat capacity equation. It should be noted that the Debye equation is verified by the experimental results of Giauque and Egan (1937). Knowing the heat capacity of the solid CO_2, its enthalpy is calculated using Equation (7):

$$h_s(T) = \int_0^T c_p dT' = h_s(T) + \varepsilon_0 \tag{7}$$

Values of the heat capacity c_p are calculated between 0 and 189.8 K. Solid enthalpies are calculated for this temperature range by steps of 0.001 K. The reference condition of Equation (7) is $T_0 = 0\ K$. Results from Equation (7) are fitted by the polynomial Equation (8) that calculates the CO_2 solid enthalpy using the same reference state used in Refprop V9.0 (Span and Wagner, 1996).

$$h_s(T) = a_1 + b_1 T + c_1 T^2 + d_1 T^3 + f_1 T^4 + g_1 T^5 + h_1 T^6 \tag{8}$$

Where:

$$a_1 = -2.93E + 05 \qquad f_1 = -9.07E - 04$$
$$b_1 = -1.39E + 02 \qquad g_1 = 4.49E - 06$$
$$c_1 = 6.19 \qquad h_1 = -7.62E - 09$$
$$d_1 = 5.51E - 02$$

T is the temperature in K and $h_s(T)$ is calculated in J.kg^{-1}. Results of Equation (8) correspond to the solid CO_2 enthalpy given by Reynolds's CO_2 diagram.

Note: Reynolds (1979) uses the triple point as reference state and a difference of 80.054 kJ.kg^{-1} exists between the CO_2 solid phase enthalpy calculated by Equation (8) and the one read from his diagram.

Figure 2 represents the solid CO_2 enthalpy calculated using Equation (8) and complementary data extracted from Reynolds's diagram (Reynolds, 1979).

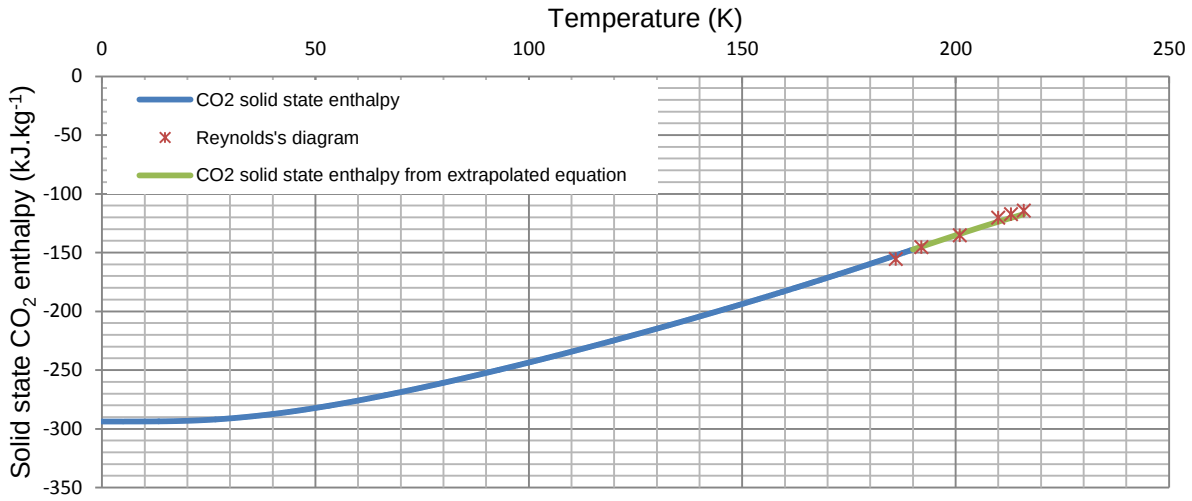

Figure 2: CO_2 solid state enthalpy given from Equation (8) and from Reynolds's diagram.

Reynolds data confirm that Equation (8) can be extrapolated up to the triple point temperature

2.2.2 Vapor state

Azreg-Aïnou (2005) calculated the vapor state CO_2 enthalpy using Equation (9):

$$h_g(T) = R[(7T/2) - (\theta_r/3)] - T^2[d(a_v/T)/dT] \quad (9)$$

Where h_g $(cal.mol^{-1})$ is the ideal gas enthalpy, R $(cal.mol^{-1})$ is the universal gas constant, $\theta_r = 0.561\,K$, T is the temperature in K, and a_v $(cal.mol^{-1})$ is the four vibrational contributions in the free energy:

$$a_v = 2a_{v1} + a_{v2} + a_{v3} \quad (10)$$

$$a_{vi} = RT\ln[1 - exp(-\theta_{vi}/T)] \qquad \theta_{v1} = 954\,K \qquad \theta_{v2} = 1890\,K \qquad \theta_{v3} = 3360\,K$$

Calculations of h_g in the temperature range between 150 K and the triple point temperature are represented in Figure 3. Note that the reference condition for this calculated h_g is at 0 K. Values plotted in Figure 3 have a reference similar to that used in Refprop V9.0. The CO_2 vapor state enthalpy is also calculated using Refprop V9.0 based on NIST equations. Figure 3 shows these values. Equation (9) and Refprop V9.0 give the same results.

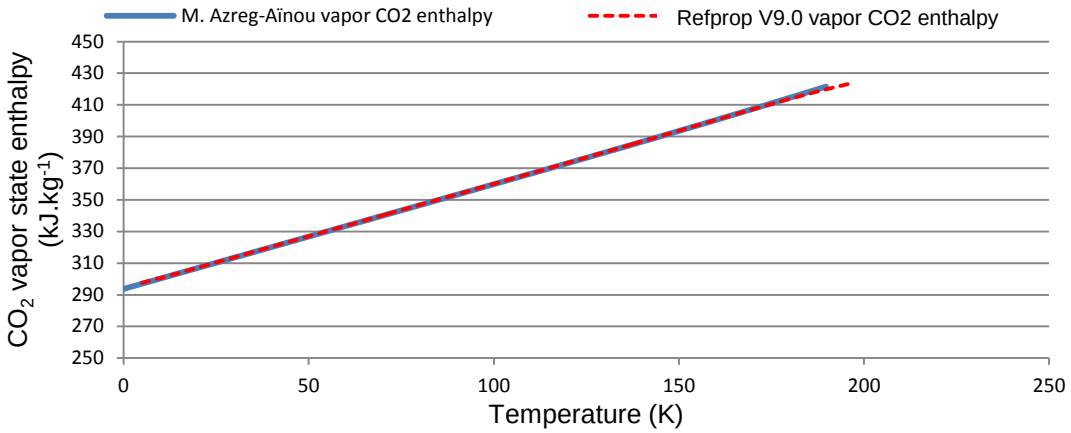

Figure 3: Vapor state CO_2 enthalpy.

2.3 Solid state CO_2 entropy

As the solid state CO_2 enthalpy, the solid state CO_2 entropy is calculated based on the solid CO_2 heat capacity. Heat capacity is calculated using Debye's equation and Giauque and Egan (1937) experimental results.

$$s_s(T) = \int_0^T \frac{c_p}{T'} dT' \tag{11}$$

Equation (11) gives the solid entropy considering T = 0 K as reference temperature. Solving the integral of entropy for the temperature range between 0 and 189.8 K allows the fitting of the equation of the solid CO_2 entropy as a function of temperature (K) in a polynomial form.

$$s_s(T) = a_2 + b_2 T + c_2 T^2 + d_2 T^3 + f_2 T^4 + g_2 T^5 + h_2 T^6 \tag{12}$$

Where

$$a_2 = -2.10E + 03 \qquad f_2 = 3.36E - 05$$
$$b_2 = -5.48 \qquad g_2 = -1.04E - 07$$
$$c_2 = 4.41E - 01 \qquad h_2 = 1.30E - 10$$
$$d_2 = -5.45E - 03$$

This equation calculates $s_s(T)$ in J.(kg.K)$^{-1}$ using the Refprop V9.0 reference state.

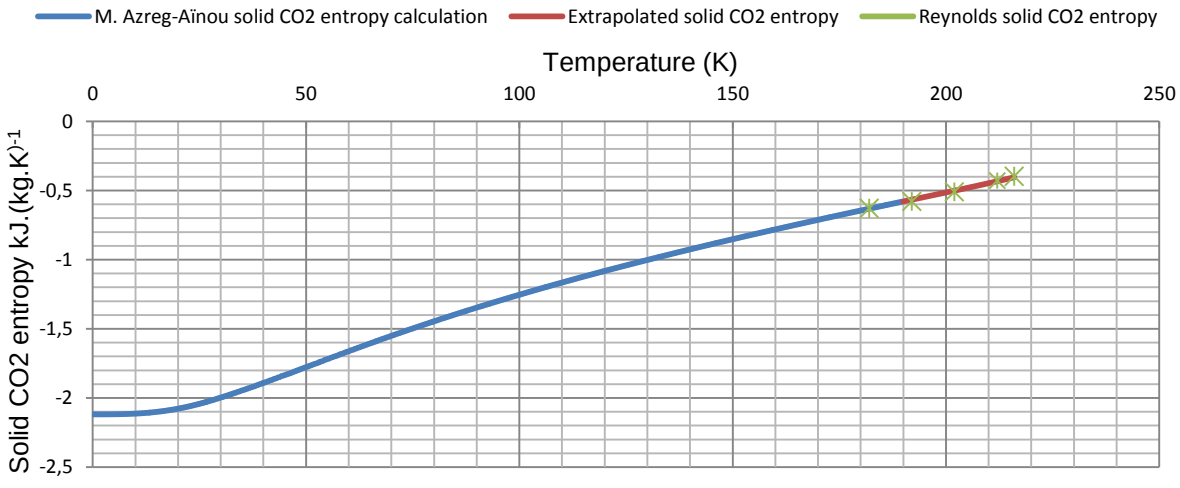

Figure 4: Solid state CO_2 entropy.

Results plotted in Figure 4 shows that solid CO_2 entropy calculation using Equation (12) gives results that match the CO_2 Reynolds's diagram values.

2.4 Solid CO_2 heat capacity

The solid CO_2 heat capacity was the object of many surveys. Azreg-Aïnou (2005) used Debye equation for the temperature range between 0 and 15.25 K to calculate this entity. In addition he used experimental results realized by Giauque and Egan (1937) for temperatures between 15.5 and 189.8 K. The equation that computes the solid CO_2 heat capacity as a function of temperature is fit using Azreg-Aïnou calculating data. 2D function finder software is used to find the equation. It has the form of Peters-Baskin Step-Stool equation.

$$c_p(kJ.kg^{-1}) = F - \ln\frac{\left(exp\left(d_2.(b_1.c_1 + L/d_1)\right) + exp(d_2.F)\right)}{d_2} \tag{13}$$

$$K = \ln\left(exp(b_2.c_1.d_1) + exp(b_2.d_1.T)\right)$$

$$L = \ln\left(exp(b_2.c_1.d_1) + exp(b_2.c_2.d_1)\right)$$

$$F = b_1.T + K/d_1$$

$$b_1 = 3.627E-03 \qquad b_2 = 1.572E-02$$

$$c_1 = 5.099E+01 \qquad c_2 = 1.384E+01$$

$$d_1 = -5.041E+00 \qquad d_2 = -1.740E+01$$

This equation is plotted in Figure 5.

O. Maass and W. H. Barnes found the solid CO_2 heat capacity equation function for temperatures going from 216 K down to 165 K. They used their experimental measuring of the solid CO_2 heat capacity to find this equation.

$$c_p = 0.40 - 2.83\,.10^{-3}\,T + 1.25\,.10^{-5}\,T^2 \qquad 165 \le T \le 216\,K \tag{14}$$

Where T is the absolute temperature and c_p is the solid CO_2 heat capacity calculated in cal.(g.K)$^{-1}$. Results of this equation are plotted in Figure 5.

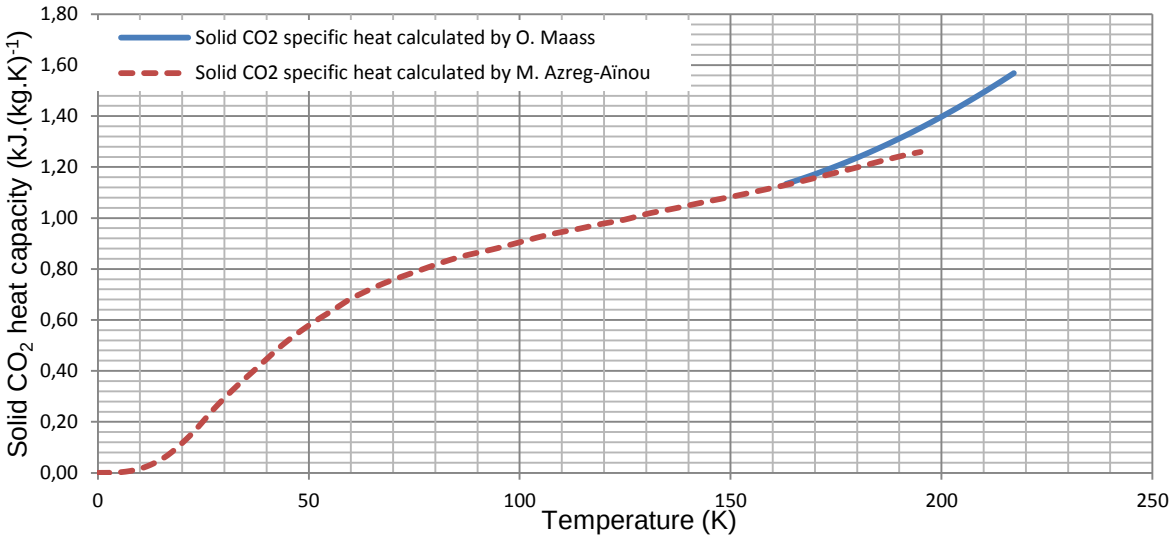

Figure 5: Solid state CO_2 heat capacity calculated using different equations.

Figure 5 shows that results obtained by Azreg-Aïnou and O. Maass are different for temperatures higher than 170 K.

2.5 Solid CO_2 density

Studies of Cook and Davey (1976) and of Shchelkunov et al. (1985) were conducted to measure the density of a porous solid CO_2 layer without measuring the pure solid CO_2 density. In order to calculate the solid CO_2 coefficient of expansion, Mass and Barnes (1926) have measured the solid CO_2 density at different temperatures. A defined mass of carbon dioxide and propane was enclosed in a glass bulb fitted with a graduated capillary tube. By cooling the glass bulb down to low temperatures under the CO_2 triple point, carbon dioxide antisublimates while the propane condensates. The total volume of the solid – liquid mixture is measured in addition to the mixture temperature. Knowing the liquid propane density variation as a function of the temperature and for defined propane and carbon dioxide weights, the density of the carbon dioxide forming the solid phase is calculated. Two different samples are used and measures are performed for different temperatures. Sample A contains 0.4767 g of propane and 4.8939 g of carbon dioxide while sample B is composed of 0.2736 g of propane and 5.3352 g of carbon dioxide. Results are plotted in Figure 6.

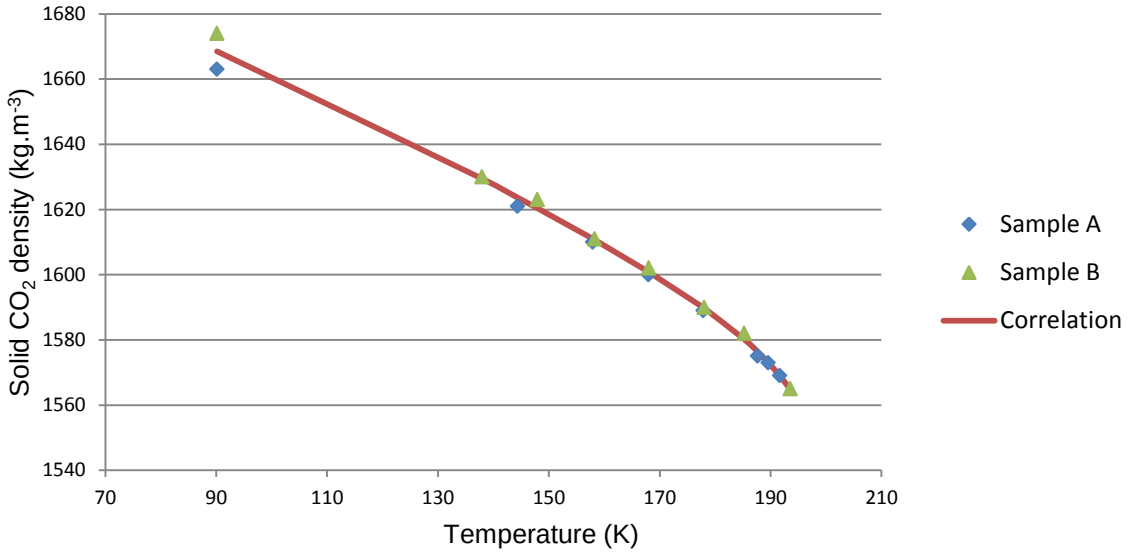

Figure 6: Solid CO_2 density measurement as function of the temperature, (Mass and Barnes, 1926).

Therefore, the solid CO_2 low-temperature density is calculated using the empirical polynomial correlation of Equation (15) and is valid for temperatures ranging from 90.15 to 193.5 K.

$$\rho_{CO_2,s} = -0.0035\ T^2 + 0.0301\ T + 1694.0060 \qquad 90.15\ K \leq T \leq 193.5\ K \tag{15}$$

2.6 Carbon dioxide T-s diagram

A new thermodynamic CO_2 T - s diagram is plotted down to 140 K using new empirical equations found and REFPROP V9.0. This diagram, presented in Figure 7, shows antisublimation line, isenthalpic lines, isochoric lines, and isobaric lines.

3. CO_2 - N_2 psychometric chart.

3.1 Antisublimation line and constant relative concentration

The solid-vapor line represents the limit at which the CO_2 crystallization in flue gases starts. Varying the CO_2 mass concentration from 0.1% to 99.9%, the CO_2 partial pressure is calculated for a total flue-gas pressure equal to the atmospheric pressure. As a first simplification, flue gases composed of N_2 – O_2 – Ar – CO_2 are considered to be a binary mixture of N_2 and CO_2. The antisublimation temperature is then calculated using Refprop

V9.0 for each partial pressure. The antisublimation line is represented by plotting the CO_2 mass concentration ratio x at the solid-vapor saturation line as a function of the antisublimation temperature. The CO_2 mass concentration ratio x is defined in Equation (17) as the ratio of the CO_2 mass to the N_2 mass in the gas mixture.

To plot constant CO_2 saturation relative concentration e curves, the partial pressure is calculated at each temperature for a fixed e value. e is given by Equation (16) and it is the ratio of the CO_2 partial pressure in a given mixture to the saturated CO_2 partial pressure at the same mixture temperature T_i. e is similar to the relative humidity in the case of humid air psychrometric chart (ASHRAE, 2005).

$$e = \frac{p_{CO_2}(T_i)}{p_{sat}(T_i)} \tag{16}$$

The gas mixture is assumed to be an ideal gas. Then the CO_2 mass concentration ratio x is calculated as a function of the temperature and e. The CO_2 saturation relative concentration curves are plotted in the psychrometric diagram for e going from 20% to 80%:

$$x = \frac{m_{CO_2}}{m_{N_2}} = \left(\frac{e.p_{sat}}{p_m - e.p_{sat}}\right)\left(\frac{M_{CO_2}}{M_{N_2}}\right) \tag{17}$$

m_{CO_2} and m_{N_2} are respectively the CO_2 and the N_2 masses in flue gases, M_{CO_2} and M_{N_2} are the CO_2 and the N_2 molar masses. p_m is the total mixture pressure equal to the atmospheric pressure.

3.2 Isenthalpic lines

Isenthalpic curves join several points (x_i, T_i) having constant enthalpy. These curves help to find the enthalpy of the gas mixture for any condition. Knowing the partial pressure or the concentration of each component in the mixture at a given temperature, the mixture enthalpy could be read on the diagram. The enthalpy of the gas mixture is calculated per kilogram of nitrogen:

$$h_m = \frac{H_m}{m_{N_2}} = h_{N_2} + x h_{CO_2} \tag{18}$$

h_m is the enthalpy of the N_2 - CO_2 mixture per unit mass of nitrogen. h_m depends on the composition of the gas mixture (i.e. the partial pressure of each component) and on the mixture temperature. h_{N_2} and h_{CO_2} are respectively the nitrogen and the carbon dioxide specific enthalpy for partial pressures and mixture temperatures. x is the CO_2 mass concentration ratio in the mixture.

To plot isenthalpic lines, the equation of CO_2 mass concentration ratio as a function of enthalpy and temperature has to be calculated. The mixture enthalpy is calculated on the antisublimation saturation line and at constant concentration lines. This calculation is made using Refprop V9 on the antisublimation line for CO_2 and on the superheated region for CO_2 and N_2. To find conditions where the enthalpy on the antisublimation line is specified, iterations are carried out, (x, T) bins are found for enthalpies ranging from 140 to 3960 kJ.(kg^{-1} N_2) using a step of 20 kJ.(kg^{-1} N_2). At these conditions the desired enthalpies are calculated with an absolute error lower than 1E^{-4} kJ.(kg^{-1} N_2) and a relative error lower than 1E^{-6} %. To find these specified values of enthalpies a 3D function finder is used. The input of this code is the 3D points (T, h_m, x) calculated for antisublimation and constant relative concentration lines. Subsequently $x = f(T, h_m)$ is found using Equation (19) where T is in Kelvin.

$$x = a + b.T + c.h_m + d.T^2 + f.h_m^2 + g.T^3 + h.h_m^3 + i.T.h_m + j.T^2.h_m + k.T.h_m^2 \tag{19}$$

$$a = 7.781E-02 \qquad b = -4.822\,E-03$$

$$c = 3.369\,E-03 \qquad d = 1.494\,E-05$$

$$f = 6.836\,E-08 \qquad g = -2.453\,E-08$$
$$h = -5.522\,E-13 \qquad i = -6.882\,E-06$$
$$j = 8.650\,E-09 \qquad k = -3.327\,E-10$$

For each specified h_m the CO_2 mass concentration ratio is calculated by varying the temperature from antisublimation temperature up to -78°C. The relative error given, using this correlation compared to input data, is less than 5 %.

3.3 Isochoric lines

To calculate the specific volume of the N_2 - CO_2 mixture, the mixture is assumed to be an ideal gas. The ideal gas constant of a gas mixture is obtained using Equation (28) (Sonntag and Borgnakke, 2003):

$$r_m = \frac{m_{CO_2}}{m_m}\frac{R}{M_{CO_2}} + \frac{m_{N_2}}{m_m}\frac{R}{M_{N_2}} \tag{28}$$

The total volume, V_m, of the mixture is calculated by Equation (29):

$$V_m = m_m \frac{T}{p_m} r_m \tag{29}$$

Thus:

$$V_m = m_m \frac{T}{p_m}.\left(\frac{m_{CO_2}}{m_m}\frac{R}{M_{CO_2}} + \frac{m_{N_2}}{m_m}\frac{R}{M_{N_2}}\right) \tag{30}$$

The specific volume of the gas mixture is obtained by dividing Equation (30) by the mass of nitrogen contained in the gas mixture:

$$v_m = \frac{RT}{p_m}\left(\frac{1}{M_{CO_2}}x + \frac{1}{M_{N_2}}\right) \tag{31}$$

Iterations are used to find antisublimation conditions (T, x) for which the specific volume of the gas mixture is equal to desired values. These conditions are found with an absolute error lower than 0.001 $m^3.(kg\ N_2)^{-1}$. The use of the ideal gas assumption is evaluated by comparing the specific volume calculated with Equation (30) to the specific volume calculated for real gas mixture using Refprop V9.0. Isochoric curves are plotted by calculating x_i fixing $(T_i, v_{m,j})$ and using Equation (31).

3.4 Antisublimation CO_2 capture process representation for coal-fired-boiler gas stream

The CO_2 – N_2 psychrometric chart is plotted in Figure (8) for a temperature range between -93 to -120°C and for a CO_2 mass concentration ratio varying from 0.00 to 0.40 kg (CO_2)/kg (N_2). Antisublimation line, isenthalpic lines, isochoric lines, and isobaric lines are plotted as a function of the absolute concentration and the temperature.

To represent the antisublimation CO_2 capture for coal-fired-boiler gas stream (Clodic et al., 2005), the CO_2 - N_2 psychrometric chart is used. At the inlet of the low-temperature heat exchanger, called CFX, the gas stream contains 22.05% w/w of CO_2 and 77.95% w/w of N_2. Subsequently the CO_2 mass concentration ratio x_{in} at the inlet is 0.283 at -94°C. For a 90% CO_2 capture, x_{out} at the outlet of the CFX is 0.023. The gas stream is superheated at the CFX inlet. It is cooled down to reach the saturation line at -99°C. No CO_2 is frosted at this stage. When the gas stream reaches the antisublimation line, it becomes saturated with CO_2 and then the CO_2 capture process begins. By cooling the gas stream throughout the CFX, the CO_2 antisublimates on the CFX fins reducing the CO_2 mass concentration ratio in the gas stream. The gas stream is assumed to be saturated in this stage.

The more the gas stream is cooled down, greater the amount of CO_2 captured and greater the decrease in the CO_2 mass concentration ratio in the gas stream. The temperature of the gas stream at the CFX outlet is fixed by the CO_2 capture rate. In this example, the CO_2 capture rate is 90%, thus the CO_2 absolute concentration x_{out} is 0.023 (kg CO_2).(kg^{-1} N_2) and the gas stream is saturated. Therefore the gas stream outlet temperature is deduced from the psychrometric chart and is -119.25°C. On the psychrometric chart, the gas stream specific volume, the entropy, the enthalpy, and the relative CO_2 concentration could be read for every state. To calculate the sensible heat required to cool the gas stream isenthalpic lines are used.

$$Q_{Sensible} = \dot{m}_{N_2} (h_{in} - h_{out}) \quad (32)$$

The latent heat cannot be calculated directly from the psychrometric chart because the CO_2 heat of sublimation depends on the temperature that varies during the CO_2 capture process. The CO_2 heat of sublimation is represented in Figure (9) as a function of the temperature (Azreg-Aïnou, 2005).

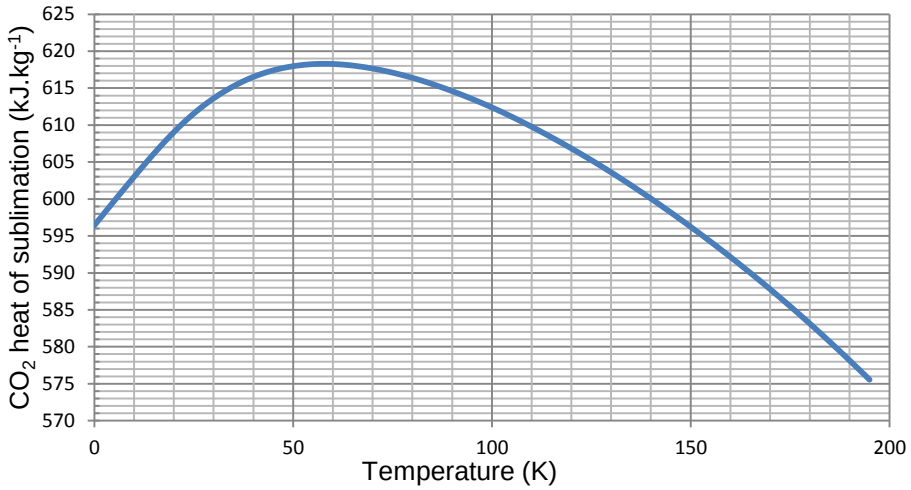

Figure 9: CO_2 heat of sublimation as a function of the temperature.

In order to decarbonize flue gases by CO_2 antisublimation, the cooling capacity is calculated using Equation (33):

$$Q_{Total} = Q_{Latent} + Q_{Sensible} = \dot{m}_{N_2}(x_{in} - x_{out}).\Delta L(T) + \dot{m}_{N_2} (h_{in} - h_{out}) \quad (33)$$

x_{in} and x_{out} are respectively the CO_2 mass concentrations ratio in the inlet and the outlet of flue gases. $\Delta L(T)$ is the CO_2 heat of sublimation at the temperature T. The total cooling capacity required to cool down flue gases and to frost the CO_2 is the sum of the latent heat and the sensible heat power. Thus, the CO_2 – N_2 psychrometric chart allows to calculate approximately the cooling capacity and the temperature required to decarbonize flue gases at given CO_2 concentrations.

4 Conclusion

The low-temperature CO_2 properties calculations found in the literature and calculated using Refprop V9.0 shows good agreements. Calculations of the cooling capacity for antisublimation CO_2 capture process using Refprop V9.0 has been demonstrated by the calculation of the sublimation pressure and the saturated vapor enthalpy and entropy below the triple point. For the solid state, enthalpy and entropy calculations by Equations (8) and (12) are used. In addition, a psychrometric chart is plotted to represent gas stream thermodynamic properties variations during CO_2 capture using the antisublimation process.

References

Kayukawa, Y., Fujii, K., 2010. Thermodynamic property evaluation of carbon dioxide. International Symposium on Next-generation Air Conditioning and Refrigeration Technology, Tokyo.

Clodic, D., El Hitti, R., Younes, M., Bill, A., Casier, F., 2005. CO_2 capture by anti-sublimation: thermo-economic process evaluation. The 4th Annual Conference on Carbon Capture & Sequestration, Alexandria, USA.

Reynolds, N.C., 1979. Thermodynamic properties in SI, graphs, tables and computational equations for 40 substances. The Department of Mechanical Engineering, Stanford University.

Azreg-Aïnou, M., 2005. Low-temperature data for carbon dioxide. Monatshefte für Chemie 136, 2017-2027.

Maass, O., Barnes, W. H., 1926. Some thermal constants of solid and liquid carbon dioxide. Proceedings of the Royal Society of London series A 111, 224-244.

Giauque, W.F., Egan, C.J., 1937. Carbon Dioxide, The Heat Capacity and Vapor pressure of the Solid, The Heat of Sublimation, Thermodynamic and Spectroscopic Values of the Entropy, J Chem. Phys. 5, 45-54.

Span, R., Wagner, W., 1996. A New Equation of State for Carbon Dioxide Covering the Fluid Region from the Triple-Point Temperature to 1100 K at Pressures up to 800 MPa. J. Phys. Chem. Ref. Data 25(6), 1509-1596.

ASHRAE, 2005. Psychrometrics, in: Handbook-Fundamentals. Atlanta: American Society of Heating, Refrigerating, and Air-Conditioning Engineers Inc., Atlanta.

Sonntag, R. E., Borgnakke, C., Fundamentals of Thermodynamics, sixth edition, Wiley, 2003.

Cook, T., Davey, G., 1976. The density and thermal conductivity of solid nitrogen and carbon dioxide. CRYOGENICS, June 1976, 363-369.

Shchelkunov, V. N., Rudenko, N. Z., Shostak, Yu. V., Dolganin, V. I., 1985. Surface desublimation of carbon dioxide from binary gas mixtures. Translated from Inzhenerno-Fizicheskii Zhurnal, Vol. 51, No. 6, 965-970.

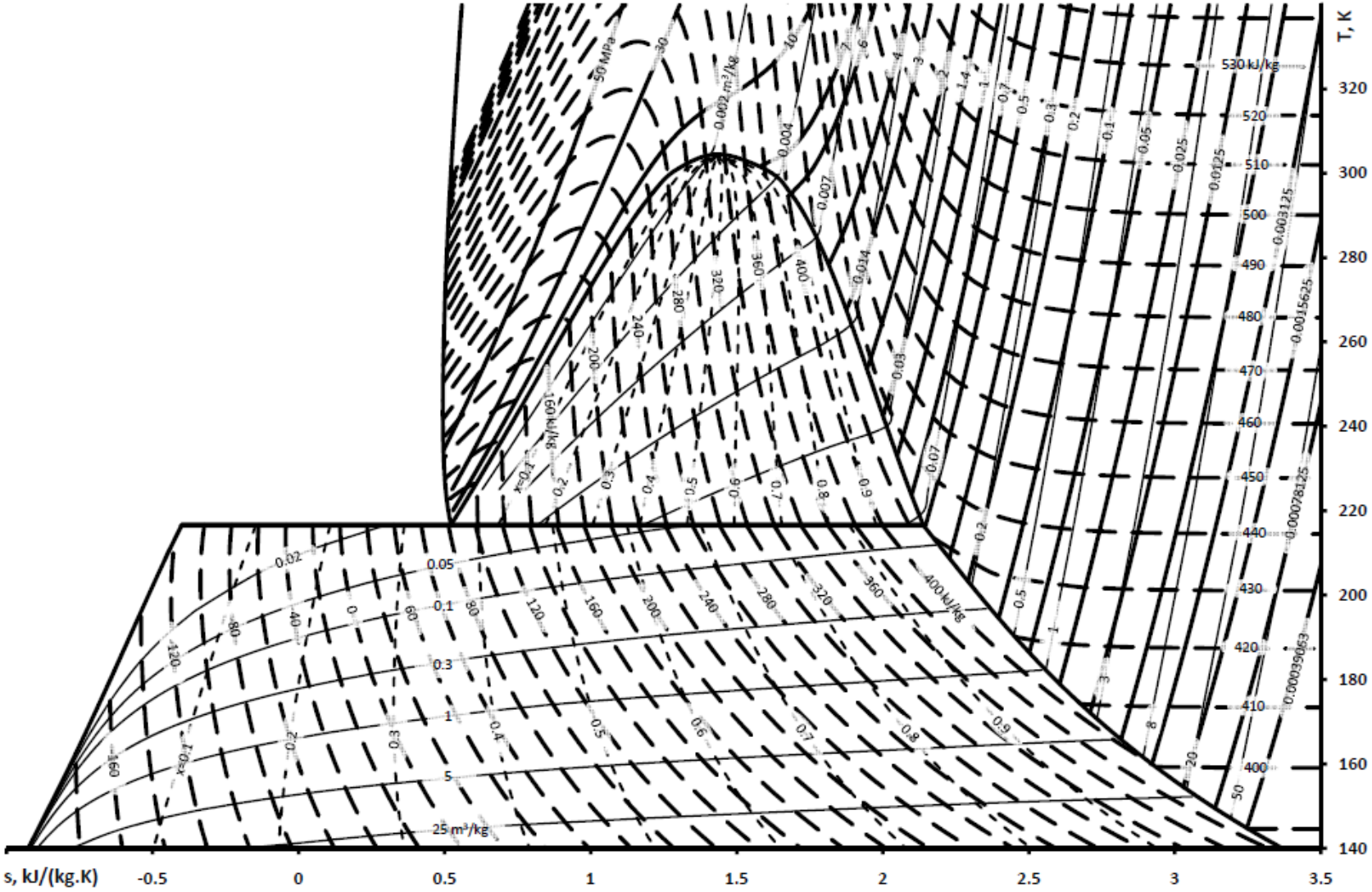

Figure 7: Carbon dioxide T - s diagram.

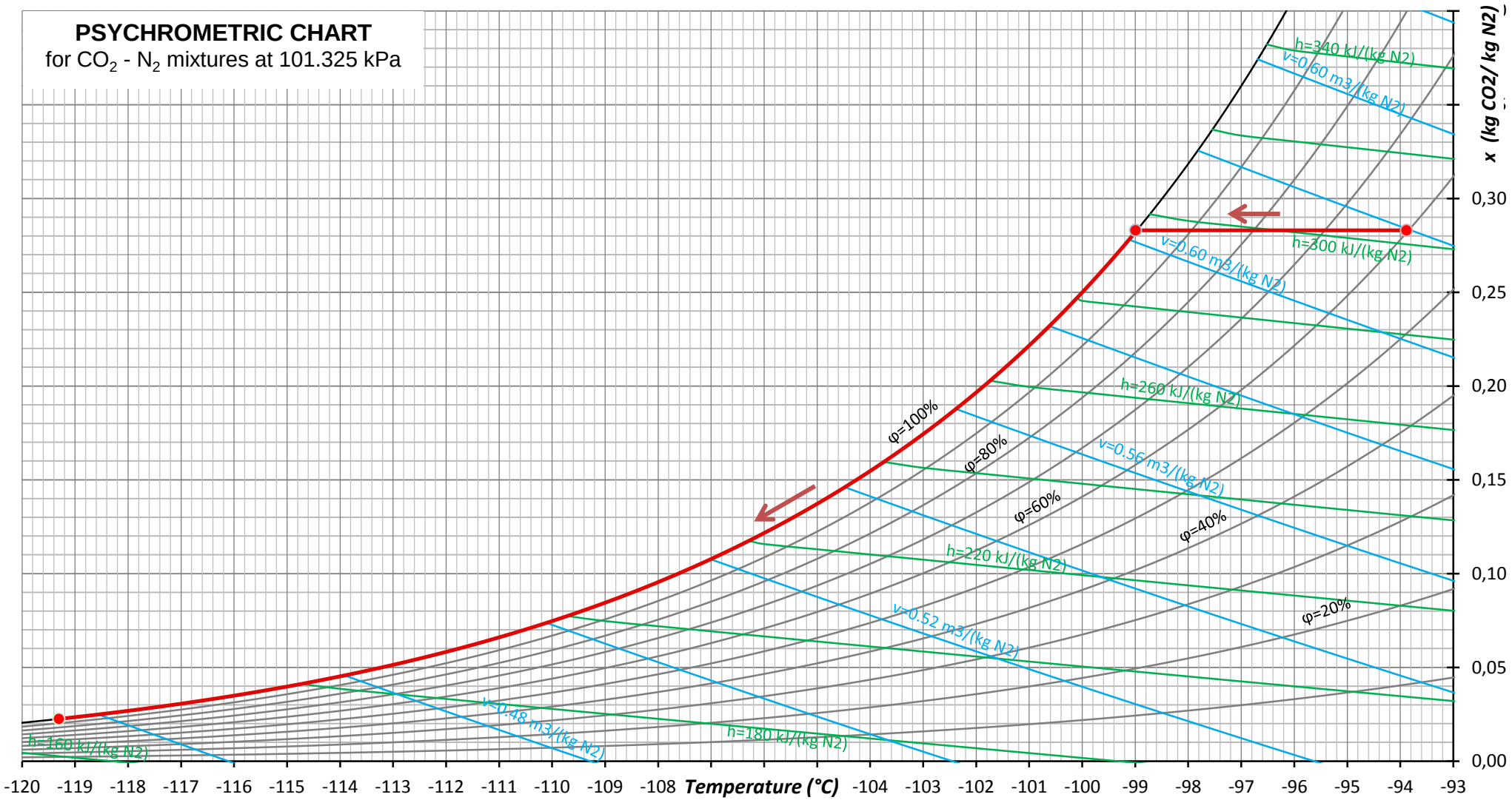

Figure 8: Antisublimation CO2 capture process representation for coal fired boilers gas stream on the CO_2 - N_2 psychrometric chart.

1.7 Solid CO_2 thermal conductivity

In their study, “Low-temperature thermal conductivity of solid carbon dioxide”, Sumarokov et al. [SUMA03] present thermal conductivity measurements of solid pure carbon dioxide in the temperature range of 1.5 to 35 K. A CO_2 crystal is prepared in a liquid helium experimental setup using vapor CO_2 with 99.999% of chemical purity. A thermal treatment is performed on the CO_2 crystal in order to avoid visible defects or voids in the tested specimen. The temperature and the temperature gradient in the specimen are measured at two locations. Steady state flow method is used to measure the solid CO_2 thermal conductivity with an error less than 10%.

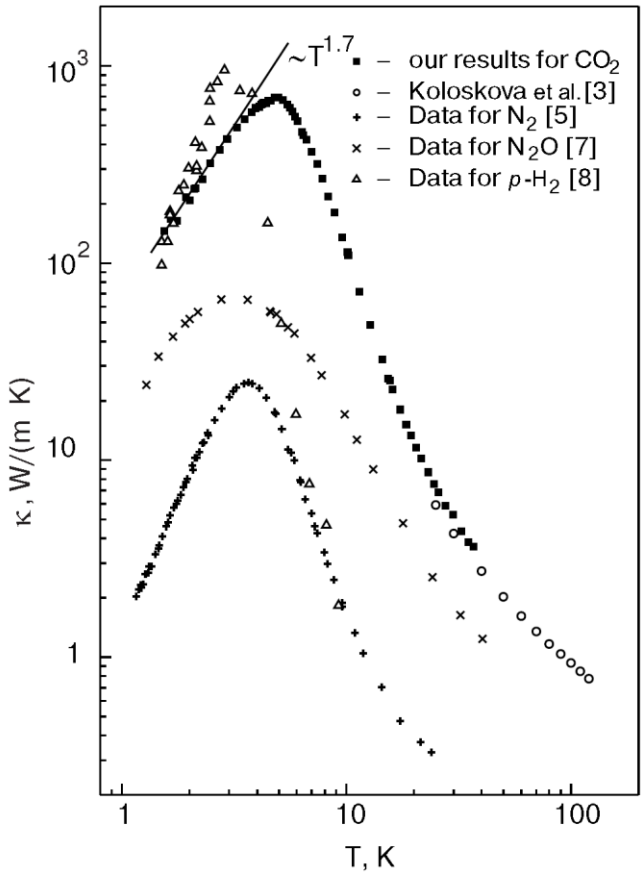

Figure 1.18: Solid CO_2 thermal conductivity as function of the temperature [SUMA03]

Measurement results are represented in figure 1.18 as function of the temperature. In addition to their measurements, Sumarokov et al. have plotted CO_2 thermal conductivity for temperatures up to 100 K using measurements performed earlier by Koloskova. For low temperatures, CO_2 thermal conductivity increases to reach its maximum of 720 $W.m^{-1}.K^{-1}$ at 5 K. For temperatures above 5 K, the thermal conductivity decreases quickly. To obtain solid CO_2 thermal conductivities at higher temperatures going between 150 and 170 K, the curve of figure 1.27 is extrapolated.

1.8 Conclusions

In this chapter the severity of CO_2 emissions from energy production and industry is presented. Carbon dioxide is the main greenhouse gas emitted all over the world and it accounted for 76.7% of anthropogenic greenhouse-gas emissions in 2004 [IPCC05].

The CO_2 antisublimation capture process, developed by the Center for Energy and Processes (CEP) of MINES ParisTech is exposed. In order to improve the process performance, heat exchanger optimization is chosen. Heat exchanger analysis is

represented showing the optimization importance of the heat exchanger arrangement and of the refrigerant blend gliding temperature during its evaporation. In addition, the effect of the CFX optimization on the whole capture process is demonstrated.

In order to calculate the total CO_2 capture-process efficiency, the minimum theoretical work consumed by separating an amount of CO_2 from the gas stream mixture is calculated. This work is calculated for perfect and imperfect CO_2 separation.

The low temperature CO_2 properties calculations found in the literature and calculated using Refprop V9.0 shows high matching level. In following calculations of the cooling capacity consumption for anti-sublimation CO_2 capture process Refprop V9.0 will be used to calculate the sublimation pressure and the saturated vapor enthalpy and entropy below the triple point. For the solid state enthalpy and entropy empiric equations are developed. The CO_2 T-s diagram is plotted down to 140 K. In addition CO_2 – N_2 psychrometric chart is plotted to represent gas stream thermodynamic properties variation during CO_2 capture using antisublimation process.

References

[IPCC05] **Intergovernmental Panel on Climate Change**, Carbon dioxide capture and storage, 2005.

[IFP10] **IFP**, Le captage du CO_2, des technologies pour réduire les émissions de gaz à effet de serre, 2010.

[CCC10] **Service de l'observation et des statistiques**, Chiffres clés du climat France et monde, 2010.

[RAU07] **Michael R. Raupach, Gregg Marland, Philippe Ciais, Corinne Le Quéré, Josep G. Canadell, Gernot Klepper, Christopher B. Field**, Global and regional drivers of accelerating CO_2 emissions, 2007.

[QUER09] **Corinne Le Quéré, Michael R. Raupach, Josep G. Canadell, Gregg Marland et al.***,* Trends in the sources and sinks of carbon dioxide, 2009.

[PWC06] **Price Water House Cooper**, Les émissions de CO_2 des 23 principaux électriciens européens qui représentent 20% des émissions de CO_2 en Europe n'ont toujours pas baissé en 2005, 2006.

[RTE07] **RTE**, Le contenu en CO_2 du kWh électrique : Avantages comparés du contenu marginal et du contenu par usages sur la base de l'historique, 2007.

[EDF10] EDF, L'énergie thermique à flamme : un atout essentiel dans le parc de production d'EDF pour répondre en temps réel aux pointes de consommation d'électricité, 2010.

[ADE05] **ADEME**, Note de cadrage sur le contenu CO_2 du kWh par usage en France, 2005.

[CLO01] **D. Clodic, M. Younes**, Procéde et système d'extraction du dioxyde carbone par antisublimation en vue de son stockage – Brevet WO 02/060561

[CLO05] **D. Clodic et al.**, CO_2 capture by antisublimation thermo-economic process evaluation, 2005.

[CLODIC2] **D. Clodic et al.**, Test results of CO_2 capture by antisublimation capture efficiency and energy consumption for boiler plants.

[HER09] **Howard Herzog, Jerry Meldon, Alan Hatton**, Advanced Post-Combustion CO_2 Capture, 2009.

[BAXTER] **Larry Baxter, Andrew Baxter, and Stephanie Burt**, Cryogenic CO_2 Capture as a Cost-Effective CO_2 Capture Process.

[BURT] **Stephanie Burt, Andrew Baxter, Larry Baxter**, Cryogenic CO_2 Capture to Control Climate Change Emissions.

[TUIN10] **M. J. Tuinier, M.van Sint Annaland, G. J. Kramer, J. A. M. Kuipers**, Cryogenic CO_2 capture using dynamically operated packed beds, Chemical Engineering Science, 65, p. 114 – 119, 2010.

[CLO06]] **D. Clodic, M. Younes**, Method of extracting carbon dioxide by means of Anti-sublimation for the storage thereof, Patent Application Publication, US 2006 / 0277942 A1, 2006.

[SPAN96] **Roland Span, Wolfgang Wagner**, A New Equation of State for Carbon Dioxide Covering the Fluid Region from the Triple-Point Temperature to 1100 K at Pressures up to 800 MPa, J. Phys. Chem. Ref. Data, 25(6):1509-1596, 1996.

[GIA37] **Giauque WF, Egan CJ**, Carbon Dioxide, The Heat Capacity and Vapor pressure of the Solid, The Heat of Sublimation, Thermodynamic and Spectroscopic Values of the Entropy, J Chem. Phys., 5, 45-54, 1937.

[AZR05] **Mustapha Azreg-Aïnou**, Low-temperature data for carbon dioxide, Monatshefte für Chemie 136, 2005.

[MAA26] **O Maass, W. H. Barnes**, Some thermal constants of solid and liquid carbon dioxide, Proceedings of the Royal Society of London, series A 111, 224-244, 1926.

[YOH10] **Yohei Kayukawa, Kenichi Fujii**, Thermodynamic property evaluation of carbon dioxide, International Symposium on Next-generation Air Conditioning and Refrigeration Technology, Tokyo, 2010.

[REY79] **N.C. Reynolds**, Thermodynamic properties in SI, graphs, tables and computational equations for 40 substances, published by the Department of Mechanical Engineering, Stanford University, 1979.

[SON03] **R. E. Sonntag, C. Borgnakke**, Fundamentals of Thermodynamics, sixth edition, Wiley, 2003.

[SUMA03] **V.V. Sumarokov, P. Stachowiak, A. Jeżowski**,Low-temperature thermal conductivity of solid carbon dioxide, FIzika Nizkikh Temperatur, v.29, No. 5, p. 603-605, 2003.

[COO76] **T. Cook, G. Davey**, The density and thermal conductivity of solid nitrogen and carbon dioxide, CRYOGENICS, 1976.

[SHC85] **V. N. Shchelkunov, N. Z. Rudenko, Yu. V. Shostak, V. I. Dolganin**, Surface desublimation of carbon dioxide from binary gas mixtures, translated from Inzhenerno-Fizicheskii Zhurnal, Vol. 51, No. 6, pp. 965-970, December, 1986. Original article submitted September 10, 1985.

[KIM07] **Youngil Kim**, Equation of State for Carbon Dioxide, Journal of Mechanical Science and Technology 21, p. 799-804, 2007.

[ZIE99] **W. Zielenkiewicz, G. L. Perlovich, M. Wszelaka-Rylik**, the Vapor Pressure and the Enthalpy of Sublimation Determination by Inert Gas Flow Method, Journal of Thermal Analysis and Calorimetry, Vol. 57, p. 225-234, 1999.

[TRI03] **Terry M. Tritt**, Thermal Conductivity Theory, Properties, and Applications, Kluwer Academic / Plenum Publishers, New York, 2004.

[SEA05] **J. D. Seader, Ernest J. Henley**, Separation Process Principles, 2nd edition, Wiley, 2005.

[SAT95]] **Klaus Sattler, Hans Jacob Feindt**, Thermal Separation Processes, VCH, 1995.

[TSI04] **A. M. Tsirlin, I. V. Titova**, Estimating the Minimum Work of Separation of an Ideal Mixture in Processes with a specified Output, Theoretical Foundations of Chemical Engineering, Vol. 38, No. 5, p. 490–498, 2004.

[DEM04] **Y. Demirel**, Thermodynamic Analysis of Separation Systems, Papers in Thermal Mechanics, 2004.

[DUD09] **Ryan James Dudgeon**, An exergy-based analysis of gasification and oxyburn processes, thesis, University of Iowa, 2009.

[AME03] **S. A. Amelkin, A. M. Tsirlin, J. M. Burzler, S. Schubert, K. H. Hoffmann**, Minimal Work for Processes of Binary Mixtures, Kluwer Academic Publishers, 2003.

[BOL06] **Olav Bolland**, Fundamental Thermodynamic Approach for Analyzing Gas Separation Energy Requirement for CO_2 Capture Processes, GHGT-8, 2006.

[BEN08] **Riad Benelmir, André Lallemand, Michel Feidt**, Analyse exergétique, Technique de l'Ingénieur BE 8 015, 2008.

[LAL08] **André Lallemand**, Thermodynamique appliquée - Bilans entropiques et exergétiques, Technique de l'Ingénieur BE 8 008, 2008.

[SHU02] **Masanori Shukuya, Abdelaziz Hammache**, Introduction to the Concept of Exergy - for a Better Understanding of Low-Temperature-Heating and High-Temperature-Cooling Systems, VTT, 2002

Chapter 2. Antisublimation Theory

2.1 Introduction

In order to minimize energy consumption of the Ansu process, the phenomenon of CO_2 antisublimation on the heat-exchanger fins has to be understood. The literature survey conducted shows that the research carried out on CO_2 frosting is limited and few data are available. An analogy with other substances is useful. The most well-known is water vapor antisublimation, where the chilled surface temperature is lower than the water vapor triple point, and several studies have been carried out on this subject. Studies that address water vapor antisublimation over fin-and-tube heat exchangers or flat plates are targeted. The goal is to identify the parameters that may affect CO_2 anti-sublimation on the fin-and-tube heat exchangers. Note that only studies taking into account the water vapor frosting at temperatures below the triple point are considered.

Antisublimation, desublimation, and precipitation are used to describe the same phenomena. It is the direct solidification of a compound from its gas phase by cooling down the gas mixture. Antisublimation occurs if both cooling surface temperature and solidified compound saturation temperature are lower than the solute triple point temperature. In the case of antisublimation CO_2 capture, flue gases are considered as the gas solution where the CO_2 is the solute dissolved in the solvent. The solvent is a gas mixture (nitrogen, oxygen, and argon) which does not precipitate at the same solute saturation temperature range (cf. Table 1.3). According to the literature, the condensation and antisublimation of water vapor have been mathematically modeled using the classical nucleation theory (CNT) in order to define the water frost deposition rate on the evaporators ([NA03A], [ROB08], [PIU08]). The CO_2 antisublimation involves a nucleation formation and growth process where the CO_2 molecules form a solid lattice. According to Mullin [MUL01], the formation in the solution of minuscule solid bodies named embryos act as centers of crystallization. Modern nucleation theories, such as self-consistent theory (SCT) [KJOH97] and Dillmann-Meier theory [FORD93], have also been developed due to improved accuracy of experimental results. In this study, the CNT will be adopted since it has proved a good accuracy with experimental results according to the experimental and modeling investigations performed on the water vapor frosting on flat-plate heat exchangers. In this chapter, the kinetic and thermodynamic classical nucleation theories are elaborated in order to understand the antisublimation phenomena, to identify parameters that affect the nucleation rate and frost morphology, and to mathematically model the CO_2 antisublimation in the context of our study.

2.2 Nucleation

Nucleation is the formation of a new phase from the initial phase named parent phase. A solute changes its phase forming a new phase dispersed in the volume of the mixture. According to Mullin [MUL01], the nucleation is divided into two categories: the primary and the secondary nucleations. The primary nucleation is used when no solute crystals are present in the mixture. Primary nucleation is divided into two types: homogeneous and heterogeneous nucleations. Homogeneous nucleation occurs when the nuclei forms into the solution or the gas mixture without any contact with the cooling surface or foreign particles like impurities that could be present in the system.

Heterogeneous nucleation takes place when the nuclei or the crystal forms on a substrate that could be a foreign particle or the crystallizer surface like the cooling surface in the frosting systems. Heterogeneous and homogeneous nucleations are represented in Figure 2.1 showing the contact angle between the crystal and the substrate. For a contact angle of 180°, the nucleation is considered as homogeneous.

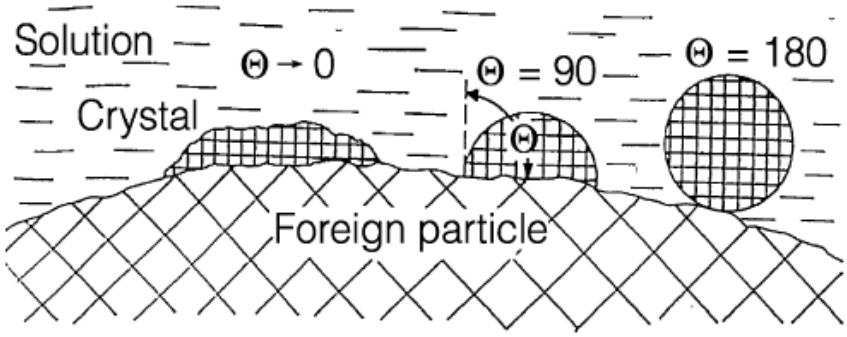

Figure 2.1: Heterogeneous and homogeneous nucleations as represented by Mersmann et al. [MERS02].

The secondary nucleation occurs when the solute crystals are already present in the solution. For this type of nucleation, a lower supersaturation degree is needed to initiate crystallization (cf. Paragraph 2.2.1). Even a supersaturated solution located in the metastable zone (Figure 2.3) crystallizes with the presence or by the deliberate addition of crystals. Several types of secondary nucleation are cited in the literature. According to Gyulai [MUL01], the secondary nucleation is induced by the motion of the solution that could strip off part of the crystal surface to form new nuclei. This phenomena is demonstrated by Powers who shown that the movement of a sucrose crystal in a supersaturated solution increases the nuclei formation. Secondary nucleation could also occur by contact nucleation where crystal-crystal collisions induce the formation of a new stable crystal. In addition, secondary nucleation can be induced by seeding a supersaturated solution by small particles of the solute to be crystallized. Figure 2.2 summarizes the different categories and types of nucleation as described in the literature.

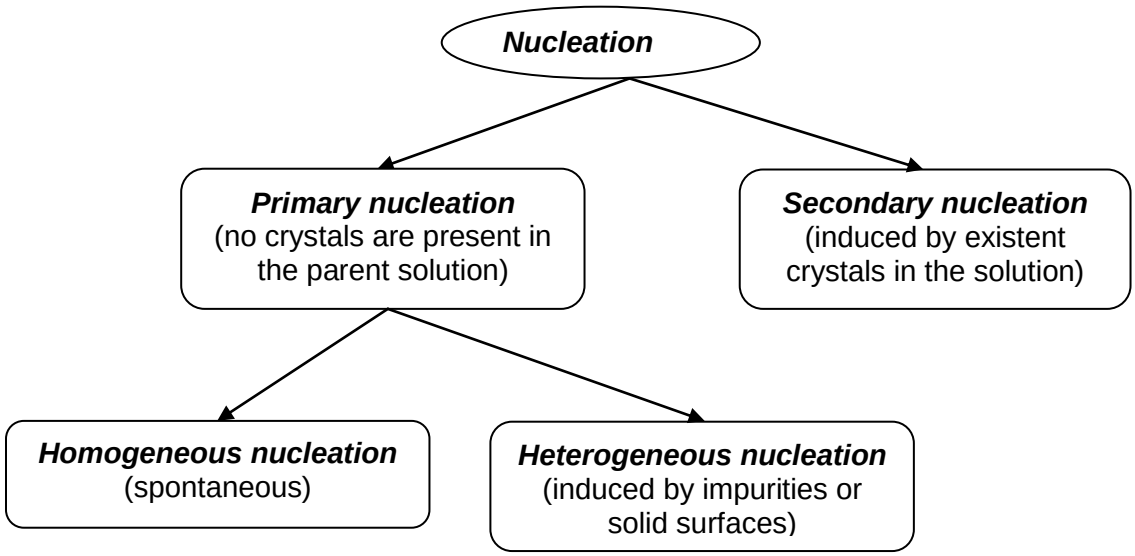

Figure 2.2: The different nucleation categories.

The notion of induction period is the time between the achievement of the solution supersaturation and the formation of the first detectable crystal in the system. The CNT of homogeneous and heterogeneous crystallization does not take into account the induction period, assuming an immediate nucleation once the solution is sufficiently supersaturated. The induction period is divided into three sub-periods [MUL01]:

$$t_{ind} = t_r + t_n + t_g \tag{2.1}$$

t_r is the relaxation time, which is the period required to achieve a quasi-steady-state distribution of molecular clusters. It depends on the solution viscosity and molecular

diffusivity, and it is evaluated by Nielsen to be equal to $10^{-17}D^{-1}$ where D is the diffusivity ($m^2.s^{-1}$). t_n is the time of formation of a stable nucleus, and t_g is the time of nucleus growth until it reaches a measurable dimension. In this study, the induction period is not taken into account since it is negligible regarding the CO_2 frosting cycle, which could exceed 10 minutes.

2.2.1 Supersaturation

The crystallization of a solute occurs when it is present in the solution at supersaturation conditions. The supercooling is the difference between the cooling surface temperature and the saturation temperature of the solute in the given mixture. Supersaturation can be reached by cooling down the solution to a temperature lower than the saturation temperature of the solute or by increasing, at constant temperature, the solute concentration in the mixture exceeding the saturation point. This process is applied by evaporating or separating a solvent compound in order to increase the solute concentration in the remaining mixture. In the case of CO_2 capture, flue gases are super-cooled reaching the super-saturation degree, named also driving potential, able to change CO_2 vapor straightforwardly into a solid deposit. The CO_2 vapor phase is named "parent phase" and the solid crystals are named "new phase".

The supersaturation is commonly expressed as a concentration driving force, Δx, a supersaturation ratio S, a relative supersaturation $S_{\%}$, or a supercooling driving potential ΔT_{sup}.

$$\Delta x = x - x_{sub} \tag{2.2}$$

$$S = \frac{x}{x_{sub}} = \frac{P}{P_{sub}} \tag{2.3}$$

$$S_{\%} = \frac{P - P_{sub}}{P_{sub}} = \frac{\Delta x}{x_{sub}} \tag{2.4}$$

$$\Delta T_{sup} = T - T_{sub} \tag{2.5}$$

Where x is the solute molar concentration and x_{sub} is the sublimation concentration at the given temperature. P is the solute partial pressure and P_{sub} is the sublimation partial pressure at the given temperature. T is the mixture temperature and T_{sub} is the solute sublimation temperature at concentration x (cf. Figure 2.3).

The supersaturation degree is an important parameter to take into account when modeling the nucleation process. Assuming that nucleation occurs when the solute is saturated in the mixture, for a given frost surface temperature, induces the overestimation of the mass transfer rate from the humid air to the frost deposit. For example, modeling water vapor frosting in a flat plate at saturation conditions leads to overestimate the frost formation by 20% compared to experimental results [NA03A].

In Figure 2.3 is represented the super-cooling process for CO_2 frosting. The CO_2 sublimation line is plotted as a function of the temperature for a total mixture pressure of 101.325 kPa. The superheated CO_2 (SH) is cooled down at a constant concentration until it reaches the sublimation conditions (SU). An additional cooling down (SU → SC) is required in order to overcome the Gibbs energy barrier, a result of the free surface energy, and to initiate the nucleation phenomena (cf. Paragraph 2.2.2.1). Therefore at sufficient supersaturation degree, when the nucleation line is exceeded, latent heat transfer frosts down the excess of CO_2 present in the mixture. The new equilibrium is reached at a lower CO_2 concentration and for which the mixture is always supersaturated. The new gas mixture has a variable CO_2 concentration ranging between the nucleation and the sublimation lines called metastable state. This resulting supersaturation degree is insufficient to frost down the excess CO_2 and to reach the saturation conditions (cf. Paragraph 2.2.2.1). In the metastable

zone new crystals can form and evaporate since the supersaturation conditions are not able to form stable nuclei.

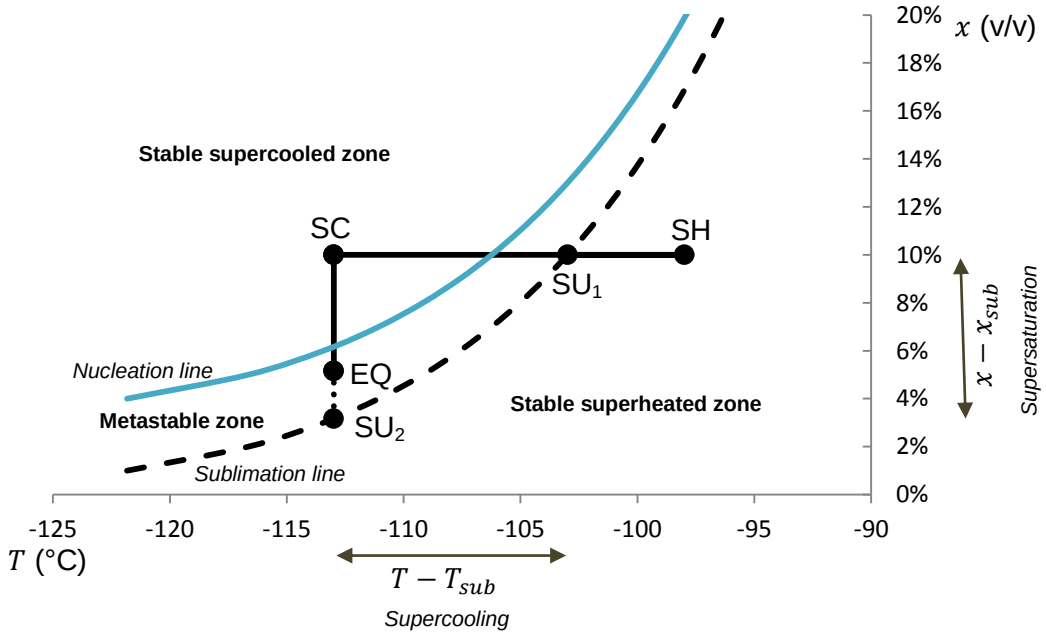

Figure 2.3: Supersaturation representation for carbon dioxide near its sublimation line.

2.2.2 Homogeneous nucleation

During the primary homogeneous nucleation, several nucleuses are able to form in the solution. Since the solute pressure at the surface of these droplets is high, they are not stable and they dissolve, except for the presence of high-local super-saturation at the nuclide that causes stability. The stable nucleus formation requires the collision of a sufficient number of molecule clusters able to form crystal. This stable crystal is called critical crystal, which has a dimension called critical dimension. The addition of new molecule clusters to the critical embryo leads to the growth of this embryo.

$$A + A \rightleftharpoons A_2$$
$$A_2 + A \rightleftharpoons A_3$$
$$\vdots$$
$$A_i + A \rightleftharpoons A_c \text{ Critical nucleus formation}$$
$$A_c + A \rightleftharpoons A_{c+1} \text{ stable nucleus growth}$$

2.2.2.1 Thermodynamic aspects

The CNT is based on Gibbs work who studied the water vapor droplet condensation. This theory is generalized in order to be applied to all crystallization processes (vapor-liquid, vapor-solid, and liquid-solid). At constant temperature and pressure, the Gibbs energy, named also free energy, required to form an embryos is given by Equation (2.6):

$$\Delta G = \Delta G_S + \Delta G_V \tag{2.6}$$

The total free energy, ΔG, transferred between a solid particle and its solute in the solution is the sum of the surface free energy ΔG_S and the volume free energy ΔG_V. ΔG_S is the excess free energy between the surface of the crystal and the solution. It is a positive quantity proportional to the external surface of the particle. ΔG_V is the free energy between a large particle and its solute in the solution. This quantity is negative for a supersaturated solution

and is proportional to the volume of the particle. For a spherical and cubic nucleus, the excess free energy ΔG (J) is given respectively in equations (2.7) and (2.8).

$$\Delta G = 4\pi r^2 \sigma + \frac{4}{3}\pi r^3 \Delta G_v \tag{2.7}$$

$$\Delta G = 6a^2 \sigma + a^3 \Delta G_v \tag{2.8}$$

Where r is the crystal radius (m), a is the dimension of a cubic crystal (m), σ is the interfacial tension, or surface energy, between the new formed nucleus and the supersaturated solution (N.m^{-1}), and ΔG_v is the free energy change of the transformation per unit volume (J.m^{-3}).

$$\Delta G_v = -\frac{k_B T \ln S}{v} \tag{2.9}$$

$k_B = R/N_A = 1.3805 \,.\, 10^{-23}$ J.K^{-1}, Boltzmann constant

Where $R = 8.314$ (J.K^{-1}.mol^{-1}) is the ideal gas constant, $N_A = 6.023 \,.\, 10^{23}$ (mol^{-1}) is the Avogadro number, S is the supersaturation ratio (Equation (2.3)), T is the temperature (K), and v is the molecular volume (m^3). For supersaturated solutions, for which S is greater than one, ΔG_v is negative.

As ΔG_S is positive and ΔG_V is negative, ΔG reaches a maximum, ΔG_{crit}, for the solid particle dimension radius r_c or a_c as represented in Figure 2.4.

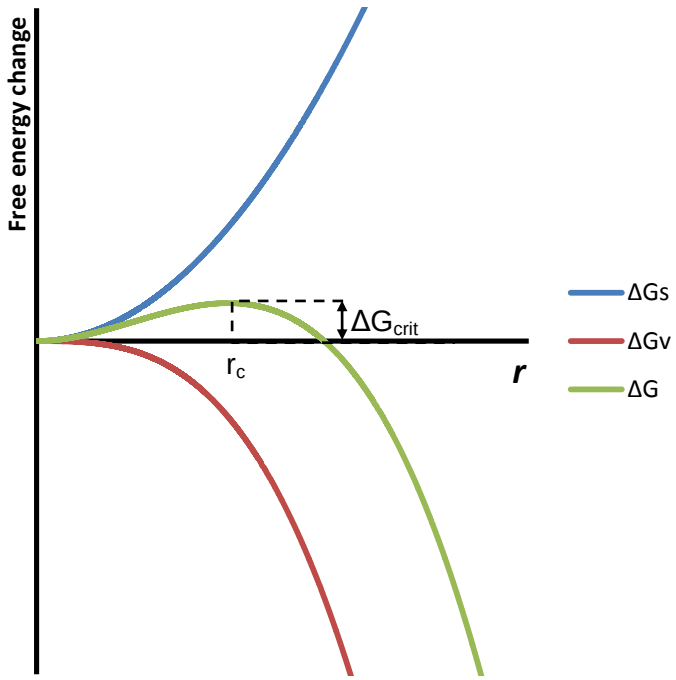

Figure 2.4: Free energy variation as a function of the nucleus radius.

r_c and a_c are the minimum dimensions of a stable nucleus. Indeed, during the phase change from the vapor phase to the solid phase, creating a crystal means a gain in surface energy by the crystal and a loss in volumetric energy as the temperature of these molecules decreases. According to the Gibbs free energy change, a new born nuclei smaller than the critical nuclei is able to re-evaporate whereas another one bigger than the critical nuclei is stable and grows by reducing its free energy. Figure 2.5 summarizes this theory.

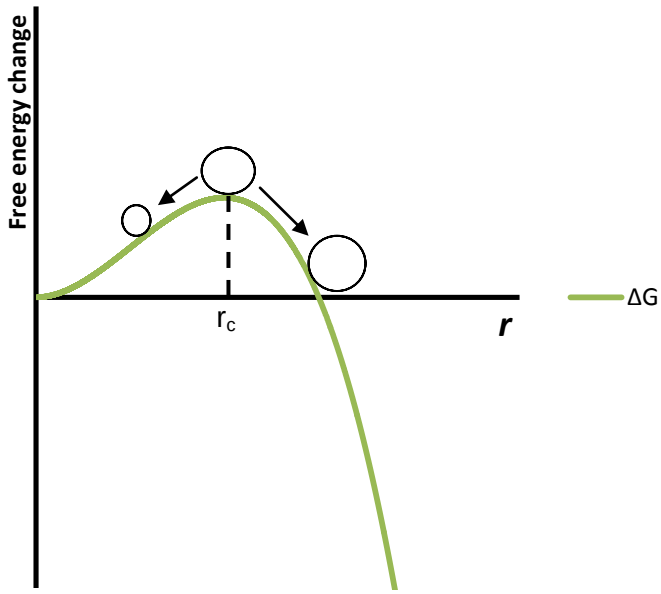

Figure 2.5: Nucleus size variation as a function of the overall excess free energy [SCH05].

In order to calculate the critical nuclei size, equations (2.7) and (2.8) are maximized calculating the critical free energy for each case. The minimum size of the particle formed, on which depends the free energy, is essential for its stability.

$$\frac{d\Delta G}{dr} = 8\pi r\sigma + 4\pi r^2 \Delta G_v = 0$$

Spherical nuclei:

$$r_c = \frac{-2\sigma}{\Delta G_v} \qquad (2.10)$$

$$\Delta G_{crit} = \frac{4}{3}\pi\sigma r_c^2$$

$$\frac{d\Delta G}{da} = 12a\sigma + 3a^2 \Delta G_v = 0$$

Cubic nuclei:

$$a_c = \frac{-4\sigma}{\Delta G_v} \qquad (2.11)$$

$$\Delta G_{crit} = 4\sigma a_c^2$$

Using the Gibbs-Thomson relationship, the supersaturation is expressed as a function of the surface tension, of the temperature, of the molecular volume, and of the nucleus size for spherical and cubic crystals:

$$\ln S = \frac{2\sigma v}{k_B T r} \qquad (2.12)$$

$$\ln S = \frac{4\sigma v}{k_B T a} \qquad (2.13)$$

Then:

$$-\Delta G_v = \frac{2\sigma}{r_c} = \frac{k_B T \ln S}{v} \qquad (2.14)$$

And:

$$-\Delta G_v = \frac{4\sigma}{a_c} = \frac{k_B T ln\, S}{v} \quad (2.15)$$

Thus, the crystal critical size and free energy can be calculated using equations (2.10) and (2.11):

Spherical nuclei:

$$r_c = \frac{2\sigma v}{k_B T ln\, S} \quad (2.16)$$

$$\Delta G_{crit} = \frac{16\pi\sigma^3 v^2}{3(k_B T ln\, S)^2}$$

Cubic nuclei:

$$a_c = \frac{4\sigma v}{k_B T ln\, S} \quad (2.17)$$

$$\Delta G_{crit} = \frac{32\sigma^3 v^2}{(k_B T ln\, S)^2}$$

These equations show that for constant pressure and temperature, the critical size and the critical free energy decrease by increasing the solution supersaturation. It is obvious that for higher supersaturation ratios, the critical free energy decreases allowing the spontaneous or homogeneous nucleation.

As well, the size of the critical nucleus depends on the solution temperature. Equation (2.16) shows that the critical radius is proportional to T^{-1} and then the critical free energy is proportional to T^{-2}. The effect of the temperature is represented in Figure 2.6 by plotting the excess free energy as a function of the nucleus radius for two different temperatures $T_1 < T_2$. For lower temperature, the crystal critical size and the critical free energy change able to produce stable solid clusters decrease.

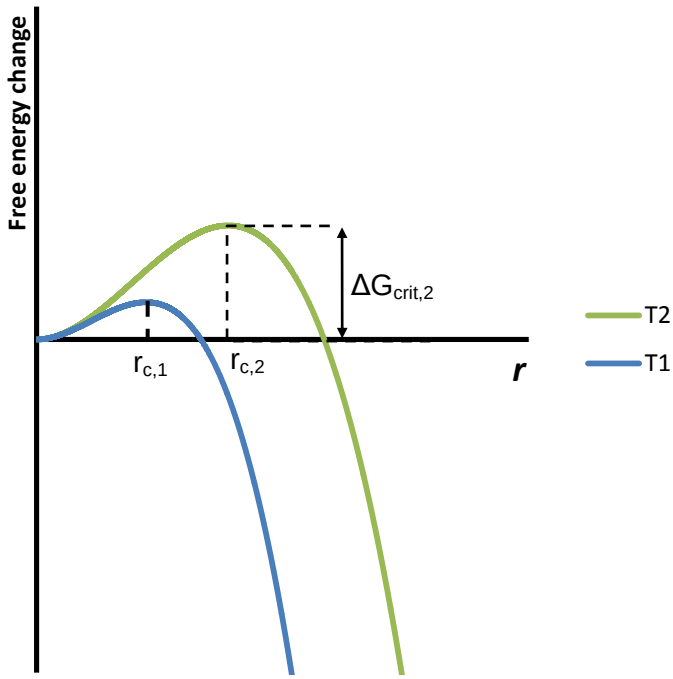

Figure 2.6: Free energy variation for different temperatures $T_1 < T_2$.

Classical homogeneous nucleation theory can also be expressed as a function of the supercooling driving potential ΔT_{sup} (Equation (2.5)). The volume free energy ΔG_v is expressed as a function of the latent heat of sublimation ΔH_{sub}, the sublimation temperature

T_{sub}, and the supercooling. The critical radius is then calculated as a function of the supercooling. Equation (2.19) gives the critical radius for a spherical nucleus.

$$\Delta G_v = \frac{\Delta H_{sub} \Delta T_{sup}}{T_{sub}} \tag{2.18}$$

$$r_c = \frac{2\sigma T_{sub}}{\Delta H_{sub} \Delta T_{sup}} \tag{2.19}$$

2.2.2.2 Kinetic aspects

In order to calculate the solute mass transfer from the parent phase to the new phase, the nucleation rate I must be defined. It is the number of nuclei formed per unit volume during a unit of time. According to the classical nucleation theory, the nucleation rate is defined using the Arrhenius reaction velocity equation.

$$I = n_c \exp\left[-\frac{\Delta G_{crit}}{k_B T}\right] \tag{2.20}$$

Where n_c is the maximum nucleation coefficient (# of nucleus.m^{-3}.s^{-1}).

The nucleation rates are given in equations (2.21) and (2.22) respectively for spherical and cubic crystal formation.

$$I = n_c \exp\left[-\frac{16\pi\sigma^3 v^2}{3{k_B}^3 T^3 (\ln S)^2}\right] \tag{2.21}$$

$$I = n_c \exp\left[-\frac{32\sigma^3 v^2}{{k_B}^3 T^3 (\ln S)^2}\right] \tag{2.22}$$

These two equations show that the nucleation rate depends mainly on the supersaturation degree and on the temperature. The effect of the temperature and of the supersaturation ratio on the homogeneous nucleation rate and on the crystal critical radius is studied in Paragraph 2.4 using a sensitivity analysis.

2.2.3 Heterogeneous nucleation

Heterogeneous nucleation takes place in nucleation systems where foreign solid surfaces are present. The solid surface has not to be constituted from the crystallizing solute unless the nucleation will be considered as secondary nucleation and not primary heterogeneous nucleation. Foreign solid surfaces could be impurities that are always present in industrial processes and their size goes from 0.005 µm up to 10 µm. As well, in some applications, foreign solid surfaces could be present in the system by using suitable catalyst particles called “sympathetic surfaces” that induce nucleation at supersaturation degrees, lower than those required for primary homogeneous nucleation. In antisublimation CO_2 capture, the heat-exchanger surfaces act as foreign substrates where heterogeneous CO_2 crystallization takes place.

2.2.3.1 Thermodynamic aspects

The heterogeneous nucleation is represented in Figure 2.7 using the Fletcher’s model. The example of solid nucleation from a vapor stream mixture is taken into account representing the process of CO_2 frosting. In the first case (*a*), a complete non-affinity exists between the solid nuclei and the foreign surface. This case corresponds to a contact angle equal to 180°. σ_{vs} is the interfacial energy determining the interfacial behavior of the solid embryo against its parent phase. It determines the solid droplet size and the amount of energy required to produce the solid-vapor interface. The new solid crystallized phase is referred to by the subscript s, the parent vapor phase by v, and the flat plate surface by p. Complete affinity,

for which the contact angle is equal to 0°, occurs when the supersaturation solution is seeded with the solute crystals. In this case no new embryos have to be formed and the secondary crystallization takes place by seed growth.

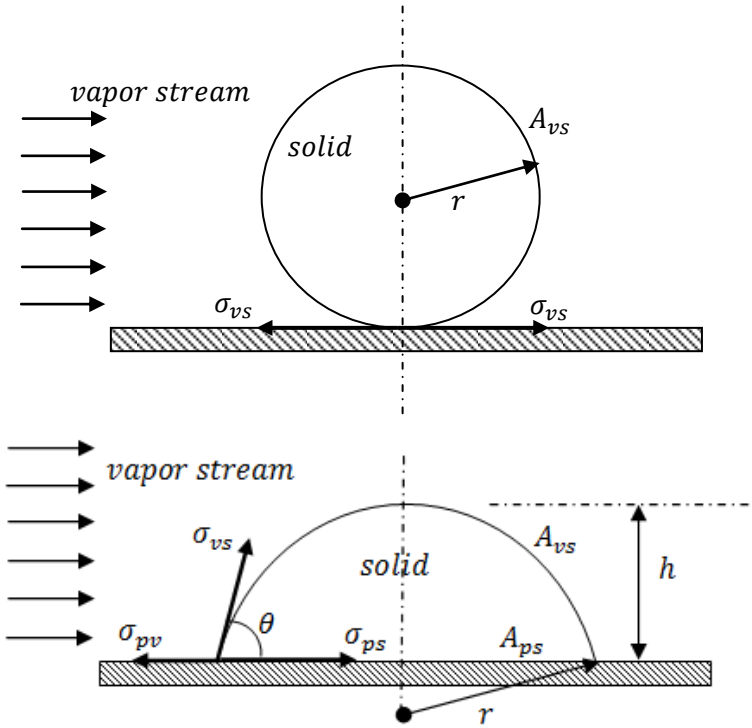

Figure 2.7: Fletcher's heterogeneous nucleation model
a) $\theta = 180°$; *b)* $0 < \theta < 180°$.

In the second case (*b*), is represented a partial affinity between the solid crystal and the substrate, for which the contact angle θ ranges between 0 and 180°. It depends on the magnitude of the three interfacial tensions. The equilibrium is adjusted in a way to ensure a force balance at the three phase contact point. The contact angle and σ_{vs} are correlated using the Young equation. It is the horizontal force balance performed at the three-phase contact point.

$$\sigma_{pv} = \sigma_{ps} + \sigma_{vs} \cos\theta \tag{2.23}$$

σ_{ps} is the plate-solid interfacial tension and σ_{pv} is the plate-vapor interfacial tension. The embryo volume is calculated in Equation (2.24) as a function of the nuclei radius r and its height from the substrate surface h.

$$V_{embryo} = \frac{\pi h^2}{3}(3r - h) \tag{2.24}$$

A_{ps} and A_{vs} are respectively the contact surface between the plate and the solid nuclei and between the solid nuclei and the surrounding vapor mixture.

$$A_{ps} = \pi r^2 (\sin\theta)^2 \tag{2.25}$$

$$A_{vs} = 2\pi r h \tag{2.26}$$

The nuclei height from the substrate surface is expressed in Equation (2.27) as a function of the contact angle and the nuclei radius:

$$h = r(1 - \cos\theta) \tag{2.27}$$

In heterogeneous nucleation, in which a solid foreign plate is present, the change in Gibbs free energy is expressed by Equation (2.28):

$$\Delta G = V_{embryo}\Delta G_v + A_{vs}\sigma_{vs} + A_{ps}(\sigma_{ps} - \sigma_{pv}) \tag{2.28}$$

Comparing the heterogeneous nucleation free energy change to the homogeneous case (Equation (2.6)), the work effect associated with the surface tension at the embryo interfaces is expressed by the additional terms present in Equation (2.28).

As represented in Figure 2.7, in heterogeneous nucleation, the interfacial tension has an effect at the phase interfaces resulting in a nuclei with smaller volume and surface area than a nuclei formed by spontaneous nucleation. As a first interpretation of Equation (2.28), it is obvious that the free energy change required to initiate heterogeneous nucleation is lower than in homogeneous nucleation.

As performed for the homogeneous nucleation case, the critical nuclei radius and the critical free energy change able to form stable nuclei are calculated by maximizing Equation (2.28). The critical radius r_c and the critical free energy $\Delta G'_{\text{crit}}$ calculated using Fletcher's model are given respectively in equations (2.29) and (2.30).

$$r_c = -\frac{2\sigma_{vs}}{\Delta G_v} \tag{2.29}$$

$$\Delta G'_{\text{crit}} = \frac{16\pi}{3}\frac{\sigma_{vs}^3}{{\Delta G_v}^2}\frac{(2+\cos\theta)(1-\cos\theta)^2}{4} \tag{2.30}$$

This critical free energy change is comparable to the one calculated for homogeneous case and they are related by the ratio φ given as a function of the contact angle in Equation (2.31).

$$\frac{\Delta G'_{\text{crit}}}{\Delta G_{crit}} = \varphi(\theta) = \frac{(2+\cos\theta)(1-\cos\theta)^2}{4} \tag{2.31}$$

The variation of the ratio φ is plotted in Figure 2.7 as a function of θ ranging between 0° and 180°. In complete affinity between the substrate and the crystallizing solute, $\theta = 0°$, φ is equal to zero. In non-affinity, $\theta = 180°$, φ is equal to unity and the free energy change in the heterogeneous nucleation is equal to the homogeneous one. φ increases between 0 and 1 for a contact angle going from 0 to 180°.

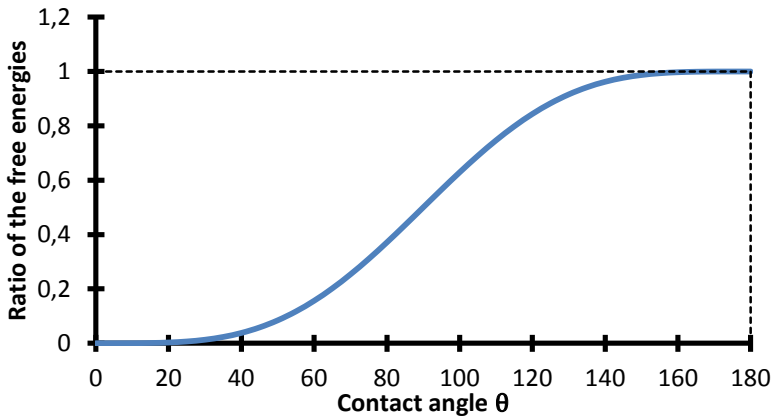

Figure 2.7: Free energy ratio variation as a function of the contact angle.

Equation 2.30 shows the effect of the affinity between solid crystals and the substrate on the nucleation process. In order to enhance the nucleation process, a substrate has to be chosen taking into account its affinity with the crystallizing solute. This affinity promotes the nucleation for lower supersaturation ratios than the homogeneous nucleation and reduces the amount of the free energy required to produce crystals.

In the case of CO_2 crystallization by cooling down flue gases, the surface of the heat exchangers formed by the fin and tube surfaces has to be chosen in order to promote heterogeneous nucleation at the beginning of the frosting cycle. According to this CNT, good affinity between solid CO_2 and the fin surface can reduce the supersaturation ratio, then supercooling, required to start the nucleation process. The CO_2 supersaturation ratio as a function of the supercooling is plotted in Figure 2.8. The case of a sublimation temperature of -100°C is taken into account. As represented, a supersaturation ratio of 1.5 requires flue-gas super-cooling of 2 K, which represents an energy penalty for the CO_2 capture process. 2-K super-cooling leads to reduce the refrigeration system performance that operates between the required temperature for CO_2 crystallization and the ambient temperature (cf. 1.4.2.3).

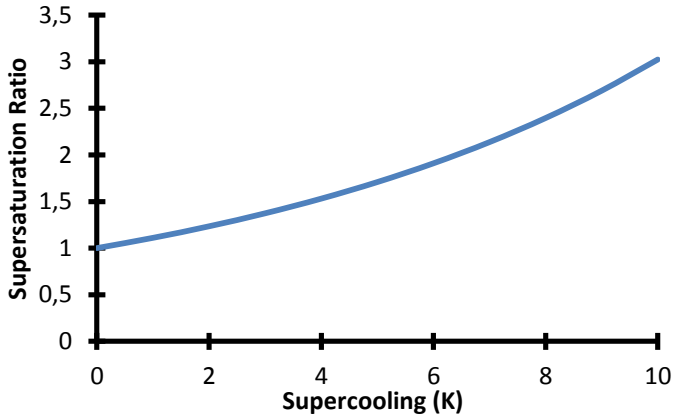

Figure 2.8: CO_2 Supersaturation variation as a function of the super-cooling.

2.2.3.2 Kinetic aspects

From a kinetic point of view, as for homogeneous nucleation, the heterogeneous nucleation rate is calculated using the Arrhenius reaction velocity equation.

$$I = n_c \exp\left[-\frac{\Delta G'_{\text{crit}}}{k_B T}\right] = n_c \exp\left[-\frac{\varphi(\theta)\,\Delta G_{crit}}{k_B T}\right] \tag{2.32}$$

As shown in Equation (2.32), the rate of heterogeneous nucleation is affected considerably by the presence of impurities or other substrates. It increases due to the decrease of the free energy change able to initiate nucleation and form stable embryos. The presence of impurities or catalyst surfaces on the nucleation rate is represented by the ratio $\varphi(\theta)$, which depends on the contact angle, then on the interfacial tension between the three phases. The nucleation rate increases exponentially when the φ ratio decreases, then with the affinity increase between the crystal solute and the substrate.

2.3 Crystal growth rate

After its formation, a stable nucleus continues its growth. This growth is a form of phase change and mass transfer between the parent phase and the new phase. It is essential to calculate this growth rate when modeling the mass transfer due to a nucleation process. The growth rate of a nucleus, equal to the change rate of its radius, is calculated by applying the heat balance to the nucleus. A spherical nucleus, formed by homogeneous nucleation, is taken into account.

$$\Delta H_{sub}\frac{dm_s}{dt} = A_{vs}\lambda(T_s - T_v) + m_s c_{ps}\frac{dT_s}{dt} \tag{2.33}$$

$m_s = \frac{4}{3}\rho_s \pi r^3$ is the weight of the nucleus, ΔH_{sub} is the sublimation heat per unit mass, $\frac{dm_s}{dt}$ is the mass transfer rate from the vapor stream to the solid nucleus, $A_{vs} = 4\pi r^2$ is the surface

contact between the nucleus and the vapor stream, λ is the convective heat transfer coefficient between the nucleus and the vapor stream, and c_{ps} is the heat capacity of the solid crystallized solute. T_v is the vapor stream temperature and T_s is the solid nucleus temperature determined using the capillarity effects and given in Equation (2.34).

$$T_s = T_{sub}\left(P_{CO_2}\right) - \left[T_{sub}\left(P_{CO_2}\right) - T_v\right]\frac{r_c}{\bar{r}} = T_{sub}\left(P_{CO_2}\right) + \Delta T_{sup}\frac{r_c}{\bar{r}} \tag{2.34}$$

Where $\bar{r}$ is the average radius and $T_{sub}\left(P_{CO_2}\right)$ is the solute sublimation temperature calculated for the local CO_2 partial pressure.

Since the nucleus is very small, the component $m_s c_{ps}\frac{dT_s}{dt}$ in Equation (2.33) can be neglected. It is the nucleus heating term and it is negligible compared to the convective heat transfer between the solid and vapor phases. The simplified form of the nucleus radius growth rate is then given by Equation (2.35).

$$\frac{dr}{dt} = \frac{\lambda(T_s - T_v)}{\rho_s \Delta H_{sub}} \tag{2.35}$$

The convective heat transfer coefficient between solid nucleus and the vapor stream is calculated using the model developed by Gyarmathy [GER03] and given in Equation (2.36).

$$\lambda = \frac{N_u\, k_v}{2r} \tag{2.36}$$

Where N_u is the Nusselt number and k_v is the vapor phase thermal conductivity.

2.4 Nucleation sensitivity analysis

Sensitivity analysis is generally used to calculate the rate of change of a system output due to small variations of its parameters. It generates an idea about the parameter disturbances or propagation of uncertainties affecting the model or the equation output. In this study, the sensitivity analysis is adopted in order to evaluate the effect of the CO_2 concentration and the temperature variations on the CO_2 frosting conditions. In CO_2 capture by antisublimation, as CO_2 is frosted through the tested heat exchanger, its concentration in the flue-gas stream decreases affecting its nucleation, i.e. the CO_2 mass transfer from the vapor to the solid phase. It is important to verify the effect of the variation of frosting parameters, through the heat exchanger, on the frosting conditions in order to verify the homogeneity of the solid deposit.

2.4.1 Sensitivity analysis due to the flue-gas CO_2 concentration perturbation

The homogeneous nucleation theory is taken into account to perform the sensitivity analysis. The nucleation rate $I\ (\#.m^{-3}.s^{-1})$ and the crystal critical radius $r_c\ (m)$ are calculated as functions of the interfacial tension $\sigma\ (N.m^{-1})$, the temperature $T\ (K)$, the molecular volume $v\ (kg.molecule^{-1})$, and the supersaturation S. It does not take into account the presence of impurity, of solid surface, and of the mass transfer by crystal growth. $\mathrm{k_B}$ is the Boltzmann constant.

$$I = n_c.\exp\left[-\frac{16\pi\sigma^3 v^2}{3\mathrm{K}_B^3 T^3(\ln S)^2}\right] = n_c.\exp\left[-\frac{B}{(\ln S)^2}\right] \tag{2.37}$$

$$r_c = \frac{2\sigma v}{\mathrm{k_B} T \ln S} \tag{2.38}$$

$$\dot{m}_{s,CO_2} = \frac{4}{3}\pi\rho_{s,CO_2} I {r_c}^3 \tag{2.39}$$

The nucleation rate and the critical radius sensitivity analysis are performed as a function of the supersaturation ratio variation, which depends on the CO_2 concentration and on the

temperature. Considering a constant temperature and constant interfacial tension, the nucleation rate is only affected by the CO_2 concentration variation since the saturation concentration is constant. The numerical differentiation by the one-sided difference scheme [OST05] is used calculating the relative variation of I, r_c, and $\dot{m}_{s,CO_2}$ as a function of the CO_2 concentration relative variation. The case considered is for $T = -100°C$ where the CO_2 saturated molar concentration is 13.72%. α_c is the CO_2 molar concentration (c_{CO_2}) variation.

$$\frac{I(c_{CO_2}+\alpha_c)-I(c_{CO_2})}{I(c_{CO_2})} = \exp\left\{-\frac{B}{\left[\ln\left(\frac{c_{CO_2}+\alpha_c}{c_{CO_2,sat}}\right)\right]^2}+\frac{B}{(\ln S)^2}\right\}-1 \tag{2.40}$$

The nucleation rate relative variation as a function of the CO_2 concentration variation is represented in Figure 2.9. Several supersaturation ratios are considered going from 1.1 to 2.0.

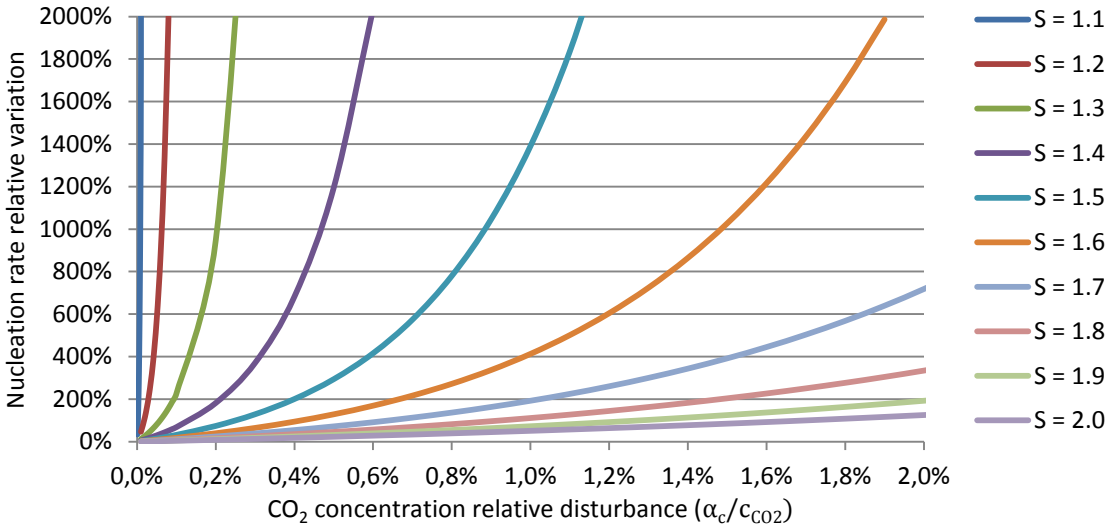

Figure 2.9: Nucleation rate relative variation function of the CO_2 concentration disturbance, T=-100°C.

Figure 2.9 shows a high variation of the nucleation rate due to the CO_2 concentration disturbance. As an example, for a supersaturation ratio of 1.3, 0.06% of CO_2 concentration increase brings about 100% nucleation rate relative increasing. This huge variation of the nucleation rate is due to its mathematical function and mostly due to the supersaturation ratios, close to unity.

As for the nucleation rate, the relative variation of the critical radius is given in Equation (2.41) and represented in Figure 2.10 for supersaturation ratios ranging between 1.1 and 2.0.

$$\frac{\left|r_c(c_{CO_2}+\alpha_c)-r_c(c_{CO_2})\right|}{r_c(c_{CO_2})} = \left|\frac{\ln S}{\ln\left(S+\frac{\alpha_c}{c_{CO_2,sat}}\right)}-1\right| \tag{2.41}$$

It is important to note that, according to Equation (2.38), the crystal critical radius decreases when the CO_2 concentration increases. So the absolute value of the solid CO_2 crystals critical radius variation as a function of the CO_2 concentration variation is plotted in Figure 2.10.

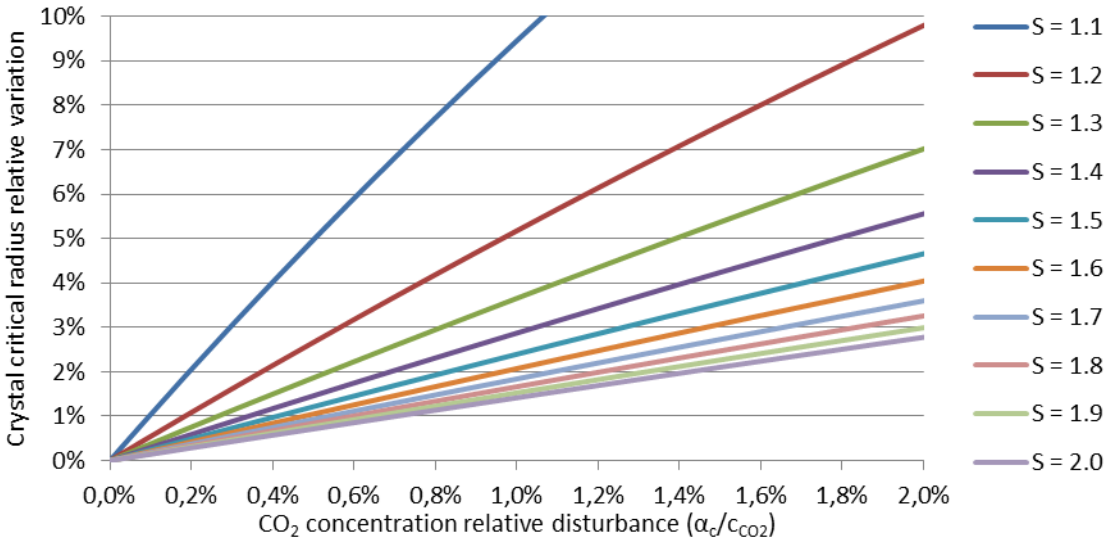

Figure 2.10: Critical radius relative variation as a function of the CO_2 concentration disturbance, T=-100°C.

The CO_2 concentration perturbation propagation is significantly lower for the solid CO_2 crystal radius than for the nucleation rate. As an example, the relative radius variation is 0.23% for a CO_2 concentration relative disturbance of 0.06% for 1.3 super-saturation ratio. The radius relative variation does not exceed 10% when a CO_2 concentration relative variation of 1% occurs for a supersaturation ratio of S=1.1.

The perturbation propagation law of the CO_2 concentration for the mass transfer by homogeneous nucleation is mostly affected by the significant variation of the nucleation rate more than by the variation of the critical radius. This nucleation theory sensitivity analysis as a function of the CO_2 concentration in flue gases shows that the mass transfer from the vapor to the solid phase is largely dependent on the supersaturation, and then on the CO_2 concentration. The mass transfer can be multiplied by a factor of 20 and more when this concentration varies for only 0.01% at low super-saturation ratios. The morphology of the solid CO_2 deposit from homogeneous crystallization is not widely affected by the CO_2 concentration variations since the crystal critical radius does not vary significantly with these disturbances.

2.4.2 Sensitivity analysis due to flue-gas temperature perturbation

Since the homogeneous nucleation theory depends on the temperature, a sensitivity analysis is performed. In addition, the nucleation depends mainly on the super-saturation ratio that is affected by the CO_2 concentration variation and by the saturation CO_2 concentration, which depends on the temperature. The numerical differentiation by the one-sided difference scheme [OST05] is used calculating the relative variation of I, r_c, and $\dot{m}_{s,CO_2}$ as a function of the temperature. The case considered is the same considered as in Paragraph 2.4.1 assuming a temperature $T = -100°C$ for which the CO_2 saturation molar concentration is 13.72%. α_T is the temperature variation.

$$\frac{I(T-\alpha_T)-I(T)}{I(T)} = \exp\left\{-\frac{B'}{(T-\alpha_T)^3.\left[\ln\left(\frac{c_{CO_2}}{c'_{CO_2,sat}}\right)\right]^2}+\frac{B'}{T^3.(\ln S)^2}\right\}-1 \qquad (2.42)$$

Where:

$$B' = \frac{16\pi\gamma^3}{3K_B^3} \qquad (2.43)$$

$c'_{CO_2,sat}$ is the CO_2 saturation molar concentration calculated for a temperature equal to $T - \alpha_T$. The surface tension σ is assumed to be constant for these small temperature variations.

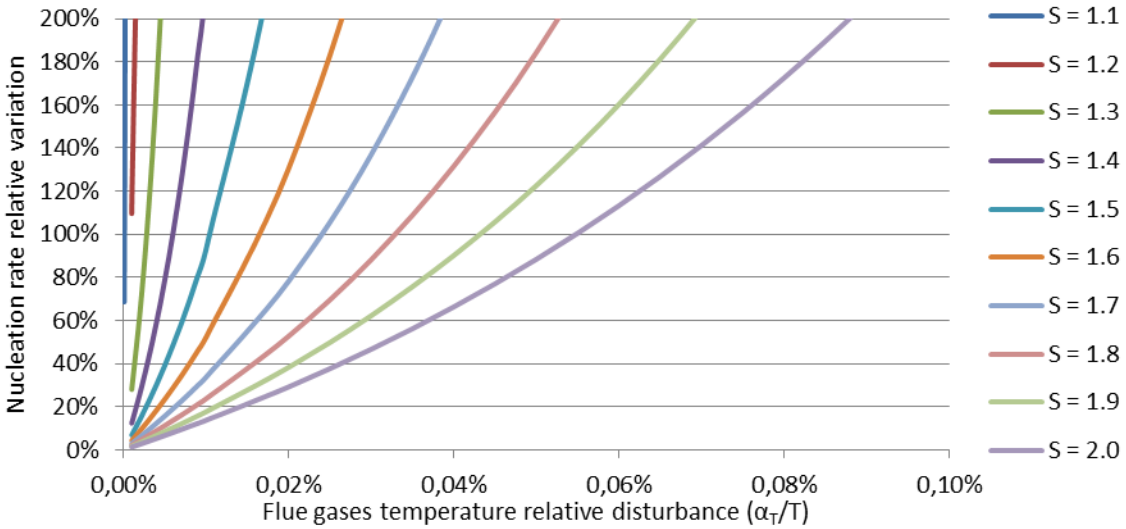

Figure 2.11: Nucleation rate relative variation as a function of the flue-gas temperature disturbance T=-100°C.

The propagation of the temperature disturbance applied to the homogeneous nucleation rate is represented in Figure 2.11. The nucleation rate increases quickly with the temperature decrease. For a supersaturation ratio of 1.3, 0.003% relative temperature decrease leads to a relative nucleation rate increase of about 100%. So the nucleation rate is more affected by a temperature variation than by a concentration variation. This fact is due to the higher increase of the supersaturation ratio due to a temperature decrease, rather than to a CO_2 concentration increase.

As for the nucleation rate, the CO_2 crystal critical radius variation due to a temperature disturbance is calculated using Equation (2.44).

$$\frac{|r_c(T-\alpha_T) - r_c(T)|}{r_c(T)} = \left| \frac{T \,.\ln S}{(T-\alpha_T).\ln\left(\frac{c_{CO_2}}{c'_{CO_2,sat}}\right)} - 1 \right| \tag{2.44}$$

It is important to determine the amount of the critical radius variation in order to evaluate the sensitivity of the deposit morphology with respect to a temperature variation α_T.

The critical radius relative variation produced by a temperature decrease is represented in Figure 2.12. The critical radius is greatly affected by the temperature variation compared to its variation following a CO_2 concentration perturbation. At a supersaturation of 1.1, the critical radius decreases by 65% for a temperature decrease of 1%.

The sensitivity analysis is performed to the classical homogeneous nucleation theory, showing the important effect of the CO_2 concentration and of the flue-gas temperature on the nucleation process. The signficant variation of the nucleation rate and the critical radius as a function of the supersaturation requires high-accuracy control of this parameter through the CO_2 frosting heat exchangers. Then, the flue gas temperature control, as a function of CO_2 partial pressure, throughout the heat exchanger is essential to the formation of homogeneous solid CO_2 deposit.

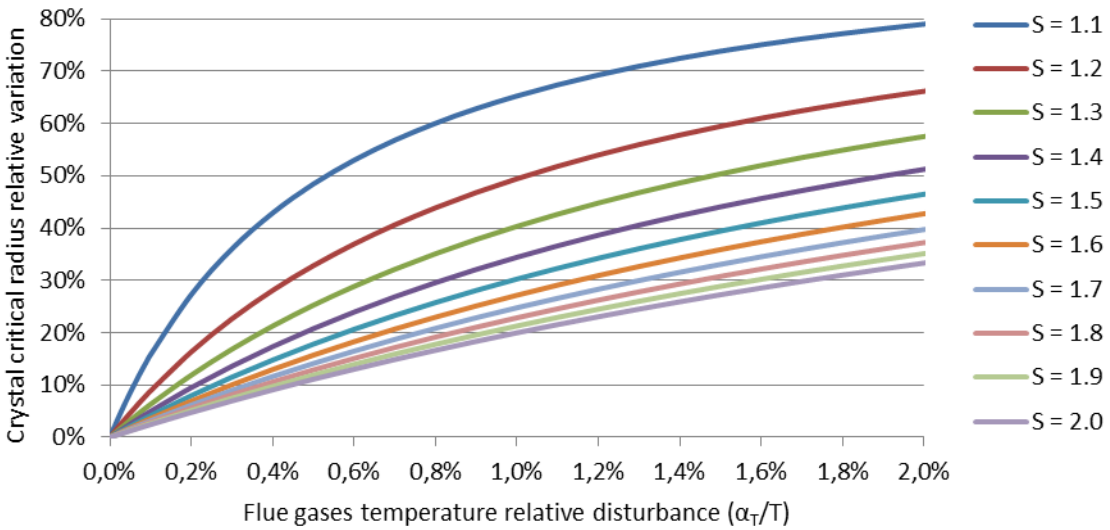

Figure 2.12: Critical radius relative variation as a function of the flue-gas temperature disturbance T=-100°C.

2.5 Evaluation of other parameters that could affect the antisublimation

2.5.1 Interfacial tension and fin surface treatment

The heterogeneous nucleation equations presented in Paragraph 2.2.3 show that the interfacial tension between crystals and the chilled plate affects the nucleation. The presence of this interfacial energy results in the formation of crystals smaller than crystals obtained by homogeneous nucleation. Subsequently, the energy required for initialization of nucleation is smaller in heterogeneous nucleation than in homogeneous nucleation. It shows the importance of the interfacial tension as a key parameter in the study of the antisublimation phenomenon [ROB08].

Factors that affect this interfacial tension are temperature, surface roughness, and the presence of impurities [NA03A]. A variation of the interfacial tension of a plate can be achieved by a surface treatment. The experimental and theoretical study of heterogeneous nucleation shows that the higher the interfacial tension between crystals and the plate, the higher the rate of crystal formation [NA03A]. Crystal formation is delayed on the plates with a low interfacial tension compared to high-affinity surfaces of crystals. This effect must be taken into account in frosting CO_2 heat exchangers where compatible fins have to be chosen in order to ensure the formation of first heterogeneous nucleus at the frosting cycle beginnings.

The experimental study of Na and Webb [NA03A] showed that the nucleation is activated in the plate areas where the interfacial tension between water crystals and plate is high. The other parts will be covered by frost by reducing the plate temperature or by increasing the water vapor concentration. This shows the necessary uniformity of the surface treatment that can be applied to the fin surfaces to increase their interfacial tension. Defects on fins will cause clogging of the heat exchanger on the zones where the interfacial tension is higher. Note that the formation of crystals on an already formed crystal is more favored than its formation on the plate due to the complete affinity between crystals formed by the same solute. In addition, experiments applied on the water vapor antisublimation have shown that the lower the contact angle, the lower the supersaturation required for the nucleation initiation. If a surface treatment is used, it must be permanent. The use of the heat exchanger should not affect and change its properties after few CO_2 frosting and defrosting cycles.

In fact, the interfacial tension effect on the CO_2 deposit formation is present only at the frosting cycle beginning. The lower the contact angle between CO_2 crystals and fin surface, the lower the super-cooling degree able to initiate frost formation. On the other side, this interfacial tension will not affect the frost layer growth. An experimental study conducted to determine the influences of surface hydrophilicity on frost formation on a vertical cold plate [LIU06] shows that interfacial tension effect can delay or enhance frost formation, but the mass transfer and solid deposit formation are unaffected after the first frost layer deposition. It should be pointed out that good affinity between crystals and fin surfaces is essential in order to avoid crystal extracting during the frosting cycle. Due to the deposit growth during the frosting cycle, the flue-gas velocity increases at the deposit surface and could be able to extract the solid crystals.

2.5.2 Solid deposit thermal conductivity

The thermal resistance of the CO_2 deposit can be calculated if its thermal conductivity and thickness are known. Thermal resistance can occur between the deposit and the fin surfaces. The thermal conductivity of the solid CO_2 deposit may depend on the arrangement of crystals according to certain directions. Visual observation of CO_2 deposit in various icing conditions showed a polycrystalline structure in which the crystal size is small compared to the thickness of the deposit, which allows considering that the thermal conductivity of the deposit is the same in all directions [COO76].

The CO_2 deposit thermal conductivity follows changes of the deposit density. Tests conducted by T. Cook and G. Davey have shown that alike density, thermal conductivity decreases rapidly at a rate of anti-sublimation of 400 $mg.m^{-2}.s^{-1}$ [COO76]. They state that the solid CO_2 deposit thermal conductivity follows exactly its density, but these two entities cannot be bound by a physical law. Figure 2.13 shows experimental results of measuring the CO_2 deposit thermal conductivity as a function of the anti-sublimation rate. This experimental study shows that the deposit thermal conductivity decreases for anti-sublimation rate greater than 400 $mg.\ m^{-2}.s^{-1}$ at 108 K to only 20% of the thermal conductivity of solid CO_2 measured by Maass [MAA26].

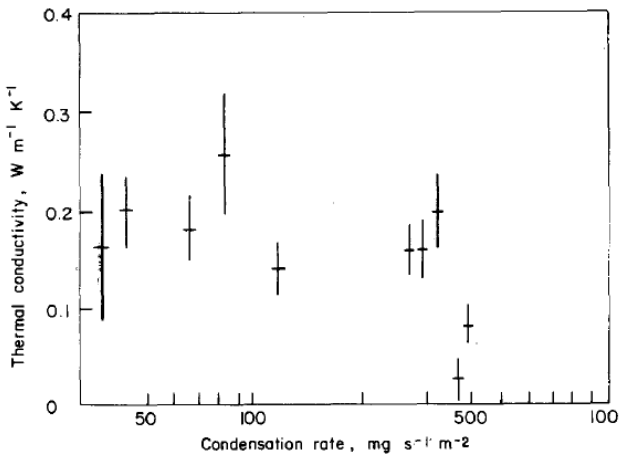

Figure 2.13: Solid CO_2 deposit thermal conductivity as a function of the nucleation rate [COO76]

2.5.3 Solid deposit density

The CO_2 deposition density is an important property determining the mass of CO_2 that can be captured within a period of icing with minimal increase in pressure loss caused by the increase in the frost thickness; so the denser the deposit, the longer the cycle and the larger the captured mass of CO_2 per unit area. In addition a high-density deposit results in increasing the thermal conductivity of the layer and thus decreasing the solid CO_2 layer surface temperature, which promotes the antisublimation driving potential.

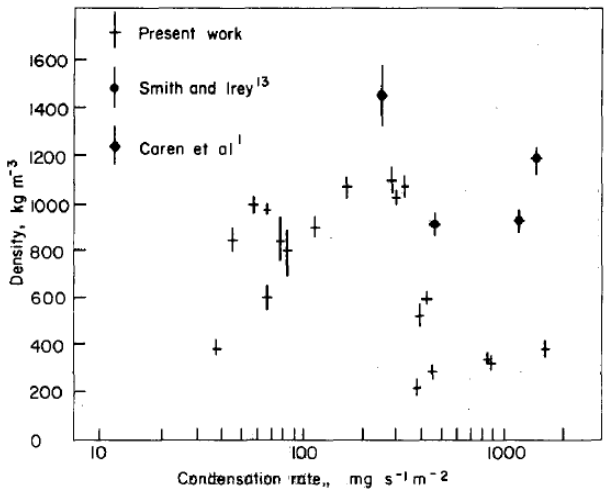

Figure 2.14: Solid CO_2 deposit density variation as a function of the antisublimation rate [COO76].

Figure 2.14 is the result of experiments of Cook and Davey [COO76]. The measured density undergoes a rapid fall when the anti-sublimation rate exceeds 400 $mg.s^{-1}.m^{-2}$ at 108 K to reach 20% of the solid CO_2 density. The carbon dioxide deposition has a low density when deposited at a high or very low anti-sublimation rate. According to Yang and Lee [YAN04] the water ice density depends on the frost surface temperature, the Reynolds number, the air relative humidity, the air temperature, and the temperature of fin surfaces. This parameter effects on the solid CO_2 density have to be studied.

2.5.4 Gas stream velocity and molecular diffusion

The vapor stream velocity directly affects the surface temperature of the frosting layer. High flue-gas velocity increases the surface temperature of the CO_2 deposit. Furthermore, it affects the diffusion of the gas phase in the solid layer increasing its density. At constant flue-gas mass flow rate, the gas stream velocity varies during a frosting cycle because the frost layer formation reduces the surface of the gas-phase passage. In addition, the experimental study of Schelkunov [SHC86] showed that when the gas stream velocity is higher than a limit, the solid CO_2 crystals could be dragged from the deposit surface.

Schelkunov [SHC86] performed an experimental study comparing CO_2 antisublimation from two different binary gas mixtures: N_2 – CO_2 and He – CO_2. Experimental results show a difference in the solid CO_2 layer evolution between these mixtures due to the difference in the CO_2 molecular interdiffusion in the thermal boundary layer of these gas mixtures. The CO_2 interdiffusion in the boundary layer is more favored in the presence of helium than nitrogen. This effect can reduce the frost layer thickness variation throughout the plate by providing the required CO_2 in the boundary layer able to crystallize at the given temperatures. In the antisublimation CO_2 capture, the molecular interdiffusion cannot be varied as the flue-gas composition is imposed, but the phenomenon of diffusion and the shape of the boundary layer can be chosen in order to improve the CO_2 diffusion. A heat exchanger with wavy fins can promote the molecular interdiffusion effect and lead to form a more homogeneous deposit. During all frost period, the antisublimation rate depends on the concentration of solute molecules at the gas-solid interface. A concentration balance is established when the supply of solute molecules to the interface equals the demand caused by the crystallization of the molecules on the solid layer.

The gas stream diffusion inside the solid layer promotes its density increase and thus the increase of its thermal conductivity following up a decrease of the frost surface temperature. This parameter is important because the CO_2 crystallization inside the solid layer is less energy intensive than its crystallization on the upper surface of the deposit, where the

temperature is higher. The diffusion is related to the deposit porosity also called tortuosity factor [NA04].

2.6 Conclusions

In this chapter, the mass transfer from a parent phase to a new formed phase is studied. The classical nucleation theory is used explaining the different types of nucleation: primary homogeneous and heterogeneous nucleations and secondary nucleation. The theories of homogeneous and heterogeneous nucleations are exposed calculating the nucleation rate, the critical radius of new formed nucleus, and the mass transfer rate between the two phases. The critical free energy change able to initiate nucleation is also calculated. For primary heterogeneous nucleation, the effect of the contact angle between the crystallized solute and the chilled surface is determined. In heterogeneous nucleation, lower supersaturation degree is able to initiate the nucleation compared to the homogeneous case. The Arrhenius reaction velocity equation is used in order to calculate the nucleation rate for both cases.

A sensitivity analysis has been performed in order to evaluate the effect of the CO_2 concentration and the flue-gas temperature variations on the CO_2 frosting conditions. The sensitivity of the homogeneous nucleation rate and of the critical radius has been calculated in order to evaluate the effect of the concentration and temperature perturbations on the mass transfer rate and on the deposit morphology. Sensitivity analysis has shown a high variation of the nucleation rate and critical radius due to the CO_2 concentration disturbance. As an example, for a supersaturation ratio of 1.3, 0.06% of CO_2 concentration increase brings about 100% nucleation rate relative increase. Results are similarly high in the temperature perturbation. Then, the supersaturation is a key parameter that has to be controlled in order to control the mass transfer from the parent to the new phase. The effect of other parameters like gas stream velocity, molecular diffusion, and frost layer porosity, density, and thermal conductivity have been exposed and discussed.

Antisublimation is divided into two main stages: primary nucleation or crystal formation and development of these crystals. Parameters affecting the formation of the solid phase are divided between the flow properties (such as velocity, temperature and pressure), the chilled surface properties of the (as its temperature and roughness) and of the frost deposit formation properties (such as surface temperature and roughness, the contact angle with the plate, porosity, density and thermal conductivity). The frost layer formation is accompanied by changes over time of the density and thermal conductivity of the solid phase and the heat and mass transfer in this layer surmounted by a moving boundary layer.

References

[NA03A] **Byeongchul Na, Ralph Webb**, A fundamental understanding of factors affecting frost nucleation, International Journal of Heat and Mass Transfer, 46, 3797-3808, 2003.

[ROB08] **Robson O. Piucco, Christian JL. Hermes, Claudio Melo, Jader Barbosa**, A study of frost nucleation on flat surfaces, Experimental Thermal and Fluid Science, 32, 1710-1715, 2008.

[SHC86] **V.N. Shchelkunov, N. Z. Rudenko, Yu. V. Shostak, V. I. Dolganin**, Surface desublimation of carbon dioxide from binary gas mixtures, Inzhenerno-Fizicheskii Zhurnal, Vol. 51, No. 6, 965-970, 1986.

[COO76] **T. Cook, G. Davey**, The density and thermal conductivity of solid nitrogen and carbon dioxide, CRYOGENICS, June 1976.

[MUL01] **J.W. Mullin**, Crystallisation, fourth edition, Reed educational and professional publishing Ltd, 2001.

[SEK03] **Deniz Seker, Hakan Karatas, Nilufer Egrican**, Frost formation on fin-and-tube heat exchangers. Part 1: Modeling of frost formation on a fin and tube heat exchangers, International journal of Refrigeration, 27, 367-374, 2003.

[YAN04] **Dong-Keun Yang, Kwan-Soo Lee**, Modeling of frosting behavior on a cold plate, International journal of Refrigeration, 28, 396-402, 2004.

[NA04] **Byeongchul Na , Ralph L. Webb**, New model for frost growth rate, International Journal of Heat and Mass Transfer, 47, 925–936, 2004.

[NA03B] **Byeongchul Na , Ralph L. Webb**, Mass Transfer on and within a frost layer, International Journal of Heat and Mass Transfer, 47, 899–911, 2003.

[ISM99] **K.A.R. Ismail, C.S. Salinas**, Modeling of frost formation over parallel cold plates, International Journal of Refrigeration, 22, 425–441, 1999.

[PIU08] **Robson O. Piucco, Christian J.L. Hermes, Cláudio Melo, Jader R. Barbosa Jr.**, A study of frost nucleation on flat surface, Experimental Thermal and Fluid Science, 32, 1710–1715, 2008.

[MAO92] **Y. Mao, R.W. Besant, K.S. Rezkallah**, Measurement and correlations of frost properties with airflow over a flat plate, ASHRAE Trans., 98, 65–78, 1992.

[FAH96] **Per Fahlén**, Frosting and defrosting of Air-coils, Ph.D thesis, 1996.

[YAN04] **Dong-Keun Yang, Kwan-Soo Lee**, Dimensionless correlations of frost properties on a cold plate, International Journal of Refrigeration, 27, 89–96, 2004.

[LEE00] **Y.B. Lee, S.T. RO**, An experimental study of frost formation on a horizontal cylinder under cross flow, International Journal of Refrigeration, 24, 468-474, 2000.

[KIM08] **Jung-Soo Kim, Dong-Keun Yang, Kwan-Soo Lee**, Dimensionless correlations of frost properties on a cold cylinder surface, International Journal of Heat and Mass Transfer, 51, 3946–3952, 2008.

[CHE02] **Chin-Hsiang Cheng , Chiuan-Che Shiu**, Frost formation and frost crystal growth on a cold plate in atmospheric air flow, International Journal of Heat and Mass Transfer, 45, 4289–4303, 2002.

[SHI03] **Jongmin Shin, Alexei V. Tikhonov, Cheolhwan Kim**, Experimental Study on Frost Structure on Surfaces With Different Hydrophilicity: Density and Thermal Conductivity, ASME, 125, 2003.

[LEN06] Kristian Lenić, Anica Trp, Bernard Franković, Unsteady heat and mass transfer during frost formation in a fin-and-tube heat exchanger, Energy and the Environment, 35-48, 2006.

[GET10] **H.M. Getu, P.K. Bansal**, New frost property correlations for a flat-finned-tube heat exchanger, International Journal of Thermal Sciences, 1-14, 2010.

[LIU07] **Zhongliang Liu, Xinghua Zhang, Hongyan Wang, Sheng Meng, Shuiyuan Cheng**, Influences of surface hydrophilicity on frost formation on a vertical cold plate under natural convection conditions, Experimental Thermal and Fluid Science, 31, 789–794, 2007.

[GER04] **A.G. Gerber, M.J. Kermani**, A pressure based Eulerian–Eulerian multi-phase model for non-equilibrium condensation in transonic steam flow, International Journal of Heat and Mass Transfer, 47, 2217–2231, 2004.

[LEE05] **Y.B. Lee, S.T. Ro**, Analysis of the frost growth on a flat plate by simple models of saturation and supersaturation, Experimental Thermal and Fluid Science, 29, 685–696, 2005.

[LEE04] **Hyunuk Lee, Jongmin Shin, Samchul Ha, Bongjun Choi, Jaekeun Lee**, Frost formation on a plate with different surface hydrophilicity, International Journal of Heat and Mass Transfer, 47, 4881–4893, 2004.

[SUT08] **Y. Sutjiadi-Sia, P. Jaeger, R. Eggers**, Interfacial tension of solid materials against dense carbon dioxide, Journal of Colloid and Interface Science, 320, 268–274, 2008.

[SCH03] **Jürn W. P. Schmelzer**, Kinetic and thermodynamic theories of nucleation, Mater. Phys. Mech., 6, 21-33, 2003.

[MCD62A] **James E. McDonald,** Homogeneous nucleation of vapor condensation I-Thermodynamic aspects, American Journal of Physics, 30, Issue 12, 870-877, 1962.

[MCD62B] **James E. McDonald,** Homogeneous nucleation of vapor condensation II-Kinetic aspects, American Journal of Physics, 30, Issue 12, 870-877, 1962.

[MER90] **A. Mersmann**, Calculation of interfacial tensions, Journal of Crystal Growth, 102, Issue 4, 841-847, 1990.

[MER02] **A. Mersmann, B. Braun, M. Löffelmann**, Prediction of crystallization coefficients of the population balance, Chemical Engineering Science, 57, Issue 20, 4267-4275, 2002.

[FER09] **Leticia Fernandez Moguel**, Modélisation par CFD de la precipitation du carbonate de barium en réacteur à lit fluidisé, Ph.D. Thesis, 2009.

[MER01] **A. Mersmann**, Crystallysation Technology Handbook, Second edition, Marcel Dekker, 2001.

[KAT92] **Joseph L. Katz**, Homogeneous nucleation theory and experiment: A survey, Pure & Appl. Chern., 64, No. 11, 1661-1666, 1992

[SCH05] **J.W.P. Schmelzer**, Nucleation Theory and Applications, WILEY-VCH Verlag, 2005.

[MAA26] **O Maass, W. H. Barnes**, Some thermal constants of solid and liquid carbon dioxide, Proceedings of the Royal Society of London, series A 111, 224-244, 1926.

[FORD93] **FORD, IJ and LAAKSONEN, A and KULMALA, M**, Modification Of The Dillmann-Meier Theory Of Homogeneous Nucleation. J CHEM PHYS , 99 (1) 764 – 765, 1993.

[KJOH97] **K.J. Oh, Xiao Cheng Zeng, H. Reiss**, Toward a molecular theory of vapor-phase nucleation. V. Self-consistency in the decoupled dimer limit, J. Chem. Phys., 107 (4), 1997.

[OST05] **Alexander Ostermann, Wolfgang Fellin**, Analyzing Uncertainty In Civil Engineering, chapter: Sensitivity analysis, 2005.

[PET06] **Linda Petzold, Shengtai Li, Yang Cao, Radu Serban**, Sensitivity analysis of differential-algebraic equations and partial differential equations, Computers and Chemical Engineering, 30, 1553–1559, 2006.

Chapter 3. Experimental investigation of the CO_2 antisublimation on a fin-and-tube heat exchanger

3.1 Introduction

As described in Chapter 1, the optimization of the CO_2 antisublimation heat exchanger has a major effect on the energy performance of the AnSU® CO_2 capture process. The optimization of the temperature profile and the temperature pinch between the flue gases and the refrigerant blend leads to make the capture process more efficient. In fact, since the flue-gas CO_2 concentration decreases along the heat exchanger, a temperature profile has to be imposed ensuring a homogeneous solid CO_2 deposit. A non-compatible temperature profile leads to form a thicker solid CO_2 deposit where the CO_2 concentration is high. This problem takes place at the heat-exchanger inlet and leads to plug it before the frosting cycle achievement.

A new fin-and-tube heat exchanger configuration has to be designed using a new hydrocarbon blend. This design has to take into account the dynamic variation of the external heat transfer coefficient that considerably affects the heat and the CO_2 mass transfer. In fact, the solid CO_2 deposit formation on the heat exchanger has an impact on the surface temperature, the flue-gas velocity, and the heat and the mass transfer variation on the external side of the heat exchanger. These dynamic condition variations during the CO_2 antisublimation cycle have to be taken into account for the heat-exchanger optimization. In other words, the combined case of heat and mass transfer with a moving boundary layer must be studied.

Few experimental investigations have been conducted to study the CO_2 frosting on a fin-and-tube heat exchanger or on a flat plate. Shchelkunov [SHC85] has performed an experimental study measuring the time evolution of the thermo-physical characteristics of the CO_2 frosting from a N_2-CO_2 and He-CO_2 binary gas mixture on a cryogenic plate. In this experimental survey, Shchelkunov verifies the effect of the molecular inter-diffusion coefficient on the homogeneity of the solid CO_2 layer. His experiments lead to the measure of the time variation of the solid phase thickness, the solid phase surface temperature, and the CO_2 concentration distribution along the plate. Experiments are conducted for CO_2 concentrations between 1% and 9% considering a super-saturation ratio higher than 10 since the plate surface temperature is regulated at temperatures between -155°C and -122°C. These experiments results are not exploited in the context of our study since the studied temperature super-saturation ranges are different from desired frosting conditions.

Another experimental investigation was performed by T. Cook and G. Davey [COO76] in order to measure the density and the thermal conductivity of solid carbon dioxide and solid nitrogen layers. In the context of enhancing the performance of ultra-high vacuum cryo-pumping processes, T. Cook et al. have studied the effect of the surface temperature on the CO_2 nucleation rate, which affects also the density and the thermal conductivity of the frost layer. The experiments are conducted for surface temperatures going from -175°C up to -159°C in order to reach very low CO_2 pressures ($6.6E^{-6}$ kPa) using this vacuum pump technology. As a result of this experimental study, T. Cook et al. have plotted the solid CO_2 deposit density and thermal conductivity as a function of the nucleation rate and the time variation of the deposit thickness. Since the temperature and the CO_2 partial pressure ranges considered in this experimental study are very low compared to flue-gas CO_2 concentrations, results cannot be used in the context of the antisublimation CO_2 capture process.

In the context of CO_2 concentration controlling in space cabin atmospheres, an experimental investigation was carried out to verify the feasibility of CO_2 freezing-out techniques [MAU68].

This experimental study was performed to thoroughly understand the antisublimation mechanism qualitatively by observing the shape of the frost deposit, and quantitatively by measuring the frost layer thickness evolution and the physical and thermal properties of the frost layer. Experiments are conducted for low CO_2 concentrations with a maximum molar concentration of 0.5%, which is the maximum admissible concentration in space cabins. Therefore their results could not be exploited and are not sufficient for the study of antisublimation CO_2 capture where the CO_2 concentration can reach 29%.

Several studies have been conducted in order to measure and visualize the water frost formation and development on plane plate, cylinder, and fin-and-tube heat exchangers [VER02], [ALJ08], [LEE01], [SHIN03], [LIU06], [DENG03], [ARG01], [MAO92], and [FAH96]. These studies are taken into account in order to retrieve experimental techniques used for measuring the frost properties like density and thermal conductivity.

An experimental study of the CO_2 antisublimation on a fin-and-tube heat exchanger is of high interest to understand the CO_2 precipitation phenomenon on the heat-exchanger fins as a function of the flow and the surface parameters. In fact, the AnSU CO_2 capture covers power production and industrial sectors emitting CO_2 at molar concentrations ranging between 4% and 29%. In addition, during the flue-gas decarbonization, the CO_2 concentration decreases throughout the CO_2 frosting heat exchanger (CFX) (cf. Figure 1.6) showing the necessity of the studying the CO_2 concentration effect on the frost morphology and properties.

3.2 Experimental study objectives

Qualitative and quantitative investigations must be performed in order to study the solid CO_2 deposition. The deposit morphology, its formation, its accumulation, and its homogeneity all over the CFX and under different frosting conditions have to be studied by visual observation. A high magnification observation of the CO_2 precipitation allows the understanding of the crystallization theory studied in Chapter 2 and verifies the effect of many parameters like CO_2 concentration, the super-saturation ratio, the solid surface temperature, the solid surface roughness, and the gas stream velocity. The CO_2 crystal shapes and dimensions can also be observed using 200x magnification zoom.

The characteristics of the frost formed on the CFX surface are calculated by the quantitative measurements. The time evolution monitoring of the CO_2 frost thickness and of the nucleation rate allows the calculation of the average density and porosity for different CO_2 concentrations and fin surface temperatures. In addition, the CO_2 concentration evolution, the flue-gas temperature, and the fluid side temperature are tracked all over the CFX. Then, the heat and mass transfer between flue gases and the refrigerant blend are calculated concluding the total cooling capacity needed to frost down CO_2 from the flue-gas stream. The effect of CO_2 frost growth on the performance of the CFX, more especially on the overall heat-transfer coefficient between the refrigerant blend and flue gases, has to be studied.

The test bench is designed in order to simulate the antisublimation CO_2 capture process in realistic operating conditions. Frosting, defrosting, and conditioning heat-exchanger functioning regimes are possible on the test bench. The coupling of the refrigerant blend evaporation inside the heat exchanger tubes and the flue-gas cooling and CO_2 precipitation on the external finned surface is necessary to understand the real CFX operating conditions. The low-temperature refrigeration machine is an integrated cascade using hydrocarbon-refrigerant blends. Studying the refrigerant side pressure drop, the refrigerant side gliding temperature, and the flue-gas gliding temperature is important to optimize the CFX efficiency. The effect of the CO_2 frost formation on the integrated cascade operation and on the circulating refrigerant composition has to be understood because of its effect on the whole process efficiency. Different fin-and-tube heat-exchanger configurations and refrigerant blend compositions could be tested in steady-state and transient operating

conditions. Transient operation takes place while switching the CFX between frosting and defrosting cycles.

In this survey, only CO_2 antisublimation on the fin-and-tube heat exchanger will be studied. The morphology of the frost thickness is visualized for different CO_2 molar concentrations and at different super-saturation ratios. The CO_2 nucleation rate and density are measured as a function of the frosting conditions.

3.3 Test bench description

This section is a brief description of the test bench. The process flow diagram (PFD) and the piping and instrumentation diagram (PID) are presented, explaining the test bench operating principle. Two main sub-systems form the test bench: the integrated cascade and the equivalent flue-gas circuit. The equivalent flue gas (EFG) is a composition-controlled blend of N_2 / O_2 and CO_2. The integrated cascade is a refrigeration machine used to produce up to 4.4 kW of cooling capacity at low temperatures down to -130°CThe EFG circuit as well as the instrumentation, the data acquisition, and the control system are described. The CFX and EFG circuits are detailed because it is the central element of the experimental test bench.

3.3.1 Process flow and instrumentation diagram

The test bench is coupling an integrated cascade and an equivalent flue-gas closed circuit ensuring to test realistic operating conditions of the antisublimation CO_2 capture process. The process flow and instrumentation diagram is presented in Figure 3.1. The temperature, the pressure, and the composition of the refrigerant blend used in the integrated cascade are measured at the inlets and the outlets of components. These measures monitor the evolution of those parameters all over the refrigeration system operating in steady state or in transient conditions, and so the process heat and balances can be performed. The two evaporators of the integrated cascade are installed in a closed flue-gas loop and operate alternatively in frosting, defrosting, and conditioning modes. A CO_2 injection and recovery system allows the control of the CO_2 concentration at the CFX inlet and the recovery of liquid and vapor CO_2 after the defrosting cycle.

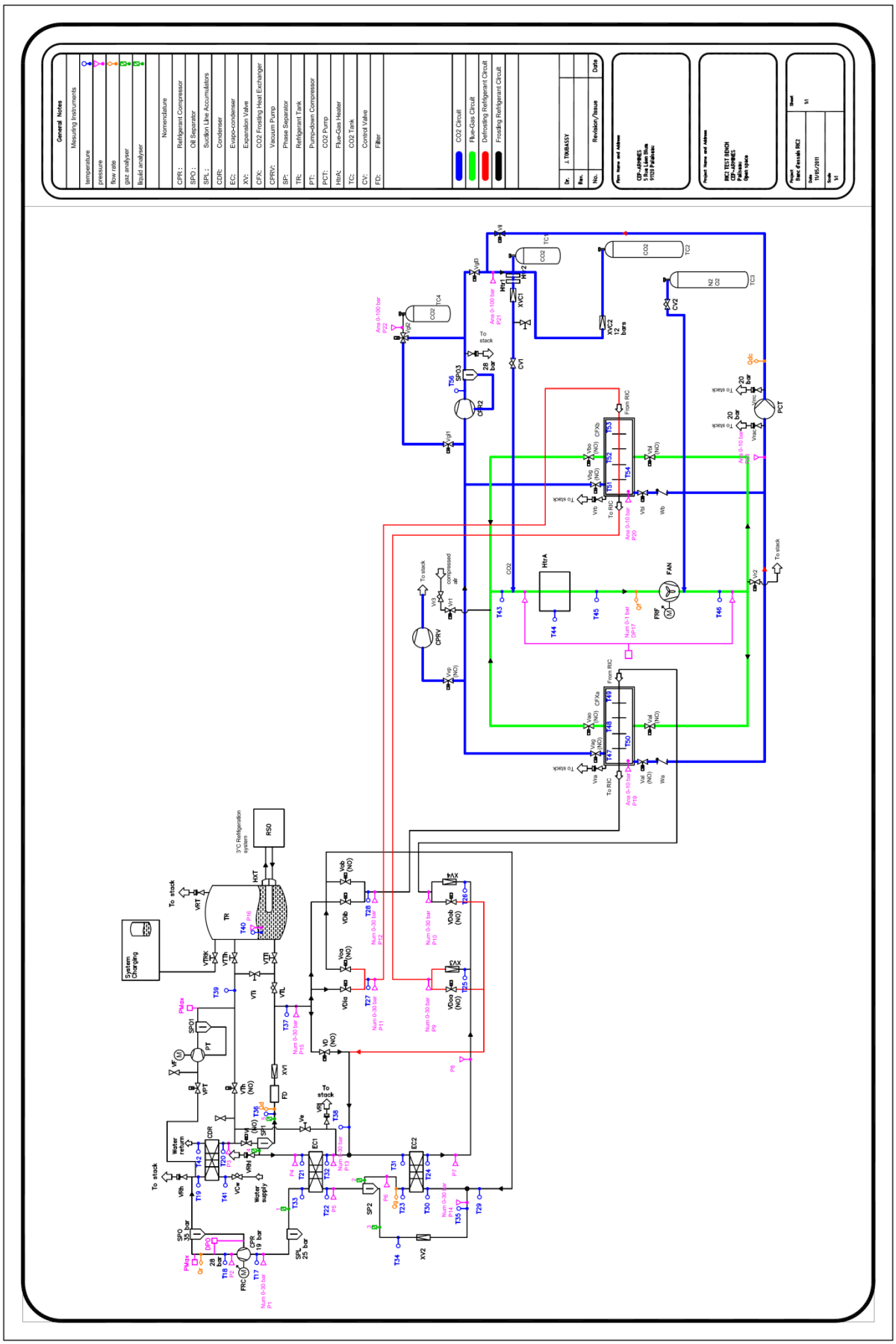

Figure 3.1: Test bench process and instrumentation flow diagramm.

3.3.2 Equivalent flue-gas (EFG) circuit

The equivalent flue-gas circuit is designed in order to control different CO_2 concentrations. It is composed of a centrifugal ventilator, two heat-exchanger enclosures where the fin-and-tube CFXs are installed, four pneumatically controlled ball valves, and a gas heater. The CO_2 / (N_2 95% - O_2 5%) mixture, called EFG is circulated in this close circuit.

Figure 3.2: centrifugal blower.

Figure 3.3: Pneumatic valves.

Figure 3.4: Gas heater.

A CO_2 injection system allows the control of the CO_2 concentration at the CFX inlet.

A centrifugal blower, ensuring 150 $m^3.h^{-1}$ EFG volume flow rate at -100°C, is used. The flow rate is controlled by a frequency convertor (Figure 3.4). This blower is certified in order to be used in explosive atmosphere, classified as zone 2 [EN60079]. The revolving joint and the electrical motor of the blower are certified ATEX category 3.

Two cryogenic ball valves are mounted at the inlet and the outlet of each CFX enclosure. These valves switch the EFG flow in the frosting CFX and isolate the defrosting one. Their pneumatic single-acting actuators are controlled by a digital 0-24 V signal.

A 2-kW circulation heater is used to reheat flue gases downstream the heat exchanger. The heating power is controlled by a thyristor unit. The power rate provided by the heater is controlled by a 4-20 mA analogical signal. A thermostat switch protects the heater from overheating. The heater is certified for being used in an explosive atmosphere classified as zone 2 [EN60079]. After CO_2 capture in the CFX, the decarbonized EFG is reheated and then enriched in CO_2.

The CFX enclosures have an internal volume of 750x450x150 mm and are designed to support an operation pressure of 800 kPa at -100°C, which are the defrosting conditions. Enclosures are made of AISI 316L stainless-steel sheets to avoid the brittle fracture for temperatures below -40°C. Enclosures are strengthened using 50x50 mm T profiles and they are designed in order to reduce their weight maintaining extreme operation conditions. Solid Works V.2009 is used for the design and for simulating the CFX-enclosure deformations under defrost operating conditions.

Figure 3.5: CFX-enclosure 3D design.

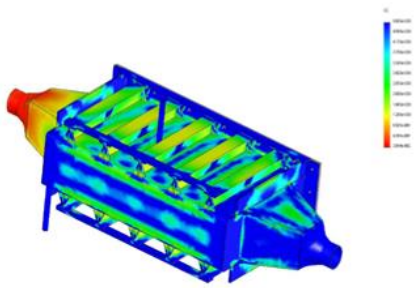

Figure 3.6: CFX-enclosure safety factor under CO_2 defrost operating conditions.

Heat-exchanger cells are mounted with 10° horizontal tilt in order to ensure the liquid CO_2 drainage during melting. Liquid and vapor CO_2 outlets ensure the complete CO_2 recovery after defrosting.

Figure 3.7: CFX-enclosure.

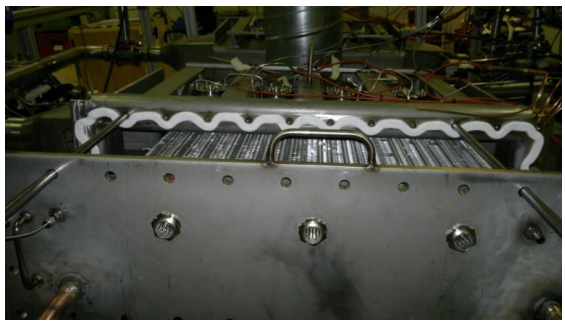

Figure 3.8: CFX installation in the enclosure.

An expanded Teflon seal is used to seal efficiently the enclosure during the defrosting process (800 kPa at -100°C).

In order to ensure a homogeneous flue-gas distribution on the frontal surface of the CFX (fin-and-tube heat exchanger), a deflector is designed at the enclosure inlet. For this purpose, Solid Works V.2009 Flow Simulation module is used. This module is run under Solid Works 2009 x64 SP3.0 edition to simulate several deflector configurations in order optimize the flue-gas distribution on the heat-exchanger inlet. A constant air mass flow rate of 0.031 $kg.s^{-1}$ at -100°C and an outlet pressure of 101.325 kPa are imposed respectively at the deflector inlet and outlet. The final deflector model and simulation results are represented in Figure 3.9 - 311.

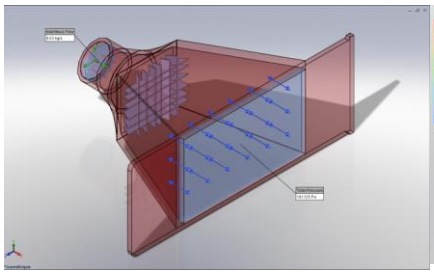

Figure 3.9: Deflector 3D model.

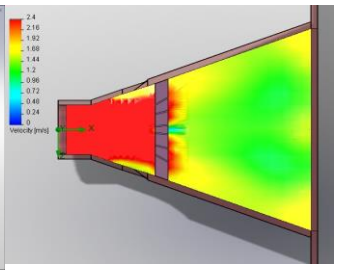

Figure 3.10: x-z velocity profile.

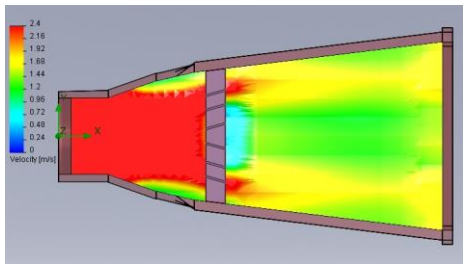

Figure 3.11: x-y velocity profile.

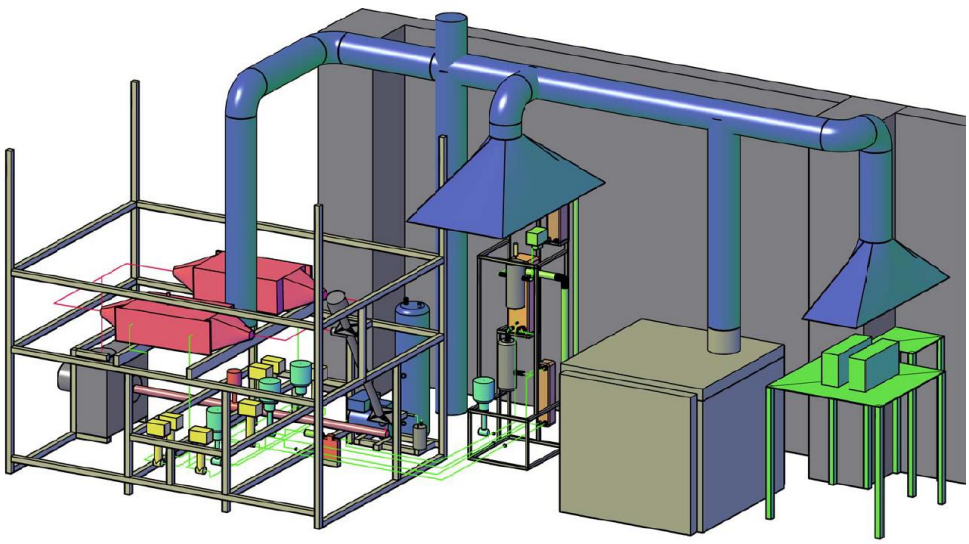

Figure 3.12: Design of the CO_2 capture test bench.

3.3.2.1 CO_2 frosting and defrosting fin-and-tube heat exchangers (CFX)

A herringbone fin-and-tube heat exchanger is used as a low-temperature evaporator (CFX) of the integrated cascade. The evaporation of the refrigerant blend in the tubes cools the EFG flow. When the EFG temperature becomes lower than the CO_2 sublimation temperature, depending on its partial pressure, the CO_2 antisublimates and precipitates on the heat-exchanger fins. The CFXs are designed to ensure 4.3-kW cooling capacity at temperatures ranging between -120°C and -100°C while frosting. These heat exchangers are not optimized in order to ensure the optimal gliding temperature; they are designed to visualize the CO_2 nucleation and to measure its nucleation rate for different concentrations. In order to measure the CO_2 nucleation rate through the heat exchangers, the flue-gas composition is measured downstream and upstream the heat exchangers and also at four positions inside the heat exchanger. Flue-gas and refrigerant temperatures are also measured in order to analyze the temperature differences.

Figure 3.13: Herringbone fin-and-tube heat exchanger (CFX).

3.3.3 Data acquisition and control

3.3.3.1 Data logger and control cabinet

National Instrument compact FieldPoint modules are used for data acquisition and test bench control. All modules are installed on two Ni cFP-1808 Ethernet interfaces and they are certified as intrinsically safe as they are used to communicate with components installed in an ATEX zone classified as zone 2. Seven NI cFP-RTD-124 temperature input modules are used to measure the temperature using 4-wire PT100 sensors. Two NI cFP-RLY-421 relay modules are used to control all electrical component power-contactors. Two NI cFP-AI-111 and one NI cFP-AI-110 analog input modules measure the 0-20 and 4-20 mA current loops and 0-10 V signals from sensors and transmitters such as pressure and mass flow rate transmitters. Two NI cFP-DO-401 digital output modules are used to control digital signals ranging from 5 to 30 V. These modules control the solenoid spool valves that are used to activate the pneumatically controlled ball valves. Two NI cFP-AO-200 analog output modules are used to control actuators such as the pneumatically controlled expansion valves, the CO_2 mass flow rate regulator, and also to control the compressor and the flue-gas blower rotation speed. 0-20 and 4-20 mA analog signal is used to control these components.

3.3.3.2 Temperature sensors

Temperatures are measured using 4-wire PT100 sensors. The high-temperature PT100 are used for positive temperature up to 150°C and low-temperature PT100 are used down to -150°C. Contact extrusive PT100 are used to measure refrigerant temperatures to avoid using tight passages since the refrigerant is a hydrocarbon blend. Intrusive PT100 sensors are used on the flue-gas circuit. The temperature measurement precision using NI cFP-RTD-124 modules and 4-wire PT100 sensors is ±0.15 K. Note that 4-wire PT100 sensors are used to eliminate the voltage drop caused by long lead wire resistance and to reduce errors caused by the signal noise generated by the frequency converters.

3.3.3.3 Pressure transmitters

Absolute pressure transmitters are used to measure the refrigerant pressures all over the integrated cascade, the pressure in both CFX-enclosures and in the CO_2 recovery circuit. The accuracy of these analog output transmitters is 0.25% of the full scale. Depending on the site where the pressure is measured, 10, 30, 50, and 100 bar full scale transmitters are used. These transmitters are certified to be used in an ATEX zone classified as zone 2. A differential pressure transmitter is used to measure the head loss between the inlet and the outlet of the frosting CO_2 heat exchanger. This measure allows studying the pressure loss evolution due to the solid CO_2 deposition on the fins of the heat exchanger. The measurement range of this differential pressure transmitter is between 0 and 0.1 bar with an accuracy of 0.03% of the full scale.

3.3.3.4 Refrigerant blend mass flow rate measurement

0-1000 $g.s^{-1}$ 0.2% of reading

Figure 3.14: Discharging line refrigerant mass flowmeter.

0-50 $g.s^{-1}$ 0.2% of reading

Figure 3.15: Defrosting liquid refrigerant mass flowmeter.

0-200 $g.s^{-1}$ 0.2% of reading

Figure 3.16: Phase separator 2 vapor outlet mass flow meter.

The water flow used to cool down the refrigerant blend in the partial condenser is measured using a KROHNE magnetic volumetric flowmeter. It allows the water flow measurement in a range between 0 and 24 $l.min^{-1}$ with an accuracy of 0.4% from the measured value ± 1 mm/s.

The refrigerant mass flow rate is measured using three Rheonic Coriolis mass flowmeters. The measure ranges and the accuracies are mentioned in Figures 3.14, 3.15, and 3.16. Flowmeters are installed on the compressor discharge line, at the liquid exit of the phase separator SP1 measuring the defrosting fluid flow rate, and at the gas outlet of the gas separator SP2 measuring the frosting fluid flow rate in the CFX. Then the refrigerant blend flow is calculated all over the integrated cascade for calculation of the compressor energy balance, the partial condenser, the two evaporators-condensers, the frosting heat exchanger and the defrosting heat exchanger. All these flowmeters and their transmitters are certified to be used in an ATEX zone classified as zone 2. Frosting and defrosting EFG flowmeters have their interior dehumidified to avoid the water frost formation on their solenoids, which can cause measurement errors.

3.3.3.5 Flue-gas mass flow rate measurement

A thermal mass flow meter is used to measure the flue-gas mass flow rate. It is calibrated to be used with the flue-gas mixture at high CO_2 concentrations and for negative temperatures from -20 down to -100°C. It allows gas flow rate measurement in the range of 0-100 $g.s^{-1}$ with an accuracy of 2% of the full scale. This technology of mass flowmeter is used because it causes no pressure drop and it is compatible with low-temperatures gas flows unlike the turbine flowmeters.

Figure 3.17: Thermal flue-gas mass flowmeter.

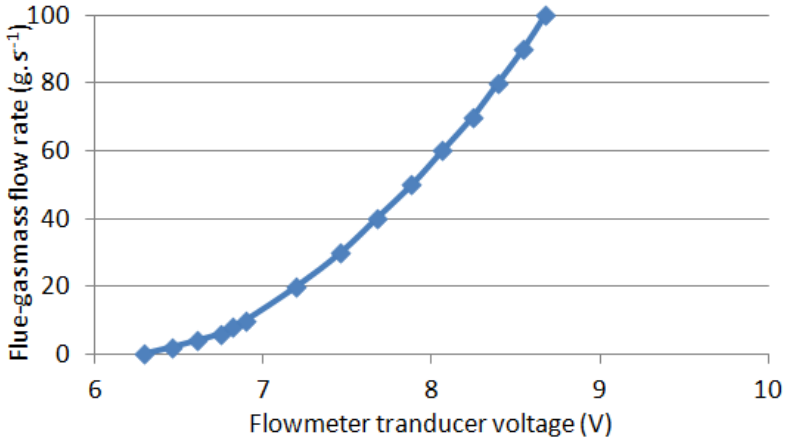

Figure 3.18: Calibrating curve correlating flow versus transducer voltage.

Flue-gas flowmeter is calibrated at 15 flow rates. The calibrating curve is represented in Figure 3.18 and the 6th degree polynomial correlation (Equation (3.1)) is used to calculate the mass flow rate. $\dot{m}_{fg}$ is the flue-gas mass flow rate in g.s^{-1} and v is the transducer voltage in V.

$$\dot{m}_{fg} = -1.69\,v^6 + 77.25\,v^5 - 1468.37\,v^4 + 14827.54\,v^3 - 83874.19\,v^2 + 251947.12\,v - 313950 \quad (3.1)$$

This flowmeter is certified to be used in an ATEX zone classified as zone 2.

3.3.3.6 Flue gas composition measurement

Four CO_2/O_2 gas analyzers are used to measure the EFG concentrations throughout the CFX. The composition of the equivalent flue gases formed by a N_2/O_2 mixture and CO_2 is controlled and the variation of the CO_2 concentration is measured all over the CFX. Knowing the total EFG mass flow rate, the weight of the captured CO_2 on the heat exchanger is calculated on 5 different elements of the CFX. Then the density of the antisublimated CO_2 layer is calculated by measuring the frost layer thickness.

Four infrared ADC SB 2000 gas analyzers are used to measure the CO_2 and O_2 concentrations all over the CFX. The CO_2 measure is made by an infrared source and the O_2 one is made by an electrochemical cell. Carbon dioxide measuring concentration range is from 0 to 30%v. and that of the oxygen is from 0 to 25%v. with an accuracy of ±1% of the full scale. This technology is chosen to measure the flue-gas composition due to their small time response, which is lower than 4 seconds. The CO_2 concentration measuring using the gas chromatography technology allows better accuracy with a time of response that normally exceeds one minute.

These gas analyzers are equipped with integrated gas pump with variable flow rate allowing the flue-gas sample recovery from the CFX-enclosure and they are calibrated using a standard gas mixture before every experiment to ensure minimum measure uncertainty.

Figure 3.19: ADC SB 2000 gas analyzers.

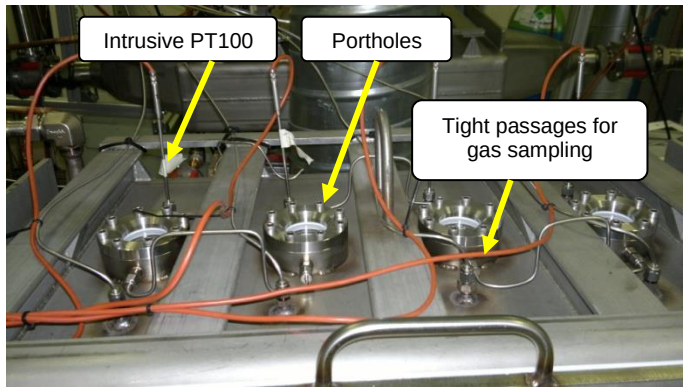

Figure 3.20: Flue-gas sampling from the CFX enclosures.

To multiply the point number where the gas composition is measured, a sampling circuit is developed (Figure 3.19, 3.20). The sample rate is composed of six three-way valves and two simple valves. 1/16" capillary tubes are used to suck up gas samples from the heat exchanger. The temperature of the gas stream is measured at the same sampling point so that the energy balance could be calculated on the flue-gas stream calculating the sensible and the latent cooling capacities consumed by the CO_2 frosting process. Samples are permanently taken at the CFX inlet and outlet, and the two other gas analyzers measure sample compositions taken from different CFX portions. Electronic sampling 3-way valves are automatically controlled, switching the sampling location every 30 seconds and to switch sampling from one CFX to the other while the frosting-defrosting cycles are permuted.

Flue-gas samples are reinjected in the closed flue-gas circuit at the suction of the flue-gas blower. An explosimeter analyses the hydrocarbon concentrations in the sample before reinjecting it in the closed flue-gas circuit in order to detect any accidental leakage at the heat exchangers.

3.3.3.7 Refrigerant blend composition measurement: Micro-GC

The CP-4900 Micro gas chromatography (Micro-GC) is used to measure the refrigerant blend composition in the integrated cascade. Since the refrigerant is a mixture of methane, ethylene, and butane, the refrigerant circulating composition varies after the condensations and the liquid separations. The measurement of the refrigerant composition at each component of the integrated cascade is important to perform the energy balance at the heat exchangers and to adapt the composition to the flue-gas frosting temperatures. The Micro-GC system consists of 4 micro chromatographs to measure the circulating vapor blend mixture at three locations of the integrated cascade. The composition is measured at the compressor suction port defining the total circulating composition. It is also measured at the vapor outlet of the phase separator SP1 allowing the calculation of the defrosting fluid composition at the liquid outlet. As well, the refrigerant composition is measured at the vapor outlet of the phase separator SP2. The composition at its liquid outlet is then calculated.

A sample of the gas mixture introduced into the Micro-GC reactor needs about 1 minute to be analyzed. Thus, mixture composition measurements at three points of the refrigerating cascade are carried out every 90 seconds. These analyzers are installed under an air extraction hoods to dilute any accidental leakage at the refrigerant sampling system.

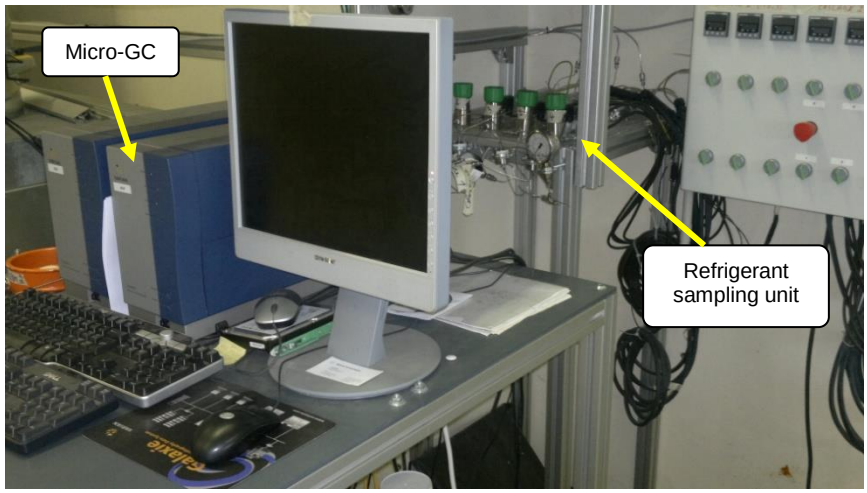

Figure 3.21: CP-4900 Micro-GC and sampling system.

Gas chromatography is the separation of a gas mixture compounds, qualitatively identification of the compounds, and quantitatively measurements of their volumetric concentration in the mixture. The sample is introduced into the injector with the sampling circuit where the sample is withdrawn from the integrated cascade to the pressure regulator and then to the oil filter. The injector is heated to 150°C to vaporize all sample solutes. Then the sample is carried to the column by the gas carrier. The temperature of the column is controlled by an oven. Every sample solute passes through the column at a velocity dependent on its physical properties and on the column configuration and temperature. The column is a small diameter tubing (0.05 – 0.53 mm) coated with a thin film (0.1 – 10.0 µm) of high molecular weight and thermally stable polymer [AGILENT]. The coating acts as a stationary phase where solute molecules are immobilized and liberated for thousands of times for each solute molecule while it passes through the column. Approximately, the entire molecule compound exits the column at the same moment because they are traveling the column at the same rate. The gas chromatography column allows that every compound, called band, exits the column during a span of time avoiding the exit of two compounds at the same time or co-eluting. The co-eluting is avoided by making each compound traveling at a different rate and by minimizing the time period during which a band exits the column. At the column exit, the solute bands enter a heated detector. The detector measures the electrical conductivity of the gas with reference to the carrier gas and generates an electronic signal. 99.95% pure helium is used as a carrier gas. The signal is plotted as a function of time and makes the chromatogram. The compound is known due to the time at which it exits the column called retention time. Its quantity is calculated as a function of the surface of the compound peak on the chromatogram. The compound concentration is correlated as a function of its peak surface using two standard gas mixtures and a high purity single gas for each compound. In Figure 3.22 is represented a chromatogram of the refrigerant blend used in the integrated cascade. The three compounds, methane, ethylene, and butane, are identified with the three peaks shown on the chromatogram. Methane is the first compound to exit the column, butane is the last one. Galaxy Chromatography Data System is used for Micro-GC data treatment and chromatogram representations.

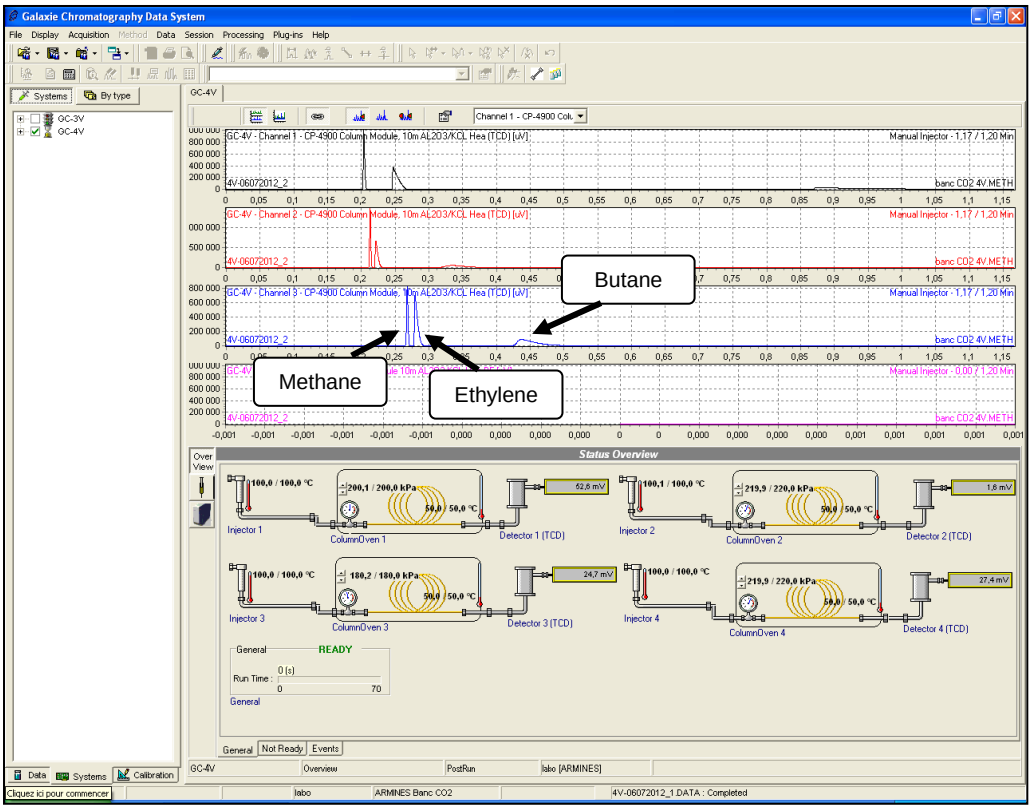

Figure 3.22: The refrigerant blend chromatogram showing no co-eluting between the three compounds.

3.3.3.8 Control and monitoring software

Data acquisition and control is developed under LabWindows/CVI V.2010 environment. This software allows reading and monitoring measurements performed by the FieldPoint modules and also to manually and automatically control all the test-bench components. Temperatures, pressures, and mass flow rates are saved every 3 seconds. The measured entities are shown on the process flow diagrams (Figures 3.1).

Figure 3.23 to 3.26 represent interfaces used for monitoring measurements and controls. Figure 3.23 is the interface of the integrated cascade monitoring where all temperatures, pressures, and flow rates are shown. All components, switch valves, and expansion valves are controlled manually and automatically via this interface. The CFX cycle switching between frosting, defrosting, and conditioning is represented. Figure 3.24 is the interface monitoring the equivalent flue-gases and refrigerant blend gliding temperatures in each CFX. The CO_2 concentration variation all over the heat exchanger is also represented. The flue-gas sampling system evolution is monitored on the interface of Figure 3.25 calculating the rate of solid CO_2 deposition on every section of the CFX. The CO_2 recovery and injection circuit is controlled by the interface represented in Figure 3.26.

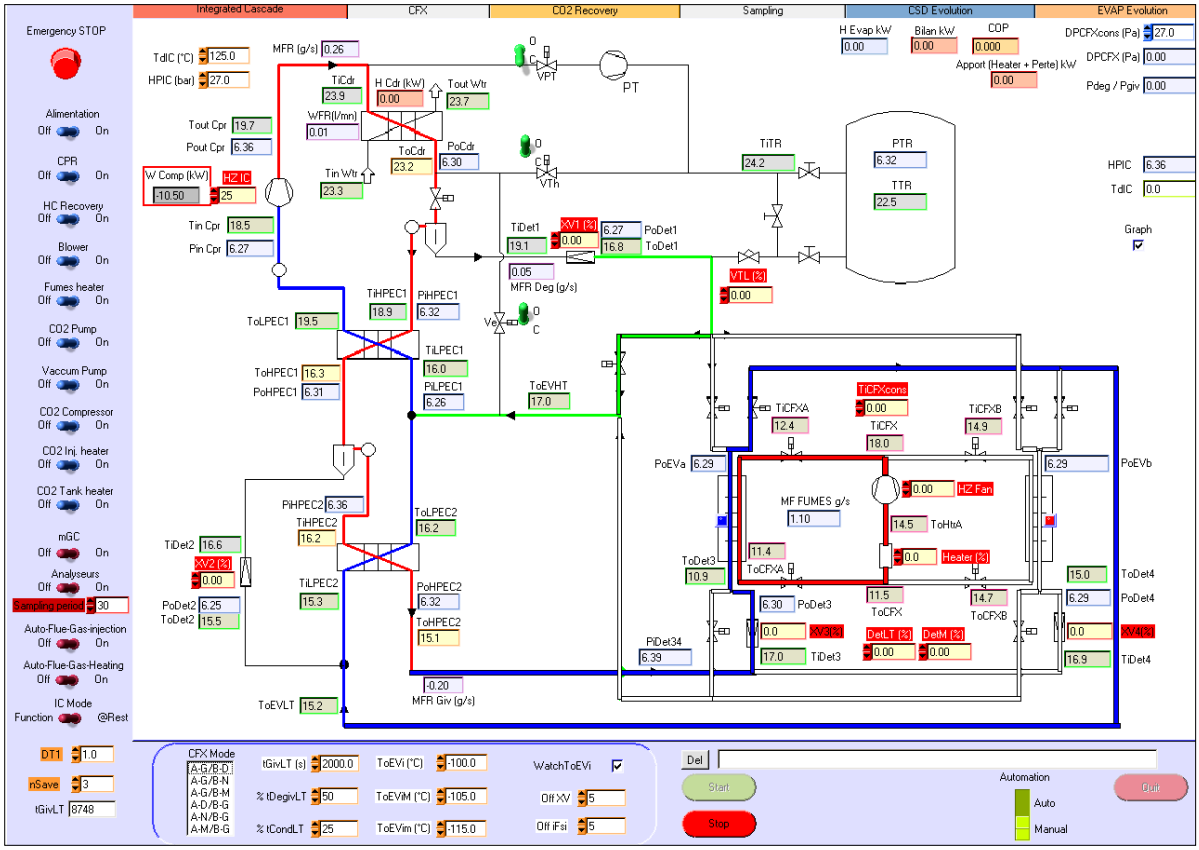

Figure 3.23: Integrated cascade and equivalent flue-gas interface.

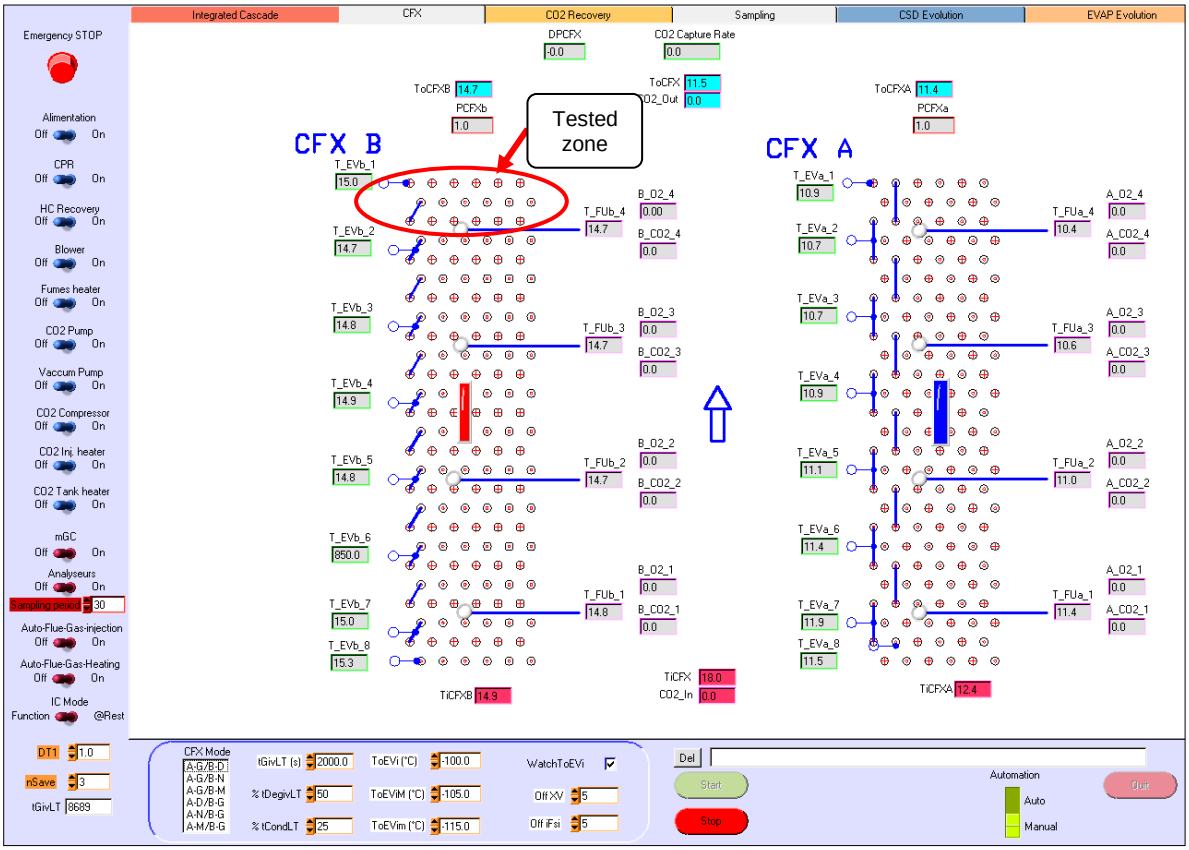

Figure 3.24: CFX interface.

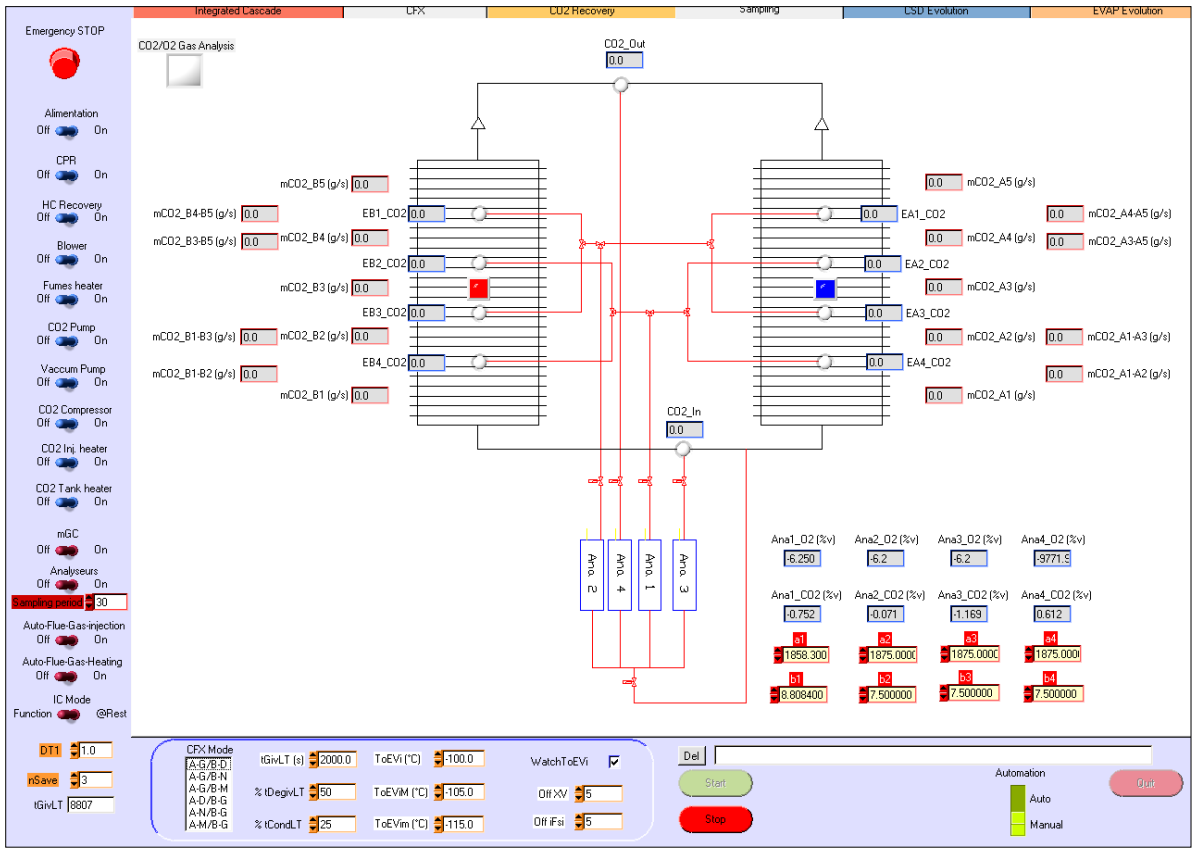

Figure 3.25: Flue-gas sampling interface.

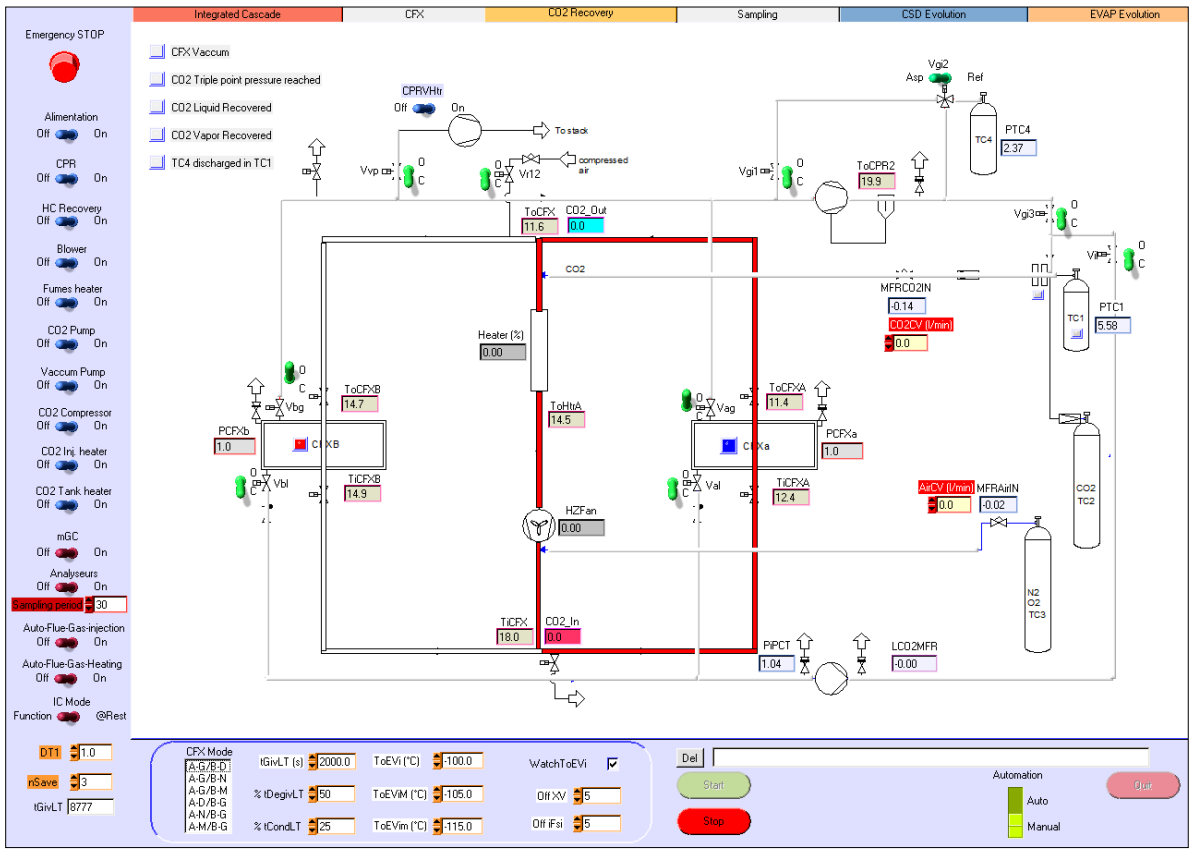

Figure 3.26: Equivalent flue-gas circuit and CO_2 recovery interface.

3.3.3.9 CO_2 frost visualization

A VHX-1000 digital microscope is used to visualize the dynamic CO_2 antisublimation on the heat exchanger fins. It is equipped with a 54-million pixels 3CCD handheld camera giving high resolution photos. The VH-Z20R objective is used allowing an optical magnification between 20x and 200x zoom objective. The integrated light source is allowed by this microscope and a step-by-step electrical motor ensures the optimization of the focal distance, eliminating the vibration disturbances during operation. The step-by-step motor, the high resolution camera, and the objective are mounted on the CFX-enclosure to visualize CO_2 frost through the portholes. Low magnification (30x) is used to visualize the solid CO_2 layer evolution on the fins and the high magnification (100x) allows following the deposition and evolution of CO_2 crystals. The image processing is performed using the VHX-1000 integrated computer. The solid CO_2 crystal and deposit measuring is possible using the VHX-1000 software. The measure software is calibrated before performing measures on the frost layer.

Portholes are designed to be used with this digital microscope allowing a viewing distance lower than 25 mm between the heat exchanger surface and the objective. The double borosilicate glass portholes are designed to support the defrosting conditions of -100°C enclosure temperature with up to 800 kPa of CO_2 internal pressure. The interior side of the porthole is inert using nitrogen injection to avoid internal frost formation due to the humidity. The outer side of the porthole is inerted by dry air injection that stagnates between the porthole outer surface and the objective lens, preventing the ambient air humidity to frost on the cool surface of the porthole.

Figure 3.27: Step-by-step motor, camera and objective.

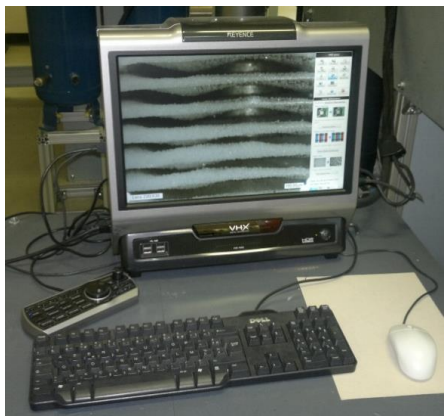

Figure 3.28: VHX-1000 monitoring, control and image processing computer.

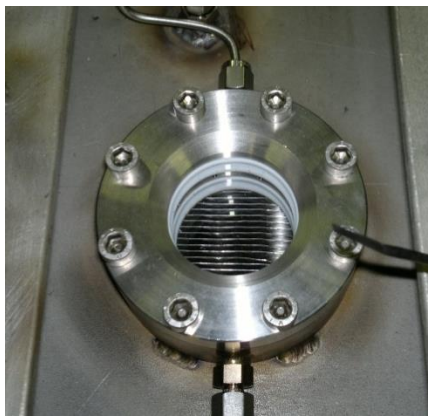

Figure 3.29: CFX-enclosure porthole.

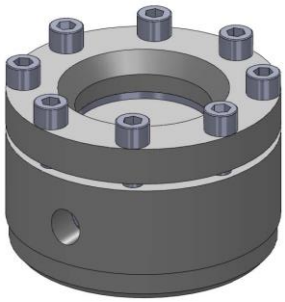

Figure 3.30: CFX-enclosure porthole 3D design.

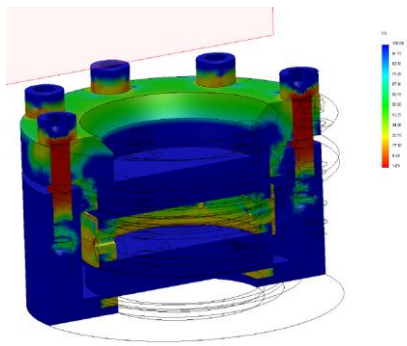

Figure 3.31: CFX-enclosure porthole safety factor under -100° C and 800 kPa (1.03 – 100).

Solid Works V.2009 is used for the design and for simulating the CFX-enclosure portholes deformation and safety factor under defrost operating conditions.

3.4 Standard uncertainty calculations

The uncertainty calculation of measured and calculated quantities in this study is based on the approach recommended by the International Committee for Weights and Measures (CIPM) and elaborated in "*The Guide to the Expression of Uncertainty in Measurement"* [EN13005]. This Guide is prepared by the International Bureau of Weights and Measures (BIPM), the International organization for Standardization (ISO), the International Electrotechnical Commission (IEC) and the International Organization of Legal Metrology (OIML). The standard confirms that the result of a measurement is an approximation of the real value of the quantity measured, named also measurand. So every result must be accompanied with a quantitative statement of its uncertainty [TAY94] in order to be compared with other quantities or with other measurements of the same measurand. According to the CIPM approach, components that affect the uncertainty of a measurement result are categorized into two groups, A and B. They are grouped according to the method used to estimate the standard uncertainty quantity.

3.4.1 Type A evaluation of standard uncertainty

A Type A evolution of a standard uncertainty is performed using a statistical analysis of series of observations. Considering n measurements q_k of a measurand Q, the experimental variance $s^2(q_k)$ of the observations that estimates the variance σ^2 of the probability distribution of q is:

$$s^2(q_k) = \frac{1}{n-1}\sum_{k=1}^{n}(q_k - \bar{q})^2 \tag{3.2}$$

Where $\bar{q}$ is the arithmetic average of the n measures:

$$\bar{q} = \frac{1}{n}\sum_{k=1}^{n} q_k \tag{3.3}$$

The Type A evolution of the standard uncertainty, $u_A(q)$, of the measurement of Q is equal to the positive square root of the experimental variance of the mean $s^2(\bar{q})$.

$$u_A^2(q) = s^2(\bar{q}) = \frac{s^2(q_k)}{n} \tag{3.4}$$

3.4.2 Type B evaluation of standard uncertainty

According to the Guide to the Expression of uncertainty in Measurement [EN13005], the Type B evaluation of standard uncertainty is based on scientific judgment based on the analysis of previous measurement data, on the general knowledge of the instrument properties, on the manufacturer specifications, on the data provided in calibration reports or on the uncertainties assigned to reference data found in the manuals. Most of the time, manufacturers specify lower and upper limits a_- and a_+ where the real value of the measurand Q lies in the range of $q_k - a_-$ and $q_k + a_+$ with a 100 percent probability where q_k is the measured value. If no information is provided by manufacturers or by calibration reports, q value is assumed to lie within the interval a_- to a_+ and with an equally probable distribution named rectangular or uniform probability distribution.

For rectangular probability distribution, the Type B evaluation of standard uncertainty is $u_B(q) = a/\sqrt{3}$ where $a = (a_+ - a_-)/2$.

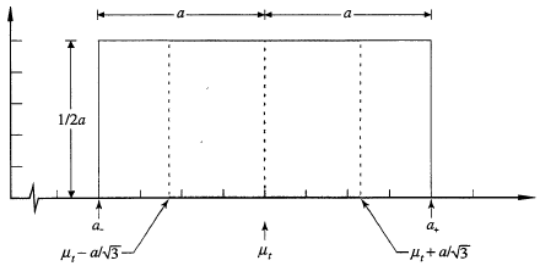

Figure 3.32: Rectangular probability distribution.

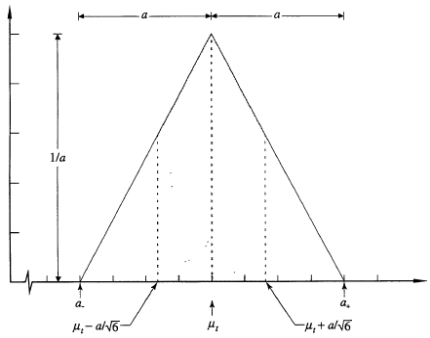

Figure 3.33: Triangular probability distribution.

For isosceles triangular probability distribution, this standard uncertainty is $u_B(q) = a/\sqrt{6}$. According to the NIST study of uncertainty evaluation, the rectangular distribution is reasonable in the absence of any other information. Triangular or normal distributions are used if it is known that it is more likely to find the measurement quantity in question near the center than near the interval limits.

Table 3.1: Type B evaluation of standard uncertainty of the test bench measurands.

Measurand	Measuring range	Manufacturer provided tolerance	Type B standard uncertainty u_B assuming rectangular probability distribution
Temperature	-150° - 150° C	±(0.15 + 0.2% |T|)	$\frac{0.15 + 0.2\% \lvert T \rvert}{\sqrt{3}}$
Absolute pressure	0-10 bar 0-30 bar 0-50 bar 0-100 bar	±0.25% of the full scale	14.43 10^{-3} bar 43.30 10^{-3} bar 72.17 10^{-3} bar 144.34 10^{-3} bar
Differential pressure	0-0.1 bar	±0.03% of the full scale	1.73 10^{-5} bar
Flue-gas flow rate	0-100 g.s^{-1}	±2% of the full scale	1.15 g.s^{-1}
CO_2 concentration	0-30%	±1% of the full scale	17.32 10^{-2} %
O_2 concentration	0-25%	±1% of the full scale	14.43 10^{-2} %
Refrigerant flow rate	0-1000 g.s^{-1} 0-200 g.s^{-1} 0-50 g.s^{-1}	±0.2% of the reading	$\frac{\dot{m}_{ref.} \times 0.2\%}{\sqrt{3}}$
CO_2 frost thickness	-	±5 µm	2.89 µm
Saturated CO_2 pressure	-	±0.2%	$\frac{P_{CO_2,sat} \times 0.2\%}{\sqrt{3}}$
Vapor CO_2 enthalpy	-	±0.15%	$\frac{h_{CO_2,vap} \times 0.15\%}{\sqrt{3}}$
Vapor CO_2 density	-	±0.05%	$\frac{\rho_{CO_2,vap} \times 0.05\%}{\sqrt{3}}$
Vapor O_2 enthalpy	-	±2%	$\frac{h_{O_2,vap} \times 2\%}{\sqrt{3}}$
Vapor O_2 density	-	±0.1%	$\frac{\rho_{O_2,vap} \times 0.1\%}{\sqrt{3}}$
Vapor N_2 enthalpy	-	±0.3%	$\frac{h_{N_2,vap} \times 0.3\%}{\sqrt{3}}$
Vapor N_2 density	-	±0.02%	$\frac{\rho_{N_2,vap} \times 0.02\%}{\sqrt{3}}$
CO_2 flow rate	0-250 l.min^{-1}	$U(\dot{v}_{CO_2}) = 8.2\ 10^{-3}\ \dot{v}_{CO_2} + 10^{-2}$	

Table 3.1 summarizes standard uncertainty of all measurements performed in this experimental study. Type B evaluation of standard uncertainty is used since the manufacturers provide the tolerance or the interval $\pm a$ where can lie the estimate y of a measurand Y following a rectangular probability distribution [MOR11]. For the vapor CO_2 volumetric flow controller, the expanded uncertainty $U(\dot{v}_{CO_2})$ is provided by the manufacturer.

3.4.3 Combined standard uncertainty

Combined standard uncertainty is used in order to calculate the uncertainty of a measurand Y, then its measurement result y, which is calculated as a function of many direct measurements x_i:

$$Y = f(X_1, X_2, \dots, X_N) \tag{3.5}$$

The measurand Y is also named the output quantity and it is estimated by output estimate y as a function of the input estimates x_1, x_2, …, x_N. Input estimates are the estimated values of the input quantities or input measurands $X_1, X_2, \dots, X_N$ [TAY94]. The output measurands could be independent or correlated variables. Only the case of independent input measurands is approached since the calculated measurand in this study are expressed as a function of independent input measurands.

$$y = f(x_1, x_2, \dots, x_N) \tag{3.6}$$

In order to calculate the combined standard uncertainty noted $u_c(y)$, the function f is approximated using Taylor series approximation. The first-order Taylor series approximation is sufficient when the non-linearity of the function f is not significant.

$$u_c^2(y) = \sum_{i=1}^{N} \left(\frac{\partial f}{\partial x_i}\right)^2 u^2(x_i) + \sum_{i=1}^{N}\sum_{j=1}^{N} \left[\frac{1}{2}\left(\frac{\partial^2 f}{\partial x_i\, \partial x_j}\right)^2 + \frac{\partial f}{\partial x_i}\,\frac{\partial^3 f}{\partial x_i\, \partial x_j^2}\right] u^2(x_i)\, u^2(x_j) \tag{3.7}$$

Equation (3.7) is named law of propagation of uncertainty where the partial derivatives $\partial f / \partial x_i$ are named sensitivity coefficients and it will be used in the following sections in order to calculate the combined standard uncertainties of calculated measurands.

3.5 Experiment procedure

In this survey, only the CO_2 antisublimation on the fin-and-tube heat exchanger is studied. The CO_2 frost morphology, its deposition rate, and density are studied. For this purpose only a section of the frosting fin-and-tube heat exchanger is studied where the inlet flue gas temperature and composition are controlled. In addition, the temperature of the fin surfaces is fixed by controlling the refrigerant blend temperature. The tested zone of the heat exchanger is limited to the three back-staging rows where flue gases are already cooled down by the upstream rows controlling their temperature (cf. Figure 3.24). The refrigerant temperature is controlled by controlling the refrigerant low pressure using the expansion valve XV4. In addition, since only three rows are tested, the visualization of the frost layer thickness at the temperature and flue-gas composition measurement site, downstream the third row counting in the direction of the refrigerant flow, is significant and allows the frost thickness measurement all over the three-row tested heat exchanger.

Before starting the integrated cascade, the closed flue-gas circuit is warmed up by circulating the nitrogen – oxygen gas mixture and using the gas heater. The nitrogen – oxygen mixture is continuously injected in the circuit by purging it in order to reduce the humidity that could be present in the circuit. In this way, the water frost formation on the heat exchangers is avoided, and so the impurity presence on the heat-exchanger surface. Then, the integrated cascade is turned on using the untested heat exchanger as evaporator in order to frost the remaining water vapor present in the gas circuit. The nitrogen – oxygen mixture circulated in the closed loop is cooled down to -60°C ensuring very low water vapor concentration in the mixture. The integrated cascade operating mode is then switched in order to use the tested

heat exchanger as the low-temperature evaporator. The tested heat exchanger is progressively cooled down to reach the desired temperature.

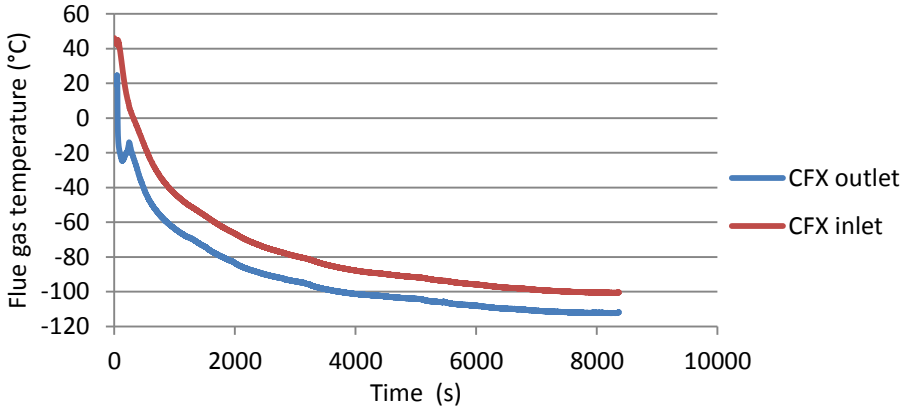

Figure 3.34: CO_2 free equivalent flue gas pre-cooling.

The CO_2 is injected in the flue-gas loop and its concentration is controlled at the inlet of the tested three row heat exchanger where the flue-gas temperature is also controlled (cf. Paragraph 3.6). The real time visualization of the heat-exchanger fins at the tested rows allows the analysis of the frost layer evolution. The frosting cycle is achieved once the frost layer is fully developed on the testing zone and the defrosting operating mode is launched. The tested heat exchanger is then fed with the defrosting refrigerant blend and the frosting refrigerant is circulated to the second heat exchanger. The defrosting CFX enclosure is confined by closing the upstream and downstream valves enabling the pressure to increase up to the CO_2 triple point pressure where solid – liquid – vapor equilibrium is reached. After the defrosting cycle achievement, liquid and then vapor CO_2 is recovered in the CO_2 storage cylinders using respectively the CO_2 liquid pump and the vapor compressor.

3.6 Flue-gas composition, mass flow rate, and temperature control

In this experimental study, the sensitivity analysis described in Paragraph 2.4 is adopted in order to evaluate the effect of the CO_2 concentration and the temperature variations in the tested three-row back-staging fin-and-tube heat exchanger on the CO_2 frosting conditions. Since the flue-gas composition and temperature are analogically controlled during the tests, the sensitivity analysis results are used to identify the acceptable control accuracy as a function of the test conditions. As for the gas composition control, the control of the equivalent flue gas and refrigerant temperature at the inlet of the tested heat exchanger is essential in order to maintain constant frosting conditions during the testing period.

3.6.1 Flue-gas composition

Flue gases are equivalent by mixing CO_2 to a N_2 – O_2 gas mixture. Flue-gas CO2 make up allows the simulations of different CO_2 concentrations going from 3% to 15% v/v for natural gas and coal-fired power plants, and up to 29% v/v for the cement industry. Equivalent flue gases are circulated in a closed loop where only CO_2 is separated on the CFX. Hence, the CO_2 concentration control is sufficient to control the ternary gas mixture composition at the inlet of the tested heat exchanger. For this purpose, a 5853S Brooks flow controller is used to inject vapor CO_2 at the heat-exchanger outlet. The CO_2 volume flow rate is controlled using an analogical algorithm and ensures a CO_2 concentration variation lower than 1% from the set point at the tested heat exchanger inlet. This concentration variation is represented in Figure 3.35 for 3 tests realized at 3, 8, and 15% v/v.

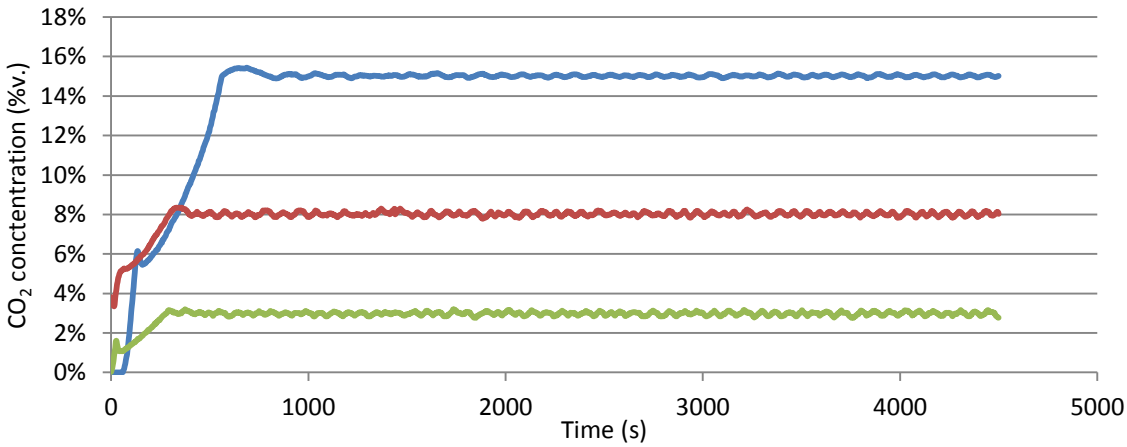

Figure 3.35: CO_2 concentration regulation at the tested heat-exchanger inlet.

3.6.2 Flue-gas and refrigerant temperature control

The flue-gas temperature at the inlet of the heat-exchanger tested zone is controlled using an analogical algorithm controlling the heating capacity supplied by the gas heater. The control is set to ensure a temperature variation lower than 1% from the set point temperature. As well, the refrigerant temperature is controlled by controlling the integrated cascade low pressure with an accuracy of 1% (Figure 3.36).

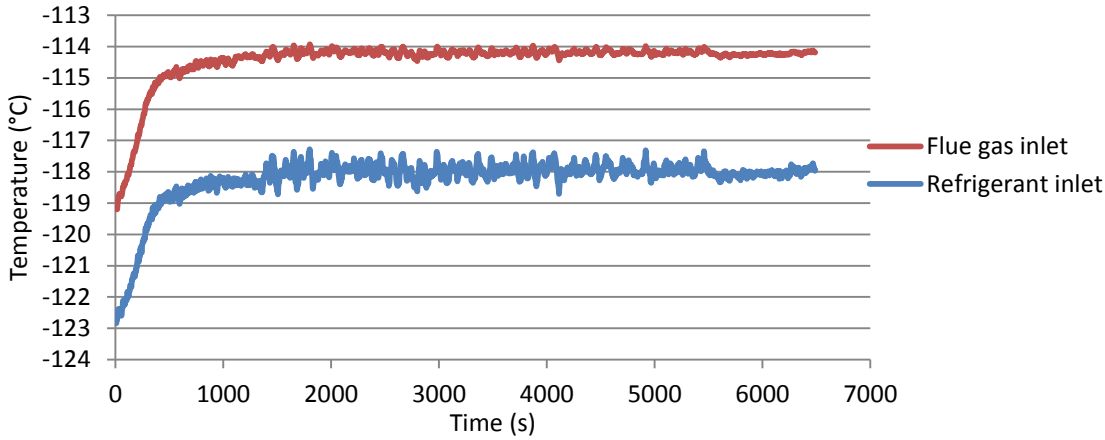

Figure 3.36: Flue-gas and refrigerant temperature control.

3.6.3 Flue-gas mass flow rate control

The flue-gas mass flow rate is also controlled at the heat-exchanger inlet in order to reproduce the realistic operating conditions of the CFX. In fact, during the CO_2 capture by AnSU process, the flue-gas mass flow rate is imposed by the industrial process and it should not be affected by the pressure head loss induced by the solid CO_2 deposit on the CFX. Figure 3.37 represents the flue-gas mass flow rate measured at the heat-exchanger inlet, which is controlled using the frequency converter that controls the blower speed.

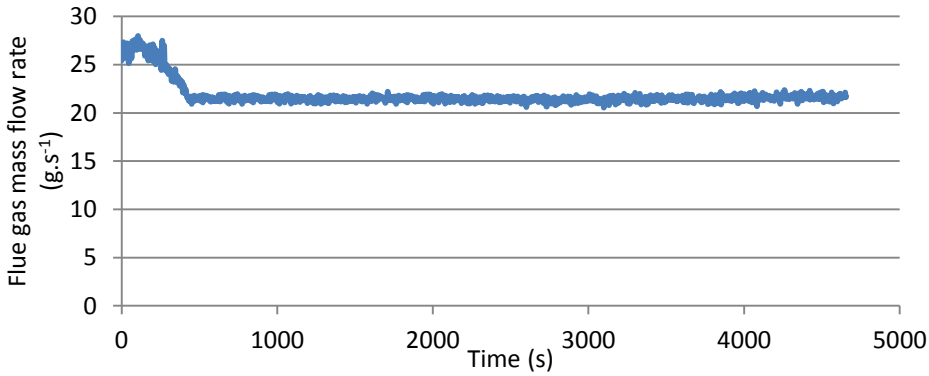

Figure 3.37: Flue-gas mass flow rate control at the tested heat-exchanger inlet.

3.7 Results

3.7.1 Super-saturation measurement

The super-saturation, known also as super-cooling, of a compound in a gas stream refers to a vapor compound having a higher partial pressure than its pressure at the solid-vapor or liquid-vapor equilibrium. It is expressed in different ways, such as the concentration driving force, the super-saturation ratio and the relative super-saturation. The concentration driving force is the difference between the supersaturated compound concentration in the mixture and its saturation concentration at the given temperature. The super-saturation ratio is the ratio between these concentrations and it is greater than unity when the compound is supersaturated. The super-saturation ratio expression is used in this study (cf. Paragraph 2.2.1).

The CO_2 partial pressure at the inlet and the outlet of the tested heat exchanger is calculated by measuring the total flue-gas pressure and the CO_2 molar concentration. The CO_2 solid-vapor equilibrium pressure or sublimation pressure is calculated using Refprop V9.0 as a function of the flue-gas temperature.

$$S_{CO_2}(t) = \frac{P_{CO_2}}{P_{sub,CO_2}(T_{fg})} = \frac{P_{fg} \,.\, v_{CO_2}}{P_{sub,CO_2}(T_{fg})} \tag{3.8}$$

The super-saturation ratios measured at the tested heat-exchanger inlet and outlet are plotted in Figures 3.38 and 3.39. Figure 3.38 presents a test performed with 8% v/v of CO_2 concentration in the flue-gas inlet and Figure 3.39 for a test with 15% v/v CO_2 concentration. In the first case, flue gases have low super-saturation ratio ranging between 1.1 and 1.15 at the heat-exchanger outlet. At the inlet, flue gases become saturated at the frosting cycle end. For the second test, at 15% v/v, flue gases are more supersaturated having a super-saturation ratio of 1.2 at the outlet. At the inlet, the super-saturation increases and reaches 1.2 at the frosting cycle end.

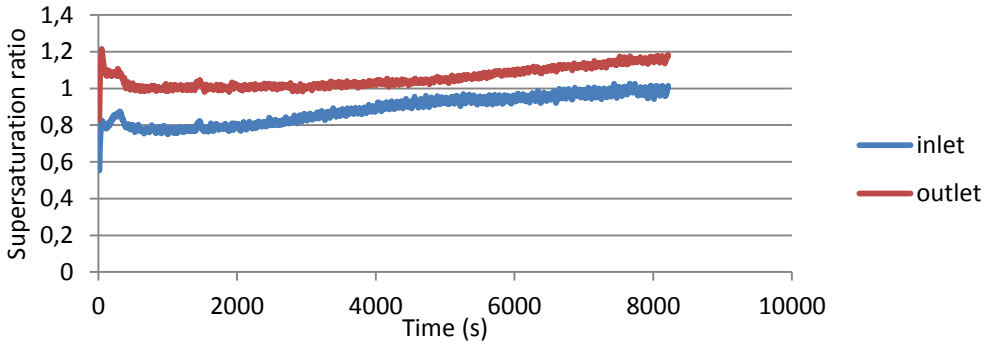

Figure 3.38: Super-saturation ratio at the inlet and the outlet of the tested heat exchanger (8% v/v).

In fact, at the end of the frosting cycle, the intrusive PT100 sensor, installed at the heat-exchanger inlet, allows the measurement of the flue-gas temperature inside the thermal boundary layer and then inside the frost layer. This explains the super-saturation increase at the end of the frosting cycle for both cases.

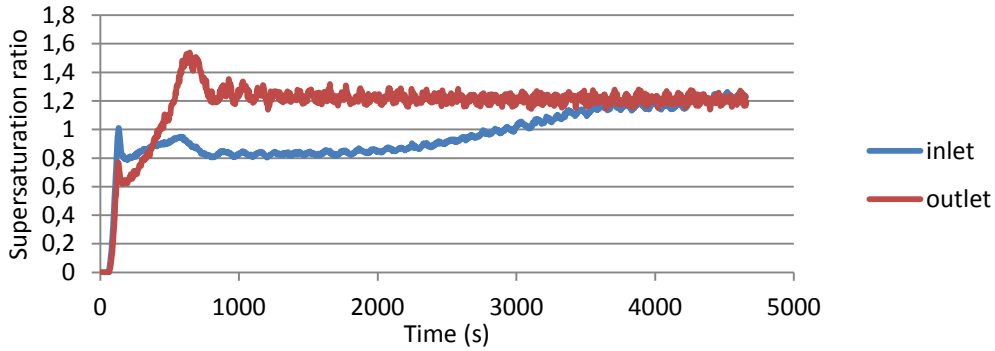

Figure 3.39: Super-saturation ratio at the inlet and the outlet of the tested heat exchanger (15% v/v).

The super-saturation is measured with a standard combined uncertainty equal to ±2.75E-02. The effect of this super-saturation difference on the frost formation is analyzed in the following sections.

As described in Figure 2.8, the super-saturation requires to super-cool the flue gases by reducing the refrigerant-evaporation temperatures. In the case of 8% CO_2 concentration, the measured super-saturation ranging between 1.1 and 1.15 means that flue gases are super-cooled by 0.86 K and 1.15 K. In the case of 15% CO_2 concentration, a measured supersaturation of 1.2 means that a super-cooling of 1.75 K is ensured. These calculations show the importance of the super-cooling, then of the refrigerant temperature control, on the frosting process evolution. A high nucleation-rate difference is measured between these two super-saturation conditions (cf. Paragraph 3.7.4.1). In addition, the good affinity between the solid CO_2 crystals and the aluminum fin surfaces (cf. Paragraph 3.7.2.1) improves the heterogeneous nucleation at relatively low super-saturation, then low refrigerant under-cooling.

3.7.2 Solid CO_2 crystal and deposit morphology

3.7.2.1 Crystal morphology

According to the literature study performed in Chapter 2, the CO_2 antisublimation proceeds following the theory of nucleation. At the beginning of the frosting cycle, heterogeneous primary nucleation occurs and solid CO_2 nucleus form on the heat-exchanger fins considered as foreign solid surface (Paragraph 2.2.3). In order to verify the heterogeneous nucleation theory in CO_2 antisublimation, the heat-exchanger fins are visualized under low (X30) and high (X200) magnification ratios in this experimental survey. Figure 3.40 shows the formation, on the heat-exchanger fins, of the first solid CO_2 deposit. Two cases are taken into account. The first considers 18% v/v of CO_2 concentration in the flue gases and the second result is for 3% v/v CO_2 concentration. Hence, independently of the solute concentration, the primary heterogeneous nucleation occurs in the CO_2 antisublimation process. Spherical nucleuses form on the fins, showing a good affinity between the solid CO_2 and the aluminum alloy. According to Paragraph 2.2.3.1, this affinity induces- the decreases of the critical free energy change required to form new nucleuses (Figure 2.7). Hence, any consideration of surface treatment to enhance primary heterogeneous nucleation is necessary.

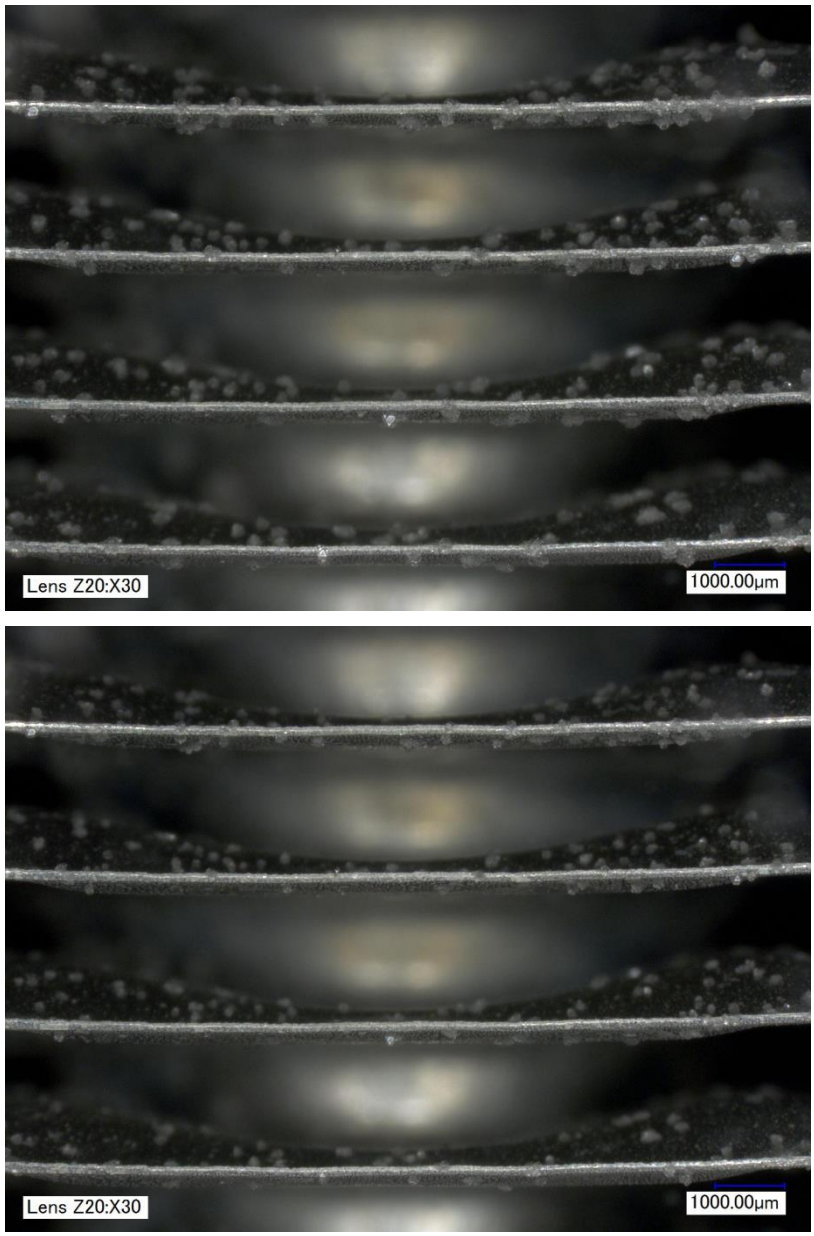

a)
(18% v/v)

b)
(3% v/v)

Figure 3.40: CO_2 heterogeneous nucleation on the heat-exchanger fins.

Figure 3.41 shows the solid CO_2 crystal formation on the aluminum fins. A good affinity between the fins and the solid crystal is observable with a contact angle of about 90°. It is important to note that this crystal is not a new born embryo. It can be visualized only after a crystal growth occurs.

The formation of these embryos at the beginning of the frosting cycle is essential to the formation of the solid deposit and its growth. These embryos form the basis of the solid layer formation. After the first embryos deposition, the mass transfer is induced by the growth of embryos and by the secondary nucleation, where new nucleus will form on the existing ones.

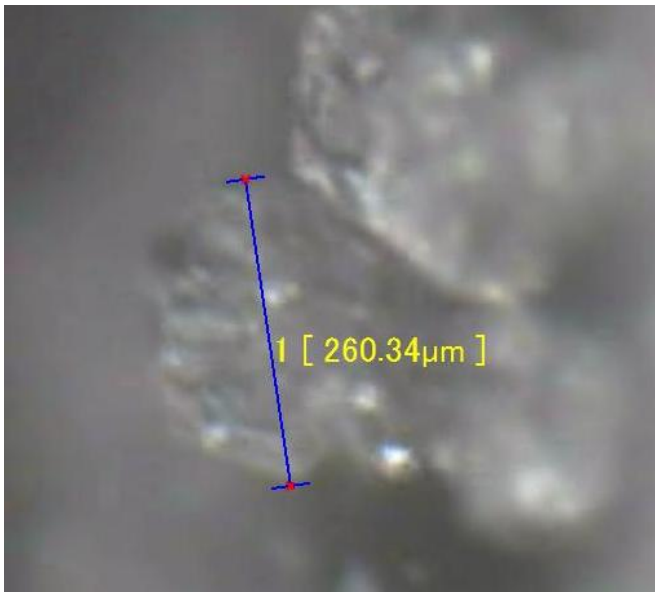

Figure 3.41: Solid CO_2 spherical crystal (magnification: 200X).

3.7.2.2 Deposit morphology

Unlike the solid CO_2 crystal morphology, the deposit morphology depends on the CO_2 concentration in the equivalent flue gases. At high CO_2 concentrations (8%, 15%, and 18% v/v), the solid deposit has a granular appearance while at low concentration (3% v/v) crystal lattice could be identified with a high porous aspect. Figure 3.42 represents the two solid layers obtained at 15% (a) and 3% v/v (b).

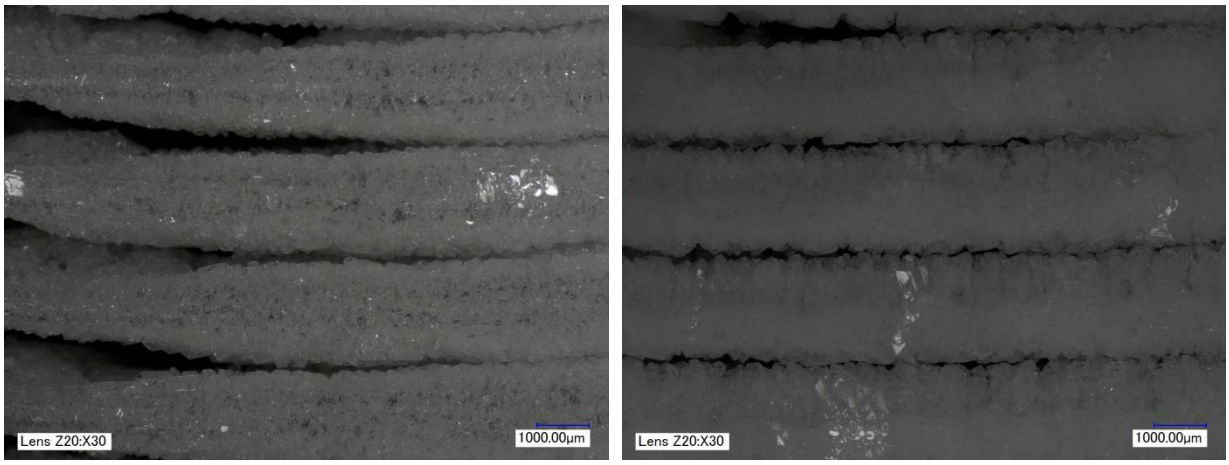

c) 15% v/v *d) 3% v/v*

Figure 3.42: Solid CO_2 deposit morphology as a function of the CO_2 concentration in flue gases.

As shown in Figure 3.42, the solid deposit seems to have a higher density at 15% than the deposit at 3% v/v CO_2 concentration since it is more transparent in the first case. The density and porosity of the solid layer are studied in Paragraph 3.7.5.

3.7.3 Solid CO_2 layer thickness evolution monitoring

A literature study is performed in order to identify the technologies already used to measure the frost thickness evolution. Four main technologies are found. The first one consists in the usage of a micrometer (Figure 3.43) and requires a good accessibility to the frost surface making it useless for fin-and-tube heat exchangers. The second technology is the light slit method used by Sanders to measure the water vapor frost formation on a flat plate [SAN74]. A light slit is reflected on the frost surface and is projected on the opposite side of the light

source. The position of the reflected light is monitored calculating the frost thickness. This technique requires also a free accessibility to the frost layer from two sides, which is not possible in our application. The third technology found in the literature is the low-energy laser beam source used by B. Na and R. Webb [NA04]. A laser beam is moved normal to the frost surface and is detected on the other side on a light meter. When the laser beam scattered on the frost surface, its position monitoring is used for calculating the frost thickness. This technique requires, as the two techniques already described, a good accessibility to the frost layer from both sides. The fourth technique is the imaging system used in several frost studies [SHIN03] and is useful since no contact with the frost layer is required. This technique is chosen for this experimental study and allows the measurement of the real time necessary to the frost layer growth.

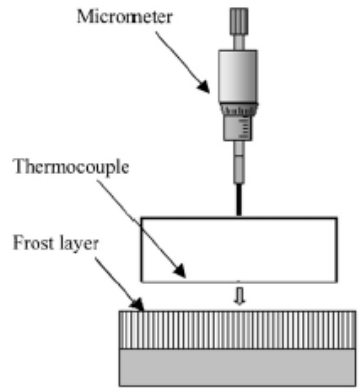

Figure 3.43: Frost thickness measuring using a micrometer [LEE01].

In this survey, the solid CO_2 deposit is monitored using a digital microscope and photos are taken every 15 s. 30x observation magnification is used to follow the solid deposit thickness evolution on 4 fins and to identify the morphology of the frost layer. The layer thickness is measured using the VHX-1000 communication software. The measurement software is automatically calibrated using a special glass scale in order to improve the measure accuracy. Using this software, measurements are performed with a precision of ±0.01 µm. The major thickness measure uncertainty is due to the operator reading errors and it is estimated to be in the order of 5 µm.

3.7.3.1 Local evolution of the solid CO_2 layer thickness

Figure 3.44 represents the solid CO_2 deposit thickness evolution as a function of the time during the frosting cycle. For the three tests performed at different CO_2 concentrations, the thickness evolution has a similar aspect and it is divided into 3 periods. During the first period, at the beginning of the frosting cycle, a first deposit takes place during which embryos form on the fins and growth. For 8% CO_2 concentration, this period lasts between 0 and 2000 s. At the end of the first period, the crystal-surface temperature increases limiting the deposit formation and growth. During the second period, which lasts between 2000 and 4000 s, the mass transfer takes place inside the solid layer by forming new embryos on the fins and by the growth of existing ones; a slight increase and decrease alternation of the layer thickness is observable. It is due to the frost surface temperature, which is close to the CO_2 sublimation temperature and not able to form stable solid crystals at the frost surface. The vapor CO_2 near the frost-layer surface is at metastable conditions (cf. Figure 2.3) where the super-cooling is not able to frost it and form stable crystals. After the phase of frost densification, the solid layer thermal conductivity increases, decreasing the frost surface temperature and starting the third frosting period. During this period, the layer thickness increases linearly at a constant deposit average density (Paragraph 3.7.5). The three frosting periods described are represented in Figure 3.54.

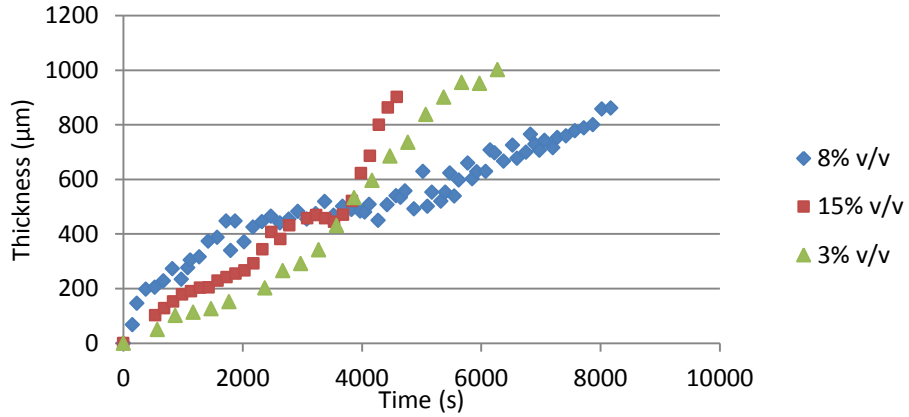

Figure 3.44: Solid CO_2 layer thickness evolution.

A thickness evolution difference is observable between the case of 8% CO_2 concentration and the two other cases for which the thickness grows faster. This fact is independent of the CO_2 concentration and depends mainly on the mass transfer rate, which depends on the super-saturation. According to Paragraph 3.7.1, the test at 8% CO_2 concentration is performed at a lower super-saturation ratio.

In Figure 3.45 are represented the solid deposit thickness measurements and visualization during the frosting cycle. It is observable that at the first frosting period, the deposit is porous and solid crystals do not form on the entire fin surface. The layer seems to be homogeneous in the visualized fin surface at T = 3975 s, when the frost is present all over the fin surface. The third period of frosting is observable in the period between 4125 s and 4725 s during which the frost thickness increases again. The granular aspect of the frost is also observable on these photos.

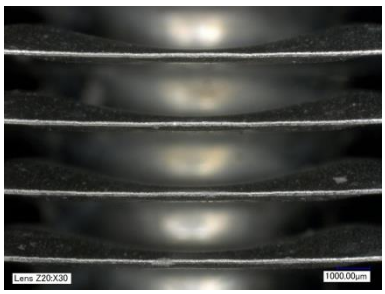
T = 0 s

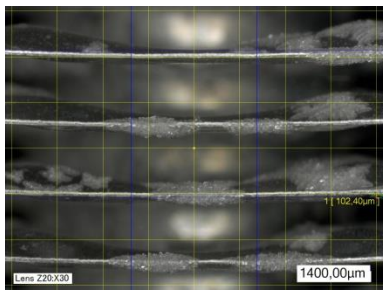
T = 375 s

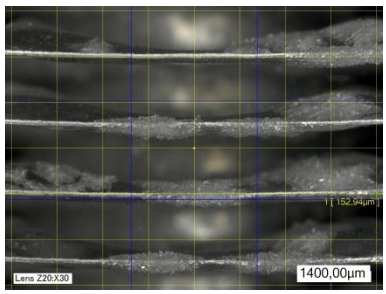
T = 675 s

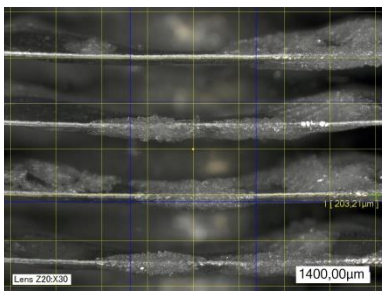
T = 1125 s

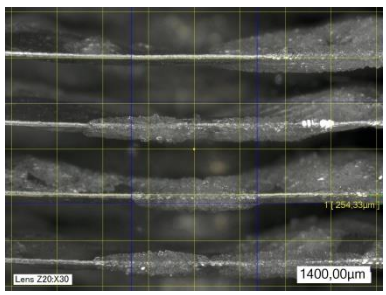
T = 1725 s

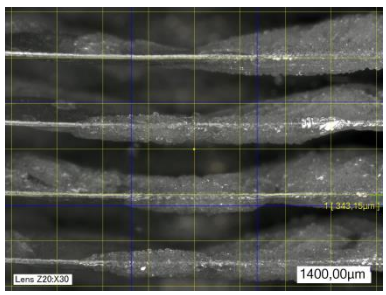
T = 2175 s

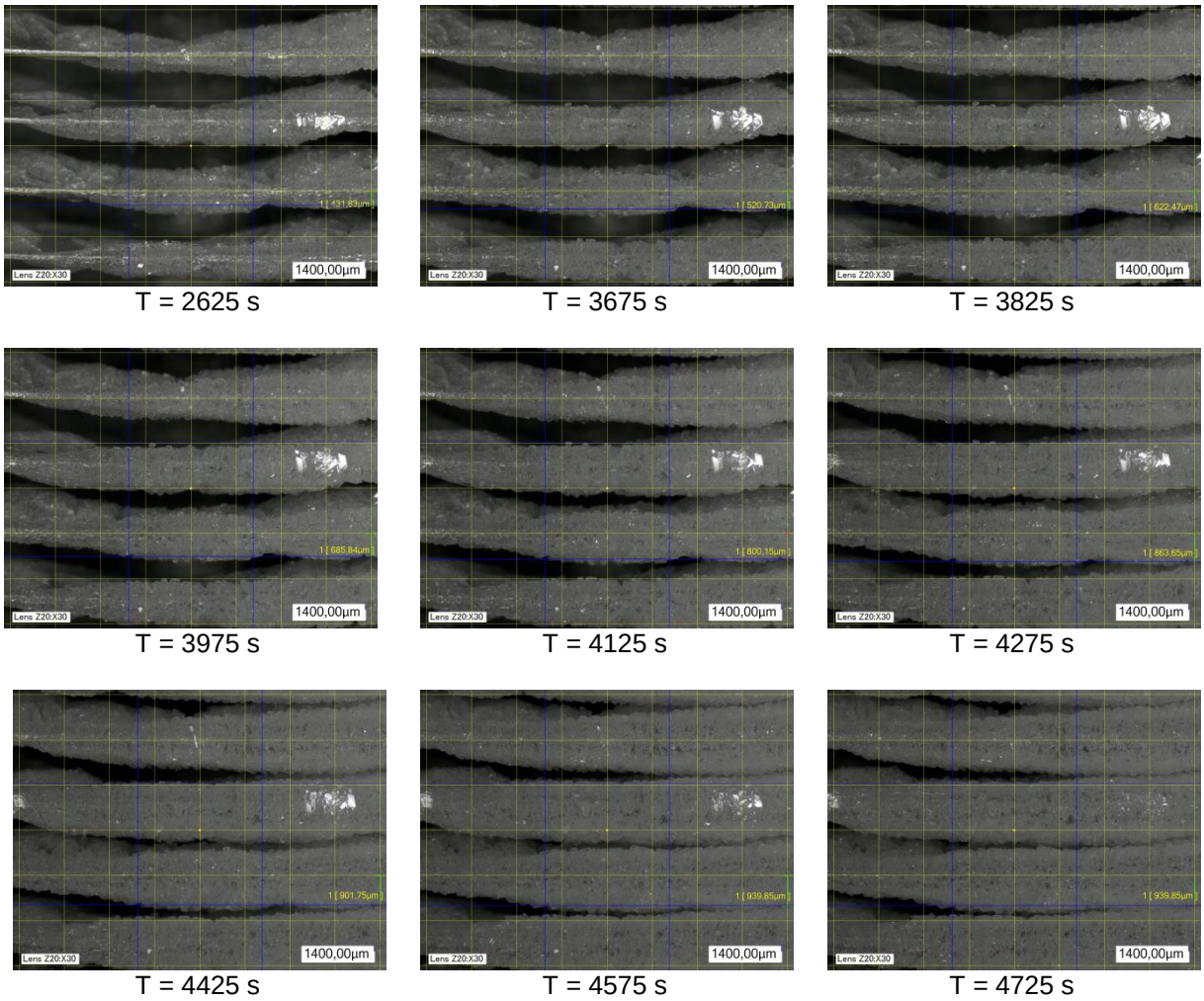

Figure 3.45: Solid CO_2 deposit thickness evolution and measurement (15% v/v).

3.7.4 Mass transfer measurement

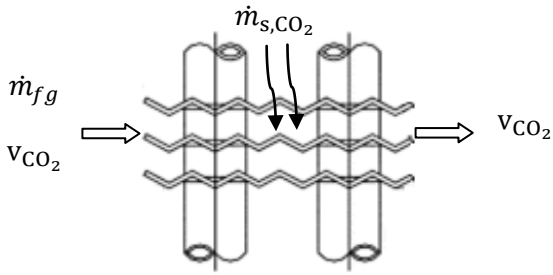

Figure 3.46: Mass transfer measurement on the tested fin-and-tube heat exchanger.

Since the EFG are composed by mixing 95% N_2 and 5% O_2 standard mixture with CO_2, the gas flow molar composition is calculated by measuring only the CO_2 molar concentration. This concentration is continuously measured at the inlet and the outlet of the tested three-row back staging fin-and-tube heat exchanger. In order to calculate the solid CO_2 nucleation rate in the tested zone, the total flue-gas mass flow rate, $\dot{m}_{fg}$, is measured at the inlet by the thermal mass flow meter. This flow rate is calculated at the outlet of the tested zone by applying the component mass conservation for the oxygen or for the nitrogen, since they are superheated in the gas stream and they do not antisublimate. The deposited solid CO_2 flow

rate is the difference between the vapor CO_2 mass flow rate at the inlet and at the outlet of the tested stages (Equation (3.9)).

$$\dot{m}_{s,CO_2}(t) = \left(\dot{m}_{CO_2}\right)_{in} - \left(\dot{m}_{CO_2}\right)_{out}$$
$$\dot{m}_{s,CO_2}(t) = \left[\dot{m}_{fg}\frac{44\ v_{CO_2}}{M_{fg}}\right]_{in} - \left[\dot{m}_{fg}\frac{\left(1-v_{CO_2}\right)}{M_{fg}}\right]_{in} \cdot \left[\frac{44\ v_{CO_2}}{\left(1-v_{CO_2}\right)}\right]_{out} \quad (3.9)$$

Where M_{fg} is the flue-gas molar weight calculated as a function of the measured CO_2 concentration at the inlet and the outlet of the tested stages:

$$M_{fg} = 15.8\ v_{CO_2} + 28.2 \quad (3.10)$$

The CO_2 nucleation rate per unit surface is calculated by dividing $\dot{m}_{s,CO_2}$ by the heat exchanging surface, which is 0.475 m²/m of finned tube (manufacturer data). For the tested three-row stages, this surface is 2.14 m².

$$I_{s,CO_2}(t) = \frac{\dot{m}_{s,CO_2}}{A_{HX}} \quad (3.11)$$

The total weight of the CO_2 deposit on the tested heat-exchanger zone is the sum of the nucleation rate multiplied by the time step $dt = 3\ s$. The weight of the gas phase contained in the porous deposit is neglected.

$$m_{s,CO_2}(t) = \sum_{0}^{t} \dot{m}_{s,CO_2}.dt \quad (3.12)$$

In Figure 3.47 are plotted the CO_2 concentrations at the inlet and the outlet of the tested heat exchanger. In addition to the measured EFG mass flow rate at the heat-exchanger inlet, these measurements allow the calculation of the mass transfer and the nucleation rate.

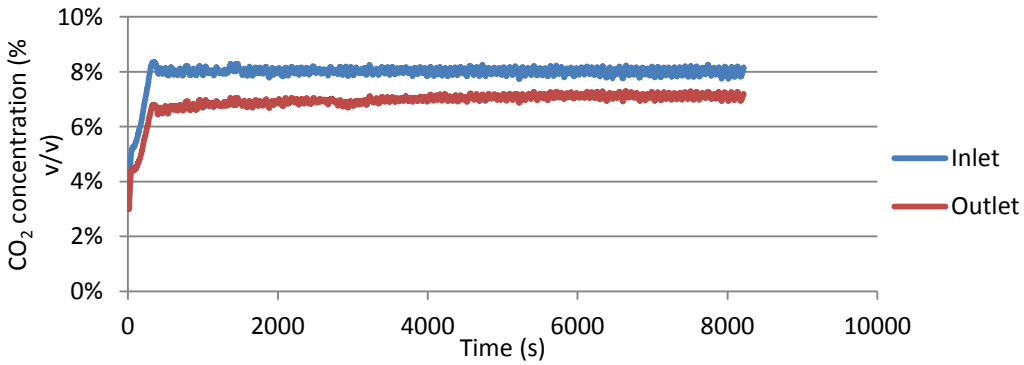

Figure 3.47: CO_2 Concentration at the inlet and the outlet of the tested heat exchanger.

In order to verify the calculation of the overall CO_2 nucleation rate by the experimental procedure described in this paragraph, the weight of the injected CO_2 cylinder in the closed flue-gas circuit is monitored (Figure 3.48).

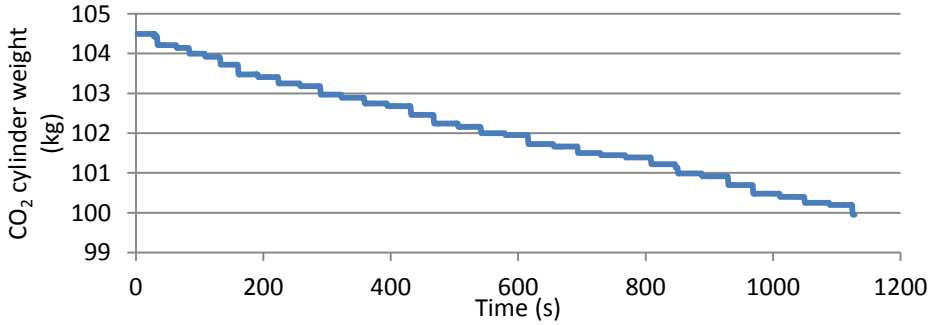

Figure 3.48: CO_2 cylinder weight monitoring.

The cumulated mass of the injected CO_2 in the EFG circuit and the total CO_2 deposit weight on the tested heat exchanger, calculated using Equation (3.12), are plotted in Figure 3.49.

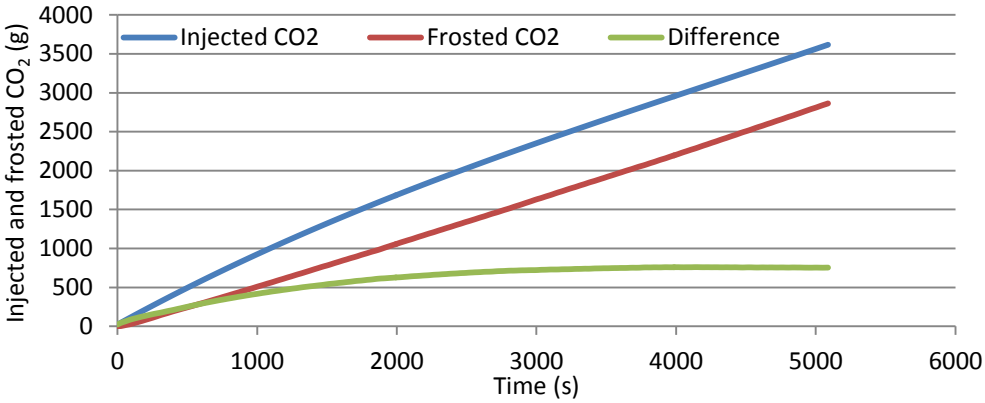

Figure 3.49: Injected and frosted CO_2 weights measured during a frosting cycle.

Figure 3.49 shows a difference, at the frosting cycle beginning, between the injected and the frosted CO_2 measured weights. This difference is explicable and it is a result of the CO_2 frosting outside the heat-exchanger tested zone. Before starting CO_2 injection, the entire heat exchanger and its enclosure are at temperatures below the CO_2 sublimation temperature. After the temperature equilibration of the circuit, the difference between these two cumulated weights becomes constant. Experimental data represented in Figure 3.49 are for the test with 3% CO_2 concentration conditions. 750 g from the injected CO_2 is frosted on the pre-cooling heat exchanger and on the flue-gas ducts. Hence, a good accuracy is proved for calculating the frosted CO_2 weight by measuring the total flue-gas mass flow rate and the CO_2 molar concentration downstream and upstream the tested zone.

3.7.4.1 Nucleation rate

In Figure 3.50 are plotted the nucleation rates measured in experiments for two different CO_2 concentrations. This nucleation rate difference is not induced by the CO_2 concentration difference between the two experiments conditions, but caused by the super-saturation ratio, which is higher in the case of 15% CO_2 concentration (cf. Paragraph 3.7.1). For the two cases, a high nucleation rate is measured at the frosting cycle beginning and it decreases during the solid layer formation. In the case of 15% v/v CO_2 concentration, for which the super-saturation is equal to 1.2, the nucleation rate reaches $3.4E^{-04}$ $kg.m^{-2}.s^{-1}$ and decreases during the frost formation, reaching $2.4E^{-04}$ $kg.m^{-2}.s^{-1}$ at the frosting cycle end. This nucleation rate ranges between $2.2E^{-04}$ and $1.2E^{-04}$ $kg.m^{-2}.s^{-1}$ for the experiment performed at 8% v/v, for which the super-saturation is equal to 1.1. This nucleation rate decrease is due to the decrease of the global heat transfer coefficient between the flue gases and the refrigerant. At the beginning of the frosting process, the roughness of the frost layer enhances the heat transfer between the flue gases and the fins. After the first deposition formation, the heat transfer decreases due to the solid deposit thermal resistance, increasing then decreasing the mass transfer from the flue gases to the solid deposit. The nucleation rate is calculated with a combined standard uncertainty of $\pm 2.23E^{-05}$ $kg.m^{-2}.s^{-1}$ calculated using Equation (3.7).

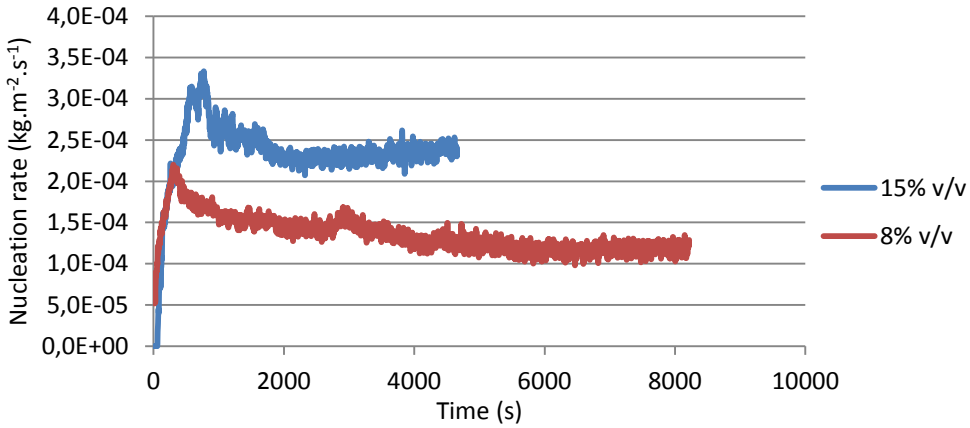

Figure 3.50: CO_2 nucleation rates measured for 15% and 8% v/v CO_2 concentrations.

In addition to the calculated nucleation rate increase, showing its dependency on the super-saturation, the effect of the later on the nucleation is observable at the frosting cycle beginning while primary heterogeneous nucleation occurs. The primary heterogeneous nucleation on the heat-exchanger fins is represented in Figure 3.51 for two different super-saturation ratios. The number of formed embryos is much higher for a super-saturation ratio of 2.0 than for 1.2 super-saturation ratio.

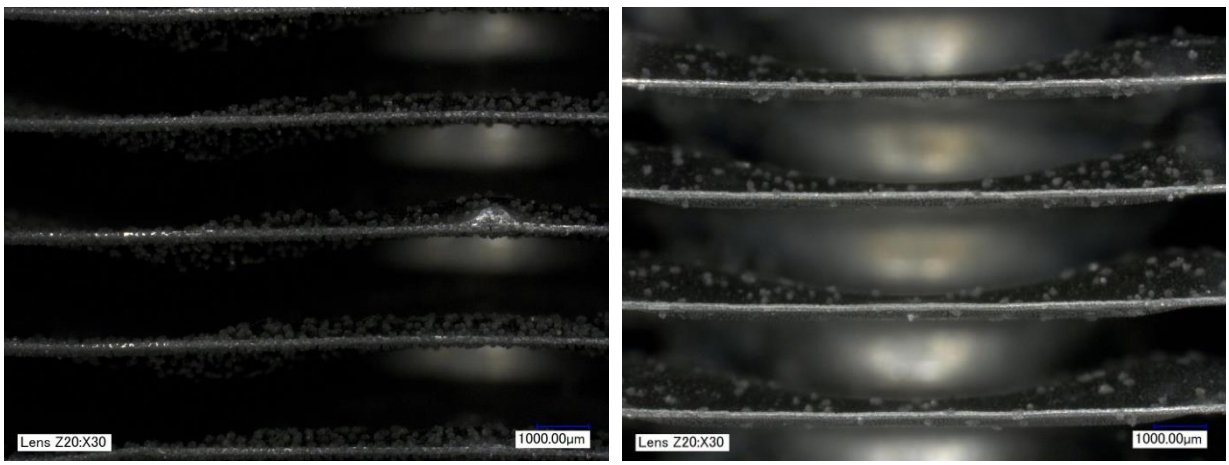

a) S = 2.0 b) S = 1.2

Figure 3.51: CO_2 primary heterogeneous nucleation on the heat-exchanger fins for two different super-saturation ratios.

This fact is very important in the antisublimation CO_2 capture process. At the frosting cycle beginning, the formation of large number of embryos on the heat-exchanger fins increases the mass transfer by nucleuses growth for a constant super-saturation ratio. The formation of larger number of embryos during the primary nucleation allows also the formation of a homogeneous solid deposit. In Figure 3.52 are represented the two solid layers formed after 2000 s of frosting. The frost deposit formed from high super-saturation ratio at the frosting cycle beginning is denser and is more homogeneous all over the heat exchanger. Hence, it is important to control a relatively high super-saturation (S = 2) at the frosting cycle beginning by super-cooling the heat exchanger during the conditioning operating mode.

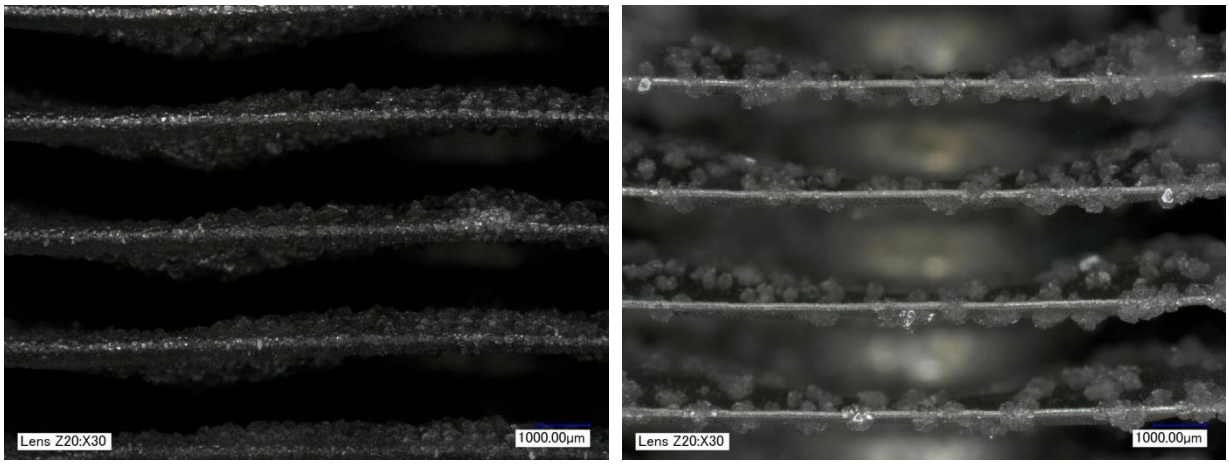

a) S = 1.2 b) S = 1.2

Figure 3.52: CO_2 solid deposit formation formed by two different beginning super-saturation ratios.

3.7.4.2 Solid CO_2 layer total weight evolution

In Figure 3.53 are plotted the total weight of the frosted CO_2 deposit evolution as a function of the temperature. Three cases are represented for different CO_2 concentrations and at different super-saturation ratios. As shown in the previous paragraph, the solid CO_2 accumulation does not depend on the concentration. This fact is observable in Figure 3.53. The accumulation rate decreases at the end of the frosting cycle due to the nucleation rate decreasing.

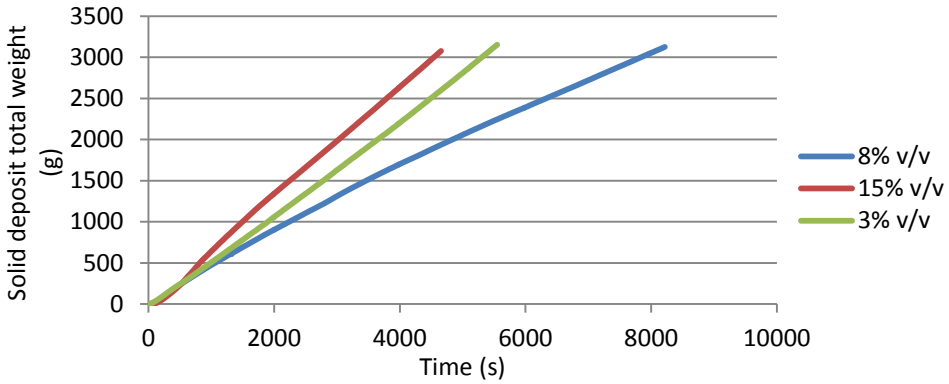

Figure 3.53: Solid CO_2 layer total weight evolution.

3.7.5 Solid CO_2 layer average density and porosity

The solid CO_2 deposit average density is calculated knowing the weight of frosted CO_2 and the deposit thickness. As noted above, the weight of the porous frost layer does not include the neglected weight of the vapor phase.

$$\bar{\rho}_{dep,CO_2}(t) = \frac{m_{s,CO_2}(t)}{\delta(t)\,.\,A_{HX}} \tag{3.13}$$

The porosity of the frost layer is calculated by dividing the vapor volume to the total volume of the deposit and it varies from 0 to 1. The porosity is also expressed as in Equation (3.14) since the total volume of the deposit is the sum of the vapor and solid volume as for its total weight.

$$\varphi_{dep,CO_2}(t) = \frac{V_v}{V_{deposit}} = \frac{\bar{\rho}_{dep,CO_2}(t) - \rho_{s,CO_2}(T)}{\rho_{fg}(T) - \rho_{s,CO_2}(T)} \tag{3.14}$$

The solid phase density is calculated using the correlated solid CO_2 density as a function of the temperature (Equation (15) in Chapter 1), while the flue-gas density is calculated by Refprop V9.0. The solid and vapor phases of the deposit are assumed to be at a temperature equal to the average refrigerant temperature between the inlet and the outlet of the test zone. This assumption does not disadvantage the accuracy of the porosity calculation since the solid CO_2 density variation is less than 1 $kg.m^{-3}.K^{-1}$ for temperatures ranging between -100°C and -120°C. The flue-gas density variation at these temperatures is approximately equal to 0.02 $kg.m^{-3}.K^{-1}$.

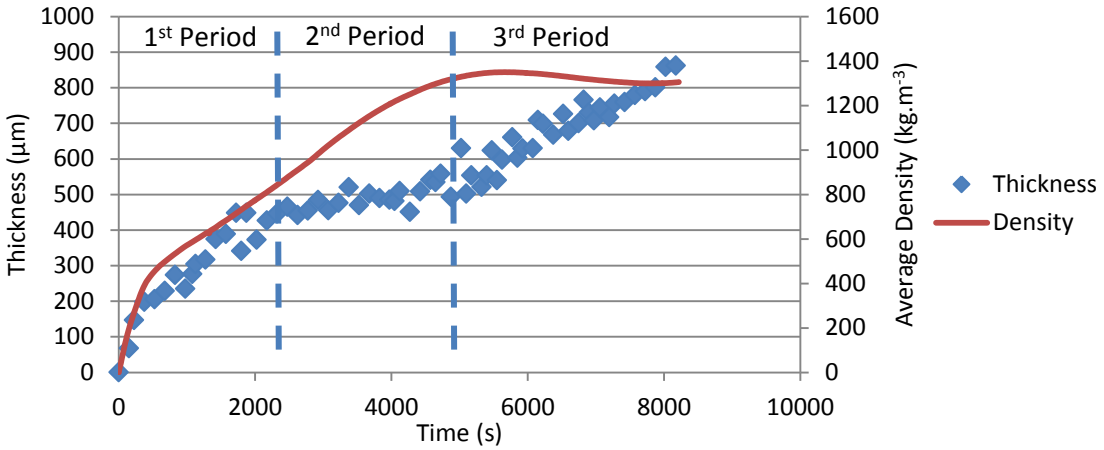

Figure 3.54: Solid CO_2 density and thickness evolution (8% v/v).

In Figure 3.54 are plotted the solid deposit average density and thickness evolution. The three phases of deposit growth discussed in Paragraph 3.7.3.1 are observable. After the first frost formation at low density (0 – 2000 s), a period of densification takes place during which the mass transfer occurs at constant thickness. During this densification, the apparent thermal conductivity of the solid deposit increases allowing the decreasing of the deposit surface temperature. The calculation of the deposit thermal conductivity is not possible since the deposit surface temperature is not measurable in this heat-exchanger configuration. The last phase of deposit growth takes place at constant average density.

For the experiment performed at 8% v/v CO_2 concentration, the average density of the solid deposit is equal to 1305 $kg.m^{-3}$. This density is equal to 1178 $kg.m^{-3}$ for the experiment performed at 15% v/v. This difference is due to the nucleation rate, which is higher in the second case. Hence, the solid deposit formed at low nucleation rate presents higher average density than deposit formed at high nucleation rate. For the case of 3% v/v of CO_2 concentration, for which the nucleation rate is ranging between the two previous cases, the measured average density is equal to 1060 $kg.m^{-3}$. This low density is the result of the porous deposit morphology different from the granular morphology obtained at high concentrations. Then, at low solute concentrations, the deposit average density is lower than the deposit formed with high concentrations.

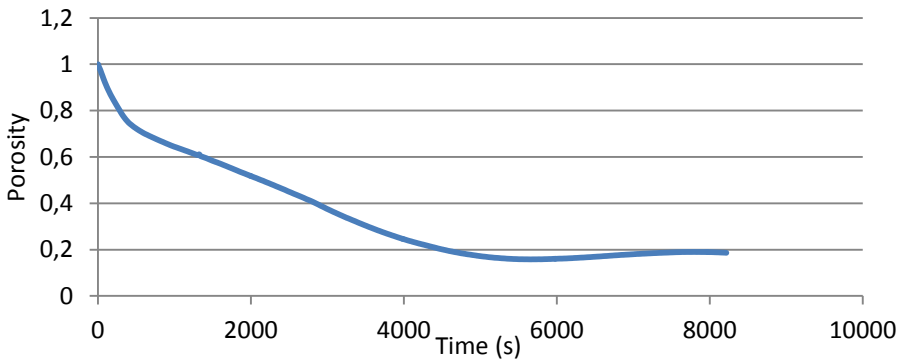

Figure 3.55: Solid CO_2 deposit porosity evolution (8% v/v).

3.7.6 Sensible and latent cooling capacity measurement

The cooling capacity delivered at the tested three-row back staging fin-and-tube heat exchanger is calculated using Equation (3.15). The EFG mass flow rates are calculated using measured flue-gas mass flow rate at the inlet of the tested heat-exchanger part and measured CO_2 molar concentration at its inlet and outlet (Equations (3.16)-(3.18)). The deposited solid CO_2 mass flow rate is calculated by Equation (3.9). The EFG enthalpies are calculated using Refprop. Knowing the partial pressure and the temperature of every substance, its enthalpy is calculated in the superheated or saturated state. The solid CO_2 enthalpy is calculated using Equation (8) (Chapter 1). The temperature of the deposited solid CO_2 is assumed to be equal to the average inlet and outlet refrigerant temperatures.

$$\dot{Q}_{fg} = \sum_{i=N_2,O_2,CO_2} \dot{m}_{i,out}\left(h_{i,vap,out} - h_{i,vap,in}\right) + \left[\dot{m}_{s,CO_2}\left(h_{s,CO_2} - h_{in,vap,CO_2}\right)\right] \tag{3.15}$$

$$\left(\dot{m}_{O_2}\right)_{out} = \left(\dot{m}_{O_2}\right)_{in} = \left[\frac{1.6\left(1 - v_{CO_2}\right)}{M_{fg}}\right]_{in} \tag{3.16}$$

$$\left(\dot{m}_{N_2}\right)_{out} = \left(\dot{m}_{N_2}\right)_{in} = \left[\frac{26.6\left(1 - v_{CO_2}\right)}{M_{fg}}\right]_{in} \tag{3.17}$$

$$\left(\dot{m}_{CO_2}\right)_{out} = \left[\dot{m}_{fg}\frac{\left(1 - v_{CO_2}\right)}{M_{fg}}\right]_{in} \cdot \left[\frac{44\, v_{CO_2}}{\left(1 - v_{CO_2}\right)}\right]_{out} \tag{3.18}$$

Sensible and latent cooling capacities are calculated and plotted in Figure 3.56. The heat transfer decreases during the frost deposit formation. The frost accumulation on the heat exchanger leads to the decrease of the global heat transfer coefficient.

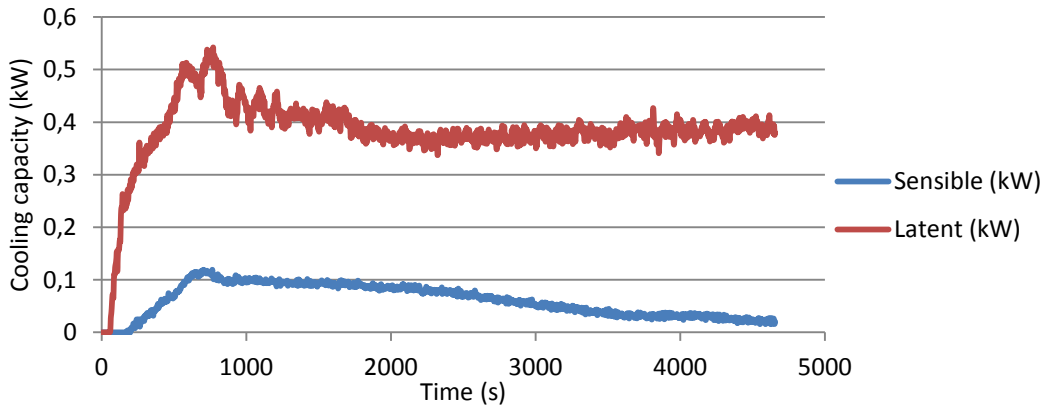

Figure 3.56: Sensible and latent cooling capacity evolution (15% v/v).

3.8 Conclusions

The experimental study of the CO_2 antisublimation in a fin-and-tube heat exchanger has shown that the antisublimation proceeds according to the classical nucleation theory. The visualization of the CO_2 solid crystal formation shows a good affinity between the solid CO_2 and the heat-exchanger aluminum fins. This good affinity, as described in the heterogeneous nucleation theory, enhances the formation of CO_2 embryos on the fin surface. Heterogeneous spherical embryos formation is independent from the CO_2 concentration in the flue gases. The same crystal morphology is observed at high and low CO_2 concentrations. The visualization of the solid deposit formation shows difference between solid layers formed at high and low CO_2 concentrations. At high concentrations, 8%, 15%, and 18% v/v, the solid layer has a granular morphology with a relative high density. At low CO_2 concentrations, 3% v/v, the solid deposit has lattice morphology where crystal plane edges are visible. The deposit formed at low solute concentration is relatively porous compared to the deposit formed at high concentrations.

By visualization of the solid CO_2 deposit growth, three periods of deposit formation are identified. The first deposit takes place as a primary heterogeneous nucleation and is directly affected by the super-saturation ratio. For higher super-saturation ratio, more solid embryos are able to form enhancing the mass transfer during the second evolution period. The second evolution period occurs at constant deposit thickness for which the mass transfer proceeds by CO_2 diffusion in the solid porous layer. During this period the average density of the deposit increases; this in turn increases the thermal conductivity of the deposit. This densification leads to the decrease of the frost surface temperature allowing the beginning of the third frost evolution period.

The measurement of the nucleation rate shows that it depends mainly on the super-saturation ratio. For higher super-saturation ratio, the nucleation rate increases. The average density of the solid deposit depends on the nucleation rate, then on the super-saturation ratio. For low nucleation rates, the average density of the solid deposit increases. At the frosting cycle beginning, super-saturation can enhance the homogeneity and increases the deposit density.

Experimental results will be used in Chapter 4 in order to validate the CFD dynamic model simulating the CO_2 frosting on a fin-and-tube heat exchanger.

References

[COO76] **T. Cook, G. Davey**, The density and thermal conductivity of solid nitrogen and carbon dioxide, CRYOGENICS, 1976.

[MAU68] **John S. MAULBETSCH**, An experimental investigation and system design for humidity and carbon dioxide level control using thermal radiation, Aerospace Medical research Laboratory, 1968.

[SHC85] **V. N. Shchelkunov, N. Z. Rudenko, Yu. V. Shostak, V. I. Dolganin**, Surface desublimation of carbon dioxide from binary gas mixtures, translated from Inzhenerno-Fizicheskii Zhurnal, Vol. 51, No. 6, pp. 965-970, December, 1986. Original article submitted September 10, 1985.

[VER02] **P. Verma, D.M. Carlson, Y. Wu, P.S. Hrnjak, C.W. Bullard,** Experimentally validated model for frosting of plane-fin-round-tube heat exchangers, International Conference of New Technologies in Commercial Refrigeration at University of Illinois at Urbana-Champaign, IL, USA, pp. 152-162, 2002.

[ALJ08] **N.F. Aljuwayhel, D.T. Reindl, S.A. Klein, G.F. Nellis,** Experimental investigation of the performance of industrial evaporator coils operating under frosting conditions, International journal of Refrigeration, Vol. 31, pp. 98 – 106, 2008.

[LEE01] **Y.B. Lee, S.T. Ro,** An experimental study of frost formation on a horizontal cylinder under cross flow, International Journal of Refrigeration, Vol. 24, pp. 468 – 474, 2001.

[SHIN03] **Jongmin Shin, Alexei V. Tikhonov, Cheolhwan Kim,** Experimental Study on Frost Structure on Surfaces With Different Hydrophilicity: Density and Thermal Conductivity, ASME, Vol. 125, pp. 84 – 94, 2003.

[LIU06] **Zhongliang Liu, Hongyan Wang, Xinhua Zhang, Sheng Meng, Chongfang Ma,** An experimental study on minimizing frost deposition on a cold surface under natural convection conditions by use of a novel anti-frosting paint. Part I. Anti-frosting performance and comparison with the uncoated metallic surface, International Journal of Refrigeration, Vol. 29, pp. 229 – 236, 2006.

[DENG03] **Dong-Quan Deng, Lie Xu, Shi-Qiong Xu,** Experimental investigation on the performance of air cooler under frosting conditions, Applied Thermal Engineering, Vol. 23, pp. 905 – 912, 2003.

[ARG01] **Thierry ARGAUD,** Optimisation Energétique Des Cycles de Givrage – Dégivrage des PAC Inversables Air/Eau sur Plancher Destinées au Secteur Résidentiel, 2001.

[MAO92] **Y.Mao, R.W. Besant, K.S. Rezkallah,** Measurement and correlations of frost properties with airflow over a flat plate, ASHRAE Trans. 98, pp. 65 – 78, 1992.

[FAH96] **Per Fahlén,** Frosting and defrosting of air-coils, Ph.D. thesis, Chalmers University of Technology, 1996.

[NA04] **Byeongchul Na, Ralph L. Webb**, New model for frost growth rate, International Journal of Heat and Mass Transfer, 47, 925–936, 2004.

[SAN74] **C.T. Sanders**, The influence of frost formation and defrosting on the performance of air coolers, Ph.D. Thesis, Delft Technical University, 1974.

[MOR11] **S. MORTADA**, Etude et modélisation d'une pompe à chaleur intégrée dans un système double flux et utilisant des échangeurs à mini-canaux, Ph.D. thesis, Ecole Des MINES ParisTech, 2011.

[ASHRAE05] **ASHRAE,** Handbook Fundamentals, 2005.

[EN60079] **NF EN 60079-10**, Norme française, Matériels électrique pour atmosphère explosive gazeuse, Partie 10 : classement des régions dangereuses

[EN13005] **NF ENV 13005**, Norme européenne, Guide pour l'expression de l'incertitude de mesure, 1999.

[TAY94] **Barry N. Taylor and Chris E. Kuyatt**, Guidelines for evaluating and expressing the uncertainty of NIST measurement results, NIST Technical Note 1297, 1994.

[DIR67] **Directive n° 67/548/CEE** du 27/06/67 concernant le rapprochement des dispositions législatives, réglementaires et administratives relatives à la classification, l'emballage et l'étiquetage des substances dangereuses.

[AGILENT] www.chem.agilent.com/cag/cabu/whatisgc.htm

Chapter 4. CFD model for CO_2 frosting prediction on a fin-and-tube heat exchanger

4.1 Introduction

As described in Chapter 1, the optimization of the CO_2 frosting fin-and-tube heat exchanger has a major effect on the antisublimation CO_2 capture energy performance. This optimization is based on the design of a heat-exchanger configuration able to frost the flue-gas CO_2 in a homogeneous solid layer and to minimize the temperature difference between flue gases and the refrigerant blend. CO_2 frosting cycle is associated with a dynamic variation of the exterior heat-transfer coefficient due to the frost layer thickness and thermo-physical property variations. These property variations are of the utmost importance for the heat-exchanger design. In addition to the experimental results described in Chapter 3, a model able to predict the frost formation and growth, showing the influence of the heat-exchanger structure on the frosting process, allows the prediction of the optimal heat-exchanger configuration.

Existing frost formation predicting models can be separated into three approaches. The first one considers that the mass transfer increases the frost thickness and the frost density [NA04]. By assuming that the solid is a porous media where the ice particles are distributed in the gas phase, the mass transfer increasing the frost density is calculated by taking into account the diffusion mechanism of vapor in the porous media. The mass transfer increases the frost thickness assuming that the density gradient at the frost surface is equal to zero. The total mass transferred from the vapor to the solid phase is estimated based on experimental results. This method predicts the frost average density and thickness evolution. Contrariwise, it cannot predict the frost behavior as a function of the chilled surface geometrical structure since the frost thickness and density at the beginning of the frost formation are given as initial conditions.

The second approach consists in predicting the mass transfer on and within the frost layer by using the Lewis analogy theory [SEK04]. This method calculates the mass transfer coefficient as a function of the heat-transfer coefficient related by the Lewis number. This model uses experimental correlations and empirical equations, and is called the semi-empirical quasi-steady model. These two methods are not able to predict the frost formation and morphology at the frosting cycle beginning. Hence, they are not able to study the influence of surface structure on frost formation. For this purpose, a new model was developed by J. Cui et al. [CUI11A] [CUI11B] predicting the transient frost formation in addition to its thermo-physical properties. He proposed a CFD (Computational Fluid Dynamics) model using the classical nucleation theory to predict the frost formation and growth.

In this chapter, a 3D CFD model is realized, based on the model proposed by J. Cui et al. [CUI11A], to simulate transient CO_2 frost formation and growth on a fin-and-tube heat exchanger. A physical model, taking into account a fin-and-tube heat exchanger configuration, allows the study of the influence of its geometry properties like the aspect ratio [PER03A] and the fin pitch. This model identifies also the effect of the refrigerant temperature on the CO_2 frost behavior and on the efficiency of the studied heat exchanger. The temperature of the refrigerant is considered as a boundary condition to the model. The energy balance during EFG cooling takes into account the sensible heat of the gases and the latent heat of CO_2 sublimation along the fin and the tube surfaces. This model is based on the nucleation theory studied in Chapter 2 in order to quantify the mass transfer between the gas and the solid phase, and also to predict the frost structure that depends on the fin and flue-gas temperature distribution. The transient local formation of the CO_2 deposit is predicted. In addition, the average thickness, average local density, the average density,

and the cooling capacity are calculated through the considered system. The simulation results are validated by comparison with the experimental results obtained in Chapter 3.

4.2 Transient CFD modeling for CO_2 antisublimation on a fin-and-tube heat exchanger

According to the experimental study of CO_2 antisublimation in a fin-and-tube heat exchanger described in Chapter 3, the frosting cycle is divided into three periods. During the first period, spherical CO_2 embryos form on the fins and grow up forming a porous solid layer. At the end of this period, the surface temperature of these crystals is sufficiently high to stop the crystal growth. The second period is characterized by a mass transfer and frost formation at constant deposit thickness accompanied with frost densification. During this period, the visualization of the frost layer surface shows alternative frost thickness increase and decrease. CO_2 sublimates at the frost surface and antisublimates due to the surface temperature variation affected by the fin and flue-gas temperature variation, and especially by the effective thermal conductivity of the solid deposit. After the densification period, the frost effective thermal conductivity increases and leads to the decrease in the frost surface temperature. The third frosting period occurs with frost thickness evolution at constant density. According to these experimental visualizations and measurements, the frost formation and growth is a complicated process because of the mass transfer variation from the parent to the new phase. This mass transfer is affected by the thermal conditions like the chilled surface and gas-phase temperatures, and also by the geometrical parameters of the system. This mass transfer occurs on two ways as a function of these thermal conditions: the CO_2 frost formation can include periods of sublimation simultaneously with antisublimation. In addition, the frost average density and effective thermal conductivity variation during the frosting cycle is a difficulty while modeling the frosting process.

In this section, the CFD model performed to simulate the CO_2 frost formation and growth on a fin-and-tube heat exchanger is introduced. The physical model representing the heat exchanger is described and then the governing equations of the pressure based on Eulerian-Eulerian multi-phase model are introduced. The masse transfer and the source terms are calculated for each phase using the classical nucleation theory. The effect of the frost formation is integrated into the governing equation by adding these source terms to the continuity, momentum, and energy equations. The numerical results are presented and compared to the experimental results of Chapter 3.

4.2.1 Physical model description

In Figure 4.1 is represented the physical model taken into account for predicting the frost formation on a fin-and-tube heat exchanger. The two vertical planes are considered as symmetry surfaces. The upper horizontal surface is also considered as a symmetry plane and it allows dividing the volume between two consecutive fins. Then, the flow and temperature fields between two consecutive fins are assumed to be symmetric on the middle section.

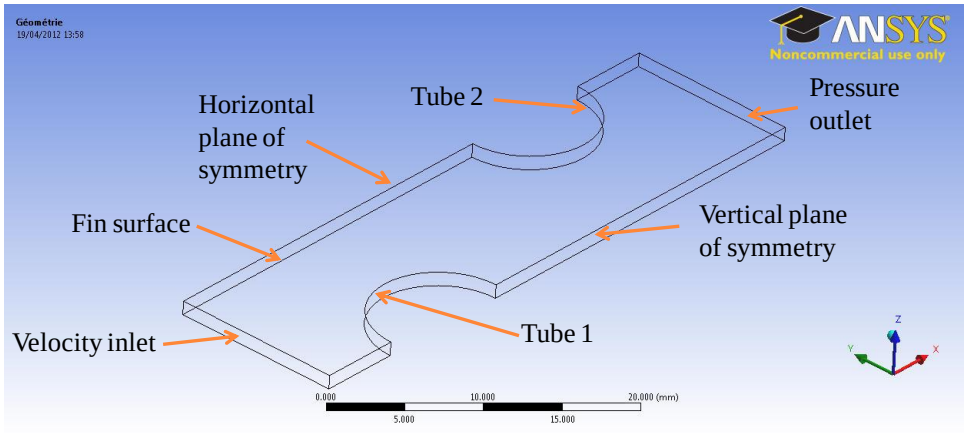

Figure 4.1: 3D heat-exchanger computational domain.

The lower horizontal surface is considered as the heat-exchanger fin. Unlike the herringbone heat exchanger tested in the experimental study, plane fins are considered in this model in order to simplify the system.

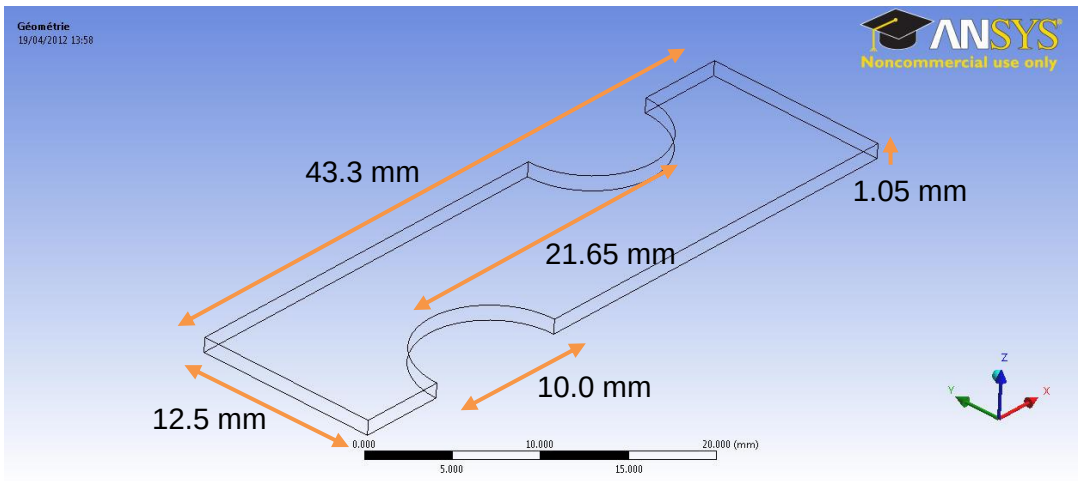

Figure 4.2: 3D heat-exchanger computational domain dimensions.

A two-row fin-and-tube heat exchanger is considered in order to take into account the periodic system geometry and to simulate the effect of the refrigerant gliding temperature on the frost behavior and growth. The tube surface temperatures are fixed as boundary conditions assuming that they are constant during the frosting cycle and independent from the flue-gas flow. These temperatures are considered to be equal to the refrigerant temperature and independent of the flue-gas side heat transfer. The tube external side temperature is automatically imposed to the contact circumferences between the tubes and the fin assuming no thermal contact resistance between them.

In Figure 4.3 is represented the computational grid used in this model. It is formed by 459,240 cells limiting the cell edges to 0.1 mm. The effect of the grid on the frost predicting is not performed in this study.

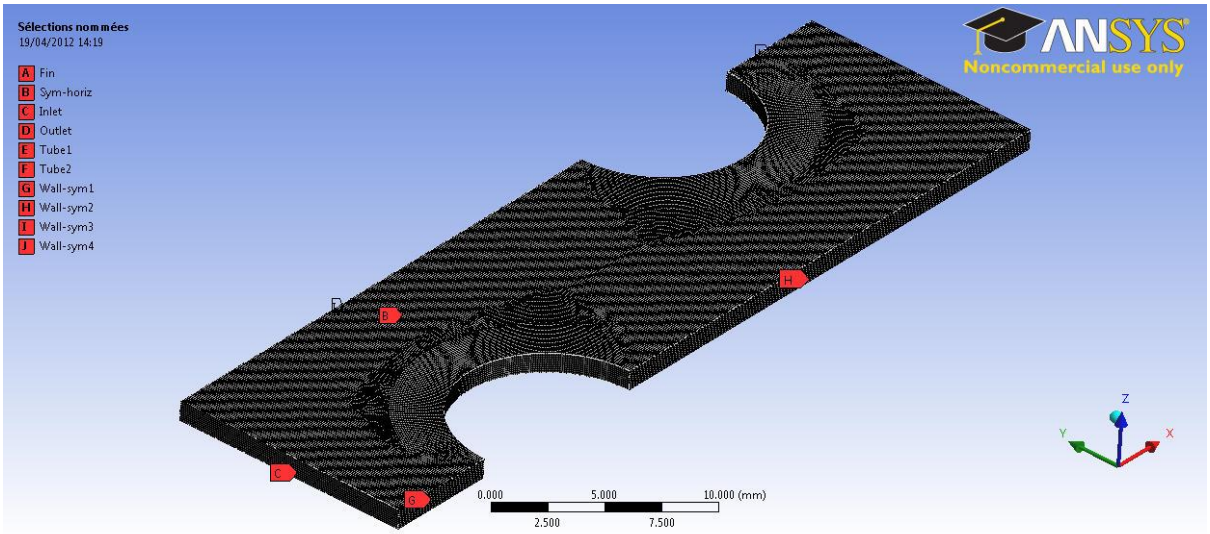

Figure 4.3: Model computational grid.

4.2.2 Mathematical model

For modeling multiphase flow, computational fluid mechanics provides currently two approaches: the Euler-Lagrange approach and the Euler-Euler approach. The Euler-Euler approach treats the different phases as interpenetrating continua using the concept of phase volume fraction to identify the presence of different phases in considered finite volumes. FLUENT provides three different Euler-Euler multiphase models: the volume of fluid model (VOF), the mixture model, and the Eulerian model [FLUENT]. The VOF model is used for predicting the interface evolution between two or more fluids. Mixture and Eulerian models are used for cases where different phases can be treated as interpenetrating continua. The mixture model solves one momentum equation for the mixture while Eulerian model solves a set of momentum, continuity, and energy equations for each phase (Table 4.1).

Table 4.1: Multi-phase models proposed in Fluent [TRO03].

	Mass equation	**Momentum equation**	**Energy equation**	**Scalar equation**
Eulerian	Phase	Phase	Phase	Phase
Mixture	Phase	Mixture	Mixture	Mixture
Volume Of Fluid (VOF)	Phase	Mixture	Mixture	Mixture

According to Fluent user guide [FLUENT], the mixture model is used if there is a wide distribution of the solid phase in the fluid and where the particles grow but do not separate from the primary flow field. Eulerian model is used when the dispersed phases are concentrated in some regions of the domain. In our case of CO_2 antisublimation modeling, the CO_2 solid phase, considered as the secondary phase in the model, precipitates near the fin-and-tube surfaces. Hence, the multiphase Eulerian model is used considering two different phases. The primary phase is the flue-gas continuous phase and the secondary phase is the solid granular CO_2 phase. The primary phase is assumed to be a binary mixture constituted from vapor nitrogen and carbon dioxide and it is treated as incompressible fluid. So, a pressure-based multiphase multi-component model is performed.

4.2.2.1 Governing equations

The governing equations of the transient multiphase and multi-component model are summarized in this section. Continuity, component, momentum, energy, and turbulence equations are presented. Considering the multiphase flow as interpenetrating continua

requires the use of the volume fraction concept. The volume fraction of the q phase α_q is the volume occupied by the phase q in a given volume. The volume of the q^{th} phase can be calculated using Equation (4.1) and the sum of the volume fraction of all phases that constitute the flow is equal to unity.

$$V_q = \int_V \alpha_q \, dV \tag{4.1}$$

$$\sum_{q=1}^{n} \alpha_q = \alpha_s + \alpha_{fg} = 1 \tag{4.2}$$

The subscript s is used to indicate the solid CO_2 phase and fg is used to show the flue-gas vapor phase.

4.2.2.1.1 The mass conservation equations

The continuity equations for the CO_2 solid and flue-gas phases are given respectively in Equations (4.3) and (4.4).

$$\frac{\partial \alpha_s \rho_s}{\partial t} + \nabla \cdot (\alpha_s \rho_s \overrightarrow{u_s}) = \vartheta_{m_s} \tag{4.3}$$

$$\frac{\partial \alpha_{fg} \rho_{fg}}{\partial t} + \nabla \cdot \left(\alpha_{fg} \rho_{fg} \overrightarrow{u_{fg}}\right) = \vartheta_{m_{fg}} \tag{4.4}$$

The term α is the volume fraction ranging between 0 and 1. ρ is the density (kg.m^{-3}) and $\vec{u}$ is the velocity of the two phases. ϑ_{m_s} and $\vartheta_{m_{fg}}$ are the mass source terms of each phase. They are equal and opposite to each other since the mass lost from the vapor phase has to be added to the solid phase due to the antisublimation process. These terms are quantified in Paragraph 4.2.2.2.

$$\vartheta_{m_s} = \left|\vartheta_{m_{fg}}\right| \tag{4.5}$$

4.2.2.1.2 The component conservation equations

In addition to the phase continuity equations, the components continuity equations are required. While frosting, the CO_2 mass transfer occurs between the CO_2 vapors present in the gas phase to the solid phase. The component conservation equation of the primary phase is given in Equation (4.6).

$$\frac{\partial \left(\alpha_{fg} \rho_{fg} Y_{fg}^i\right)}{\partial t} + \nabla \cdot \left(\alpha_{fg} \, \rho_{fg} \overrightarrow{u_{fg}} \, Y_{fg}^i\right) = -\nabla \cdot \alpha_{fg} \, \vec{J}_{fg}^{\,i} + \vartheta_{Y_{fg}^i} \tag{4.6}$$

Y_{fg}^i is the mass fraction of the component i in the flue-gas mixture. $\vec{J}_{fg}^{\,i}$ is the diffusion flux of the component in the mixture. $\vartheta_{Y_{fg}^i}$ is the component source terms induced by the mass transfer between the multi-component flue-gas phase to the solid secondary phase. In this case, binary flue-gas mixture is considered and the sum of the CO_2 and N_2 mass fractions is equal to unity.

$$\sum_{i=1}^{3} Y_{fg}^i = 1 \tag{4.7}$$

4.2.2.1.3 The momentum equations

The momentum equation of phase i (present in the model with the phase j) is given in Equation (4.8). Subscripts i and j are used to identify the two phases.

$$\frac{\partial (\alpha_i \rho_i \overrightarrow{u_i})}{\partial t} + \nabla \cdot (\alpha_i \, \rho_i \overrightarrow{u_i} \, \overrightarrow{u_i}) = -\alpha_i \, \nabla \mathrm{p} + \nabla \cdot \overline{\overline{\tau}}_i \cdot + K_{ji}\left(\overrightarrow{u_j} - \overrightarrow{u_i}\right) + \vartheta_{ui} \tag{4.8}$$

Where p is the pressure, $\overline{\overline{\tau}}_i$ is the i^{th} phase stress-strain tensor given in Equation (4.9), ϑ_{ui} is the momentum source term induced by the mass transfer, and K_{ji} is the exchange coefficient between the phases expressed in Equation (4.10).

$$\overline{\overline{\tau}}_i = \alpha_i \mu_i \left(\nabla \overrightarrow{u_i} + \nabla \overrightarrow{u_i}^T \right) + \alpha_i \left(\lambda_i - \frac{2}{3}\mu_i \right) \nabla \cdot \overrightarrow{u_i} \overline{\overline{I}} \tag{4.9}$$

$$K_{ji} = \frac{\alpha_i \, \alpha_j \, \rho_i f}{\tau_j} \tag{4.10}$$

μ_i and λ_i are the shear and bulk viscosity of the phase i, $\overline{\overline{I}}$ is unit tensor, f is the drag fraction, and τ_j is the particulate relaxation time expressed in Equation (4.11) where $\bar{r}$ is the average solid CO_2 droplet radius.

$$\tau = 2\rho\bar{r}^2/9\mu \tag{4.11}$$

More details on the calculation of these quantities are given in FLUENT User's Guide [FLUG].

4.2.2.1.4 Energy conservation equations

A phase enthalpy equation is used in Eulerian model to describe the energy conservation.

$$\frac{\partial(\alpha_i \rho_i h_i)}{\partial t} + \nabla \cdot (\alpha_i \, \rho_i \overrightarrow{u_i} \, h_i) = \nabla \cdot (k_i \nabla T_i) + \vartheta_{hi} \tag{4.12}$$

h_i is the specific enthalpy of phase i and ϑ_{hi} is the energy source term due to the mass transfer process.

4.2.2.1.5 Turbulence model

In order to simulate the flow behavior during the frosting cycle, the standard $k-\varepsilon$ turbulent model is used. Even if the Reynolds number is lower than its critical value, 2300, at the frosting cycle beginning, it increases and reaches values greater than 2300 after the formation of the solid layer and the decrease in the flue-gas stream passage sections. Then the laminar model is not able to simulate the fluid flow behavior downstream the tubes and inside the frost layer. The standard $k-\varepsilon$ turbulent model has also been used by J. Cui et al. [CUI11A] [CUI11B], by D. Yang et al. [YAN06], in order to predict the frost formation on a cold surface and on a fin-and-tube heat exchanger under turbulent flow.

For modeling turbulence in multiphase flows, Fluent provides three methods that use the turbulent $k-\varepsilon$ model: mixture turbulence model, dispersed turbulence model, and per-phase turbulence model. These methods treat the coexisting phases in different manners depending on the studied flow behavior and the importance of the secondary phase turbulence. The mixture turbulence model uses mixture velocities and mixture properties for modeling turbulence. It is used for the applications where secondary phases separate from the primary one and it is limited for models where the density ratio between phases is close to unity. The mixture turbulence model is not useful for modeling CO_2 frost formation since a high-density difference exists between the solid phase (~1500 $kg.m^{-3}$) and the gas phase (~2.5 $kg.m^{-3}$). The dispersed turbulence model is used for applications where the secondary phase is dispersed and diluted in the primary phase and the particle collisions of the secondary phase are negligible. Hence, this turbulence model is not useful for the CO_2 antisublimation modeling. In the case of $k-\varepsilon$ turbulence model for each phase, the multiphase turbulence model solves a set of transport equations for each phase. This model is used to compute turbulence transfer among the phases. This turbulence model is used for our application and the $k-\varepsilon$ transport equations are given in Equations (4.13) and (4.14).

$$\begin{aligned}\frac{\partial}{\partial t}(\alpha_q\rho_q k_q) + \nabla\cdot(\alpha_q\rho_q\vec{U}_q k_q) \\ = \nabla\cdot\left(\alpha_q\frac{\mu_{t,q}}{\sigma_k}\nabla k_q\right) + (\alpha_q G_{k,q} - \alpha_q\rho_q\varepsilon_q) + \sum_{l=1}^{N} K_{lq}(C_{lq}k_l - C_{ql}k_q) \\ - \sum_{l=1}^{N} K_{lq}(\vec{U}_l - \vec{U}_q).\frac{\mu_{t,l}}{\alpha_l\sigma_l}\nabla\alpha_l + \sum_{l=1}^{N} K_{lq}(\vec{U}_l - \vec{U}_q).\frac{\mu_{t,q}}{\alpha_q\sigma_q}\nabla\alpha_q\end{aligned} \quad (4.13)$$

$$\begin{aligned}\frac{\partial}{\partial t}(\alpha_q\rho_q\varepsilon_q) + \nabla\cdot(\alpha_q\rho_q\vec{U}_q\varepsilon_q) \\ = \nabla\cdot\left(\alpha_q\frac{\mu_{t,q}}{\sigma_\varepsilon}\nabla\varepsilon_q\right) \\ + \frac{\varepsilon_q}{k_q}\Bigg[C_{1\varepsilon}\alpha_q G_{k,q} - C_{2\varepsilon}\alpha_q\rho_q\varepsilon_q \\ + C_{3\varepsilon}\left(\sum_{l=1}^{N} K_{lq}(C_{lq}k_l - C_{ql}k_q) - \sum_{l=1}^{N} K_{lq}(\vec{U}_l - \vec{U}_q).\frac{\mu_{t,l}}{\alpha_l\sigma_l}\nabla\alpha_l \right. \\ \left. + \sum_{l=1}^{N} K_{lq}(\vec{U}_l - \vec{U}_q).\frac{\mu_{t,q}}{\alpha_q\sigma_q}\nabla\alpha_q\right)\Bigg]\end{aligned} \quad (4.14)$$

The model parameters proposed by Launder and Spalding [FLUG] are used:

$C_{1\varepsilon} = 1.44$ $C_{2\varepsilon} = 1.92$ $C_{3\varepsilon} = 1.3$

$\sigma_\varepsilon = 1.3$ $\sigma_k = 1$ $\mu_t = 0.09\rho k^2/\varepsilon$

More details about these transport equations are given in FLUENT User's Guide [FLUG].

4.2.2.2 Source terms

In order to quantify the mass transfer between flue gases and the solid CO_2 deposit, the classical nucleation theory described in Chapter 2 is used. The mass transfer prediction defines the source terms of the conservation equations for each primary and secondary phases. According to the nucleation theory, the mass transfer from the parent to the new phase occurs by both nucleus formation and growth. In order to simplify the model, the nucleation process is assumed to occur by homogeneous spherical nucleation neglecting the effect of the fin surface and impurity presence during the nucleation process. In fact, nucleus formation at the fin surface occurs by heterogeneous nucleation as seen in the theory introduced in Chapter 2 and experimental results presented in Chapter 3. This assumption is taken into account to simplify the source term calculation algorithm, which takes four times more processing time in the case of heterogeneous nucleation calculation. In addition, the mass transfer between the two phases is assumed to be a one-way transfer occurring from the gas to solid phase. The CO_2 sublimation from the solid deposit when its surface temperature becomes higher than the sublimation temperature is not taken into account. For each iteration, the mass transfer is calculated as a function of the flue-gas and solid CO_2 properties. According to the homogeneous nucleation theory, the mass transfer rate $\dot{m}_{CO_2\to s}$ $(kg.m^{-3}.s^{-1})$ from the gas to the solid phase is calculated as in Equation (4.15).

$$\dot{m}_{CO_2\to s} = \frac{4}{3}\pi\rho_s I r_c^3 + 4\pi\rho_s\eta\bar{r}^2\frac{\partial\bar{r}}{\partial t} \quad (4.15)$$

Where ρ_s is the solid CO_2 density calculated using Equation (15) of Chapter 1. I is the nucleation rate (#.m^{-3}.s^{-1}) calculated by Equation (2.21). r_c (m) is the critical radius of the spherical nucleus calculated using Equation (2.16). η is the number of solid CO_2 nucleus

formed in the finite volume from the beginning of the frosting cycle and $\bar{r}\ (m)$ is the average CO_2 nucleus radius that is formed in the finite volume. $\frac{\partial \bar{r}}{\partial t}\ (m.s^{-1})$ is the nucleation growth rate calculated by Equation (2.35). The mass transfer rate is calculated for conditions where CO_2 is supersaturated in the given volume. Otherwise, the mass transfer rate is equal to zero.

$$\eta = \sum_{t=0}^{t} I(t) \tag{4.16}$$

Therefore, the mass source terms of the continuity equations are given in Equation (4.17). In each finite volume, the mass of CO_2 lost by the gas phased is added to the solid phase.

$$\vartheta_{ms} = -\vartheta_{m\,fg} = \dot{m}_{CO_2 \to s} \tag{4.17}$$

As well, the source term of component equation for the vapor CO_2 of the primary phase is calculated by Equation (4.18).

$$\vartheta_{Y_{fg}^{CO_2}} = -\dot{m}_{CO_2 \to s} \tag{4.18}$$

The momentum source terms of the flue-gas phase and the solid deposit phase are given respectively in Equations (4.19) and (4.20).

$$\vartheta_{u\,fg} = -\dot{m}_{CO_2 \to s}\, \vec{u}_{fg} \tag{4.19}$$

$$\vartheta_{u\,s} = \dot{m}_{CO_2 \to s}\, \vec{u}_{s} \tag{4.20}$$

Where $\vec{u}_{fg}$ and $\vec{u}_s\ (m.s^{-1})$ are the velocity vectors of the two phases.

The energy source terms for both phases are given in Equations (4.21) and (4.22).

$$\vartheta_{h\,fg} = -\dot{m}_{CO_2 \to s}\, h_{CO_2} \tag{4.21}$$

$$\vartheta_{h\,s} = \dot{m}_{CO_2 \to s} \left(h_{CO_2} + \Delta H_{sub}\right) \tag{4.22}$$

$h_{CO_2}\ (J.kg^{-1})$ is the vapor CO_2 enthalpy in the flue gases and ΔH_{sub} is the CO_2 latent heat of sublimation at the given partial pressure (Figure 9 of Chapter 1).

These source terms are calculated and added to the conservation equations by using the User Defined Function interface provided by FLUENT [FLUDF].

4.2.3 Boundary and initial conditions

The CO_2 frosting modeling is performed for the conditions of the experimental test taking into account flue gases with 15% v/v of CO_2 concentration at the domain inlet. Inlet flue-gas and tube temperatures are also considered equal to the experimental measurements in order to compare the simulation and experimental results.

4.2.3.1 Velocity Inlet boundary

In order to take into account the periodic aspect of the fin-and-tube heat exchanger, a first simulation is performed predicting the velocity, the temperature, and CO_2 concentration profile at the domain outlet. These profiles are used as inlet boundary conditions for the transient model predicting the frost formation. As the experimental measurements, the average velocity, the vapor CO_2 molar concentration, and the flue-gas temperature at the domain inlet are considered as follows:

$$\bar{Y}_{in,fg}^{CO2} = 15\%\ v/v$$

$$Y_{in,fg}^{N_2} + Y_{in,fg}^{CO_2} = 1$$

$$\bar{u}_{fg,in} = 0.27\ m.s^{-1}$$

$$T_{fg,in} = -98.8°C$$

$$\alpha_s = 0$$

The solid CO_2 volume fraction at the inlet boundary is considered to be zero. In Figures 4.4 and 4.5 are represented the flue-gas velocity and CO_2 concentration profiles at the domain inlet.

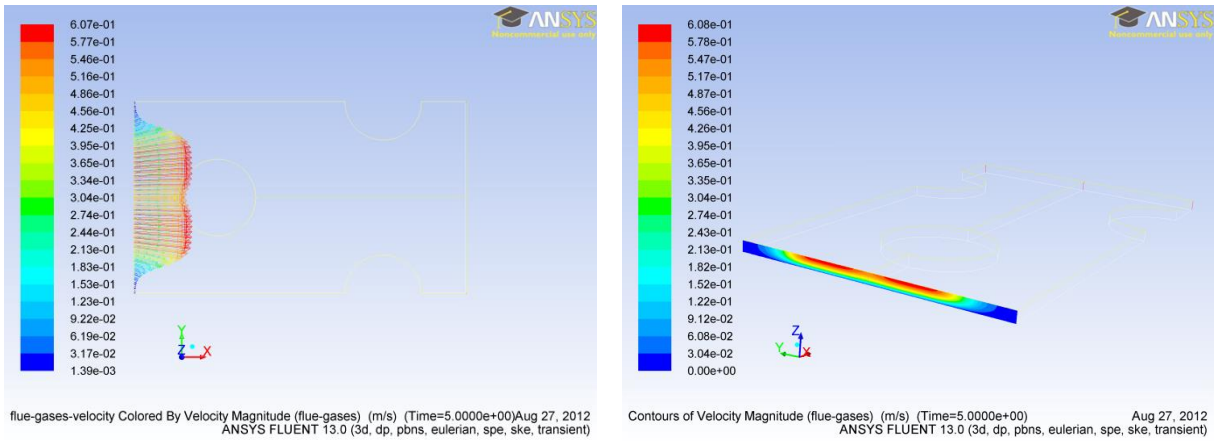

Figure 4.4: Flue-gas inlet velocity profile taking into account the pre-fin region.

These profiles show the velocity and concentration distributions as if a similar domain exists upstream the computational domain. The effect of pre-domain tubes and fin is well visible on the plotted profiles.

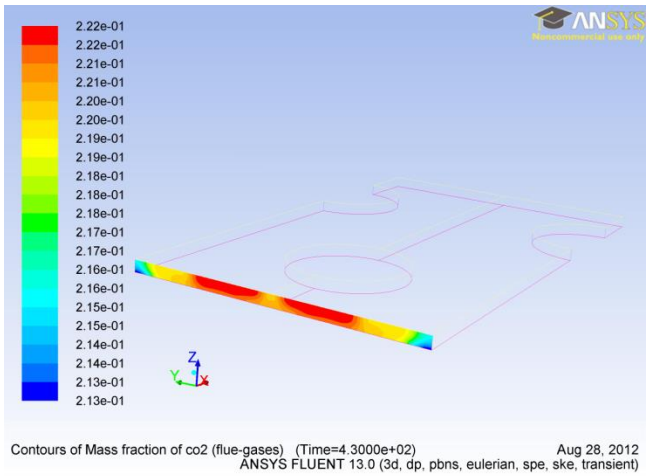

Figure 4.5: Flue-gas inlet CO_2 mass fraction profile.

4.2.3.2 Fin: shell conduction boundary

The fin is considered as a stationary aluminum wall of 0.1-mm thickness. Since the conduction in the planer direction of the fin is so important in this model, the shell conduction approach is used. The shell conduction approach is provided by FLUENT [FLUG] and is used to model thin sheets taking into account the wall thermal resistance. The fin temperature profile is plotted in Figure 4.6 before the frosting cycle beginning and this profile is used as an initial condition of CO_2 frosting cycle. The temperatures at the fin-tube interferences are considered to be equal to the tube temperatures.

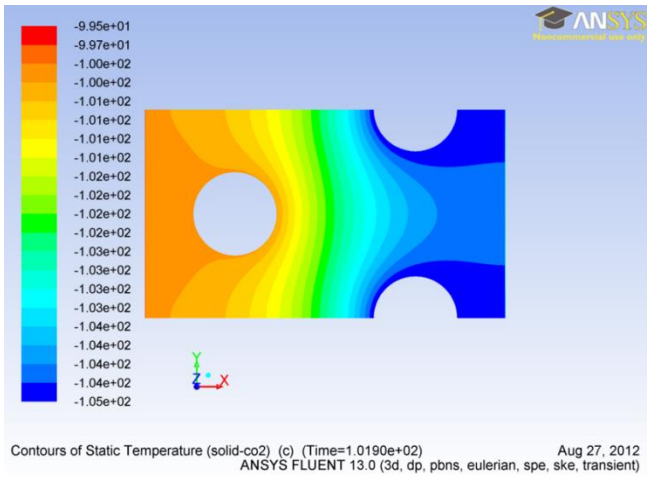

Figure 4.6: Fin temperature profile.

4.2.3.3 Tubes: stationary wall boundary

The two tubes in the computational domain are considered as copper stationary walls at constant temperatures. The first tube near the flue-gas inlet is considered to be at -100.2°C equal to the measured refrigerant temperature at the tested heat-exchanger refrigerant outlet. The second tube, near the flue-gas outlet, is considered to be at -104.5°C equal to the measured refrigerant temperature at the tested heat-exchanger refrigerant inlet.

4.2.3.4 Symmetry boundary

Two vertical and one horizontal symmetry planes are considered for the computational domain. At these surfaces, the normal velocity and normal gradients of all variables of both phases are equal to zero.

4.2.3.5 Pressure outlet

A constant static pressure is specified at the flue-gas outlet of the computational domain. This pressure is assumed to be equal to -10 Pa gauge. Backflow conditions are specified since the flow reverses its direction downstream the second tube during the solution process.

4.3 Simulation results and comparison with experimental data

In this paragraph, the results of the CO_2 frost behavior and property modeling are presented. The simulation is performed with a time step of 0.1 s and with a total flow time of 100 s. This simulation is conducted only to predict the frost formation during the first frosting period able to predict the homogeneity of the frost layer all over the computational domain. The frost deposit behavior, its thickness, the mass transfer rate, its local density, its average density, and the total cooling capacity are presented.

4.3.1 Solid CO_2 frost behavior

The presence of the frosted solid phase into the domain is quantified by using the volume fraction of the secondary phase term. For a given cell, when $\alpha_s = 1$ the cell is considered as filled fully with the solid phase and when $0 < \alpha_s < 1$ the cell contains a mixture of both flue-gas and solid CO_2 phases. Hence, the frosting process is tracked by the evolution of the solid CO_2 volume fraction into the domain. In Figure 4.7 is represented the evolution of the frost layer on the simulated two-row fin-and-tube heat exchanger. The presence of the frost layer is identified considering a solid volume fraction greater than 10^{-5}.

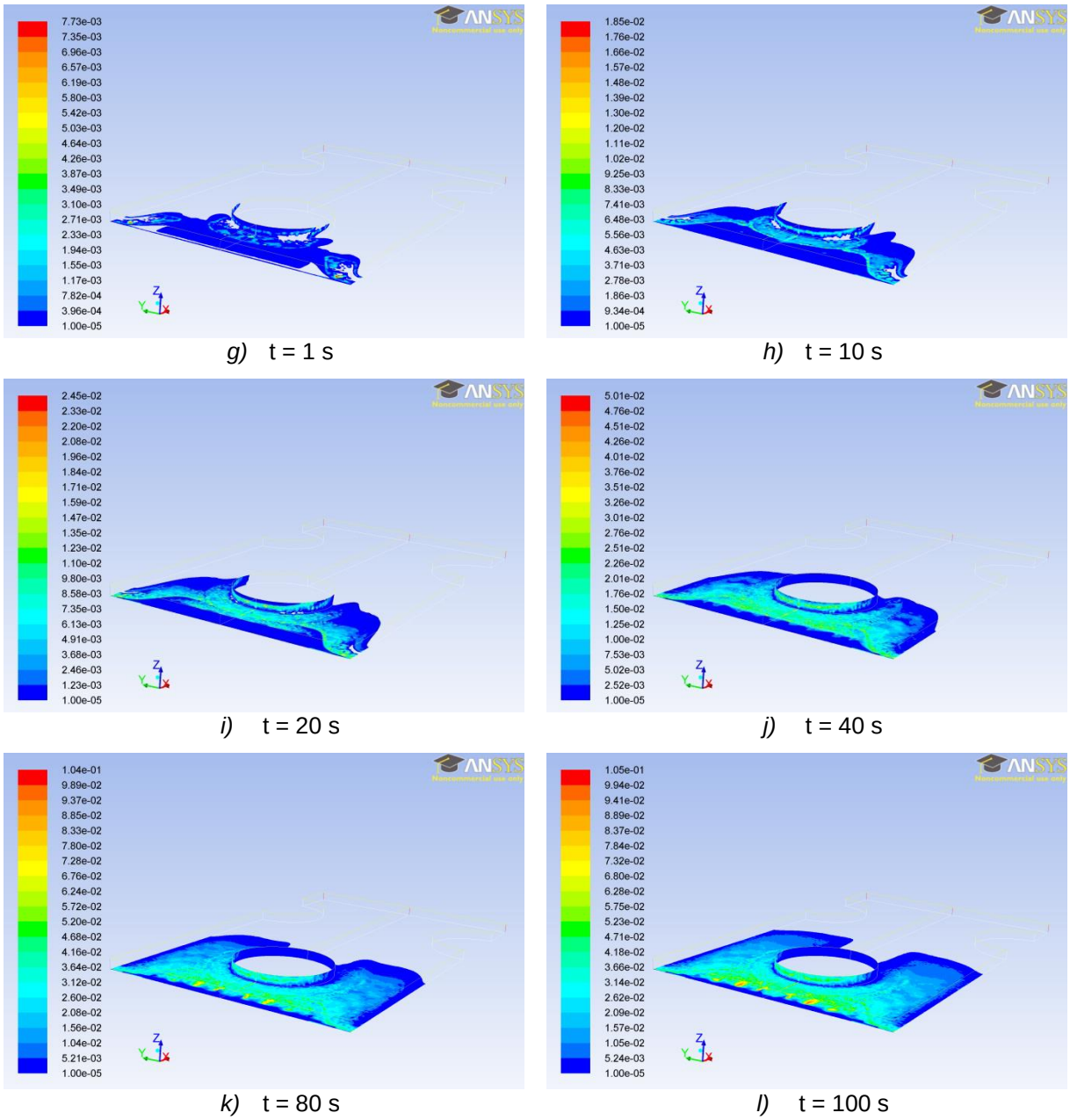

Figure 4.7: Frost layer evolution on the two-row fin-and-tube heat-exchanger surface.

The evolution of the CO_2 frost layer formation is observable. The frost layer appears at the domain inlet (on the fin and the first tube) and it spreads inwardly the domain. The densification of the existing layer is identified by the evolution of the secondary phase volume fraction as seen in Figure 4.7. Since the CO_2 is frosted at the heat-exchanger inlet, its concentration in the flue gases decreases, limiting the frosting process near the outlet for these simulated conditions.

In order to evaluate the ability of this CFD model to predict the frost layer behavior as a function of the heat-exchanger surface and flow conditions, a simulation is performed considering a higher flue-gas inlet velocity equal to 0.41 $m.s^{-1}$. The solid volume fraction profile at the fin and tube surfaces is plotted in Figure 4.8 for a flow time equal to 10 s.

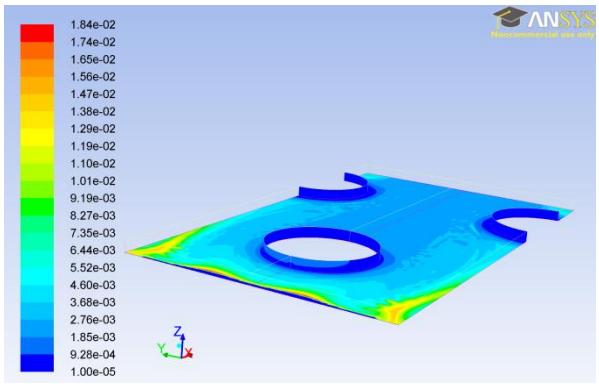

Figure 4.8: Frost layer profile for $\bar{u}_{fg,in} = 0.41\ m.s^{-1}$, t = 10 s.

For a higher flue-gas mass flow rate, the solid layer is formed all over the fin surface. By comparing Figures 4.8 and 4.7.b, the effect of the flue-gas inlet velocity is observable. In addition, it is clear that the frost formation at the first tube surface is lower for the higher flue-gas velocity due to the drag force that can tear out the CO_2 crystals at higher flow velocity.

4.3.2 Frost layer average thickness evolution

In order to evaluate the CO_2 frost thickness all over the modeled two-row heat exchanger, the secondary phase volume fraction is tracked. The local thickness is calculated by assuming that, for a given local surface fin, the frost level is at the middle section of the cell present on the frost layer surface. The calculation method of the local frost thickness is shown in Figure 4.9.

The frost deposit average thickness $\bar{\delta}_{fr}$ is calculated using Equation (4.23).

$$\bar{\delta}_{fr} = \frac{\sum \delta_{fr} \,.\, A_i}{\sum A_i} \tag{4.23}$$

Where δ_{fr} is the local frost thickness and A_i is the local fin surface. $\sum A_i$ is the total fin surface.

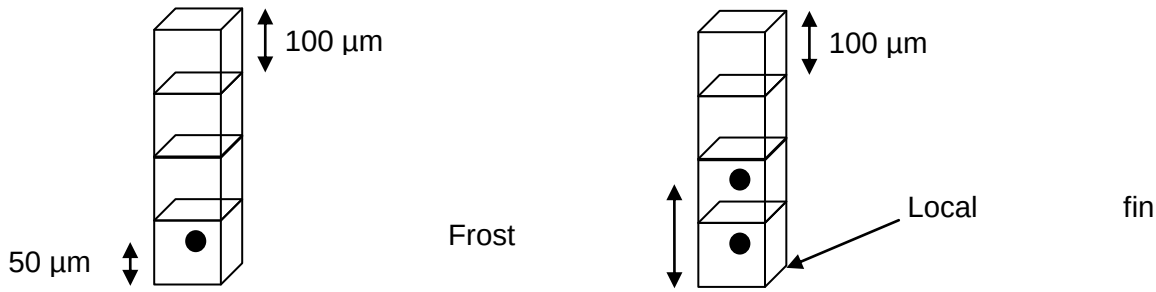

c) First CO_2 frost deposition d) CO_2 frost growth

Figure 4.9: Calculation method of the local frost thickness using the computational grid.

In Figure 4.10 are plotted the frost average thickness evolution for experimental and simulation results. It shows good agreement between the frost thicknesses predicted using this CFD model and the other one measured on the tested fin-and-tube heat exchanger (Chapter 3). The observable difference at the frosting cycle beginning is due to the method used to calculate the local frost thickness that is overestimated. During the first CO_2 frost deposition, the local frost thickness is assumed to be equal to 50 µm in the cells where the solid phase exists (Figure 4.9).

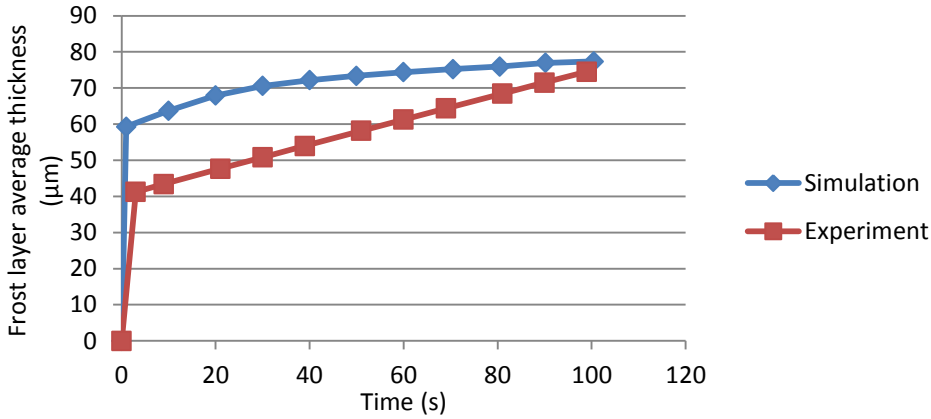

Figure 4.10: The frost average thickness evolution for model and experimental results.

The homogeneity of the frost surface, all over the computational domain, can be verified by calculating the standard deviation between the local frost thickness and the average frost thickness.

4.3.3 Solid CO_2 mass transfer evolution

The CO_2 nucleation rate in the entire computational domain is calculated after each time step by summing the mass source terms (Equation 4.17) calculated in each cell using the user defined function. The variations of the CO_2 nucleation rate predicted by the CFD model and measured during the experiment are plotted in Figure 4.11. These results show a good agreement between the predicted and the measured nucleation rate. Since the nucleation is assumed to be homogeneous, the CFD model slightly underestimates the mass transfer.

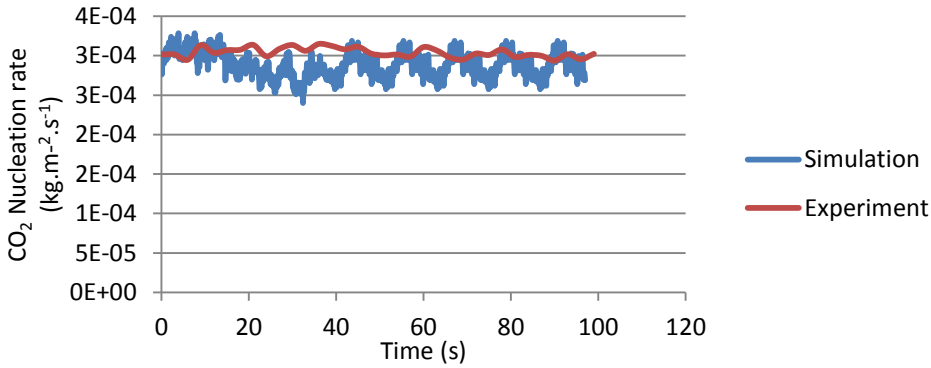

Figure 4.11: CO_2 nucleation rate evolution given by CFD model and experimental data.

The total mass evolution, $m_s(t)$, of the solid CO_2 layer formed into the simulated domain is calculated by Equation (4.24).

$$m_s(t) = \sum_{0}^{t} \dot{m}_s \, dt \tag{4.24}$$

Where $\dot{m}_s$ is the global nucleation rate at the time flow t and dt is the model time step. The total solid CO_2 mass evolutions for model and experimental results are plotted in Figure 4.12.

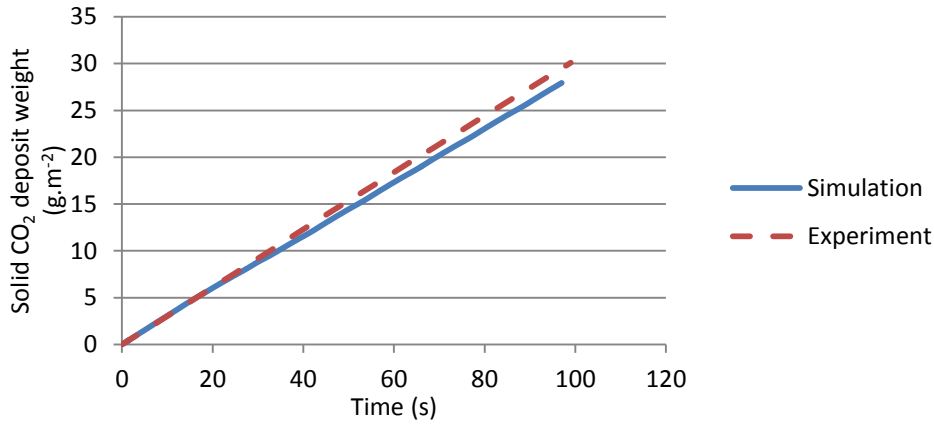

Figure 4.12: The total solid CO_2 mass evolution given by CFD model and experimental data.

The CFD model underestimates the CO_2 frosting by 7% relative error due to the usage of the homogeneous nucleation theory in lieu of the heterogeneous nucleation theory.

4.3.4 Frost layer average density evolution

The local frost average density profile is calculated in the computational domain as a function of the primary and secondary phase volume fractions and their densities, as given in Equation (4.25).

$$\rho_{fr} = (1 - \alpha_s)\rho_{fg} + \alpha_s \,.\, \rho_s \tag{4.25}$$

This local frost average density is plotted in Figure 4.13 at t = 100 s. After the primary frost deposition, the frost layer local density increases and reaches 300 $kg.m^{-3}$ at the domain inlet.

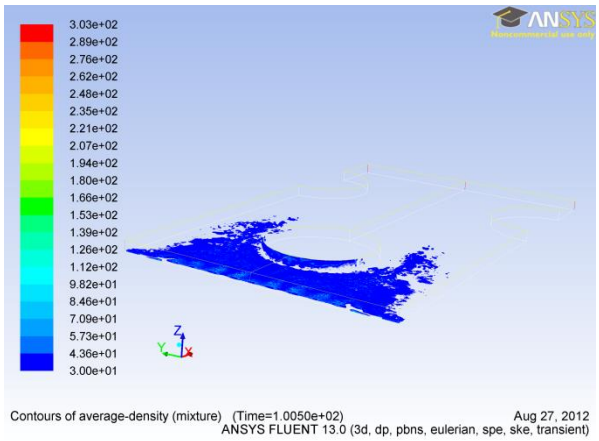

Figure 4.13: Local frost average density , t = 100 s.

The global frost deposit average density $\bar{\rho}_{fr}\ (kg.m^{-3})$ is calculated using Equation (4.26) where V_i is the local cell volume and $\sum V_i$ is the total volume of the frost layer.

$$\bar{\rho}_{fr} = \frac{\sum \rho_{fr} \,.\, V_i}{\sum V_i} \tag{4.26}$$

In Figure 4.14 is plotted the global frost deposit average density evolution. The densification process of the frost layer is observable showing the frost formation by CO_2 volume diffusion into the frost layer.

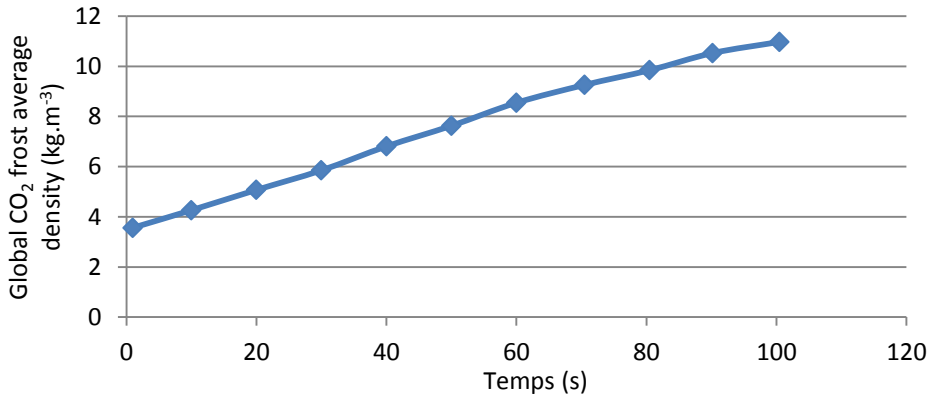

Figure 4.14: Global frost deposit average density evolution.

4.3.5 Local cooling capacity profile

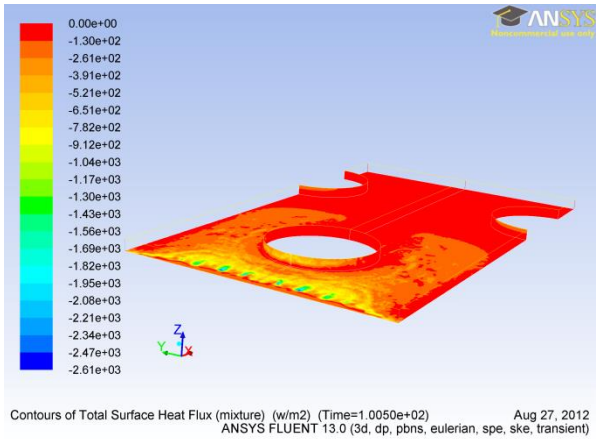

Figure 4.15: Local heat flux on the fin and tube surfaces, t = 100 s.

In Figure 4.15 is represented the surface heat flux (W.m^{-2}) transferred between the flue-gas flow and the tube-and fin-surfaces. The effect of the frosting process is observable since the heat flux is high at the fin surface zones where the CO_2 frost is formed and is growing by densification and thickness increase.

4.4 Conclusions

In this chapter a CFD multiphase model is proposed in order to predict the CO_2 frost formation and growth in a two-row fin-and-tube heat exchanger. By considering the flue-gas flow as the primary phase and the formed solid CO_2 as secondary phase, the mass, momentum, and energy transfer between these phases are calculated by adding source terms to the model conservation equations. The mass transfer is calculated using the classical nucleation theory. The model is validated by comparing the frost average thickness and weight with experimental values measured for the same frosting conditions.

The influence of the inlet flue-gas velocity on the CO_2 frost layer behavior is qualitatively identified. For a higher velocity, the solid deposit will form more rapidly all over the fin surface. The influence of the tube temperature, of the flue-gas inlet temperature, and of the CO_2 inlet concentration can be analyzed by using this model. In addition, the heat-exchanger structure effect on the frost formation can be identified.

Hence, this model is able to be used for CO_2 frosting heat-exchanger design and optimization. Many configurations of fin-and-tube heat exchangers can be compared using this model by a fin efficiency analysis under frosting conditions [PER03]. The simulation of different configurations with different aspect ratios and fin pitches will be able to identify the better configuration by comparing their exergo-energy performances. The optimal heat-

exchanger configuration depends on the frosting conditions like flue-gas velocity, inlet temperature, and CO_2 concentration. In addition, the effect of the refrigerant temperature can be analyzed by simulating, for a constant configuration and flue-gas conditions, the CO_2 formation and growing for different sets of tube temperatures. The optimal refrigerant gliding temperature will be able to ensure the CO_2 frosting at the higher exergo-energy performances. The refrigerant blend and flow distribution on the heat-exchanger tubes can be then determined. In addition to the exergy efficiency, the optimal configuration has to ensure the formation of a homogeneous deposit all over the heat exchanger.

References

[CUI11A] **J. Cui, W.Z. Li, Y. Liu, Z.Y. Jiang**, A new time- and space-dependent model for predicting frost formation, Applied Thermal Engineering, 31, 447-457, 2011.

[CUI11B] **J. Cui, W.Z. Li, Y. Liu, Y.S. Zhao**, A new model for predicting performance of fin-and-tube heat exchanger under frost condition, International Journal of Heat and Fluid Flow, 32, 249–260, 2011.

[FLUDF] **ANSYS, inc.**, ANSYS FLUENT UDF Manuel, Release 13.0, 2010.

[FLUG] **ANSYS, inc.**, ANSYS FLUENT User's Guide, Release 13.0, 2010.

[HE05] **Y.L. He, W.Q. Tao, F.Q. Song, W. Zhang**, Three-dimensional numerical study of heat transfer characteristics of plain plate fin-and-tube heat exchangers from view point of field synergy principle, International Journal of Heat and Fluid Flow, 26, 459-473, 2005.

[ISM99] **K.A.R. Ismail, C.S. Salinas**, Modeling of frost formation over parallel cold plates, International Journal of Refrigeration, 22, 425–441, 1999.

[LEE04] **Hyunuk Lee, Jongmin Shin, Samchul Ha, Bongjun Choi, Jaekeun Lee**, Frost formation on a plate with different surface hydrophilicity, International Journal of Heat and Mass Transfer, 47, 4881–4893, 2004.

[LEN06] **Kristian Lenić, Anica Trp, Bernard Franković**, Unsteady heat and mass transfer during frost formation in a fin-and-tube heat exchanger, Energy and the Environment, 35-48, 2006.

[NA04] **Byeongchul Na, Ralph L. Webb**, Mass transfer on and within a frost layer, International Journal of Heat and Mass Transfer, 47, 899–911, 2004.

[NA04B] **Byeongchul Na, Ralph L. Webb**, New model for frost growth rate, International Journal of Heat and Mass Transfer, 47, 925–936, 2004.

[PER03] **Thomas PERROTIN, Denis CLODIC**, Fin efficiency calculation in enhanced fin-and-tube heat exchangers in dry conditions, International Congress of Refrigeration, Washington, D.C., 2003.

[SEK04] **Deniz Seker, Hakan Karatas, Nilufer Egrican**, Frost formation on fin-and-tube heat exchangers.Part I—Modeling of frost formation on fin-and-tube heat exchangers, International Journal of Refrigeration, 27, 367–374, 2004.

[TRO03] **Andrey Troshko**, Modeling Multiphase Flows with Heat and Mass Transfer, Fluent software training, UGM 2003.

[YAN04] **Dong-Keun Yang, Kwan-Soo Lee**, Dimensionless correlations of frost properties on a cold plate, International Journal of Refrigeration 27, 89–96, 2004.

[YAN05] **Dong-Keun Yang, Kwan-Soo Lee**, Modeling of frosting behavior on a cold plate, International Journal of Refrigeration, 28, 396–402, 2005.

[YAN06] **Dong-Keun Yang, Kwan-Soo Lee, Dong-Jin Cha**, Frost formation on a cold surface under turbulent flow, International Journal of Refrigeration, 29, 164–169, 2006.

Conclusions and perspectives

The post-combustion CO_2 antisublimation capture process is described. The CO_2 frosting heat-exchanger exergy optimization is able to improve the process performance. Heat-exchanger exergy analysis is introduced showing the optimization importance of the heat-exchanger structure and of the refrigerant blend gliding temperature. In addition, the effect of the CFX exergy optimization on the whole capture process is demonstrated by showing the effect of the process low temperature on the integrated cascade performance. Optimized heat-exchanger and refrigerant blends have to be able to ensure the appropriate gliding temperature through the separation process forming a homogeneous CO_2 deposit on the flue-gas side and maximizing the refrigerant evaporation temperatures. The minimum theoretical work required to separate CO_2 from flue gases is calculated for perfect and imperfect separation. This minimum work is used to calculate the global CO_2 capture-process efficiency. The gap existing in the solid CO_2 properties under triple point is closed. The solid CO_2 enthalpy, entropy, density, and heat conductivity are expressed by empiric equations developed by using several literature collected data. The CO_2 T-s diagram is plotted down to 140 K. The CO_2 capture using anti-sublimation process is presented using a $CO_2 – N_2$ psychrometric chart. The gas stream thermodynamic properties variation through the separation process is plotted on this diagram.

The classical nucleation theory is used in order to quantify the mass transfer rate between the flue-gas stream and the crystallized CO_2 layer. The anti-sublimation process occurs according to the nucleation process. Primary homogeneous and heterogeneous nucleations and secondary nucleation are exposed from thermodynamic and kinetic aspects. By using this theory, the nucleation rate, the critical radius of new formed nucleus, and the mass transfer rate between the two phases can be calculated. The effect of the crystallized CO_2 affinity with solid surfaces is determined. For heterogeneous nucleation, a good affinity between solid CO_2 and chilled surfaces leads to improve the nucleation process by increasing the nucleation rate and decreasing the free energy change able to form new embryos. Then, a lower supersaturation ratio is able to frost down CO_2 for heterogeneous nucleation. The main parameters that affect the nucleation process are identified. A sensitivity analysis has been performed in order to evaluate the effect of the CO_2 concentration and the flue-gas temperature variations on the CO_2 frosting conditions. The variation of the nucleation rate and critical crystal radius as a function of CO_2 concentration and temperature variation is analyzed. A high variation of the mass transfer and deposit morphology is induced by supersaturation perturbation. The supersaturation ratio is a key parameter that has to be controlled in order to control the mass transfer from the parent phase to the new phase. The effect of other parameters like gas stream velocity, molecular diffusion, and frost layer porosity, density, and thermal conductivity have been exposed and discussed.

Based on the conducted experimental study, the CO_2 visualization using high magnification proves that the antisublimation proceeds according to the classical nucleation theory. A good affinity between solid CO_2 and heat-exchanger aluminum fins is observed. This affinity, shown by a low contact angle between the two bodies, proves that the aluminum fins are suitable for the CO_2 capture application since they enhance the nucleation process. For high (15% v/v) and low (3% v/v) CO_2 concentrations, heterogeneous spherical embryos are formed showing the independence of the nucleation phenomenon from the solute concentration. Contrariwise, the visualization of the solid deposit at low magnification ratios shows an aspect difference between solid layers formed at high and low CO_2 concentrations. At high concentrations, the deposit has a granular aspect while it has multi-directional lattice

morphology at low concentrations. Hence, the deposit formed at low solute concentration is relatively porous compared to the deposit formed at high concentrations.

Three periods of deposit formation and growth are identified. The first deposit takes place as a primary heterogeneous nucleation and is directly affected by the super-saturation ratio. For higher super-saturation ratio, more solid embryos are able to form enhancing the mass transfer during the second evolution period. The second evolution period occurs at constant deposit thickness for which the mass transfer proceeds by CO_2 diffusion in the solid porous layer. During this period the average density of the deposit increases; this in turn increases the deposit thermal conductivity. This densification leads to the decrease in the frost surface temperature allowing the beginning of the third frost evolution period, which takes place at constant density. Quantitative measurements show that the nucleation rate depends mainly on the super-saturation ratio. A higher solid layer average density is formed at low super-saturation frosting conditions. When the frosting cycle begins, the super-cooling of the fin surfaces leads to enhance the heterogeneous nucleation and the formation of more homogeneous and dense deposit.

In order to predict the CO_2 frost formation and growth in a two-row fin-and-tube heat exchanger, a CFD multiphase model is proposed and validated by comparing the predicted frost average thickness and weight with experimental results. Considering the flue gases as a primary phase and the solid CO_2 crystals as a secondary precipitating phase, the interaction between them is represented by adding mass, momentum, and energy source terms to each phase conservation equations. The mass transfer source term is calculated using the classical nucleation theory. This model originality lays in its ability to predict frost layer depending on the surface structure. The influence of the inlet flue-gas velocity on the CO_2 frost layer behavior is qualitatively identified. For a higher velocity, the solid deposit will form more rapidly all over the fin surface. The influence of the tube temperature, of the flue-gas inlet temperature, and of the CO_2 inlet concentration can be analyzed by using this model.

Hence, this model is able to be used for CO_2 frosting heat-exchanger design and optimization. Many configurations of fin-and-tube heat exchangers can be compared using this model by a fin efficiency analysis under frosting conditions. Many fin-and-tube heat-exchanger configurations have to be compared to identify the effect of the structure aspect ratio and fin pitch on the heat and mass transfer efficiency and on the homogeneity of the solid depository. The comparison of different configurations will be made by using exergo-energy performance criteria. The optimal heat-exchanger configuration depends on the frosting conditions like flue-gas velocity, inlet temperature, and CO_2 concentration. In addition, the effect of the refrigerant temperature has to be analyzed by simulating, for a constant configuration and flue-gas conditions, the CO_2 formation and growing for different sets of tube temperatures. The optimal refrigerant gliding temperature will be able to ensure the CO_2 frosting at the higher exergo-energy performances. The refrigerant blend and flow distribution on the heat-exchanger tubes can be then determined. In addition to the exergy efficiency, the optimal configuration has to ensure the formation of homogeneous deposit all over the heat exchanger.

The effective thermal conductivity of the CO_2 solid layer has to be calculated using the multiphase model. Contrariwise to the experimental study, the frost surface temperature can be calculated during the frost formation. The effective thermal conductivity can be correlated as a function of the average frost density and porosity. As well, the mass transfer by volume diffusion and surface deposition has to be studied.

Experimental study by coupling the refrigerant blend evaporation inside the heat-exchanger tubes and the flue-gas cooling and CO_2 precipitation on the external finned surface is necessary to understand the real CFX operating conditions. After the calculation of the flue-gas temperature glide by using the multiphase model, refrigerant blends have to be defined in order to ensure optimal exergo-energy efficiency. The study of the refrigerant side

pressure drop is important since it affects the evaporation temperature. This pressure drop has to be studied for the heat-exchanger tubes and elbows, and it can be controlled for ensuring the optimal gliding temperature profile. It is important to note that the temperature difference between the heat-exchanger inlet and outlet can reach 20 K. The effect of the CO_2 frost formation on the global heat transfer between flue gases and the refrigerant has to be identified. The cooling capacity variation during a CO_2 frosting cycle affects the integrated cascade operating conditions and it affects the overall process efficiency. In addition, in order to improve the process efficiency, the CO_2 frosting cycle has to be controlled by identifying the optimal operating mode. The frosting cycle period has to be defined by taking into account the degradation of the CO_2 separation rate, the total heat transfer through the heat exchanger, and the pressure drop at the flue-gas side induced by the frost formation and growth. Hence, the CFX switching between frosting, defrosting, and conditioning operating modes has to be identified.

Eventually, the economic aspect has to be taken into account while designing the CO_2 frosting heat exchanger. For this purpose, an exergo-economic study has to be performed. The use of exergy optimization is not sufficient. In fact, the increase in the average refrigerant evaporation temperature ensuring a functioning at low-supersaturation ratio leads to decrease the CO_2 nucleation rate ($kg.m^{-2}.s^{-1}$). Then more frosting surfaces will be required to ensure constant rate CO_2 separation. An optimum nucleation rate will be defined taking into account the exergy performance of the process and its economic competitiveness with other separation processes.

Etude et modélisation du givrage du CO_2 sur un évaporateur à glissement de température

RÉSUMÉ :

Le captage et le stockage du dioxyde de carbone est la solution pour réduire les émissions de CO_2 des grandes sources fixes. Le captage du CO_2 par « Antisublimation » consiste à refroidir les fumées sous le point triple du CO_2 qui passe alors directement de la phase vapeur à la phase solide. La variation de la concentration de CO_2 induit une variation de la température d'environ 20 K à travers l'échangeur de chaleur. Son optimisation exergétique est une nécessité pour améliorer la séparation du CO_2 et la performance énergétique du procédé.

De nouvelles équations sont proposées pour calculer les propriétés thermodynamiques du CO_2 à l'équilibre solide-vapeur qui sont jusqu'alors mal définies. Un diagramme psychrométrique CO_2-N_2 est développé pour représenter le glissement de température. L'étude du transfert de chaleur et de masse côté fumées nécessite la compréhension de l'antisublimation. La théorie classique de la nucléation est adoptée pour identifier les paramètres qui influent sur le transfert de masse et de la morphologie du givre. Une étude expérimentale qualitative et quantitative est effectuée pour étudier la formation de givre et sa dépendance vis-à-vis de la sursaturation et de la concentration du soluté. L'observation du CO_2 solide sous 200x de grossissement prouve que l'antisublimation se fait par nucléation hétérogène. Un modèle CFD transitoire multi-phase et multi-composant est proposé pour simuler la formation du givre et sa croissance en fonction de la structure de l'échangeur et des conditions d'écoulement.

Mots clés : Captage de CO_2, antisublimation, exergie, CO_2 solide, nucléation, diagramme psychrométrique, CO_2-N_2, glissement de température, échangeur, modèle diphasique transitoire.

Study and modeling of the CO_2 frosting on a gliding temperature evaporator

ABSTRACT:

The carbon dioxide capture and storage is the solution to reduce CO_2 emissions from large stationary sources. CO_2 capture by "Antisublimation" consists in cooling flue gases under the CO_2 triple point, which goes then directly from vapor to solid phase. The CO_2 concentration variation induces a temperature variation of about 20 K through the heat exchanger. The exergy optimization of the heat exchanger is a necessity to improve the CO_2 separation and the process energy performance.

Since the CO_2 properties under the triple point are not defined, new equations are proposed to calculate CO_2 thermodynamic properties for solid-vapor equilibrium. A CO_2-N_2 psychrometric chart is developed to represent the flue-gas gliding temperature. The study of the flue–gas side heat and mass transfer requires antisublimation understanding. The classical nucleation theory is adopted to identify parameters that affect the mass transfer and frost morphology. A qualitative and quantitative experimental investigation is performed to study the frost formation and its dependence on the supersaturation and solute concentration. The solid CO_2 observation under 200x magnification ratio proves that antisublimation occurs by heterogeneous nucleation. A CFD multiphase and multi-component transient model able to predict the frost formation and growth as a function of the heat-exchanger structure and flow conditions is proposed.

Keywords : CO_2 capture, antisublimation, exergy, solid CO_2, nucleation, psychrometric chart, CO_2-N_2, gliding temperature, heat exchanger, transient multiphase model.

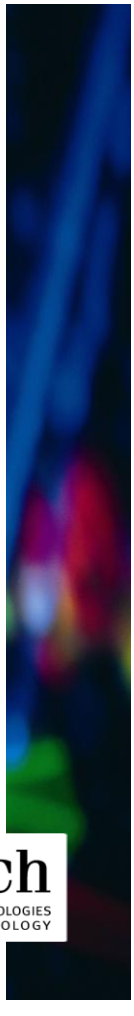

MINES ParisTech

ParisTech
INSTITUT DES SCIENCES ET TECHNOLOGIES
PARIS INSTITUTE OF TECHNOLOGY